Transmission Lines Loaded with Electrically Small Resonators: Modeling, Analysis and Applications to Microwave Sensors

Lijuan Su

Universitat Autònoma de Barcelona

Transmission Lines Loaded with Electrically Small Resonators: Modeling, Analysis and Applications to Microwave Sensors

Ph.D. Thesis written by

Lijuan Su

Supervised by

Ferran Martín Antolín

Bellaterra (Cerdanyola del Vallès), July 2017

cimitec

Universitat Autònoma de Barcelona

Transmission Lines Loaded with Electrically Small Resonators: Modeling, Analysis and Applications to Microwave Sensors

Ph.D. Thesis

Author:

Lijuan Su

Supervisor:

Prof. Ferran Martín

Universitat Autònoma de Barcelona

Doctorado en Ingeniería Electrónica y de Telecomunicación

Departamento de Ingeniería Electrónica, UAB

Centro de Investigación en Metamateriales para la Innovación en Tecnologías Electrónica y de Comunicaciones, CIMITEC – UAB

cimitec

Bellaterra (Cerdanyola del Vallès), July 2017

Universitat Autònoma de Barcelona

The undersigned, Dr. Ferran Martín Antolín, Professor of the Electronics Engineering Department (Engineering School) of the Universitat Autònoma de Barcelona,

CERTIFIES:

that the thesis entitled "Transmission Lines Loaded with Electrically Small Resonators: Modeling, Analysis and Applications to Microwave Sensors," has been written by Lijuan Su under his supervision.

And hereby to acknowledge the above, sign the present.

Ferran Martín Antolín Lijuan Su

Universitat Autònoma de Barcelona

Doctorado en Ingeniería Electrónica y de Telecomunicación

Departamento de Ingeniería Electrónica, UAB

Centro de Investigación en Metamateriales para la Innovación en Tecnologías Electrónica y de Comunicaciones, CIMITEC – UAB

Bellaterra (Cerdanyola del Vallès), July 2017

Contents

Acknowledgments

Firstly, I would like to express my sincere gratitude to my supervisor Prof. Ferran Martín, who guided me during the road towards the world of metamaterials/microwaves and gave me innovative ideas, motivations, and continuous support on research, without whom, the completion of this thesis would not be possible. Also, I would like to thank my colleagues from CIMITEC, the Department of Electronic Engineering and Escola d'Enginyeria: Pau Aguilà, Cristian Herrojo, Jordi Selga, Jordi Bonache, Ferran Paredes, Paris Vélez, Gerard Zamora, Armando Fernández (exchange postdoctoral researcher from Universidad de Sevilla), and former members of CIMITEC: Jordi Naqui, Marco Orellana and Simone Zuffanelli. Specially, I am very grateful to Javier Mata, who spent lots of time patiently explaining and helping me to solve the problems I encountered during the realization of my PhD thesis. My sincere thanks also go to Anna Cedenilla, especially for her warm help during the hardest time I experienced in Barcelona when a car accident happened to me.

Besides, I am also grateful to the people in the Department of Electronics Engineering, Universitat Autònoma de Barcelona. Thanks also give to China Scholarship Council for supporting me to conduct my PhD in Universitat Autònoma de Barcelona.

Last but not least, I would like to thank my family and my friends. Words cannot express how grateful I am to my parents and my brother. At the end, a special gratitude to you, Gerard, who suffered my difficult and stressful moments during the writing of my thesis, and who brings brightest sunshine into my life. If I know what love is, it is because of you!

Lijuan

July, 2017

Barcelona

Summary

This thesis focuses on the modeling, analysis and applications of planar transmission lines loaded with electrically small resonators as microwave sensors. The sensing techniques are based on frequency splitting and frequency variation. For frequency splitting strategy, structures could be used as comparators and microwave sensors. The principle is, for structures of transmission lines loaded with two identical resonators, transmission zero splits to two if one of the resonators is loaded with a sample under test (SUT) which is different from the loaded reference material in the other resonator. Otherwise, only one transmission zero exists. For dielectric characterization, a step with materials possessing known dielectric properties to calibrate the structure is needed before characterizing the SUTs. Through different output results by loading SUTs, with the relation to variable causing the changes, the dielectric permittivities of SUTs could be obtained. As for frequency variation, an accurate circuit model including not only the loss of the substrate, but also the losses of the CSRR (conductive loss from conductive strip and loss from substrate), is proposed, and analytical expressions to obtain the dielectric constant and loss tangent of SUTs are provided.

Planar transmission lines loaded with electrically small resonators as material characterization have the advantages of easy to fabricate, low manufacturing cost, compactness in size and simple sample preparation, thus it is the method utilized in this thesis to design different structures. The electrically small resonators used throughout the thesis are split ring resonators (SRRs), complementary split ring resonators (CSRRs), stepped impedance resonators (SIRs) and the complementary counterpart – slot-SIRs. These resonators are subwavelength particles, in contrast to the usual transmission line resonators, typically one tenth of the guided wavelength or less at their fundamental resonant frequencies. Therefore, high level of miniaturization is expected by using these particles. In addition, they have strong response to an electromagnetic field and their properties are substantially affected by materials under test (MUTs).

Several common transmission lines loaded with those electrically small resonators have been studied in this thesis. Their lumped element equivalent circuit models have been proposed and analyzed, through which analytical expressions to predict transmission zeros are deduced as well. Among all the proposed structures serving as sensing purpose, it is noticeable that the mutual coupling between the loaded resonators forming the pair has the effect of degrading the sensitivity. Topologies to prevent this inter-resonator coupling are introduced, i.e., microstrip section with each line loaded with a CSRR or a SIR, in a splitter/combiner configuration, and a microstrip line loaded with two SIRs, in cascade configuration. For the splitter/combiner configuration, each resonator individually coupled to a line, if perturbing the resonators by extra dielectrics, the new emerging transmission zeros positons are influenced by an interfering phenomenon of two resonator-loaded lines (affected by the electric length of the microstrip section). In order to obtain enhanced sensitivity for small perturbations, the short circuit to ground caused by resonating the shunt circuit branch (where the resonator locates) has to be translated to the input/output, which provide a condition to get

optimum electric length of these lines, to obtain improved sensitivity. As for the cascade configuration, two SIRs separate from each other through a transmission line with a certain electric length (long enough to avoid inter-resonator coupling). From the equivalent circuit model, the positions of two transmission zeros do not change even if the line in-between the two SIRs is different when two resonators are perturbed. But if the electric length of the transmission line in-between the SIRs is set to be π, the circuit model could be simplified to the same as the structure with two SIRs directly in contact with the line in the same junction, without mutual inter-resonant coupling, thus improve the sensitivity.

In order to demonstrate applications as comparators and sensors, proof-of-concept prototypes have been fabricated and experiments have been performed, validating the structures and application purposes. The results from the measurements are in good agreement with lumped equivalent circuit model simulations and EM simulation results.

Chapter 1

Introduction

Motivations

Microwave sensing is a promising and developing technology which has been successfully used for various applications from industry, such as measuring solutions concentration and materials moisture content, to therapeutic medicine (for example discriminating normal and malignant cancerous tissues in human body), and to biomedical analysis including monitoring glucose concentrations for diabetic patients, etc. Among them, characterization of dielectric property of a material plays an important role, since it is intrinsic property of a material which depends on the physical phenomena and shows a typical behavior as a function of frequency. Thus microwave sensors could be utilized and be able to measure the response over a range of frequencies, from which the material can be characterized.

The microwave techniques for material characterization generally fall into non-resonant methods and resonant methods. Non-resonant methods are often used to get general knowledge of electromagnetic properties over a frequency range. However, accurate measurement of material properties is required for a number of applications in industry, medicine and in pharmaceuticals. Resonant techniques offer the potential for accurate measurement at a single or discrete set of frequencies. Besides, by applying the resonant methods in planar transmission line, unlike their counterparts by using resonant methods in coaxial or waveguide cavity which are normally very bulky or difficult to construct and in some cases destructive to materials, it provides advantages of compactness, robustness, ease of fabrication, high sensitivity and no destruction to materials under test.

This thesis focuses on the design, analysis, circuit modeling and applications of microwave sensors based on planar transmission lines loaded with electrically small resonators. One of the novelties of the proposed planar sensor concept is differential sensing, providing robustness against variations in ambient factors, since such changes are seen as common-mode perturbations. Besides, the use of planar transmission line makes the sensors easy to integrate with other circuit and gives high flexibility in terms of geometry.

This thesis is written as a compendium of articles. Therefore, most of the research has already been published in international journals and conference proceedings. The articles included in this thesis could be found in **Articles in the Ph.D. Thesis**. All the author's publications and contributions to conferences are listed in **Publications by the Author**. The work conducted during the realization of this thesis was carried out within the centre CIMITEC, which is a technology transfer centre and research group of Electronic Engineering Department of Universitat Autònoma de Barcelona. This thesis is also supported by the joint scholarship of China Scholarship Council and Universitat Autònoma de Barcelona under the grant number 201306950011.

Outline

This thesis is organized as follows:

Chapter 1 presents the motivation and the target of this thesis, the outline is listed as well.

Chapter 2 introduces the fundamental theory of dielectric properties of the materials. Several techniques for dielectric material characterization over microwave frequencies are mentioned, along with their advantages and disadvantages for different sensing applications. Then, emphasis is put on the explanation of planar transmission lines loaded with resonators, which is also the aim of this thesis. Firstly, commonly used planar transmission lines are described. After that, several types of electrically small resonators are introduced. To finalize this chapter, it provides the common sensing techniques normally used for microwave sensing. Among them, the methods of frequency splitting and frequency variation are the main principles for the microwave sensors and comparators designed throughout this thesis.

Chapter 3 proposes several structures of transmission lines loaded with electrically small resonators, which include a coplanar waveguide (CPW) loaded with a pair of split ring resonators (SRRs), a microstrip line loaded with a pair of complementary split ring resonators (CSRRs), coplanar waveguide/microstrip line loaded with stepped impedance resonators (SIRs), and coplanar waveguide loaded with slotted stepped impedance resonators (Slot-SIRs). Their lumped element equivalent circuit models are presented, which could offer superior accuracy and numerical reliability to validate the structures. Some comparisons of the equivalent circuit models among those structures and their mapping relations between the lumped elements are provided for better understanding of the structures. In addition, the effects of inter-resonator coupling between the resonators in one unit cell on the transmission zero frequencies and sensitivity of the structures are mentioned too.

Chapter 4 addresses some improved structures based on splitter/combiner configuration and cascade configuration, with the intention to prevent mutual inter-resonant couplings between the loaded pair of resonators. Two structures of splitter/combiner microstrip sections loaded with CSRRs and loaded with SIRs, respectively, are analyzed and their equivalent circuit models are proposed. According to the circuit models and several experiments conducted by perturbing the resonators, it is found that the optimum sensitivities could be achieved if the electrical lengths of the microstrip line sections satisfy certain conditions. Additionally, a microstrip line loaded with a pair of SIRs in cascade connection is also designed for avoiding inter-resonant coupling between SIRs, and condition for enhanced sensitivity is discussed as well.

Chapter 5 devotes to the applications of the proposed structures of transmission lines loaded with resonators, mainly for comparators and sensors as materials characterization. Firstly, based on frequency splitting strategy, the structures are normally loaded with a pair of resonators. The principle is that two transmission zeros appear when the two resonators are asymmetrically loaded. As comparators, the structures solely compare if the SUTs are the same as reference sample or not (one resonator loaded with known reference material, the other resonator loaded with SUT). In order to simultaneously detect several SUTs, three-

section splitter/combiner microstrip lines loaded respectively with CSRRs and with SIRs are introduced for multiple sensing validations. While in terms of the application as sensors for dielectric characterization, variations between the transmission zeros and magnitudes of the transmission zeros are used to calculate the permittivities of SUTs. Secondly, another sensing method is based on frequency variation. Accurate equivalent circuit model of a microstrip line loaded with a single CSRR is applied, including not only the losses of the substrate, but also losses in the loaded CSRR (the part from the substrate and the part from CSRR conductive copper), to calculate the complex permittivities of the samples. An improved structure by etching a liquid container on the ground plane surrounding the CSRR region is utilized to estimate the complex permittivities of liquids.

Chapter 6 summarizes the most relevant results and contributions in this thesis. Some future developments based on the exiting results are mentioned as well.

Chapter 2

Fundamentals of Microwave Sensors for Complex Permittivity Characterization of Materials

Complex permittivity is considered to be one of the most important physical properties of materials when they interact with external electromagnetic fields. Thus, accurate dielectric characterization of materials has gained significant attention in the recent decades. Numerous burgeoning applications cover from industry, chemistry, biomedical and other fields. Many techniques have been proposed for measuring the complex permittivity of materials. These techniques can be generally classified as non-resonant methods and resonant methods. Which one suits better for a desired application depending on the nature of materials under test (MUTs), both physically and electrically, the frequency of interest, and the required accuracy, etc.

This chapter is devoted to get knowledge about the dielectric properties of materials and the measurement and sensing techniques. Section 2.1 provides a brief introduction to the state-of-art applications of microwave sensors as materials characterization, a short description of general dielectric properties of materials included as well. In section 2.2, emphasis is put on the general introduction of different measurement techniques for material characterization, their advantages, limitations and application areas. Finally, section 2.3 is addressed to the explanation of planar transmission lines loaded with electrically small resonators, which is also the main method utilized throughout this thesis for sensing purpose. Specifically, the main focus is aimed at frequency splitting and frequency variation, through resonant perturbations. In addition, some typical transmission lines (including microstrip lines, coplanar waveguides) and electrically small resonators (including SRRs, CSRRs and SIRs) that are used throughout the design of the sensors in this thesis are mentioned as well.

2.1 Microwave sensors for material characterization

In the recent decades, interest in material characterization at microwave frequency has considerably increased for various applications in industry [1], chemistry [2,3], medicine [4,6] and biomedical area [7,8]. Electrical characteristics of materials depend on their dielectric properties, whose main parameter is the complex permittivity. It describes the material behavior when it is subjected to an external electromagnetic field. For most applications, properties such as material composition, moisture or water content, etc., of the sample under test carry valuable information by which the complex permittivity could be deduced, from which a material could be characterized.

In the food industry, the interest in dielectric properties of agricultural and food materials has been principally for predicting microwave heating rates [9,10]. Microwave heating for food preservation and processing applications have been popular since the early 1970s and products such as rubber, wood, paper and many other agricultural products have been studied extensively [11]. Another important application of microwaves in the food industry has been the quality control of some products, for example, moisture content (different water concentration) could change the dielectric properties of materials such as granular solids, meats, vegetables and fruits [12,13]. Besides these, microwave sensing methods for maturity stage of agricultural products have also been very popular, because the storage time of the agricultural products under measure may affect the dielectric properties during the ripening processes [14].

In the field of chemistry, dielectric measurements serve as a fundamental tool for the characterization and evaluation of solvent materials [15,16]. Another important application for liquids is their use as dielectric reference materials, which is very common to check the operation of dielectric measurement systems or to calibrate them [17,18].

Permittivity characterization has also gained significantly interest for biomedical applications [19-22]. As for some liquids carry a relatively good match of their complex permittivity over the frequency range from 300 MHz to 6 GHz to that of biological tissues [19,23], they are normally used as components of tissue-equivalent materials, which could be useful to monitor and analyze glucose concentrations for diabetic patients [24-26]. Additionally, Microwave sensors also hold the ability to discriminate between the normal and malignant cancerous tissues [27-29]. It even leads to the development of many non-invasive techniques for early detection of cancer and harmful tumors in human body [30-32].

Microwave engineering and the development of electronic components require also precise knowledge of the electromagnetic properties of materials at microwave frequencies [33,34], e.g., applications as radar [35,36], detection of movement [37-39], shape or dimensions of objects [40,41], etc.

This thesis aims at the design of microwave sensors for material characterization, especially dielectric substrates which are widely used in circuit fabrication in microwave engineering and industry. The determination of complex permittivity of liquids is briefly introduced as well because of the aforementioned wide applications of liquids in chemistry, medicine and biomedical field. The principle of the microwave sensing is based on the reflection and scattering of different materials to microwave signals [42], and the reflection and scattering properties of a material are mainly determined by the electromagnetic properties of the object such as complex permittivity [43]. Thus, in order to better understand the next chapters about the measurement techniques, section 2.1.1 provides basic knowledge about dielectric properties of materials.

2.1.1 Dielectric properties of materials

All materials have dielectric properties [44]. Although most of the materials including living organisms and most agricultural products can conduct electric currents to some degree, they are still classified as dielectric materials. There are lots of different terms in use today to describe electromagnetic characteristics of materials and they exhibit considerable change over frequency and temperature [33]. For the dielectric properties the main interest is the complex permittivity (ε_r), which is a physical quantity that describes the interaction of a material with an external electric field applied on it. Complex permittivity (normally being relative to the permittivity of free space ε_0) is defined by [17]:

$$\varepsilon_r = \frac{\varepsilon}{\varepsilon_0} = \varepsilon_r' - j\varepsilon_r'' = \varepsilon_r'(1 - jtan\delta) \quad (1.1)$$

The electric field interacts with materials in two ways: energy storage and energy dissipation.

- Energy storage: energy may be exchanged between the field and material, in a lossless manner. This energy storage is represented by the real part of permittivity (ε_r'), sometimes called dielectric constant associated to material's capacitance which is able to store energy.

- Energy dissipation: energy may be permanently lost from the field, and absorbed in the material (usually as heat). This energy loss is represented by the imaginary part of permittivity (ε_r''). Another term often seen on data sheets is loss tangent. Loss tangent is also equivalent to the dissipation factor and reverse to quality factor, defined as:

$$tan\delta = \frac{\varepsilon_r''}{\varepsilon_r'} = \frac{1}{Q} \quad (1.2)$$

  where Q is quality factor. It is a measure of the energy lost relative to the energy stored. In some areas, e.g., biomedical measurement, it is common to express loss as an equivalent conductivity, σ, measured in S/m, where $\sigma = \omega\varepsilon_r''\varepsilon_0$, measures the ability of material's to conduct an electric current.

2.2 Measurement techniques for material characterization

The microwave methods for materials characterization generally fall into non-resonant methods and resonant methods [45]. Non-resonant methods are often used to get a general knowledge of dielectric properties over a frequency range, while resonant methods are used to get accurate knowledge of dielectric properties at single frequency or several discrete frequencies. In this section, the state-of-the-art of measurement techniques is introduced, including their strengths, limitations and applications.

2.2.1 Non-resonant methods

In non-resonant methods, the properties of the materials are inferred mainly from reflection method or transmission/reflection method [46]. In a reflection method, material properties are

calculated on the basis of the reflection from the sample, and in a transmission/reflection method, the material properties are calculated on the basis of the reflection from the sample and the transmission through the sample. Non-resonant methods require a means of directing the electromagnetic energy towards a material, then collecting what is reflected from the material and what is transmitted through the material. In principle, all types of transmission lines can be used to carry the wave for non-resonant methods, such as coaxial line, hollow metallic waveguide, dielectric waveguide, planar transmission line, and free space.

2.2.1.1 Coaxial probe method

Coaxial probe method is one of the most convenient and frequently used techniques to measure lossy materials at high frequencies (RF and microwave). Commonly it is known as coaxial probe or an open ended coaxial-line method. It is used with network analyzers, which measures complex reflection coefficient [47].

Coaxial line uses a metallic probe which senses reflected signal (phase and magnitude) from MUT. For flat surfaces probe touches sample and for liquids it immersed into sample, as shown in Figure 1.1 [43]. It is quite simple method and it makes possible to carry out dielectric measurements over broad frequency range around 0.5 GHz to 110 GHz. It is best for characterizing permittivity of lossy materials. Examples are human phantoms for specific absorption rate tests, tissue samples for medical researching, bio-and chemical samples [23,48-50]. Also any sample with high water content, such as food products that will be heated in a microwave [51,52], and many other materials that will be dried using microwaves [53].

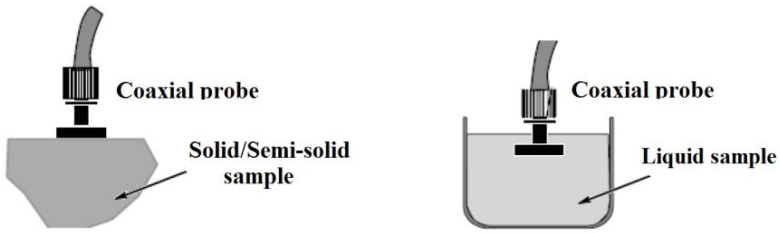

FIGURE 1.1: Coaxial probe methods [43].

2.2.1.2 Transmission line method (waveguide)

Transmission line method is another common technique by which a material sample is put inside the center of enclosed transmission line (as shown in Figure 1.2) [54-57]. For measurements both reflection and transmission coefficients are used. It has higher accuracy and more sensitivity than the coaxial probe, but relatively it has a narrower frequency range than coaxial probe. Sample preparation is relatively difficult, thus it is more time consuming, because sample must cover entire cross-section area of a line, therefore it must be in slab or annular geometry form.

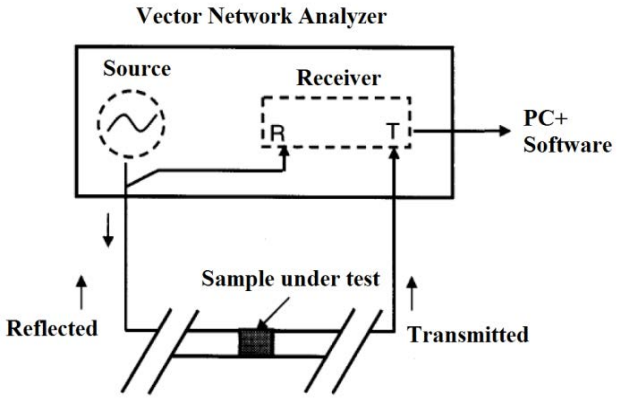

FIGURE 1.2: Transmission line (waveguide) method [56].

2.2.1.3 Free space method

This technique is non-contacting and nondestructive, typically uses at higher frequencies [58]. In Free-space method the large, flat and both side proper-faced samples of homogeneous (uniform without irregularities) solid materials are used to measure the dielectric characteristics. In a typical free-space transmission technique, a sample is placed between a transmitting and a receiving antenna, and the attenuation and phase shift of the signal are measured, from which the dielectric properties of the sample can be determined. Figure 1.3 shows a typical arrangement of a free space measurement setup [42]. The advantage of using free-space measurement technique is to get reflection and transmission coefficients with no physical contact to the sample, which is best for thin flat materials.

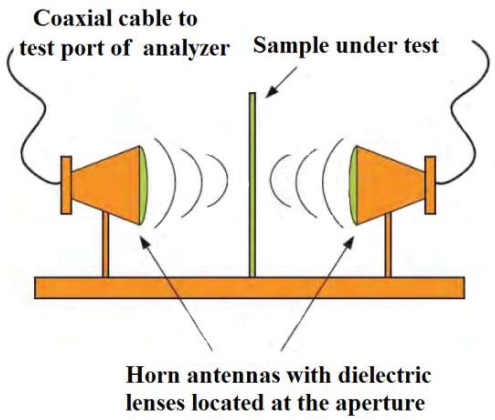

FIGURE 1.3: Free space method [42].

2.2.2 Resonant methods

Resonant methods usually have higher accuracies and sensitivities than non-resonant methods, because they operate at a single frequency or a discrete set of frequencies, and they are most suitable for low loss samples. Resonant methods can generally be classified into resonator methods and resonant perturbation methods [42]. Resonator methods are those in

which the material to be measured serves as a resonator and are only applicable to extremely low loss samples. The different types of resonators used for this purpose can be further classified into dielectric, coaxial cavity, and split resonators [33]. Resonant perturbation methods are those in which the sample is introduced into a resonant structure causing a perturbation in the response. The perturbation results in a shift of the resonant frequency and a decrease in the unloaded quality factor of the resonator from which the dielectric properties of the sample can be derived. The resonant perturbation technique is well suited for low and moderate loss samples.

2.2.2.1 Resonant cavity

This method uses a resonant cavity for the sample holder, and a network analyzer to measure the resonant frequency and Q of the cavity, both empty and with the sample loaded (see Figure 1.4) [57]. From this, permittivity can be calculated. This method has the best loss factor resolution. It is suitable for both moderate and high loss samples [59]. The common frequency range for this technique is in 1 GHz to 20 GHz, although higher frequency resonant fixtures are available. At high frequencies it can become difficult to separate out the useable resonant frequency modes.

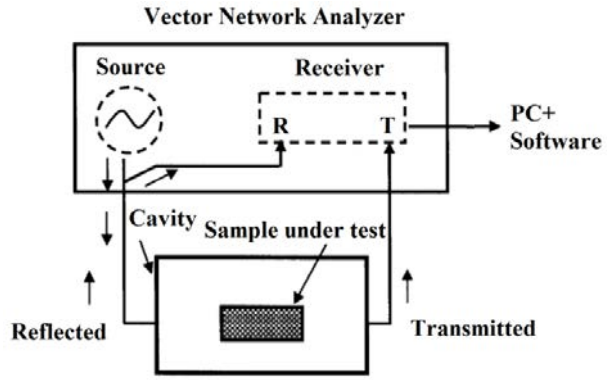

FIGURE 1.4: Cavity resonator method [57].

2.2.2.2 Open ended resonant lines

A very important but not so widely used resonant method is the resonant open ended line method [60]. It normally consists of a long coaxial line with the input feed line located a distance $L_1 = \lambda/4$ away from the shorted end and $L_2 = \lambda/2$ away from the open end section (see Figure 1.5) [42]. At resonance, the fields are concentrated at the open end aperture of the resonator where the material to be tested is brought into contact. This method is ideally suited for measuring high loss samples and does not require any sample preparation. The sensor is calibrated in air before bringing it in contact with the material under test. The effect of the material in contact with the aperture of the sensor detunes the response. The response is then tuned back to the original frequency by adjusting length L_1. This change in the length is directly proportional to the permittivity of the material. The deterioration in the quality factor of the resonator after tuning provides information on the loss of the sample.

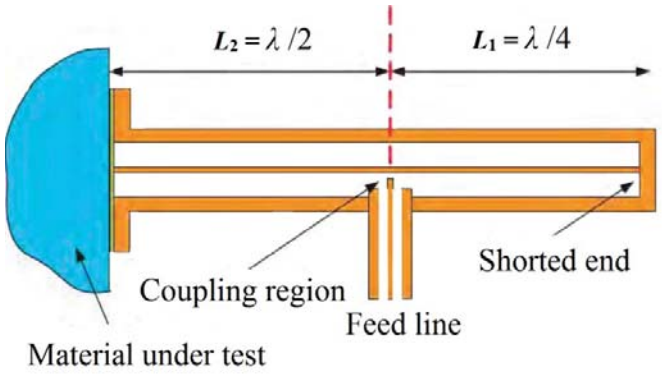

FIGURE 1.5: Open ended resonant line [42].

2.2.2.3 Planar transmission line loaded resonators

This method lies in that the sample under test forming either a substrate (in case of solid) or superstrate (for both, solid and liquid) would cause a noticeable shift in the resonant frequency and a change in quality factor, which can be used to extract the dielectric properties of a sample [17]. To take measurement, a sample is placed on top of the resonator (as shown in Figure 1.6), which would modify the substrate or air-boundary. Then the resonant frequency changes, from which the dielectric constant of the sample could be extracted [42]. It is notable that the effect of dielectric sample is more prominent when using it as substrate rather as overlay test material [61].

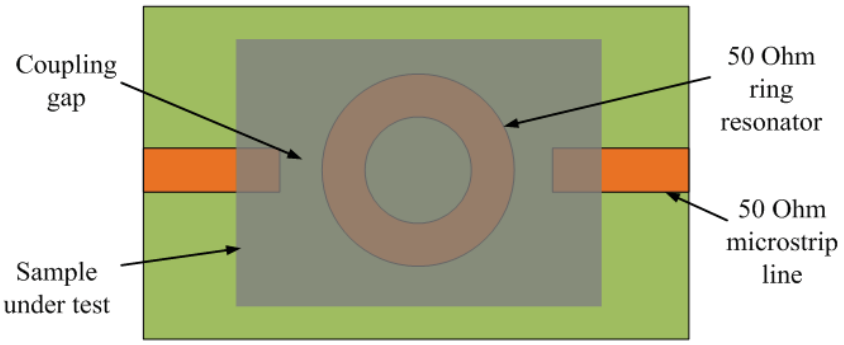

FIGURE 1.6: Planar transmission line method [42].

In all the methods introduced above, which one suits best for the design depends on different factors: (i), frequency of interest, expected value and required measurement accuracy; (ii), properties of materials under test such as whether it is homogeneous and isotropic, or the form of a material, for example liquid, powder, solid, or sheet material, and also sample size restrictions (if the sample is large or small); (iii), It depends also on whether it is a problem if a measurement destroys samples, in other words, if it is destructive or non-destructive. Likewise, if a sample can be touched or contactless; (iv), temperature is an important factor too. Sometimes it is desirable to measure a sample that is very hot or cold. So which technique is best depends on many things [17]. Table 2.1 shows the conclusion of different methods introduced above and their strengths, limitations and application areas [17].

Table 2.1 Dielectric sensing techniques [17].

	Recommended Materials	Frequency Range	Advantages	Disadvantages
Coaxial probe	Liquids and semi-solids	Broadband	Easy to use, non-destructive, simple sample preparation, high accuracy for high loss materials.	Large samples and solids must show a flat surface, air gaps cause errors, repetitive calibrations.
Transmission line (waveguide)	Liquids and solids	High frequency	More accurate and sensitive than the probe method.	Sample preparation is difficult and time-consuming (fills fixture cross section), cannot use below few GHz due to practical sample length limitation.
Free space	Solids	MW range	Non-destructive, easy sample preparation, both high and low losses samples, high temperatures.	A large flat, thin, parallel-faced sample, special calibration.
Parallel plate	Thin, flat smooth surface sheet	< 100 MHz	Inexpensive, high accuracy, high loss samples.	Limited frequency range, sheet sample very thin.
Cavity resonator	Solids	1 MHz–100 GHz, single frequency	Easy sample preparation, low loss materials, high temperature capability, no repetitive calibration.	Single or discrete frequencies, small size samples, complex analysis.
Planar Transmission line loaded resonator	Liquids and solids	Single frequency	Simple, cost-effective and rapid, no special sample handling, high temperature measurement, no calibration needed.	Low quality factor, air gap causes error.

2.3 Planar transmission lines loaded with electrically small resonators

Planar transmission lines loaded with resonators are widely used for sensing. Microstrip line is the most common and simplest structure for characterizing dielectric materials. It is easy to fabricate, with low manufacturing cost while compactness of structure makes it more suitable for electronic and industrial applications. Although all planar methods suffer from low quality factors and as a result measurements are suitable for low to moderate lossy samples. But the advantages (comparison made in Table 1.1) surpass limitations. Since this thesis is dedicated to the structures of different transmission lines loaded with different resonators, mainly for low to moderate lossy dielectrics, of course emphasis is also put on common liquids detection included in the last chapter of this thesis, this section gives brief

explanations about the common planar transmission lines and electrically small resonators which would be used throughout this thesis. In addition, details about the sensing methods based on resonant perturbation are given as well, specifically, coupling modulation, amplitude modulation, frequency splitting, and frequency variation, where the last two are the main methods used for the design of the sensors in this thesis.

2.3.1 Introduction to common planar transmission lines

The three most common types of planar transmission lines used widely for materials characterization are stripline, coplanar waveguides and microstrip line. Unlike their coaxial and waveguide counterparts, they have the attractive features of compactness, easy fabrication and inexpensive construction [42,62,63]. Since our aim is primarily to utilize microstrip lines and coplanar waveguides (because stripline suffers from a relative complicated multilayer construction), emphasis is only laid on the introduction of these two types.

A microstrip line consists of a strip conductor and a ground plane separated by a dielectric substrate as shown in Figure 1.7(a). Since the dielectric constant of the substrate is much higher than that of air, the field is concentrated near the substrate. The field distribution on a microstrip line is shown in Figure 1.7(b). Microstrip lines support a single fundamental mode of propagation. The effective permittivity and the characteristic impedance of a microstrip line can be determined using the well- known closed form expressions found in the literature [64].

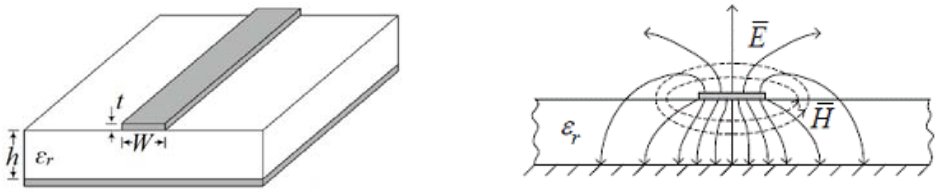

(a) (b)

FIGURE 1.7: (a) Geometry of a microstrip line (cross section), and (b) Field distribution at the cross section of a microstrip line [65].

Coplanar waveguide (CPW) consists of conductors formed by a center strip separated by a narrow gap from two ground planes on either side, as shown in Figure 1.8 [63]. In CPW, two propagating modes are supported: CPW mode (even mode) and slot mode (odd mode), respectively. Typically, CPW mode is excited by feeding the central strip and by grounding the lateral planes, whereas the slot mode is a parasitic mode, where air bridges between ground planes usually are applied to suppress the undesired slotline mode [66]. In this thesis, CPWs are always excited by the even mode.

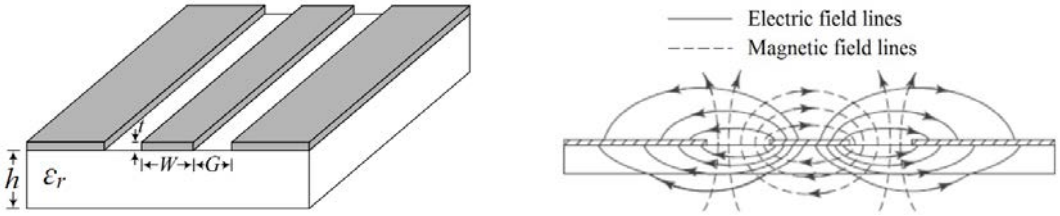

(a) (b)

FIGURE 1.8: (a) Geometry of a coplanar waveguide; (b) Field distribution at the cross section of a coplanar waveguide [63].

It is also worth mentioning that microstrip lines and CPWs are inhomogeneous propagating structures, since part of the electromagnetic fields extends to the air. Nevertheless, the propagation modes supported by the lines are of quasi-TEM (transverse electromagnetic) nature, and are characterized by their characteristic impedance and propagation constant. An important point in microstrip lines is their ground plane lies in the back side of the substrate, which effectively isolates the structures, preventing from possible interferences. For CPW, it only needs one single metallic layer, and its characteristic impedance does not univocally determine the transverse dimensions (*W* and *G*), providing design flexibility.

2.3.2 Introduction to electrically small resonators

This section analyzes several electrically small resonators which are used throughout this thesis, specifically, SRRs, CSRRs, and SIRs. The main purpose of this section is to gain insight into the electromagnetic characteristics and the equivalent circuit models of these resonators.

The reason for choosing those resonators is that they are sub-λ structures, in contrast to the usual transmission line resonators, i.e., their dimensions are electrically small at the resonant frequency (typically one tenth of the guided wavelength or less). Therefore, high level of miniaturization is expected by using these particles. Due to their very small electrical size, they can be addressed as semi-lumped resonators. In addition [67], they have strong response to an electromagnetic field and easy electric/magnetic coupling between resonators and materials under test (MUT).

2.3.2.1 Split ring resonators (SRRs)

Split ring resonators (SRRs) consist of a pair of concentric metallic split rings, etched on a dielectric substrate, with cuts on opposite sides of each concentric ring, as shown in Figure 1. 9(a) [68]. It was initially proposed by Pendry *et al.* [69] to build up a negative permeability medium [70].

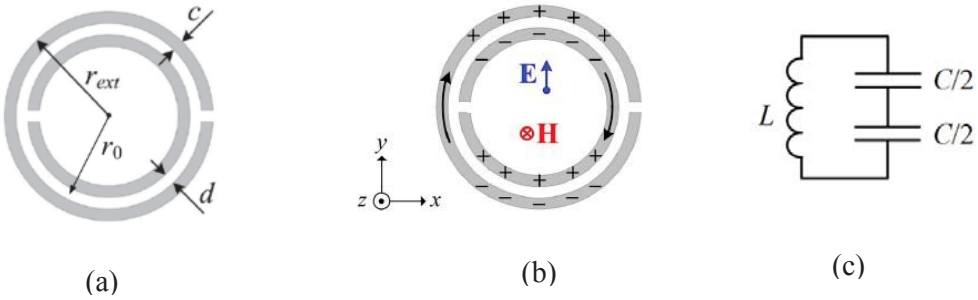

FIGURE 1.9: (a) Circular topology of a split ring resonator; (b) Sketch of the charge distribution and currents at fundamental resonance; and (c) Equivalent circuit model (SRR behaves as an externally driven LC resonator) [71].

When it is excited by a time-varying external magnetic field directed along the *z*-axis, the cuts on each ring force the electric current to flow from one ring to another across the slot between them, taking the form of a strong displacement current as shown in Figure 1.9(b). The slot between the rings therefore behaves as a large distributed capacitor that can lower the resonant frequency. This would not happen in closed rings. The overall SRR can be represented by the equivalent lumped circuit of a resonator shown in Figure 1.9(c) that may couple to external electromagnetic fields [72], as long as the perimeter of the SRR can be considered small with regard to a half-wavelength of the exciting wave, and the capacitance associated with the cuts on each ring can be neglected. The inductor L represents the self-inductance of the SRR, which can be calculated as the average inductance of the two rings, i.e. as the inductance of a single closed loop with identical width to that of the individual rings (c) and identical mean radius (r_0) [68,73]. The capacitor C stands for the total capacitance across the slot between the rings, which is divided into two series components corresponding to the two identical halves of the resonator ($C = 2\pi r_0 C'$, where C' is the per-unit-length capacitance along the slot between the rings, and $r_0 = r_{ext} - c - d/2$ is the mean radius) [68]. It is worth mentioning that a more detailed circuit model with distributed elements and taking into account the gap capacitance was reported [74,75]. The two gap capacitances, produced by the accumulation of electric charges, can be regarded as being added in parallel to the inter-ring capacitance. It was shown that such a distributed model converges to the previous model when the gap capacitances are neglected and the electrical length of the SRR is small [76].

2.3.2.2 Complementary split ring resonators (CSRRs)

By invoking the concept of duality and complementarity [77,78], a CSRR can be derived from a SRR in a straightforward way. This new particle can be defined as the negative image of a SRR, by exchanging the apertures (slots) for the solid (metallic) parts of the particle [79], as shown in Figure 1.10(a). It exhibits an electromagnetic behavior which is almost the dual of that of the SRR, according to electromagnetic duality (also often referred to as Babinet's Principle) [79]. It should be pointed out that duality in complementary structures strictly applies to infinite, planar, zero thickness, and perfectly conducting electric screens [77].

Although in practice such ideal conditions cannot be fulfilled, for very thin good conductors and metallic planes substantially larger than the wavelength and the slot region, Babinet's Principle predicts the actual behavior to a high degree [80]. One of the most relevant discrepancies due to deviations from ideal conditions is a shift in the resonance frequency. The value of the resonant frequency of CSRR can be deduced, at least in a first approximation, from that of the SRR. Taking into account that, in a quasi-static analysis, duality still holds between a SRR and a CSRR printed on an infinitely thick substrate. Therefore, for relatively thick substrates (in comparison to *c* and *d*), the resonant frequency of both the CSRR and the SRR should be approximately the same.

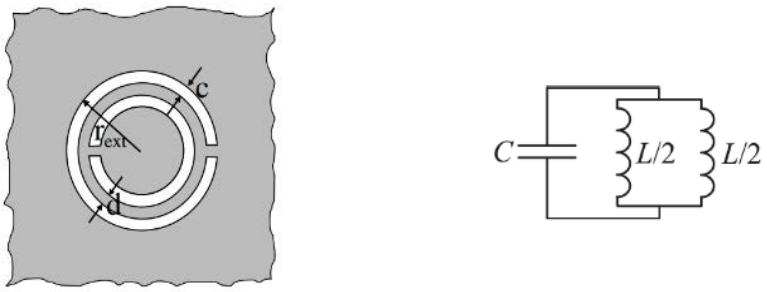

(a) (b)

FIGURE 1.10: (a) Typical topology of circular complementary split ring resonator, and (b) Equivalent circuit model, with the total inductance $L = 2\pi r_0 L'$ divided into equal parallel contributions, where L' is the per-unit length inductance of an equivalent CPW [76].

Finally, it may be shown that electromagnetic duality implies circuit theory duality. Consequently, any planar structure and its complementary screen are dual in circuit theory as well [81]. Thus, the equivalent circuit model of a CSRR may be inferred by the dual circuit model corresponding to a SRR, as shown in Figure 1.10(b). By applying circuit duality, inductances are replaced by capacitances, and series-connected circuit elements become parallel-connected circuit elements. The capacitance of the CSRR may be calculated as the capacitance of a disk of radius $r_0 - c/2$ with $r_0 = r_{ext} - c - d/2$, surrounded by a metal plane at a distance *c* of its edge (analytical expressions have been derived [71]. The CSRR inductance is given by the parallel combination of the two inductances connecting the inner disk to the outer metallic region of the CSRR [82]. Such inductances may be calculated as the inductance of a CPW with a strip width *d* and slot width *c*.

2.3.2.3 Stepped impedance resonators (SIRs)

Stepped impedance resonators (SIRs) are common planar building blocks for the design of compact filters [83-85]. They are typically implemented by means of a tri-section structure where a narrow strip (high characteristic impedance section) is sandwiched between two wide sections (low characteristic impedance). The typical topology is depicted in Figure 1.11(a), it exhibits an electric wall at the bi-section plane of the resonator (indicated in the figure) at the fundamental resonance, and there is an electric dipole moment orthogonal to this plane. Thus,

it can be excited by means of a time-varying electric field, with a non-negligible component in the direction of the electric dipole moment.

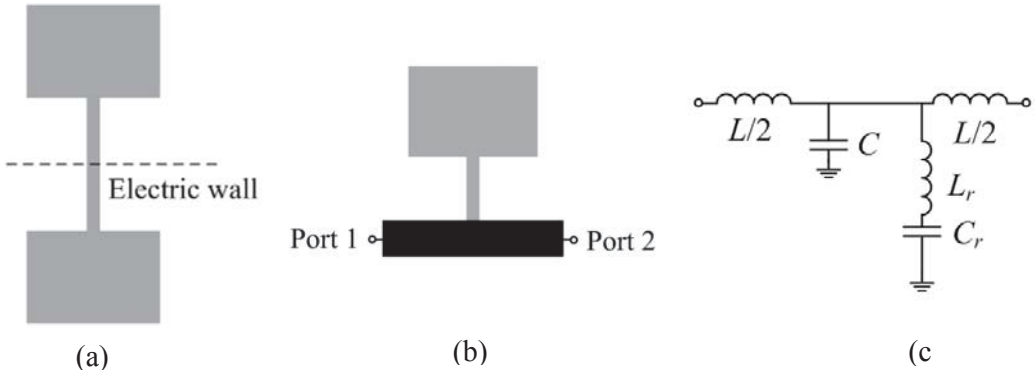

FIGURE 1.11: (a) Typical topology of a tri-section SIR; (b) SISS attached to a microstrip line, and (c) Equivalent circuit model of the structure of Figure 1.11(b).

There are many different configurations and variations of SIRs topology and feeding. In most of the previous applications, the resonators are coupled or attached to a host transmission line. A high level of miniaturization has been achieved in SIR-based coplanar waveguide (CPW) structures, where elliptic filters [86] and radiofrequency (RF) barcodes (or spectral signature barcodes) [87] have been demonstrated.

In this thesis, one of our focuses is on the stepped impedance shunt stubs (SISS) as shown in Figure 1.11(b), based on microstrip technology (in the next chapter we still call it SIR in order to keep consistence as it is called in most of literature). It consists of half of the structure in Figure 1.11(a) directly in contact with a host microstrip line. To a first order approximation the SISS can be modeled as a shunt connected series LC resonator as shown in Figure 1.11(c), where L_r models the high impedance part of the SIR (narrow strip), and C_r models the broadside capacitance of the SIR (the wide patch) [88].

2.3.3 Planar transmission lines loaded with electrically small resonators for sensing based on resonant perturbation method

As mentioned before, planar transmission lines have been used extensively in the past to measure electromagnetic properties of materials including thin films [89,90], sheet samples [91] and substrate samples [92]. They can offer many attractive features which include compactness, ease of fabrication, and even use in a disposable manner. Electrically small resonators, i.e., SRRs, CSRRs, SIRs, etc., have electrical sizes significantly smaller than the wavelengths at their fundamental resonant frequencies and strong response to an electromagnetic fields. Thus, planar transmission lines loaded with those resonators offer compactness, higher sensitivity and accuracy, therefore have been the focus of attention.

Four sensing approaches for the implementation of microwave sensors based on electrically small resonators have been reviewed [93], which are based on transmission lines loaded with those resonant elements. Such sensing strategies are coupling modulation through symmetry disruption (causing variation of the notch depth), amplitude modulation of a harmonic signal,

frequency splitting (exploiting symmetry properties), and resonance frequency variation. Since the aim of this thesis is primarily to characterize substrates and some liquids, we would therefore focus our attention on the last two methods based on resonant perturbation, where the loaded electrically small resonators are perturbed either by capacitive dimensions or by external materials under test (MUTs), thereby resonant frequencies and quality factors are changed, through which dielectric properties of MUTs could be extracted.

2.3.3.1 Sensors based on coupling modulation

This sensing approach belongs to the so-called symmetry-based sensing [67,76,94], where symmetry properties are exploited for the implementation of sensors. In these sensors, a transmission line is loaded with a single symmetric resonator (electromagnetically coupled to the line), and the sensing principle is the control of the level of coupling between the line and the resonator, caused by the measurand, and related to the disruption of the symmetry. These sensors are particularly useful for the measurement of special variables (e.g., alignment, displacement, velocity, etc.) [37,39,95].

2.3.3.2 Sensors based on amplitude modulation

These types of sensors consist of a transmission line fed by a harmonic signal tuned to the fundamental frequency of a certain resonator coupled to it. The amplitude of the feeding signal at the output port of the line depends on the level of coupling between the line and the resonant element. Namely, if the coupling is negligible, the line is transparent, and the amplitude at the output port is maximized. Conversely, if the coupling is significant, the injected signal is reflected back to the source, minimizing the amplitude of the output signal. Thus, line-to-resonator coupling effectively modulates the amplitude of the output signal, and this can be used for sensing purposes. Specifically, these amplitude modulation sensors are very appropriate for measuring angular velocities [96-99].

2.3.3.3 Sensors based on frequency splitting

In this approach, the sensors are composed of a transmission line loaded with a pair of resonators in a symmetric configuration. The sensing principle is based on resonance frequency splitting. Thus, in the reference (symmetric) state the structure exhibits a single notch, but two notches appear when the symmetry is broken, and the frequency separation between them is related to the level of asymmetry [76].

Typically, these sensors find applications in material characterization. A test region in the vicinity of the resonators should be defined. By adding a material or substance in those regions, a single transmission zero appears if the material distribution (specifically the permittivity) is symmetric. On the contrary, if the loaded material is not symmetric, two notches in the transmission coefficient, indicative of such asymmetry, arise. Note that this strategy is useful for the implementation of sensors and comparators. Such sensors are differential sensors, able to provide the difference between two permittivity values. As comparator, the structure solely compares two permittivities, indicating if their values are the same or not. This latter application is useful for the detection of defects or abnormalities in

material samples as compared to a well-known reference. Frequency splitting sensors are robust in front of changing environmental conditions since a true differential measurement is performed in such sensors.

One important drawback of these frequency splitting sensors is the coupling between resonators (in one unit cell), unavoidable if these resonators are close enough. Coupling tends to degrade sensor performance, specifically, the sensitivity to small perturbations. More details about the effects of inter-resonator couplings on the response of sensors would be discussed in Chapter 4.

2.3.3.4 Sensors based on frequency variation

A transmission line loaded with a resonant element (either coupled to it or in contact with it) exhibits a set of transmission zeros in the frequency response. These transmission zeros occur at those frequencies where the resonant element produces an open or a virtual ground to the line, and the injected power is completely reflected back at these frequencies (excluding the effects of losses). Typically, the frequency of interest for microwave circuit and sensor design is the first (fundamental) resonance of frequency, where the electrically small resonators can be used in order to achieve compact dimensions. This frequency (and higher order harmonic frequencies) may be altered by the effects of external stimulus or perturbations (e.g. moisture, temperature), by the relative position or orientation between the line and the resonant element (distance, lateral displacement, etc.), or by the presence of substances/materials surrounding the resonant element. Therefore, it follows that resonance frequency variation can be used for sensing many different variables, including position, velocity, material characterization (e.g., permittivity), moisture, etc. These sensors are in general very simple, but may suffer from cross-sensitivities, defined as the sensitivity of the sensors to other variables different than the one of interest (measurand). For example, since permittivity depends on environmental conditions (e.g., temperature), the resonance frequency can be unintentionally shifted by spurious effects in permittivity sensors. Nevertheless, in many applications, external factors such as temperature or humidity do not experience significant variations. Moreover, these frequency variation based sensors are typically calibrated for accurate measurements. Therefore, these sensors are useful in many applications where design simplicity and low-cost are key aspects.

Chapter 3

Transmission Lines Loaded with Electrically Small Resonators: Modelling and Analysis

In this chapter, different structures of planar transmission lines loaded with electrically small resonators are introduced, which include a CPW loaded with a pair of SRRs, a microstrip line loaded with a pair of CSRRs, a CPW loaded with a 5-section SIR, a microstrip line loaded with a pair of SIRs connected directly in the same junction of the line, and a CPW loaded with slot-SIR. Their lumped equivalent circuit models consisting of all the elements (transmission lines and array of loaded resonators) as well as all the involved inter-element couplings are presented, which could offer superior accuracy and numerical expressions of the transmission/reflection responses, from which the lumped elements parameter could be extracted through the results performed through commercial electromagnetic simulation software (*Keysight* ADS software). Then the structures are fabricated and validated by showing the good agreement among the circuit responses, EM simulation results and measured data. Since the target of this thesis is the design of different structures with transmission lines loaded with electrically small resonators (discussed in section 2.3.2), using as microwave sensors. So the modelling and analysis of these structures are important for tailoring them to meet our aims as sensing purpose.

This chapter is divided into four sections. Section 3.1 and section 3.2 are devoted to the structures of CPW loaded with a pair of SRRs and of microstrip line loaded with a pair of CSRRs, respectively. Afterwards, a comparison based on the lumped equivalent circuit models of these two structures is addressed to obtain a mapping relation of their lumped elements, which could be useful to tailor or transform these two structures. Section 3.3 deals with the structure of CPW loaded with 5-section SIRs, with emphasis also laid on the introduction of a microstrip line loaded with a pair of coupled SIRs connected in parallel configuration. Lastly, section 3.4 completes the analysis of the structure of a CPW loaded with a pair of slotted SIRs, which is also the complementary counterpart structure of microstrip line loaded with a pair of coupled SIRs in section 3.3.

3.1 Coplanar waveguide loaded with a pair of coupled split ring resonators

Article **AWPL15** analyzes the structure of a CPW loaded with a pair of SRRs, providing the lumped equivalent circuit model of a unit cell of this structure and also taking into account the magnetic coupling between the SRRs forming the pair for the first time. A typical topology (unit cell) of a CPW loaded with a pair of SRRs is depicted in Figure 3.1(a). The orientation of the symmetry plane of the pair of SRRs is considered to be orthogonal to the symmetry plane of the CPW. With such orientation, the single coupling mechanism between

the line and the SRRs is magnetic (mixed coupling avoided) [100]. The corresponding lumped element equivalent circuit model is proposed in Figure 3.1(b) [101,102]. It is assumed that the dominant coupling mechanism between the SRRs. forming the pair is magnetic and the coupling between adjacent resonators does not apply in single stage of the structure or the distance between SRRs of adjacent stage is set to be high enough to neglect this additional inter-resonator coupling [103]. By analyzing the lumped equivalent circuit model [104], transmission zeros (or resonant frequencies of the coupled resonators) are given by the poles of the series reactance, could be expressed as:

$$\omega_{\pm}^2 = \frac{\omega_1^2 + \omega_2^2 \pm \sqrt{(\omega_1^2 - \omega_2^2)^2 + 4M'^2\omega_1^4\omega_2^4 C_1 C_2}}{2\,[1 - M'^2\omega_1^2\omega_2^2 C_1 C_2]} \qquad (3.1)$$

where $\zeta_1 = (L_1C_1)^{-1}/2$ and $\zeta_2 = (L_2C_2)^{-1}/2$ are the intrinsic resonance frequencies of each isolated resonator. Note that these frequencies do not depend on the mutual couplings, M_1 and M_2, between the line and the SRRs, but on the mutual coupling, M', between the SRRs. If inter-resonator coupling is negligible (M'=0), reasonable if the SRRs are separated enough, the solutions of (3.1) are simply ζ_1 and ζ_2.

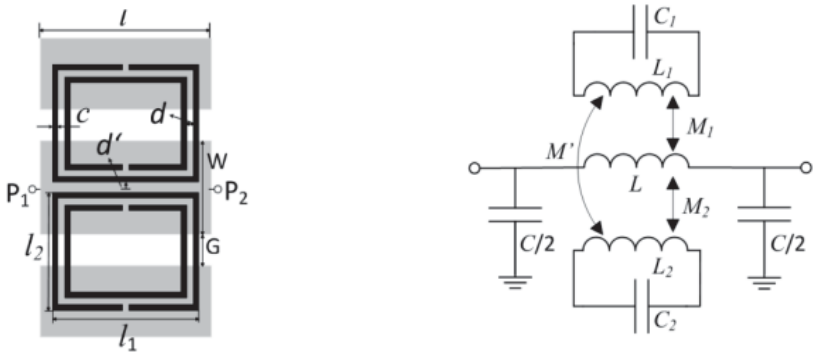

(a) (b)

FIGURE 3.1: (a) Typical topology of a CPW loaded with a pair of SRRs, and (b) lumped element equivalent circuit model, considering magnetic coupling between SRRs.

From the model and the expression of zeros in transmission coefficient, different situations are considered: symmetric loading (identical SRRs), asymmetric loading (different SRRs with the same resonant frequencies), and general asymmetric loading (different SRRs) [105].

A. Symmetric loading

In this case, SRRs are identical with $\zeta_1 = \zeta_2 = \zeta_0$. From (3.1), only one effective transmission zero appears at:

$$\omega = \frac{\omega_0}{\sqrt{1 + \dfrac{M'}{\sqrt{L_1 L_2}}}} = \frac{\omega_0}{\sqrt{1 + k_M}} \qquad (3.2)$$

where k_M is the magnetic coupling coefficient (note that $L_1 = L_2 = L_r$ due to symmetric loading). From (3.2), it is obvious that the inter-resonator coupling between SRRs has the ability to lower the transmission zero frequency (to the left of ζ_0).

B. Asymmetric loading (different SRRs with the same resonant frequencies)

In this case, the SRRs are different in physical size, but they have the same resonant frequencies, i.e., $\zeta_1 = \zeta_2 = \zeta_0$ and $L_1 \approx L_2$, $C_1 \approx C_2$. According to (3.1), two transmission zero frequencies exist at:

$$\omega_{\pm} = \frac{\omega_0}{\sqrt{1 \mp \frac{M'}{\sqrt{L_1 L_2}}}} = \frac{\omega_0}{\sqrt{1 \mp K_M}} \qquad (3.3)$$

Different from symmetric case which possesses only one transmission zero frequency, this case in general has two transmission zeros frequencies, with one above and the other below $\zeta 0$. It is worthy to note that there is one exception, when the extracted lumped parameters of the SRRs satisfy: $\sqrt{\frac{L_1}{L_2}} = \sqrt{\frac{C_2}{C_1}} = \frac{M_1}{M_2}$, then only one transmission zero is expected (the one smaller than ζ_0).

C. General case

In this general case, the transmission zeros are given by (3.1), and mutual coupling between the SRRs (M') tends to further or split the transmission zeros, i.e.,

$$\omega_+^2 - \omega_-^2 = \frac{\sqrt{(\omega_1^2 - \omega_2^2)^2 + 4M'^2\omega_1^4\omega_2^4 C_1 C_2}}{[1 - M'^2\omega_1^2\omega_2^2 C_1 C_2]} > \omega_1^2 - \omega_2^2 \qquad (3.4)$$

It also means the two transmission zeros separate further as the distance between the pair of SRRs gets closer.

3.2 Microstrip line loaded with a pair of complementary split ring resonators

As the counterpart of the structure of a CPW loaded a pair of SRRs in section 3.1, this section deals with the structure of a microstrip line loaded with a pair of CSRRs. The details of the analysis of this structure are explained in Article **AWPL16** and [106].

The topology and the proposed lumped equivalent circuit model of a microstrip line loaded a pair of CSRRs are depicted in Figure 3.2. The distance between the CSRRs forming the pair (d') is very small in order to guarantee the electric coupling between the microstrip line and the two CSRRs. Hence, the equivalent circuit model takes into account not only the electric coupling between each CSRR and the microstrip line (C_{c1} and C_{c2}), but also the electric inter-resonant coupling between the CSRRs pair (C_M). Transmission zeros of this structure exist when the reactance of the shunt branch is forced to be zero [71], which leads to [107]:

$$\omega_{\pm}^2 = \frac{\omega_1^2 + \omega_2^2 \pm \sqrt{(\omega_1^2 - \omega_2^2)^2 + 4C_M^2\omega_1^4\omega_2^4 L_1 L_2}}{2\,[1 - C_M^2\omega_1^2\omega_2^2 L_1 L_2]} \quad (3.5)$$

where

$$\omega_i = \frac{1}{\sqrt{L_i(C_i + C_i)}} \quad (3.6)$$

with i = 1,2, are the transmission zero frequencies of the isolated resonators (i.e., without inter-resonator coupling).

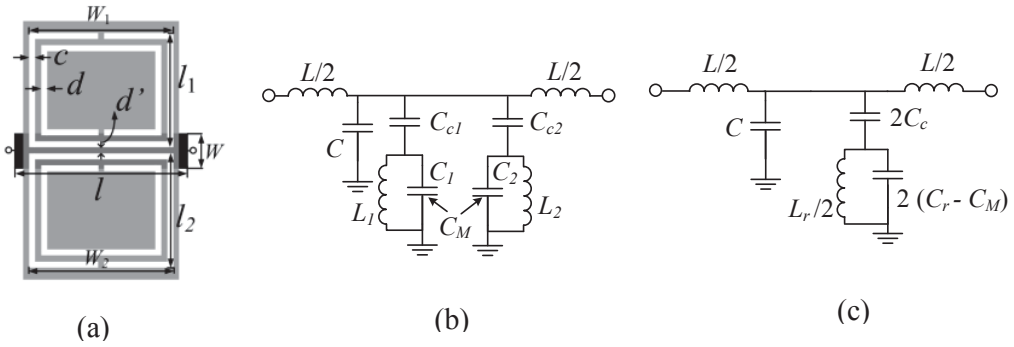

FIGURE 3.2: (a) Typical topology of a microstrip line loaded with a pair of CSRRs; (b) lumped element circuit model, and (c) lumped element circuit model for the symmetric case (CSRRs are identical or loading the same dielectric loadings). The CSRRs (etched in the ground plane which is depicted in grey) are depicted in white (as slots in ground plane) and the conductor strip (upper metal) is depicted in black.

Similarly to the analysis procedure of CPW loaded pairs of SRRs in section 3.1, there are also three specific situations to be considered here for this structure, i.e., symmetric loading (identical CSRRs), asymmetric loading (different CSRRs with the same resonant frequencies), and general asymmetric loading (different CSRRs).

A. Symmetric loading

In this case, the structure is symmetric with regard to the line axis, then $C_{c1} = C_{c2} = C_c$, $L_1 = L_2 \equiv L_r$, and $C_1 = C_2 \equiv C_r$ (giving also $\xi_1 = \xi_2 = \xi_0$), and the effective solution of (3.5) is:

$$\omega = \frac{\omega_0}{\sqrt{1 - \frac{C_M}{C_r + C_c}}} = \frac{1}{\sqrt{L_r(C_c + C_r - C_M)}} \quad (3.7)$$

Note that the inter-resonator coupling (C_M) between CSRRs has the effect of increasing the transmission zero frequency (to the right of ξ_0), just conversely to its counterpart structure of a CPW loaded a pair of SRRs in section 3.1.

B. Asymmetric loading (different CSRRs with the same resonant frequencies)

In this asymmetric case, two CSRRs are different (i.e., $L_1 \approx L_2$, $C_1 \approx C_2$), but satisfying the condition $\xi_1 = \xi_2 = \xi_0$. Thus, expression (3.5) gives:

$$\omega_{\pm} = \frac{\omega_0}{\sqrt{1 \mp \frac{C_M}{\sqrt{(C_1 + C_{c1})(C_2 + C_{c2})}}}} \qquad (3.8)$$

Both solutions are physical solutions of the structure (none of them correspond to poles of the shunt reactance), and these two transmission zeros are located to the left (ω_-) and right (ω_+) of ω_0, which possesses the same phenomenon as the structure of a CPW loaded SRRs in section 3.1. Similarly, there is also a balanced condition which is:

$$\frac{C_{c1}}{C_{c2}} = \frac{\sqrt{C_1 + C_{c1}}}{\sqrt{C_2 + C_{c2}}} = \frac{\sqrt{L_2}}{\sqrt{L_1}} \qquad (3.9)$$

to obtain only one transmission zero (at ω_+)), since the reactance exhibits a pole at ω_-.

C. General case

For the general case, i.e., an asymmetric structure with arbitrary resonator frequencies ($L_1 \approx L_2$, $C_1 \approx C_2$) and $\xi_1 \approx \xi_2$, the transmission zeros are given by the two solutions of (3.5). The coupling capacitance C_M enhances the distance between the transmission zeros, i.e.,

$$\omega_+^2 - \omega_-^2 = \frac{\sqrt{(\omega_1^2 - \omega_2^2)^2 + 4C_M^2\omega_1^4\omega_2^4 L_1 L_2}}{[1 - C_M^2\omega_1^2\omega_2^2 L_1 L_2]} > \omega_1^2 - \omega_2^2 \qquad (3.10)$$

3.2.1 Comparison between the lumped equivalent circuit models of a CPW loaded with a pair of SRRs and a microstrip line loaded with a pair of CSRRs

In section 3.1 and section 3.2, emphasizes are laid on the analysis of the equivalent circuit models and the equations that provide the transmission zeros frequencies. However, both structures exhibit very similar phenomenology, despite their corresponding equivalent circuit models are described completely different. Article **AWPL16** and [108] discuss a mapping between the elements of both models which offers identical results for the analytical expressions, providing the resonant frequencies (transmission zeros) that these lines exhibit.

Table 3.1 shows this mapping between the lumped elements of these two structures, from which the general solutions of (3.1) and (3.5) are identical. Apparently, there is an asymmetry in the mapping relation, i.e., $L_{1,2} \uparrow \quad C_{1,2} + C_{c1,2}$, which is not the inverse mapping of $C_{1,2} \uparrow$ $L_{1,2}$. This is due to the fact that the circuit in Figure 3.2(b) is expressed with the mutual couplings between the microstrip line and the two CSRRs. In order to obtain perfect parallelism between both models, an alternative circuit model is proposed as shown in Figure

3.3(a). In this case, the mapping shown in Table 3.1 as $L_{1,2} \uparrow \quad C_{1,2} + C_{c1,2}$, could rewrite as $L_{1,2} \uparrow \quad C_{1,2new}$.

Table 3.1 Mapping relations of lumped elements of the equivalent circuit models between CPW loaded with SRRs and microstrip line loaded with CSRRs.

CPW loaded SRRs	Microstrip line loaded CSRRs
M	C_M
$C_{1,2}$	$L_{1,2}$
$L_{1,2}$	$C_{1,2} + C_{c1,2}$ or $C_{1,2new}$

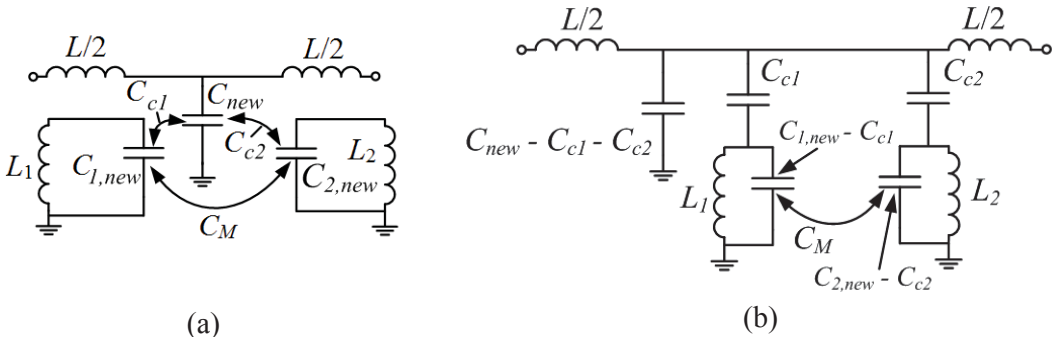

FIGURE 3.3: (a) Alternative circuit to express the circuit model of a microstrip line loaded with a pair of CSRRs, and (b) transformed model.

3.3 Microstrip lines and CPWs loaded with stepped impedance resonators

Article **MOTL16 (3)** and article **micromachines15** introduce the structure of a microstrip line loaded with a pair of stepped impedance resonators (SIRs) and a CPW loaded with a 5-section stepped impedance resonator (5s-SIR). Due to the high electric coupling between the line and the resonant elements, the structures are electrically small, i.e., dimensions are small as compared to the wavelength at the fundamental resonance [88]. Thanks to the advantage of electrical small size, it is possible to propose equivalent lumped circuit models to analyze the behavior of the structures.

3.3.1 A microstrip line loaded with pairs of SIRs

In article **micromachines15**, a microstrip line loaded with a pair of SIRs is introduced. Figure 3.4(a) depicts its typical topology. Assuming that the microstrip line is electrically short, and that there is a high impedance contrast between the narrow and wide sections of the SIR [83], the structure can be described by the lumped element equivalent circuit shown in Figure 3.4(b) [107]. The model takes into account of the coupling (magnetic) between the two SIRs, which is modeled through the mutual inductance M (such coupling is negative because the currents in the inductances flow in opposite directions).

The transmission zeros of the structure are given by those frequencies that null the reactance of the shunt branch which could be easily inferred from Figure 3.4(c), that is:

$$\omega_{\pm}^2 = \frac{A \pm \sqrt{B}}{D} \qquad (3.11)$$

with

$$A = L_1C_1 + L_2C_2$$

$$B = (L_1C_1 - L_2C_2)^2 + 4C_1C_2M^2$$

$$D = 2C_1C_2(L_1L_2 - M^2)$$

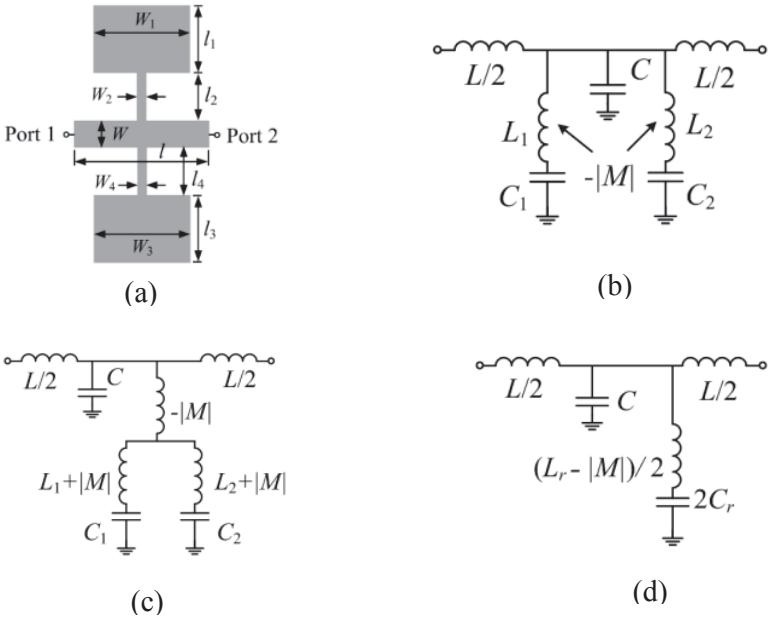

FIGURE 3.4: (a) Microstrip line loaded with a pair of SIRs (in parallel); (b) lumped element equivalent circuit model; (c) transformed equivalent circuit model; and (d) equivalent circuit model for symmetric case of the structure.

If the structure is symmetric (i.e., $L_1 = L_2 \equiv L_r$ and $C_1 = C_2 \equiv C_r$), then the lumped equivalent circuit model could by simplified as shown in Figure 3.4(d), from which the only one transmission zero frequency could be inferred and the mathematical solution of (3.11) which provide this transmission zero frequency is at:

$$\omega = \frac{1}{\sqrt{(L_r - |M|)C_r}} \qquad (3.12)$$

Thus, the mutual coupling between the two inductors of the SIRs pair has the effect of increasing the notch frequency.

3.3.2 CPW loaded with 5-section-SIR (5s-SIR)

Article **MOTL16 (3)** dedicates to the structure of a CPW loaded with 5-section-SIR (5s-SIR). As compared to the structure of a microstrip line loaded SIRs, the 5s-SIR-loaded CPW structure presented in this section exhibits more design flexibility as long as it is described by a circuit model where the resonant elements (5s-SIR) is electrically coupled to the line (by contrast, in the structure reported in section 3.3.1 the pair of SIRs are in direct contact with the line).

Figure 3.5(a) shows the typical topology of a CPW loaded with 5s-SIR, which is transversely etched on the back substrate side and consists of a wide (capacitive) central and external sections cascaded with narrow (inductive) sections. The central section is placed below the central strip of the CPW, whereas the external sections are located below the ground planes. This provides a large resonator capacitance that makes the particle electrically small. The inductive sections are etched beneath the slot region. All the sections must be electrically short for a correct description of the structure by means of a lumped element circuit.

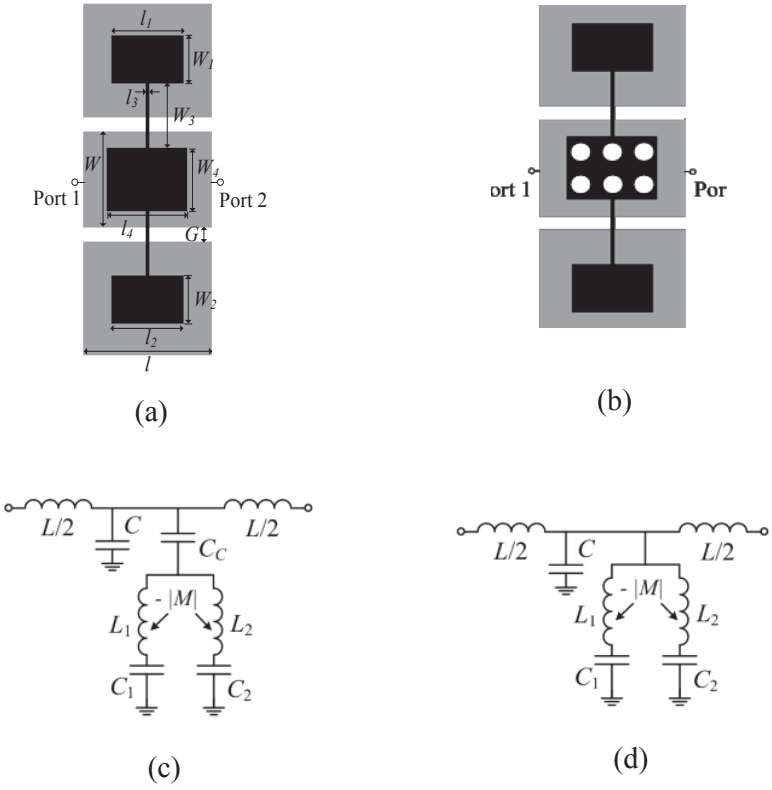

FIGURE 3.5: (a) Typical topology of a CPW loaded with a 5s-SIR; (b) a CPW loaded with a 5s-SIR directly in contact to the central strip of the CPW through metallic vias; (c) the equivalent circuit model of the structure in Figure 3.5(a); and (d) the equivalent circuit model of the structure in Figure 3.5(b).

As shown in Figure 3.5(c), in order to accurate model this structure, the equivalent circuit model accounts not only for the different semi-lumped planar (inductive and capacitive) elements of the 5s-SIR, but also for the two kinds of coupling mechanisms existing here, i.e.,

the electric coupling between the 5s-SIR and the line, through C_c (the broadside capacitance between the central strip of the CPW and the central section of the 5s-SIR), and the other one is the magnetic coupling between the two inductances of the resonator, through M (such coupling is negative because the currents in the inductances flow in opposite directions).

According to the same procedure of analyzing the circuit model in section 3.1 and section 3.2, transmission zero frequencies appear when the reactance of the shunt branch nulls from the circuit model of Figure 3.5(c). These two transmission zero frequencies are of the same form as (3.11), but with:

$$A = C_1C_2(L_1 + L_2 - 2M) + C_c(L_1C_1 + L_2C_2)$$

$$B = C_1^2C_2^2(L_1 + L_2 - 2M)^2 + C_c^2(L_1C_1 - L_2C_2)^2 + 2C_cC_1C_2 \times$$

$$\{L_1C_1(L_1 - L_2 - 2M) + L_2C_2(L_2 - L_1 - 2M) + 2M^2(C_1 + C_2 + C_c)\}$$

$$D = 2C_cC_1C_2(L_1L_2 - M^2)$$

Similarly, if the structure is symmetric, (i.e., $L_1 = L_2 \ldots L_r$ and $C_1 = C_2 \ldots C_r$), only one transmission zero exists at:

$$\omega = \frac{1}{\sqrt{(L_r - |M|)\dfrac{C_cC_r}{C_c + 2C_r}}} \qquad (3.13)$$

The mutual coupling (M) between the SIRs has the effect of increasing the notch frequency, with a behavior identical to the structure of a microstrip line loaded with SIRs in section 3.3.1.

In addition, article **micromachines16** proposes a variation of the previous 5s-SIR-loaded CPW structure, which consists of a direct connection (through vias) of the 5s-SIR to the central strip of the CPW, as depicted in Figure 3.5(b). This effectively shorts the capacitance C_c, and the resulting circuit model is identical to the one depicted in Figure 3.4(b), therefore possesses the same behavior of transmission coefficient response.

3.4 Coplanar waveguide loaded with a pair of slotted stepped impedance resonators

As complementary counterpart of SIRs-loaded microstrip line, article **MOTL16 (11)** dedicates to the structure of a CPW loaded with pairs of slotted SIRs (slot-SIRs) which is etched in the ground planes, as shown in Figure 3.6(a). The analysis and modeling of the structure is necessary for the design purpose [109-111]. The proposed equivalent circuit model is depicted in Figure 3.6(b). It is assumed that the structure can be described as a pair of split transmission lines (the central strip being a common conductor), each one loaded with a series-connected parallel resonant tank (L_{si}-C_{si} with i = 1,2). The electrical length and characteristic impedance of the transmission line sections are θ and $2Z_c$ (where Z_c is the CPW characteristic impedance), respectively. It has been found that for reasonable widths of the

CPW central strip, electric coupling between the resonators arises, and this effect is accounted for by including a mutual capacitance, C_m, for an accurate modeling [112].

Since the slot-SIRs loaded CPW is designed electrically small, the hybrid lumped - distributed model could be transformed by a lumped element equivalent circuit, as shown in Figure 3.6(c). Using this model, the resonance frequencies are obtained analytically, by calculating the poles of the reactance of the series branch in the π-model of it. The solutions are of the same form as (3.11), but with:

$$A = L_{s1}L_{s2}(C_{s1} + C_{s2} - 2C_m) + 4L(L_{s1}C_{s1} + L_{s2}C_{s2})$$

$$B = L_{s1}^2L_{s2}^2(C_{s1} + C_{s2} - 2C_m)^2 + 16L^2(L_{s1}C_{s1} - L_{s2}C_{s2})^2 +$$

$$8LL_{s1}L_{s2}\{L_{s1}C_{s1}(C_{s1} - C_{s2} - 2C_m) + L_{s2}C_{s2}(C_{s2} - C_{s1} -$$

$$2C_m) + 2C_m^2(L_{s1} + L_{s2} + 4L)\}$$

$$D = 8LL_{s1}L_{s2}(C_{s1}C_{s2} - C_m^2)$$

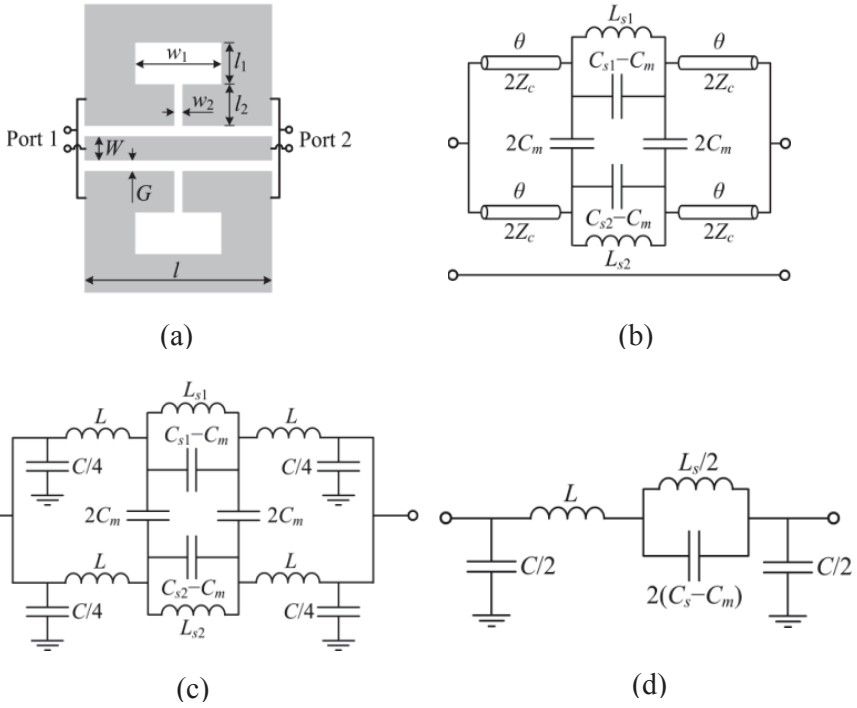

FIGURE 3.6: (a) A CPW loaded with a pair of coupled slotted SIRs; (b) hybrid lumped-distributed model; (c) lumped model when CPW is electrically short; and (d) simplified lumped circuit model for a symmetric pair of resonators.

If the structure is symmetric (i.e., $L_{s1} = L_{s2} \equiv L_s$ and $C_{s1} = C_{s2} \equiv C_s$), the equivalent circuit model could be transformed as shown in Figure 3.6(d), where the mathematical solution (the transmission zero frequency) is:

$$\omega = \frac{1}{\sqrt{L_s(C_s - C_m)}} \quad (3.14)$$

which means the mutual electric coupling ($C_m < 0$) between the slot-SIRs has the effect of decreasing the notch frequency, with a reversed behavior to the structures of microstrip line loaded SIRs and CPW loaded 5s-SIR in section 3.3.

3.4.1 Comparison between the lumped equivalent circuit models of SIR-loaded CPWs and slot-SIR-loaded CPWs

In section 3.3 and section 3.4, analysis and circuit model of the structures of SIR-loaded CPWs and slot-SIRs-loaded CPWs are introduced. In addition, article **MOTL16 (3)** also explains a lumped element mapping between these two structures, as shown in Table 3.2. Despite the fact that the 5s-SIR- and slot-SIR-loaded CPW structures are significantly different, with the mapping the expressions providing the pair of transmission zero frequencies in both structures are identical. Neither these structures are dual, nor are the equivalent circuits circuit duals [81]. However, the poles of the dual circuit of the resonant shunt branch of the 5s-SIR-loaded CPW (see in Figure 3.5(c)), depicted in Figure 3.7, are identical to those of the circuit of Figure 3.6(c), and this explains the formal coincidence of the two equations providing the transmission zero frequencies.

Table 3.2 Mapping relations of lumped elements equivalent circuit models between CPW loaded with 5s-SIR and CPW loaded with slot-SIRs.

CPW loaded 5s-SIR	CPW loaded slot-SIRs
C_c	$4L$
$C_{1,2}$	$L_{s1,2}$
$L_{1,2}$	$C_{s1,2}$
M	C_m

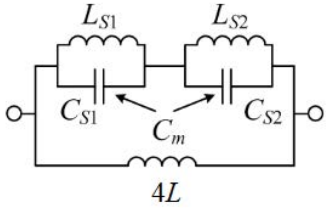

FIGURE 3.7: Circuit dual of the resonant shunt branch of the equivalent circuit of the 5s-SIR-loaded CPW shown in Figure 3.5(c). Note that the reactive elements have been designated according to the mapping.

3.5 Effects of inter-resonator couplings on sensitivity

Among all the structures and their corresponding equivalent circuit models that we have introduced in this chapter, there exist two kinds of coupling mechanisms, one being the coupling between the resonators and loaded transmission lines, the other one being the mutual coupling between the loaded resonator pairs, which is normally called inter-resonator coupling. It is important to note that the structures introduced in this chapter only take into

account one unit cell of the structures, thus couplings between adjacent resonators belonging to different cells do not exist [113].

The mutual coupling between the loaded resonator elements has the effect of further splitting the transmission zero frequencies, thus degrading the sensitivity of the structures. Article **AWPL15** and [106] provide frequency responses for the structures of a CPW loaded with a pair of SRRs introduced in section 3.1 and a microstrip line loaded with a pair of CSRRs in section 3.2, respectively. As shown in Figure 3.8, both of the mutual inter-resonator couplings (M' in Figure 3.8(a) and C_M in Figure 3.8(b)) have the effect of splitting further the two transmission zeros. Note in Figure 3.8(a) the value of d' represents the quantity of mutual coupling, as d' getting smaller, the mutual coupling M' becoming bigger.

Sensitivity can be defined as the variation in the difference between the resonant frequencies (transmission zeros) due to the difference in the perturbations which cause the shifting or changing of the transmission zeros. It is also noted that for small perturbations the further two transmission zero frequencies split, the worse the sensitivity. Thus, in order to improve the sensitivities of the proposed structures, the inter-resonator couplings should be avoided or minimized. This issue will be discussed in more details and be solved in chapter 4.

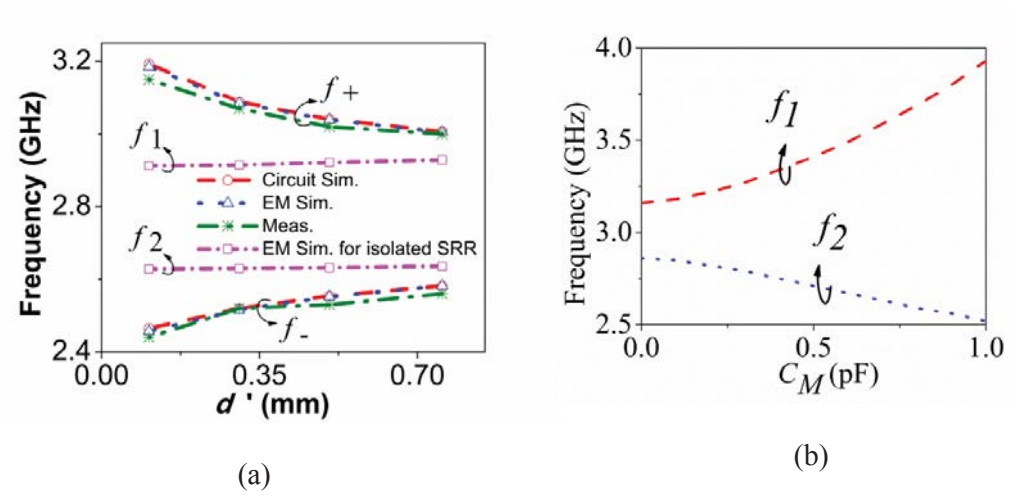

(a) (b)

FIGURE 3.8: (a) Variation of transmission zeros as a function of d' for the structure of a CPW loaded with SRRs perturbed by increasing the dimension of the bottom SRR, and (b) the effect of mutual coupling C_M on transmission zero frequencies for the structure of a microstrip line loaded with CSRRs, which was recorded by changing different values of C_M to a particular asymmetric case.

Chapter 4

Strategies to Optimize Sensitivity based on Frequency Splitting

This chapter is focused on the optimization of sensitivity based on frequency splitting. It is divided into three parts related to three structures, i.e., microstrip lines loaded with CSRRs and with SIRs, implementing in splitter/combiner and cascade configurations, respectively. As mentioned in section 3.5, inter-resonator coupling degrades the sensitivity of the structure, thus two resonators forming a pair are placed far enough from each other to avoid this inter-resonator coupling. As will be discussed later in splitter/combiner configurations, sensitivity is also degraded by the length of the loaded transmission lines, and sensing, also related to symmetry disruption (unbalanced loads) and based on the separation between transmission zeros (the output variable), is influenced by the interference between the pair of resonator-loaded lines. This chapter targets on obtain necessary conditions (length of loaded transmission lines) to achieve such optimization of sensitivity for small perturbations of the structures.

The organization of this chapter is as follows. Section 4.1 presents a splitter/combiner microstrip section loaded with pairs of CSRRs, including the lumped equivalent circuit models and the optimized condition for enhancing sensitivity. Section 4.2 devotes to microstrip lines loaded with SIRs, in parallel and cascade configurations, respectively. Similarly their equivalent circuit models are provided for accurately analyzing the behavior of the structures, and comparison is made between these two configurations to confirm that cascade method offers enhanced sensitivity since the two transmission zeros are independent to each other (only one resonant frequency of the perturbed resonator shifted), while for parallel configuration frequency splitting is characterized by a shift in two resonant frequencies due to the existence of mutual inter-resonator coupling and resonator perturbations. Lastly, section 4.3 explains a splitter/combiner microstrip section loaded with a pair of SIRs, a form similar to the structure in section 4.1, but loaded with SIRs. This structure is also based on the principle of the structure in section 4.2, but with the splitter/combiner section, the inter-resonator coupling between the SIRs in parallel way is eliminated (in section 4.2 the proposal of cascade configuration is also to avoid this mutual inter-resonator coupling). Similar to the sensitivity analysis in section 4.1, if the electric length of the parallel branch of loaded microstrip lines satisfies with a certain condition, the optimum sensitivity could be achieved for small perturbation of resonators.

4.1 Splitter/combiner microstrip section loaded with pairs of complementary split ring resonators

For a microstrip line loaded with a pair of CSRRs, if these two CSRRs forming the pair are far enough from each other to avoid inter-resonant coupling, the CSRRs would not be able to be coupled with the microstrip line [67,76,114]. Therefore, article **TMTT16 December** and conference article **IMS16** propose a new structure, i.e., a pair of microstrip lines individually loaded with two CSRRs, and the pair of lines is cascaded in between a power divider and combiner, resulting in a two-port device that can be fed and characterized by means of single-ended ports.

The typical topology of the considered power splitter/combiner microstrip structure with CSRRs etched individually in the ground plane of each line is shown in Figure 4.1(a). Each branch consists of a 50 Z line loaded with a CSRR. To match the structure to the 50 Z ports, impedance inverters implemented by means of 35.35 Z quarter wavelength transmission line sections are cascaded between the ports and the T-junctions. The circuit schematic, with distributed and lumped elements, is shown in Figure 4.1(b). An asymmetric structure is considered as general case, but asymmetry refers to the dimensions of the CSRRs, rather than the transmission line section. The lumped elements account for the CSRR-loaded microstrip line section. Thus, L_u (L_l) and C_u (C_l) model the inductance and capacitance of the microstrip lines, respectively, above the CSRR in the upper (lower) parallel branch, and the resonators (CSRRs) are accounted for by the tanks L_{Cu}-C_{Cu} (upper CSRR) and L_{Cl}-C_{Cl} (lower CSRR) [71]. The distributed elements account for the transmission line sections which are not located on top of the CSRRs. The line impedance Z_i and the electrical length τ_i (with i = 1,2) define such line sections [115,116].

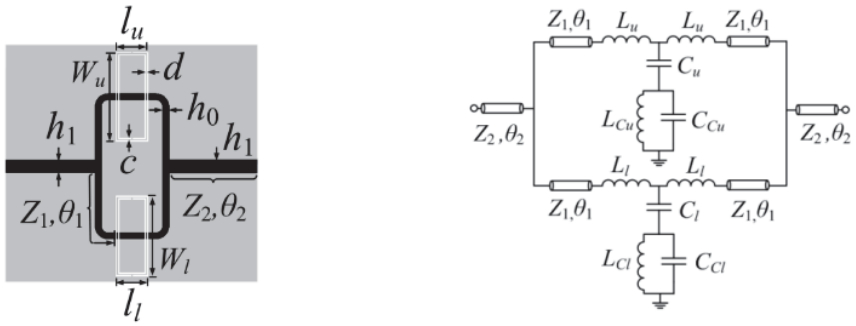

(a) (b)

FIGURE 4.1: (a) Typical topology of a power splitter/combiner microstrip section loaded with two CSRRs, and (b) equivalent circuit model.

The transmission zeros are not only dictated by the intrinsic resonance frequency of the resonators, but also by the length of the lines, and such transmission zeros occur at those frequencies where the signals at the end of each loaded line exactly cancel [65]. Note that in order to predict the transmission zero frequencies through Figure 4.1(b), the input and output transmission line sections can be neglected (such sections do not have influence on the position of the notches). The resulting two-port network exhibits transmission zeros at those

frequencies satisfying $Y_{12} = Y_{21} = 0$, and/or $Y_{11} = Y_{22} = \infty$, where Y_{11}, Y_{12}, Y_{21} and Y_{22} are the elements of the admittance matrix [65]. Since this two-port consists of two parallel connected two-ports (i.e., the upper and the lower CSRR-loaded branches of the splitter/combiner), Y_{21} is simply given by:

$$Y_{21} = Y_{21,u} + Y_{21,l} \tag{4.1}$$

and $Y_{21,u}$ and $Y_{21,l}$ (the sub-indexes *u* and *l* refer to the upper and lower branches of the parallel part) can be determined by first obtaining the ABCD matrix of each branch, from which the elements of the right-hand side in (4.1) are given by $Y_{21,u} = -1/B_u$ and $Y_{21,l} = -1/B_l$, where B_u and B_l are the B elements of the ABCD matrix for the upper and lower branches, respectively [65]. Thus, the transmission zeros are given by:

$$\frac{1}{B_u} + \frac{1}{B_l} = 0 \tag{4.2}$$

with

$$B_u = j\left(Z_1 sin2\theta_1 + 2\omega L_u cos^2_{\theta_1}\right) + j\frac{(Z_1 sin\theta_1 + \omega L_u cos\theta_1)^2}{\frac{\omega L_{Cu}}{1-\frac{\omega^2}{\omega^2_{Cu}}} - \frac{1}{\omega C_u}} \tag{4.3a}$$

$$B_l = j\left(Z_1 sin2\theta_1 + 2\omega L_l cos^2_{\theta_1}\right) + j\frac{(Z_1 sin\theta_1 + \omega L_l cos\theta_1)^2}{\frac{\omega L_{Cl}}{1-\frac{\omega^2}{\omega^2_{Cl}}} - \frac{1}{\omega C_l}} \tag{4.3b}$$

with $\zeta_{Cu} = (L_{Cu}C_{Cu})^{-1}/2$ and $\zeta_{Cl} = (L_{Cl}C_{Cl})^{-1}/2$. The general solution of (4.2) is not straightforward. But if the two CSRRs are identical, the structure is symmetric, and (4.2) provides a single solution (transmission zero) with angular frequency given by

$$\omega_z = \frac{1}{\sqrt{L_r(C_r + C)}} \tag{4.4}$$

where $L_{Cu} = L_{Cl} = L_r$, $C_{Cu} = C_{Cl} = C_r$, and $C_u = C_l = C$. Note that (4.4) is the frequency that shorts to ground the reactance of the identical shunt branches of the lumped two-port T-networks of Figure 4.1(b), as expected.

Except for the symmetric case, the general transmission zeros is possible to obtain numerically by (4.2), which are the consequence of an interfering phenomenon between the parallel CSRR-loaded line sections. By inspection and analysis on the positions of these transmission zeros we could determine the optimum conditions to enhance sensitivity.

The other alternative situation providing transmission zeros, that is, $Y_{11} = Y_{22} = \clubsuit$ with $Y_{21} = Y_{12} \approx \clubsuit$. In this case, we can analyze each branch independently. The reason is that $Y_{11,u} = \clubsuit$ and/or $Y_{11,l} = \clubsuit$ suffices to guarantee that $Y_{11} = Y_{11,u} + Y_{11,l} = \clubsuit$. From Figure 4.1(b) $Y_{11,u}$ can

be expressed as a function of Y_u, which is the admittance of the shunt branch (formed by C_u, L_{cu}, C_{cu}):

$$Y_{11,u} = \frac{cos2\theta_1 - \frac{\omega L_u}{Z_1} sin2\theta_1 + jY_u(\omega L_u cos2\theta_1 + Z_1 \frac{sin2\theta_1}{2} - \omega^2 L_u^2 \frac{sin2\theta_1}{2Z_1})}{j\left(2\omega L_u cos_{\theta_1}^2 + Z_1 sin2\theta_1\right) - Y_u(Z_1 sin\theta_1 + \omega L_u cos\theta_1)^2} \quad (4.5)$$

Inspection of (4.5) reveals that in order to guarantee $Y_{11,u}$ = ♣, the following condition should be satisfied:

$$Z_1 sin\theta_1 + \omega_0 L_u cos\theta_1 = 0 \quad (4.6)$$

where ξ_0 is the frequency where Y_u = ♣. From (4.6), the following result is inferred:

$$\theta_1 = \arctan\left(-\frac{\omega_0 L_u}{Z_1}\right) = \pi - \arctan\left(\frac{\omega_0 L_u}{Z_1}\right) \equiv \theta_{1,\infty} \quad (4.7)$$

which gives the electrical length at ξ_0 that is necessary to obtain a transmission zero. The physical interpretation of this transmission zero is very clear. The solution of τ_1 provided by (4.6) corresponds to the electrical length of the microstrip line necessary to translate the shunt branch to the input or output port. Note that if L_u = 0, such electrical length is simply τ_1 = σ, as expected. Thus, if the frequency that nulls the reactance of the shunt branch satisfies (4.6), a short is present in the input and output ports of the upper branch, hence providing a transmission zero to the whole structure. Note that such transmission zero frequency does not depend on the characteristics of the other (lower) branch, and hence it is not associated to an interfering phenomenon, contrary to the other transmission zero (assuming asymmetry) which is still related to the destructive interference of the two branches.

In order to demonstrate that the electric length condition of (4.6) provides the optimum sensitivity [117], experiments with three different electric lengths of microstrip lines are carried out by perturbing the upper CSRR with the width dimension changed. The pairs of transmission zeros as a function of variations of CSRR width are shown in Figure 4.2.

In order to analyze the sensitivity, firstly it is defined as the variation of the frequency difference between the two transmission zeros with the variable that generates the asymmetry (typically a difference in dielectric constant between two loaded samples). In Figure 4.2, the asymmetries are caused by varying the width dimension of the lower CSRR. So the sensitivity is defined as:

$$S = \frac{\partial \Delta f_z}{\partial \Delta W_l} \quad (4.8)$$

where Γf_z = f_{z1} 0 f_{z2}. The sensitivity for the three considered cases is depicted in Figure 4.3, where it can be appreciated that the sensitivity for small unbalanced perturbations is clearly optimized when $\tau_1 = \tau_{1,\clubsuit}$ (note that if the optimum electrical length, 0.84σ in our case, is not considered, but it is very close to this value, the sensitivity is expected to approach the optimum value for practical unbalanced loads).

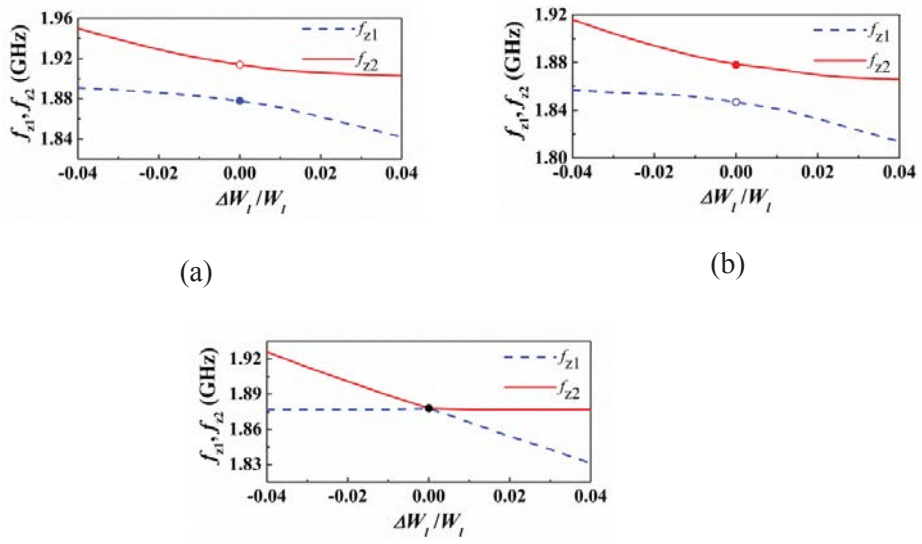

FIGURE 4.2: Variation of the transmission zeros as a function of the variation of the width of one of the CSRRs ($\Delta W_l / W_l$) for different electrical lengths of the transmission lines: (a) $\tau_1 = 0.672\sigma < \tau_{1,\clubsuit}$ (b) $\tau_1 = 1.008\sigma > \tau_{1,\clubsuit}$ (c) $\tau_1 = 0.84\sigma = \tau_{1,\clubsuit}$.

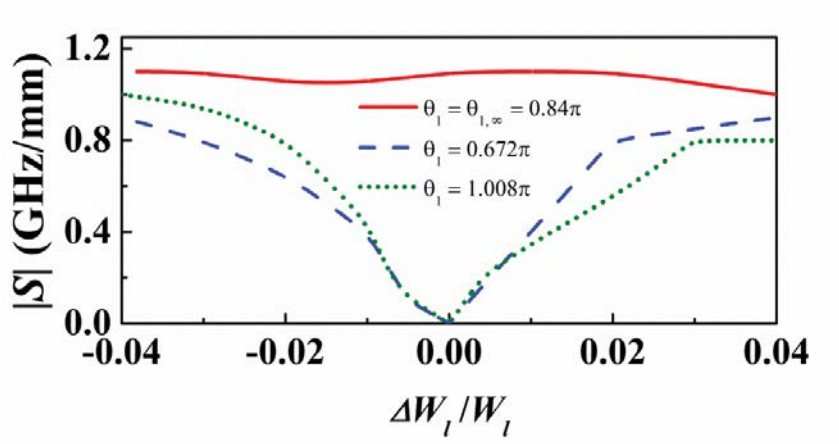

FIGURE 4.3: Sensitivity as a function of $\Delta W_l/W_l$ for different values of the electrical length of the microstrip lines.

4.2 Microstrip line loaded with stepped impedance resonators

Article **TMTT16 November** describes a new structure of a microstrip line loaded with a pair of SIRs in cascade connection. Compared with the structure of a microstrip line loaded with a pair of SIRs connecting directly in contact with the line in parallel configuration (introduced in section 3.3.1) [117], the advantage of this new structure is the improvement of sensitivity for small perturbations because of the elimination of inter-resonator coupling, which will

explain later in this section. The other advantage lies on the differential measurement, which is robust against variable ambient conditions provided that these conditions perturb in the form of a common-mode stimulus [8,39,118,119].

Firstly, the proposed topology is illustrated in Figure 4.4(a), and consists of a transmission line loaded with a cascade connection of two identical SIRs which are spaced apart by a microstrip line section of length l_s. If the SIRs are loaded on the same side of the line, as is considered, the resonators may be coupled not only magnetically, but also electrically. However, the resonators are placed sufficiently separated so that it may assume that the mutual inter-resonator coupling is negligible.

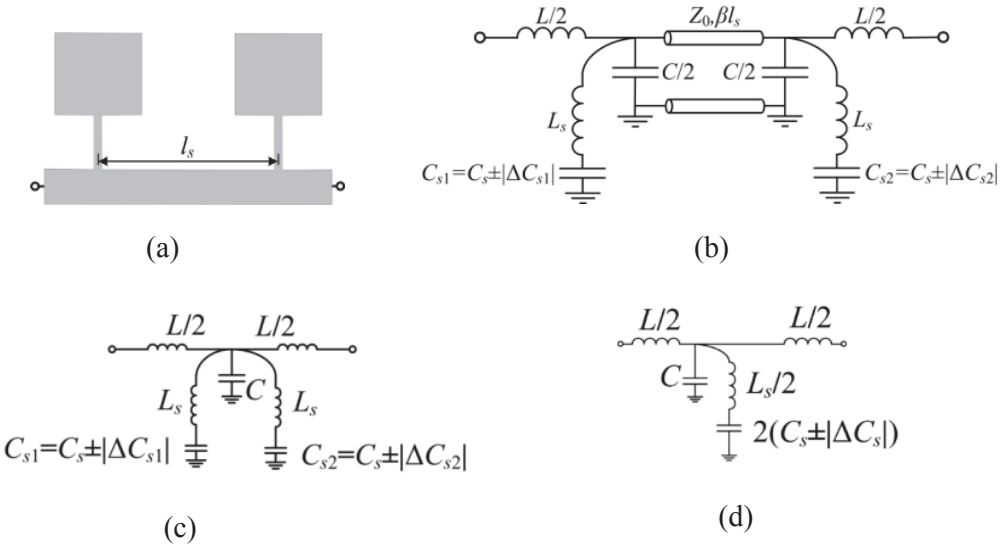

FIGURE 4.4: (a) A microstrip line loaded with a pair of identical SIRs in cascade connection; (b) Equivalent hybrid circuit/TL model including arbitrary capacitive perturbations; (c) Simplified equivalent circuit model when the resonators are spaced half-wavelength apart, i.e., the in-between transmission line section has an electrical length of $\beta l_s = 180°$; (d) Simplified equivalent circuit model for $\beta l_s = 180°$ in the case of balanced perturbations.

The proposed circuit model is that represented in Figure 4.4(b) [107]. Regardless of the length of the transmission line section between resonators, l_s, the transmission zero frequencies are given by:

$$\omega_l = \min\left(\frac{1}{\sqrt{L_s(C_s \pm |\Delta C_{s1}|)}}, \frac{1}{\sqrt{L_s(C_s \pm |\Delta C_{s2}|)}}\right) \quad (4.9a)$$

$$\omega_u = \max\left(\frac{1}{\sqrt{L_s(C_s \pm |\Delta C_{s1}|)}}, \frac{1}{\sqrt{L_s(C_s \pm |\Delta C_{s2}|)}}\right) \quad (4.9b)$$

where ω_l and ω_u denote the lower and upper resonance frequencies, respectively. According to these expressions, the two resonances can be shifted independently like using single SIRs, even for unbalanced perturbations. Clearly, the resonance frequency splitting phenomenon, which emerges from unbalanced perturbations, is of different nature in the two configurations

with SIRs loaded in shunt and cascade ways. In cascaded SIRs, splitting occurs as a mere result of frequency shifting (depends on the quantity of perturbation), whereas in parallel SIR there is a combination of frequency shifting and inter-resonator coupling.

In order to compare two configurations, it is convenient to assume a particular case where the in-between microstrip line section is half-wavelength long (l_s = λ/2, where λ is the guided wavelength at fundamental resonant frequency). As the input impedance of a load seen through a λ/2 line is unchanged, the circuit in Figure 4.4(b) is equivalent to that shown in Figure 4.4(c). Note that the SIRs are virtually connected at the same junction so that the structure behaves like if the SIRs were physically located at the same junction. So in this case, the equivalent circuit models of these two configurations are similar, except in cascade case without mutual inter-resonator coupling. If the perturbations are identical ($\omega_l = \omega_u = \omega_0$), the structure is symmetric. In this circumstance, the circuit in Figure 4(c) derives to the one in Figure 4(d), which is formally identical to that with parallel SIRs depicted in Figure 3.4(d).

Therefore, for parallel structure, when one of the resonators is perturbed ($\Delta C_{s2} \neq 0$), the two transmission zero frequencies change based on the effects of perturbation and mutual coupling. However, for cascade configuration, only the resonant frequency of the perturbed resonator is changed, the other transmission zero corresponding to the unperturbed resonator is always unchanged, as shown in Figure 4.5(a).

In Figure 4.5(a) and (b) unbalanced perturbations have been introduced by a capacitive variation in one of the SIRs ($\Delta C_{s1} = 0$, $\Delta C_{s2} \neq 0$). It is clear that as mutual coupling M becomes bigger, frequency splitting increases, as we expected in section 3.5, thus sensitivity tends to be worse. Indeed, the maximum sensitivity corresponds to the case of (uncoupled) cascaded SIRs. As was stressed earlier, even for loose coupling coefficients, inter-resonator coupling cannot be neglected for similar perturbations. For small inputs, since the inter-resonator coupling in parallel SIRs decreases the sensitivity, parallel-connected SIRs are apparently not much appropriate to properly operate as a sensor. Conversely, SIRs in cascade connection are expected to achieve high sensitivities and discriminations. Nevertheless, the parallel configuration can be useful when the perturbations differ from each other significantly. In these situations, coupling plays an insignificant role.

In the previous studies, capacitive perturbations have been produced by changing the physical dimensions of the resonators. Evidently, in practice, the capacitive perturbations in a permittivity sensor must be due to permittivity perturbations of samples under test (SUTs). Figure 4.5(c) and (d) show the resonant frequencies and sensitivities by permittivity perturbations. It is obvious that the results for capacitive and permittivity perturbations are similar, but the sensitivity for small perturbations is much better in cascade configuration than in parallel configuration. More accurately and specifically, the sensitivity to a permittivity perturbation ($\Delta\varepsilon_{r2}/\Delta\varepsilon_r$) is a bit smaller than that to a capacitive perturbation ($\Delta C_{s2}/\Delta C_s$) with the same amount of relative perturbation. This is because the capacitance is not exactly proportional to the permittivity.

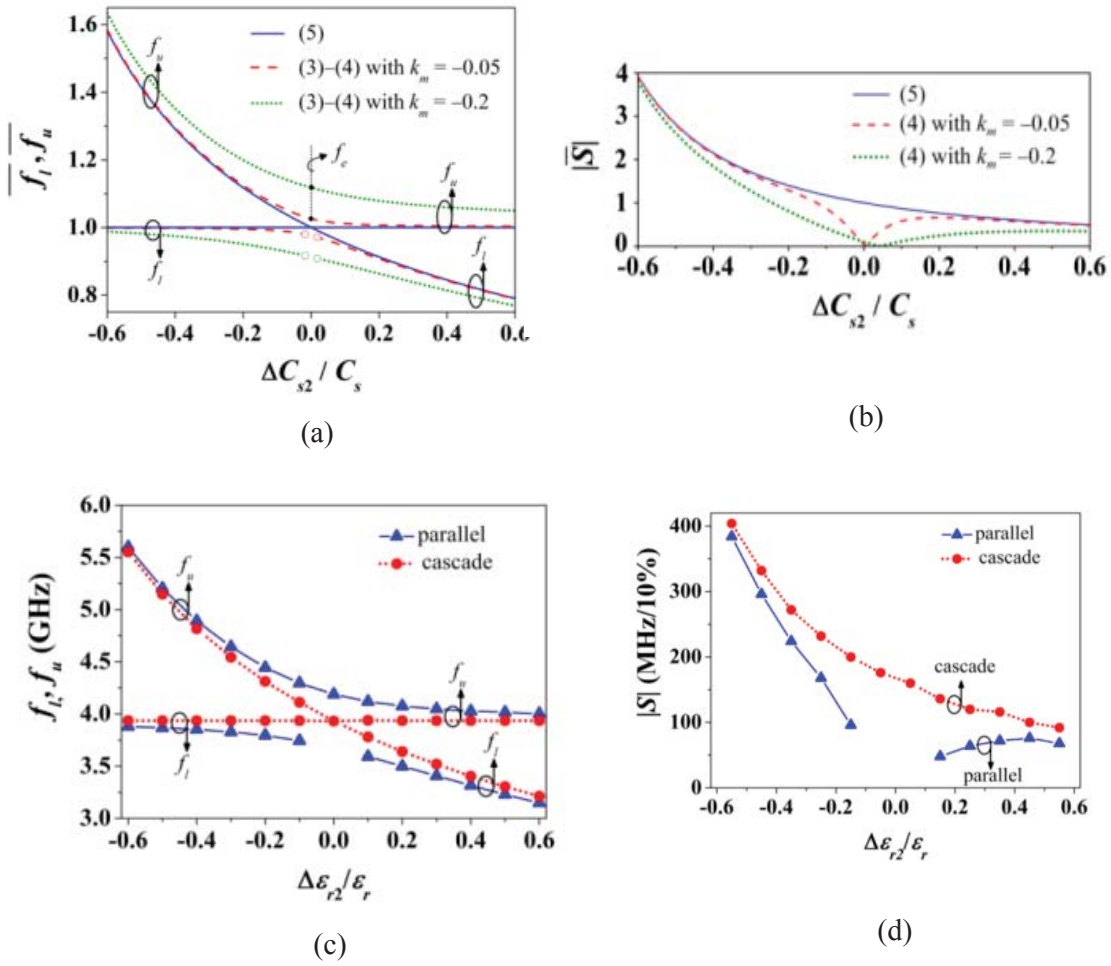

FIGURE 4.5: Resonant frequencies for microstrip lines loaded with parallel and cascaded SIRs, and their sensitivities. (a) For capacitive perturbations with resonant frequencies normalized to the constant resonant frequency of the non-perturbed uncoupled SIR determined by (4.9). The capacitive perturbations are $\Delta C_{s1} = 0$ and $-0.6 \le \Delta C_{s2} / C_s \le 0.6$; (b) For capacitive perturbations, sensitivity magnitude normalized to the case of balanced perturbations ($\Delta C_{s2} = 0$) for the cascaded configuration and for the parallel arrangement, sensitivity is calculated similarly using (3.11); (c) For permittivity perturbations, the relative permittivity is perturbed by steps of ±10% so that $1.352 \le \varepsilon_{r2} \le 5.408$ ($-0.6 \le \Delta\varepsilon_{r2}/\varepsilon_r \le 0.6$) where $\varepsilon_r = 3.38$; (d) Sensitivities for permittivity perturbations, by steps of $\Delta\varepsilon_{r2}/\varepsilon_r = \pm 0.1$ (±10%).

In terms of the robustness of differential measurements against cross sensitivities, transmission line loaded with a single resonator would have wrong readout because of the transmission zeros drift differently in the presence of cross sensitivities which may change over time. By contrast, when loading identical samples, the cascaded structure is immune to cross sensitivities, so it is real differential sensing. But note that if loading different samples, the spurious caused by environment or other stimulus would take different effects on response, then it is not real differential sensor, but it minimizes the effect of cross sensitivity.

4.3 Splitter/combiner microstrip section loaded with pairs of stepped impedance resonators

Different to the cascade configuration discussed in section 4.2, article **sensors16** proposes another solution to prevent inter-resonator coupling between the pair of SIRs, which is using a splitter/combiner microstrip section, similar to the structure in section 4.1.

The typical topology of the considered SIR-loaded power splitter/combiner microstrip section is depicted in Figure 4.6(a). Each branch consists of a 50 Z line loaded with a SIR. To match the structure to the 50 Z ports, impedance inverters implemented by means of 35.35 Z quarter wavelength transmission line sections are cascaded between the ports and the T-junctions [65]. The circuit schematic, including distributed and lumped elements, is shown in Figure 4.6(b), where the general case of an asymmetric structure is considered. However, asymmetry concerns SIR dimensions, rather than the distributed elements (transmission line sections). The lumped elements account for the SIRs; therefore, L_u-C_u and L_l-C_l model the upper and lower SIRs, respectively. The distributed elements in the model describe the different transmission line sections, and are characterized by the line impedance Z_i and electrical length τ_i (with i = 1,2).

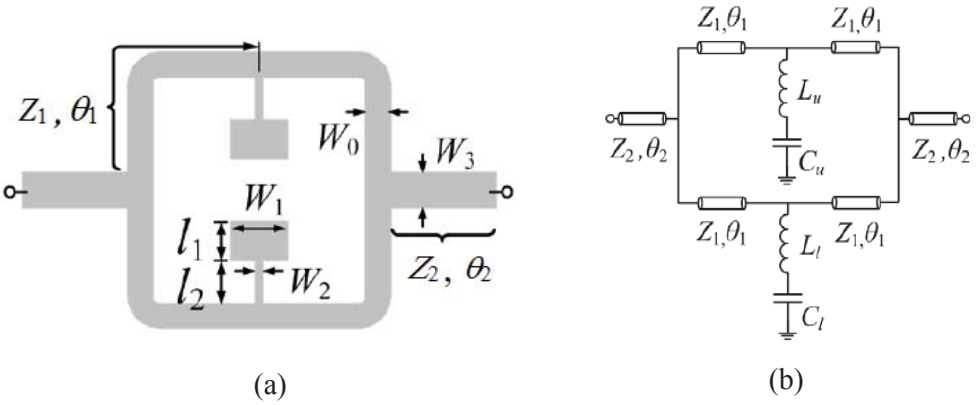

FIGURE 4.6: (a) Topology and relevant dimensions of the SIRs-loaded power splitter/combiner microstrip structure, and (b) circuit schematic.

It is assumed in the model that the SIRs are separated enough so as to neglect coupling between them [100]. Nevertheless, note that unless the resonators are identical, situation that provides a single transmission zero at the fundamental SIR resonance, the two transmission zeros that should appear for asymmetric resonators (or unbalanced perturbations) are not generally given by the resonance frequencies of the SIRs. The reason is that in this splitter/combiner structure, a short in one of the parallel microstrip lines does not guarantee a transmission zero in the whole structure since the power can be transmitted through the other line [120]. Indeed, for asymmetric SIRs, the transmission zeros are in general consequence of an interfering phenomenon. To gain insight on this, we use the same procedure as in section 4.1 to analyze the equivalent circuit model in Figure 4.6(b). As compared with the equivalent circuit model in Figure 4.1(b), the only difference is the shunt resonant branches. Thus, (4.1)

and (4.2) are applicable here to obtain the transmission zeros, only with different shunt branches, which are:

$$B_u \cong jZ_1 \sin 2\tau_1 0 \frac{Z_1^2 \sin^2 \tau_1}{Z_u} \tag{4.10a}$$

$$B_l \cong jZ_1 \sin 2\tau_1 0 \frac{Z_1^2 \sin^2 \tau_1}{Z_l} \tag{4.10b}$$

where Z_u and Z_l being the impedance of the SIRs of the upper and lower branches, respectively. i.e.,:

$$Z_u \cong j\left(\xi L_u 0 \frac{1}{\xi C_u} \right) \tag{4.11a}$$

$$Z_l \cong j\left(\xi L_l 0 \frac{1}{\xi C_l} \right) \tag{4.11b}$$

From (4.2) and (4.10), if the resonators are different and exhibit different resonance frequencies, the transmission zeros appear at those frequencies where $B_u = 0B_l$, and are consequence of signal interference. However, if the distance between the T-junction and one of the SIRs is o/2, or $\tau_1 = \sigma$, in this case, one of the transmission zeros is given by the resonance frequency of the corresponding SIR, whereas the other one is given by the solution of (4.2) and (4.10). Note that if $\tau_1 = \sigma$, the shunt reactance is translated to the T-junction, providing a short at this point and hence a transmission zero, regardless of the characteristics of the other parallel branch.

In order to validate the structure and illustrate that the optimum sensitivity could be achieved when $\tau_1 = \sigma$ is satisfied, we consider three different electric lengths of the microstrip lines, i.e., $\tau_1 = 0.8\sigma$, $\tau_1 = \sigma$, and $\tau_1 = 1.2\sigma$, and perturb the lower SIR by increasing or decreasing the length of the patch capacitance (capacitive perturbations through dimensions), with the upper SIR unchanged. In all the cases, the transmission zeros as a function of this perturbed length are shown in Figure 4.7.

As can be seen, the transmission zeros tend to separate as the asymmetry increases. However, such zeros do not cross in the limit of small asymmetries (emulating small asymmetric perturbations or loads). Hence, the sensitivity, defined as the variation of the differential output with the differential input, is degraded in this limit. Note that the differential output is the difference between the transmission zeros, whereas the differential input can be, for instance, the difference in the capacitances of the SIRs. When the electric length of the lines satisfies $\theta_1 = \pi$, in this case, the curves giving the two transmission zeros cross (see Figure 4.7(c)), and one of the transmission zeros does not vary with the level of asymmetry, as anticipated before. In conclusion, by choosing $\theta_1 = \pi$, we achieve a similar performance as

the one of the cascaded configuration (see Figure 4.3 in section 4.1) in terms of sensitivity optimization.

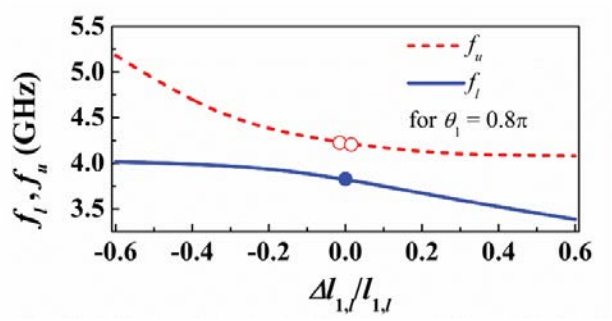

(a)

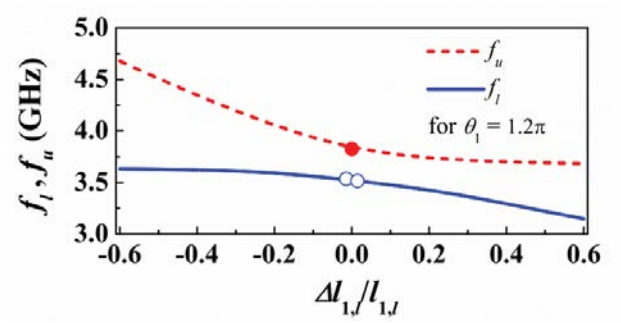

(b)

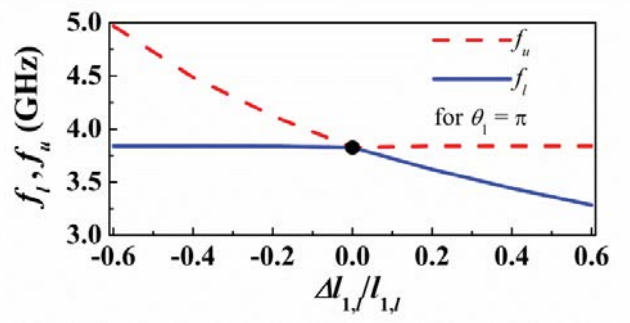

(c)

FIGURE 4.7: Variation of transmission zeros as a function of the length of one of the SIR capacitive patch, for different electrical lengths of the transmission lines: (a) $\theta_1 = 0.8\pi$, (b) $\theta_1 = 1.2\pi$, (c) $\theta_1 = \pi$.

Chapter 5

Applications of Microwave Sensors for Comparators and Dielectric Characterization

This chapter is focused on applications of the structures discussed in the previous chapters based on two techniques. One technique is based on frequency splitting, which could be useful as comparators and for dielectric characterizations. When it is used as comparators, the principle is, when the structures with identical resonators are loaded by SUTs, specifically, with one resonator loaded with a reference material, while the other resonator is loaded with an unknown SUT, the transmission zero splits to two if the SUT is different from the reference material. Otherwise, the SUT is the same as the reference. It could be of interest, for instance, for the detection of defects in industry products or abnormalities in organic tissues. When it is used as dielectric characterization, it is also normally considered a symmetric structure, which means transmission lines loaded with identical resonators, firstly loaded with dielectrics or materials with known permittivities, afterwards by loading SUTs, the permittivities of SUTs could be obtained from the different output results. The other technique is based on frequency variation, which could be used to obtain complex permittivities of loaded samples, including both solids and liquids. The structure consists of a microstrip line loaded with a single CSRR. The key point is the accurate equivalent circuit model of the structure including not only the losses of the substrate, but also the conductive loss and dielectric loss of the resonator, from which we obtain analytical expressions to infer the complex permittivity of SUTs.

This chapter consists of two sections. Section 5.1 devotes to frequency splitting method, from which several structures with combinations of different transmission lines loaded with different electrically small resonators are fabricated and utilized for the purpose of comparators and sensors. Section 5.2 explains a structure of a microstrip line loaded with a CSRR based on frequency variation, and its application as microwave sensors is illustrated.

5.1 Applications as comparators and microwave sensors based on frequency splitting

This chapter illustrates the previous proposed structures as comparators and sensors. In frequency splitting method, the structures are composed of transmission lines loaded with a pair of resonators in a symmetric configuration. The principle is based on resonance frequency splitting. Thus, in the reference (symmetric) state, the structures exhibit a single notch, but two notches appear when symmetry is disrupted, and frequency separation between them is related to the level of asymmetry by loaded samples. Firstly, we introduce the application as comparators. Afterwards, several examples are given to explain the application as microwave sensors

5.1.1 Applications as comparators based on frequency splitting

According to the theory of frequency splitting technique, this category of structures includes a pair of identical resonators, and it solely compares two permittivities (with one as reference), indicating whether their values are the same or not [76]. It is useful for detection of defects or abnormalities in material samples as compared to a well-known reference [28,121,122]. Moreover, it is also possible to detect three or more SUTs simultaneously by cascading three or more sections together, while each resonator pairs in those different sections are set to resonate at different frequencies. By loading asymmetrically all the resonators in each subsections, multi-sensing purpose is realized.

5.1.1.1 Transmission lines loaded with resonators in one section

In section 3.2 and section 3.3.1, microstrip lines loaded with a pair of CSRR and with a pair of SIRs connected to the line in parallel way are introduced, respectively. In both structures when the symmetric resonators-loaded microstrip lines are loaded with dielectric slabs, as shown in Figure 5.1(a) and (c), this asymmetry would cause a frequency splitting that can be easily detected. As can be appreciated in Figure 5.1(b) and (d), two notches, indicative of the asymmetric loading of the structures, appear. It is worth to note that the two transmission zeros shift when even only one resonator is loaded with dielectric slab, which is the effect of the mutual inter-resonator couplings , as discussed in section 3.5.

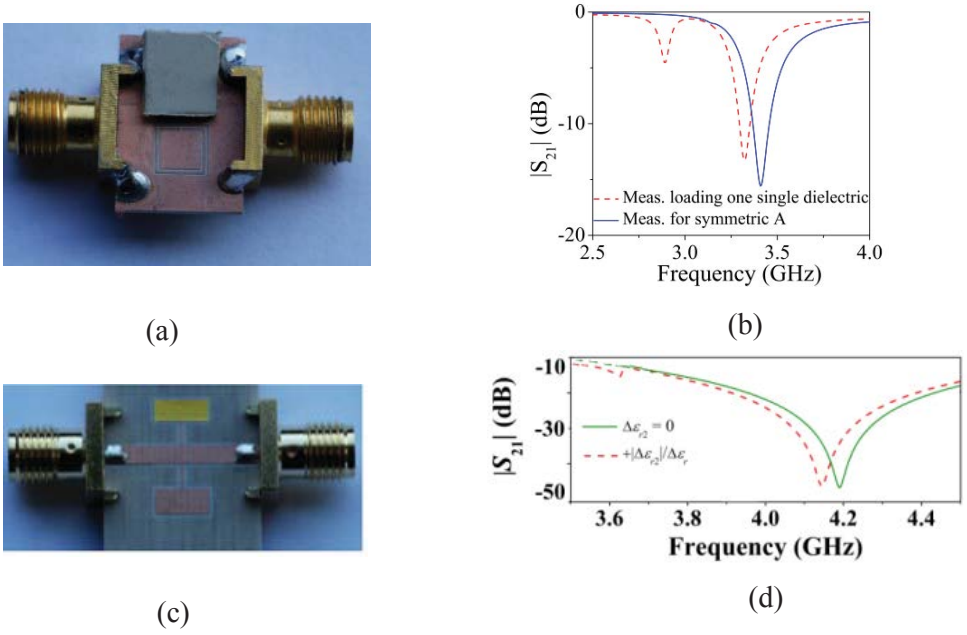

FIGURE 5.1: (a) Photograph of a microstrip line loaded with a pair of CSRRs, with a dielectric slab loaded in the upper CSRR; (b) Measured frequency response of Figure 5.1(a); (c) Photograph of a microstrip line loaded with a pair of SIRs in parallel connection, with a dielectric slab loaded in the upper SIR; (d) Measured frequency response of Figure 5.1(c).

In order to avoid mutual inter-resonant couplings, section 4.1 proposes a structure of splitter/combiner microstrip lines loaded two CSRRs, with each one coupled to a single microstrip line. In this configuration the mutual inter-resonator coupling is avoided since the two CSRRs separate far enough from each other. In Figure 5.2(a), the two identical CSRRs are asymmetrically loaded, i.e., the bottom CSRR loaded with a reference sample, and the upper CSRR loaded with the same sample but defected by several vias (caused different effective permittivity from the reference sample). In addition, the electric lengths of two parallel microstrip lines are set according to (4.6) to obtain enhanced sensitivity, with this condition satisfied, we could observe from Figure 5.2(b) that two transmission zeros appear when the two loadings are different, but the transmission zero regarding to the bottom branch of the line loaded CSRR (the branch with microstrip line length satisfying (4.6)) is always unchanged, thus improve the sensitivity.

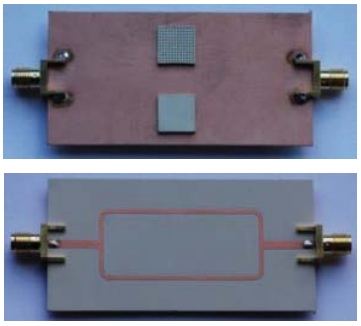

(a)

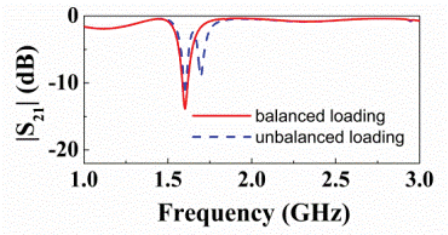

(b)

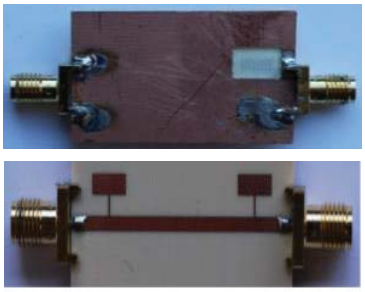

(c)

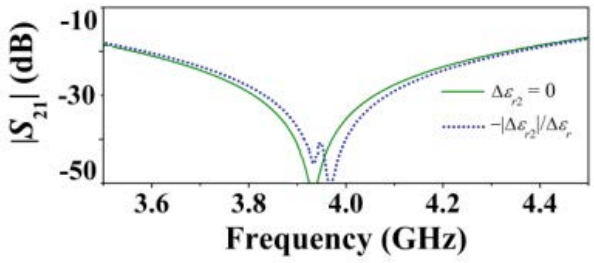

(d)

FIGURE 5.2: (a) Photograph of a splitter/combiner microstrip section loaded with two CSRRs individually loaded with the reference sample (bottom) and the SUT (upper); (b) Measured frequency response of Figure 5.2(a); (c) Photograph of a microstrip line loaded with a pair of SIRs in cascade configuration. In order to implement reduction of dielectric permittivity, the substrate below the right SIR's capacitive patch is removed (cause decrease of right SIR capacitance). (d) Measured frequency response of Figure 5.2(c).

Article **TMTT16 November** introduces a cascade connection of a microstrip line loaded with two SIRs, with two resonators placing far enough from each other to eliminate inter-resonator coupling. As a proof of concept as comparator, we remove part of the substrate below the right SIR to mimic asymmetric loading, as shown in Figure 5.2(c). The response is also

shown in Figure 5.2(d), demonstrating the difference of two SIRs, and the notch corresponding to the unloaded SIR is always not shifted.

5.1.1.2 Multi-section transmission lines loaded resonators

In order to simultaneously characterize multiple samples, Article **Sensors16** proposes a structure with several splitter/combiner sections like the one shown in Figure 5.2(a) cascaded together, each one loaded with a pair of SIRs tuned at different frequencies, as shown in Figure 5.3(a). With this configuration, in absence of loading or with balanced loads in each pair of SIRs, three transmission zeros (each one at the resonance frequency of the SIRs in each section) are expected. However, with an unbalanced perturbation in a pair of SIRs, it is expected that the corresponding frequency splits. By the placement of the pairs of SIRs at a distance of $\lambda/2$ from the T-junctions, sensitivity and discrimination for small unbalanced perturbations is optimized, as discussed before. To demonstrate this structure as comparator to detect multiple samples or multi-sensor, each pair of SIRs in all three sections are asymmetrically loaded with dielectric slabs possessing different permittivities (dielectric constants $\varepsilon_r = 2.43$ and $\varepsilon_r = 10.2$, respectively). Frequency splitting (see Figure 5.3(b)) points out the difference in the dielectric constants of both slabs loading the different pairs of SIRs. In this case, however, the two notches are shifted to lower frequencies, as compared to the resonance positions in Figure 5.2(b) where one transmission zero is unaltered. It is interesting to highlight that the notch positions for the structure with two different slabs for each pair are a result of an interfering phenomenon (the optimum condition is changed by loading both resonators with slabs). For that reason the pair of notches generated by each splitter/combiner section shift.

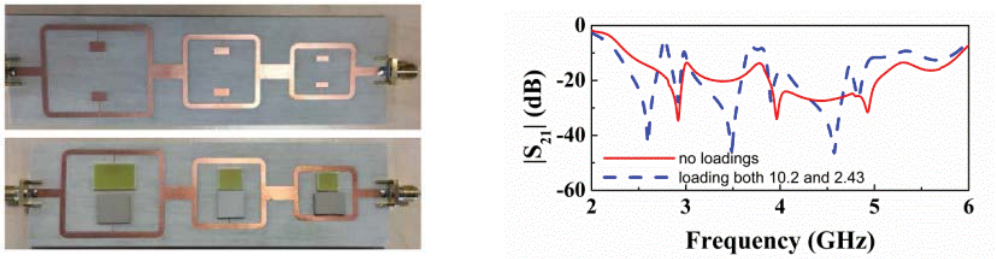

(a) (b)

FIGURE 5.3: (a) Photograph of the fabricated structure of cascaded three-section splitter/combiner microstrip lines loaded SIRs and when it is loaded with two different dielectric slabs for each pair of every section, and (b) Measured responses of empty structure and perturbed structure in Figure 5.3(a).

Similarly, conference article **IMS16** also introduces a three-section symmetric structure composed of three different splitter/combiner microstrip sections loaded with CSRRs, resonant at three different frequencies. The theory is the same as the three-section microstrip sections loaded SIRs in Figure 5.3(a). Figure 5.4 experiments the symmetric structure asymmetrically by loading the upper CSRRs of the first two sections with two dielectric slabs

with permittivity 10.2 and 3.38, and the response validates the structure for detecting different dielectric loadings.

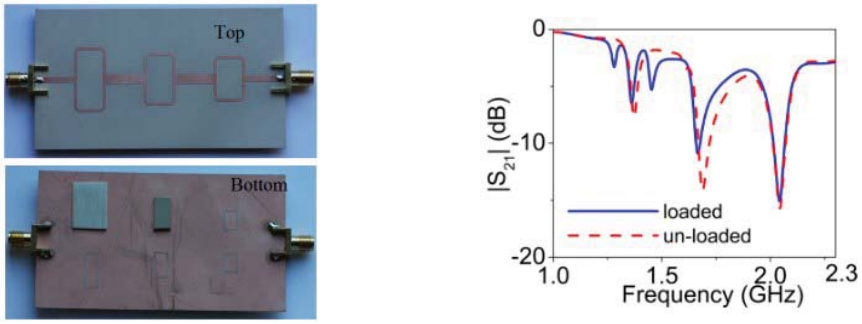

(a) (b)

FIGURE 5.4: (a) Photograph of the fabricated structure of cascaded three-section splitter/combiner microstrip lines loaded CSRRs and when the upper CSRRs of the first two sections loaded with two dielectric slabs with permittivity 10.2 and 3.38, and (b) Measured responses of empty structure and perturbed structure.

5.1.2 Application as microwave sensors based on frequency splitting

For the application as microwave sensors based on frequency splitting, the structures are designed symmetrically, i.e., the two resonators are identical. The principle is to disrupt the symmetry of the structures by means of SUTs, located on top or in the vicinity of one of the resonant elements, and the other resonator loaded with a reference material with known permittivity. From the difference of the two notch frequencies and the magnitude of notches in transmission coefficient, the permittivity of the loaded SUT could be inferred.

5.1.2.1 Microstrip line loaded with a pair of SIRs in cascade configuration

Article **TMTT16 November** provides the procedure to determine the complex permittivity of SUT. As shown in Figure 5.2(c), the sensitive area is set in the cavity below the right SIR which is implemented by a drilling machine, however, not all the substrate material is completely removed, since the SIR needs some material for mechanical stability. Therefore, the measurement results provide the effective dielectric constant of the structure below the SIR, including not only the SUT but also the presence of a narrow dielectric layer of relative permittivity (3.38 in this case). Nevertheless, we have proposed a method to determine this thickness that subsequently allows us to obtain the dielectric constant of a SUT once the permittivity of the substrate and the thickness of the SUT are known. The cross section of the structure is depicted in Figure 5.5. The method is based on the fact that the effective dielectric constant of the composite formed by the substrate layer on top of the cavity plus the SUT, η_{eff}, is related to the respective dielectric constants by:

$$\frac{\varepsilon_{eff}}{h} = \frac{\frac{\varepsilon_{r1}}{h_1}\frac{\varepsilon_{r2}}{h_2}}{\frac{\varepsilon_{r1}}{h_1} + \frac{\varepsilon_{r2}}{h_2}} \qquad (5.1)$$

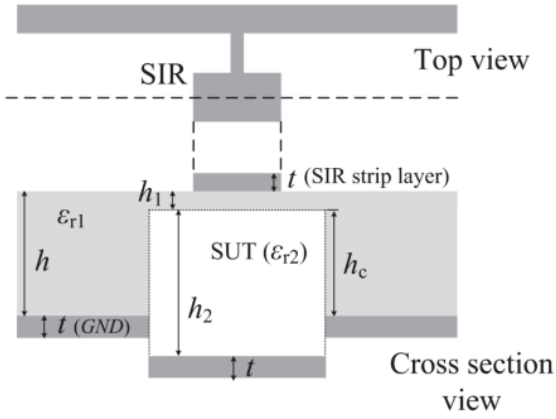

FIGURE 5.5: Sketch of the top and cross section view of the SIR and cavity loaded with a SUT.

From the previous expression, the dielectric constant of the SUT can be isolated:

$$\varepsilon_{r2} = \frac{\varepsilon_{eff}\varepsilon_{r1}h_2}{\varepsilon_{r1}h - \varepsilon_{eff}h_1} \quad (5.2)$$

When the structure is loaded with a known sample, from the effective dielectric constant (see Figure 4.5(c)) and the height of the sample, h_1 can be obtained from (5.1). Once h_1 is known, the dielectric constant of the SUT could be calculated from (5.2) with the effective dielectric constant ε_{eff} obtained from Figure 4.5(c).

In terms of loss tangent estimation of a SUT, it is based on the depth of the notch (a structure with a single SIR is discussed for simplicity, in article **TMTT16 November**). From the equivalent circuit model of a microstrip line loaded with a SIR, like in Figure 3.4(d), but including the metallic loss (mainly associated to the narrow inductive strip of the SIR) and dielectric loss (from the SUT), an accurate circuit model could be achieved. By relating the magnitude of the measured transmission zero frequency with the resistance of the shunt branch impedance at notch frequency, the loss tangent of SUT could be obtained. It is important to note that a reference SUT with known permittivity is necessary to be used firstly to get R_M.

5.1.2.2 Splitter/combiner microstrip lines loaded with CSRRs

To demonstrate the potential as sensors, in article **TMTT16 December**, the lower CSRR of the structure (splitter/combiner microstrip section loaded with CSRRs) is firstly loaded (i.e., the lower CSRR, acting as an active sensor region) with small dielectric slabs with different permittivities (the other CSRR is kept unloaded). Specifically, we have cut square-shaped pieces of un-metalized commercial microwave substrates with dielectric constants of 10.2 (*Rogers* RO3010), 3.55 (*Rogers* RO4003C) and 2.43 (*Arlon CuClad* 250). The measured responses are depicted in Figure 5.6(a), whereas the variation of frequency splitting, Γf_z, with the dielectric constant, exhibiting roughly a linear variation, is shown in Figure 5.6(b). This

curve can be used to determine the dielectric constant of unknown substrates/samples from the measurement of the resulting frequency splitting. The dielectric constant of a SUT can in principle be arbitrarily small. Nevertheless, as the dielectric constant of a sample approaches unity, the two notches may merge in a single one by the effect of losses of the device (metallic and dielectric). Therefore, the discrimination is limited by this effect. Considering SUTs with large dielectric constant would force us to consider additional samples with known large dielectric constants in order to extend the span of the calibration curve. Apart from that, the curve of Figure 5.6(b) reveals a significant variation of Γf_z with the dielectric constant. If we assume that frequency differences (for different samples) of the order of 0.01 GHz can be distinguished (reasonable on account of the peaked responses at the notches), then differences in dielectric constants of the order of 0.35 or even less, can be detected.

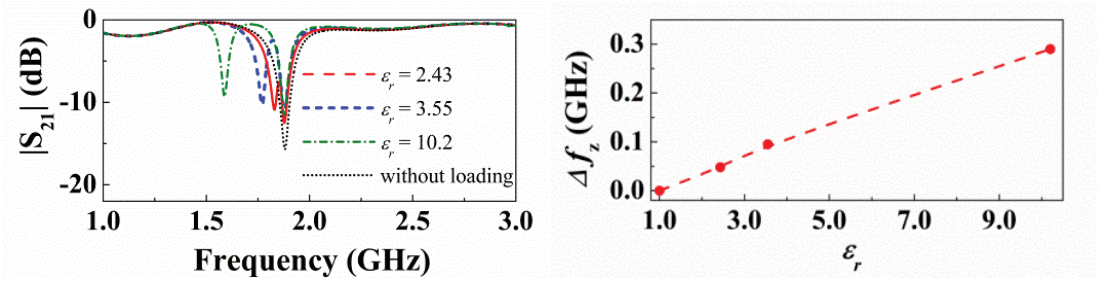

FIGURE 5.6: (a) Response of a CSRR-loaded combiner/splitter structure to different dielectric loads, and (b) variation of Γf_z with the dielectric constant of the considered loads.

5.2 Application as microwave sensors based on frequency variation

In section 2.3.3.4, the principle of microwave sensor based on frequency variation is explained in detail. Different from the sensing technique based on frequency splitting, the strategy of frequency variation is normally consisted of transmission lines loaded with a single resonator element (either coupled to it or in contact with it). The single transmission zero (we only consider the fundamental resonant frequency) may be altered by the effect of external stimulus or perturbations (e.g., moisture, temperature), or by the presence of materials surrounding the resonant element. From the variation of the transmission zeros (before and after loading SUTs), the permittivity of SUTs could be obtained [123-127]. However, it should note here that this kind of sensors may suffer from cross-sensitivities, i.e., the transmission zero can be unintentionally shifted by spurious or environmental conditions. Therefore, they are typically calibrated for accurate measurements.

Conference article **IMS17** proposes a new equivalent circuit model of CSRR-loaded microstrip line that takes into account of the substrate (dielectric) losses and distinguishes between the metal and dielectric losses of the CSRR [124,128]. The cross section, layout, and the proposed circuit model (including losses) of the considered CSRR-loaded line are depicted in Figure 5.7. In microstrip lines working at moderate microwave frequencies, ohmic losses related to the finite conductivity of the metallic strip are very small. Therefore, losses are assumed to be entirely due to the considered substrate (with known loss tangent) and CSRR. Substrate losses are accounted for by the resistance R_S, whereas CSRR losses are

described by R_M, physically representing the ohmic losses of the narrow inductive strips connecting the inner and outer metallic regions of the CSRR, and by R_D, corresponding to the losses associated to the dielectric material surrounding the CSRR.

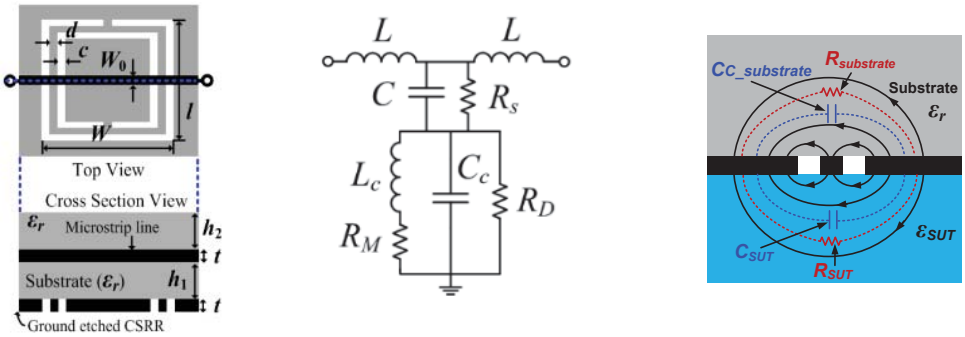

(a) (b) (c)

FIGURE 5.7: (a) Top and cross section views of a CSRR-loaded embedded microstrip line; (b) The improved lumped element equivalent circuit model; (c) Cross section view of the slot region of the CSRR loaded with a SUT, with electric field lines and contributions of the total CSRR plus SUT capacitance and resistances (losses).

By inspection of Figure 5.7(b), transmission zero occurs at the frequency where the shunt branch resonates (the imaginary part of the impedance of the shunt branch nulls). When the structure is empty (using air as calibration reference), and by setting the central strip of microstrip line covered by a substrate the same as the microstrip line (to guarantee a homogeneous material for the line in order to analytically obtain the resistive loss R_s from known loss tangent of the substrate), the conductive loss R_M of the CSRR could be inferred (details are given in conference article **IMS17**).

Figure 5.7(c) shows the cross section of the slot region of the CSRR when it is loaded with a sample. After placing a SUT in contact with the CSRR and with the size big enough to cover all the area of the CSRR, the total capacitance and resistance of the resonant tank are changed. The contributions from the SUT are shown in Figure 5.7(c). Obviously, the transmission zero would change as well, as compared to the one of the empty structure (i.e., without SUT), the dielectric constant of the SUT could be obtained from:

$$\varepsilon_{SUT} = 1 + \frac{(\omega_0'^{-2} - \omega_0^{-2})}{L_r C_r}(1 + \varepsilon_r) \qquad (5.3)$$

where ω_0' is the resonance frequency with the presence of a SUT.

Since the conductive loss R_M of the CSRR is known, by using a similar procedure to the one used for the estimation of R_M, the new value of R_D including both substrate loss and SUT loss could be calculated according to the frequency and the magnitude of the new transmission zero. Then we can decompose the contribution of the SUT (since $R_{substrate}$ - the contribution of the substrate to R_D is known), and the loss tangent of the SUT can be inferred.

To validate this method for the estimation of the complex permittivity of a dielectric slab, we have loaded the CSRR-based line by means of a *FR*4 slab (see Figure 5.8(a)) with thickness 2.54 mm (much larger than *c* and *d*). The measured frequency response is also depicted in Figure 5.8(b). From the new value of the notch frequency and according to (5.3), the dielectric constant is found to be $\eta_r = 3.9$ and $R_D = 2919\ \Omega$. Consequently, the loss tangent is found to be $tan\gamma_{SUT} = 0.0056$. These values are in reasonable agreement with the measured values for *FR*4, i.e., $\eta_r = 4.2$ and $tan\gamma = 0.0074$, obtained by means of the commercial *Agilent* 85072A split cylinder resonator.

(a)

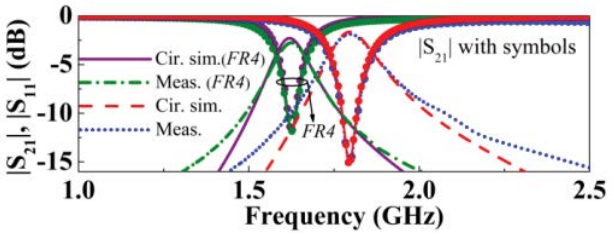

(b)

FIGURE 5.8(a) Photograph of the considered CSRR-loaded line with the CSRR empty and loaded with a piece of *FR*4 slab, and (b) Insertion and return losses.

In theoretical view it is certain that the structure in Figure 5.7 could also be used to estimate the complex permittivity of liquids. The problem is to improve the structure in order to accommodate liquids [22,125,129-134]. Conference article **Pavia17** modifies the structure by attaching a liquid container surrounding the CSRR, as shown in Figure 5.9(a). Following the similar procedure for estimating the complex permittivity of solid dielectrics, the complex permittivity of LUTs (liquids under test) could be obtained. In order to validate this structure, the container is filled with DI-water, the responses with and without DI-water are shown in Figure 5.9(b), from which, the dielectric constant and loss tangent of the LUT are found to be $\eta_{LUT} = 69.08$ and $tan\gamma = 0.01$. These values are in reasonable agreement with tabulated values of DI-water at the considered frequency (the dielectric constant is in the vicinity of 76.7-78.2, whereas the loss tangent varies between 0.005 at 100 MHz and 0.157 at 3GHz) [1,135,136].

It is worth mentioning that we have carried out the measurements with LUT just after loading, in order to avoid the effects of liquid absorption by the substrate. With DI-water, absorption is a slow process, but this is not the case with other liquids such as ethanol. For this reason, the present method is valid for low-absorption liquids [3].

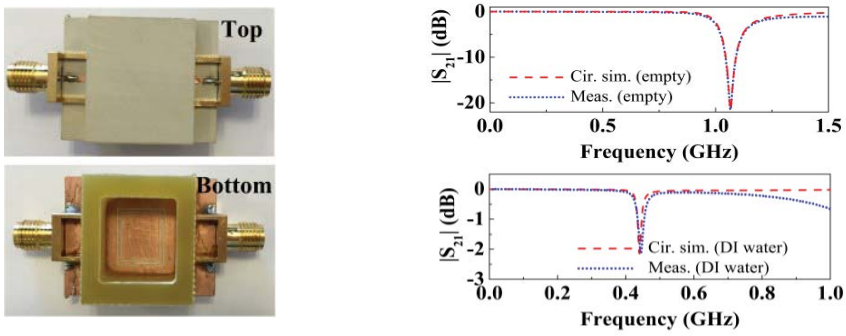

(a) (b)

FIGURE 5.9: (a) Photograph of the empty CSRR-loaded line with a liquid container fabricated by *FR*4 substrate, and (b) transmission coefficients for the considered CSRR-loaded line without and with LUT.

Chapter 6

Conclusions and Future Work

Conclusions

In this thesis, we have explicitly studied several transmission lines loaded with electrically small resonators. Their lumped element equivalent circuit models are provided and analytical expressions to predict transmission zeros in transmission coefficient responses are deduced as well, from which we could design different structures to catering our purposes as sensing or detecting. Two sensing strategies based on frequency splitting and frequency variation are utilized in this thesis to design our targeted comparators and sensors for dielectric characterization. Firstly, transmission lines loaded with two identical resonators could be used as comparators. The principle is that if one of the resonators is loaded with an unknown SUT, while the other resonator is loaded with a reference material, the transmission zero in transmission coefficient would split to two zeros if the SUT is different from the reference, otherwise, only one transmission zero appears. It could be of interest, for instance, for the detection of defects in industry products or abnormalities in organic tissues. Secondly, transmission lines loaded with two identical resonators could be used as sensors for dielectric characterization. Different from the principle of comparators, the principle as sensors records not only the appearance of frequency splitting, but also the quantity of variation. Specifically, by loading the resonators with different materials, the variation of two splitting transmission zeros depends on the degree of asymmetry, so from the different output results, the properties of SUTs could be obtained. It is important to note that calibrations are normally necessary to build a relationship between the output results with variables causing the differences. The other strategy is based on frequency variation, which could be used as sensors to detect dielectric properties of loaded samples, including both solids and liquids. The key point for this method is an accurate equivalent circuit model of the structure, including not only the losses of the substrate, but also the conductive loss and dielectric loss of the resonator, from which we could obtain analytical expressions to infer the complex permittivity of SUTs.

In order to implement the sensors and comparators as we mentioned above, firstly, some background of microwave sensors as material characterizations is introduced in chapter 2, specifically, the dielectric properties of materials, the measurement and sensing techniques, and wide application area of microwave sensors as material characterizations. The microwave methods for material characterization generally fall into non-resonant methods and resonant methods. Non-resonant methods are often used to get a general knowledge of dielectric properties over a frequency range, while resonant methods are used to get accurate knowledge of dielectric properties at single frequency or several discrete frequencies. In all these methods, planar transmission line loaded with resonators has the advantage of easy to fabricate, low manufacturing cost, compactness in size and simple sample preparation, thus it is widely used. Electrically small resonators are subwavelength structures, in contrast to the

conventional transmission line resonators, typically one tenth of the guided wavelength or less at their fundamental resonant frequencies. Therefore, high level of miniaturization is expected by using these particles. In addition, they have strong response to an electromagnetic field and easy electric/magnetic coupling between resonators and materials under test (MUTs). This thesis is dedicated to the planar transmission lines loaded with electrically small resonators, based on frequency splitting and frequency variation.

In chapter 3 some combinations of different transmission lines loaded with electrically small resonators are modeled and analyzed. Specifically, CPWs loaded with SRRs and loaded with SIRs (also slot-SIRs - the complementary counterpart of SIRs), microstrip lines loaded with CSRRs and loaded with SIRs. Among all the structures, their lumped element equivalent circuit models have been proposed, according to which analytical expressions to predict transmission zero frequencies are deduced too. We have fabricated all the structures and extracted lumped element parameters through EM simulation results. Good agreement among circuit simulations, EM simulations and measurements validates the circuit models. In addition, it is noted that mutual inter-resonator coupling between loaded resonators tends to degrade the sensitivity of the structure, thus it should be avoided.

In order to avoid the mutual inter-resonator coupling between the resonators, new structures are explained in chapter 4, i.e., microstrip lines individually loaded with two CSRRs and two SIRs, respectively, in splitter/combiner configuration, and a microstrip line loaded with two SIRs in cascade configuration. In splitter/combiner configuration, resonators individually load a microstrip line, and the distance between two resonators is far from each other, thus inter-resonator coupling is prevented. However, the transmission zeros appear as a consequence of interfering phenomenon of two resonator-loaded microstrip branches. In other words, the transmission zeros are not only dictated by the intrinsic resonant frequency of the resonators, but also by the length of the lines, and such transmission zeros occur at those frequencies where the signals at the end of each loaded line exactly cancel. By analyzing the circuit models, the conditions for electric length of the loaded lines are provided for achieving enhanced sensitivity. Another configuration to avoid inter-resonator coupling is in cascade connection, i.e., a microstrip line loaded with two SIRs, separated a far enough distance. From the equivalent circuit model, the transmission zeros positions do not change even if the line in-between the two SIRs is different. But if the electric length of the transmission line in-between the SIRs is set to be π, the circuit model could be simplified to the same as the structure with two SIRs directly in contact with the line in the same junction, without mutual inter-resonant coupling, thus improving the sensitivity.

In chapter 5, validations of proof-of-concept prototypes have been performed on the previous mentioned structures, illustrating the applications as comparators and microwave sensors for dielectric characterization for both solids and liquids. Two structures forming by cascading three microstrip sections loaded with SIRs and with CSRRs (resonators in each section resonant at different frequencies) respectively have introduced and validated as multi-sensing prototypes too.

Future work

Some future work may be carried out as an improvement and expansion to the results that have been achieved through this thesis.

- Design a microwave sensor suitable for liquids, mainly based on the improvement of the structure proposed in conference article **IMS17**, which could find applications for quality control in food and chemistry industries.

- Development of microwave sensors for biomedical applications, e.g., monitor and analyze glucose concentrations and other parameters in blood, discriminate between the normal and malignant cancerous tissues, non-invasive techniques for early detection of cancer and harmful tumors in human body, etc.

References

[1] R. N. Clarke, A. P. Gregory, D. Cannell, M. Patrick, S. Wylie, I. Youngs, and G. Hill, "A guide to the characterisation of dielectric materials at RF and microwave frequencies," *Inst. Meas. Control. Phys. Lab.*, 2003.

[2] F. M. Battiston, J.-P. Ramseyer, H. P. Lang, M. K. Baller, C. Gerber, J. K. Gimzewski, E. Meyer, and H.-J. Güntherodt, "A chemical sensor based on a microfabricated cantilever array with simultaneous resonance-frequency and bending readout," *Sensors Actuators B Chem.*, vol. 77, no. 1, pp. 122–131, 2001.

[3] A. P. Gregory and R. N. Clarke, "A review of RF and microwave techniques for dielectric measurements on polar liquids," *IEEE Trans. Dielectr. Electr. Insul.*, vol. 13, no. 4, pp. 727–743, 2006.

[4] M. Golio, *Microwave and RF product applications*. CRC Press, 2003.

[5] A. Rosen, D. Rosen, G. A. Tuma, and L. P. Bucky, "RF/microwave-aided tumescent liposuction," *IEEE Trans. Microw. Theory Tech.*, vol. 48, no. 11, pp. 1879–1884, 2000.

[6] R. M. Rosenbaum, A. J. Greenspon, S. Hsu, P. Walinsky, and A. Rosen, "RF and microwave ablation for the treatment of ventricular tachycardia," in *Microwave Symposium Digest, 1993., IEEE MTT-S International*, 1993, pp. 1155–1158.

[7] T. Chen, D. Dubuc, M. Poupot, J.-J. Fournie, and K. Grenier, "Accurate nanoliter liquid characterization up to 40 GHz for biomedical applications: Toward noninvasive living cells monitoring," *IEEE Trans. Microw. Theory Tech.*, vol. 60, no. 12, pp. 4171–4177, 2012.

[8] M. Schueler, C. Mandel, M. Puentes, and R. Jakoby, "Metamaterial inspired microwave sensors," *IEEE Microw. Mag.*, vol. 13, no. 2, pp. 57–68, 2012.

[9] M. E. C. Oliveira and A. S. Franca, "Microwave heating of foodstuffs," *J. Food Eng.*, vol. 53, no. 4, pp. 347–359, 2002.

[10] E. Grant and B. J. Halstead, "Dielectric parameters relevant to microwave dielectric heating," *Chem. Soc. Rev.*, vol. 27, no. 3, pp. 213–224, 1998.

[11] S. O. Nelson, "Dielectric properties of agricultural products-measurements and applications," *IEEE Trans. Electr. Insul.*, vol. 26, no. 5, pp. 845–869, 1991.

[12] R. E. Mudgett, "Electrical properties of foods," *Eng. Prop. foods*, vol. 2, pp. 389–455, 1986.

[13] A. W. Kraszewski, S. Trabelsi, and S. O. Nelson, "Moisture content determination in grain by measuring microwave parameters," *Meas. Sci. Technol.*, vol. 8, no. 8, p. 857, 1997.

[14] D. El Khaled, N. Novas, J. A. Gazquez, R. M. Garcia, and F. Manzano-Agugliaro, "Fruit and vegetable quality assessment via dielectric sensing," *Sensors*, vol. 15, no. 7, pp. 15363–15397, 2015.

[15] K. Saeed, A. C. Guyette, I. C. Hunter, and R. D. Pollard, "Microstrip resonator technique for measuring dielectric permittivity of liquid solvents and for solution sensing," in *Microwave Symposium, 2007. IEEE/MTT-S International*, 2007, pp. 1185–1188.

[16] M. Yoo, H. K. Kim, and S. Lim, "Electromagnetic-based ethanol chemical sensor using metamaterial absorber," *Sensors Actuators B Chem.*, vol. 222, pp. 173–180, 2016.

[17] M. T. Khan and S. M. Ali, "A brief review of measuring techniques for characterization of dielectric materials," *Int. J. Inf. Technol. Electr. Eng.*, vol. 1, no. 1, 2012.

[18] T. Chretiennot, D. Dubuc, and K. Grenier, "A microwave and microfluidic planar resonator for efficient and accurate complex permittivity characterization of aqueous solutions," *IEEE Trans. Microw. Theory Tech.*, vol. 61, no. 2, pp. 972–978, 2013.

[19] S. Gabriel, R. W. Lau, and C. Gabriel, "The dielectric properties of biological tissues: II. Measurements in the frequency range 10 Hz to 20 GHz," *Phys. Med. Biol.*, vol. 41, no. 11, p. 2251, 1996.

[20] C. Dalmay, A. Pothier, P. Blondy, F. Lalloue, and M.-O. Jauberteau, "Label free biosensors for human cell characterization using radio and microwave frequencies," in *Microwave Symposium Digest, 2008 IEEE MTT-S International*, 2008, pp. 911–914.

[21] M. A. Stuchly, A. Kraszewski, S. S. Stuchly, and A. M. Smith, "Dielectric properties of animal tissues in vivo at radio and microwave frequencies: comparison between species," *Phys. Med. Biol.*, vol. 27, no. 7, p. 927, 1982.

[22] K. Grenier, D. Dubuc, P.-E. Poleni, M. Kumemura, H. Toshiyoshi, T. Fujii, and H. Fujita, "Integrated broadband microwave and microfluidic sensor dedicated to bioengineering," *IEEE Trans. Microw. Theory Tech.*, vol. 57, no. 12, pp. 3246–3253, 2009.

[23] M. Lazebnik, E. L. Madsen, G. R. Frank, and S. C. Hagness, "Tissue-mimicking phantom materials for narrowband and ultrawideband microwave applications," *Phys. Med. Biol.*, vol. 50, no. 18, p. 4245, 2005.

[24] K. Grenier, D. Dubuc, P.-E. Poleni, M. Kumemura, H. Toshiyoshi, T. Fujii, and H. Fujita, "Resonant based microwave biosensor for biological cells discrimination," in *Radio and Wireless Symposium (RWS), 2010 IEEE*, 2010, pp. 523–526.

[25] M. Schüßler, M. Puentes, C. Mandel, and R. Jakoby, "Multi-resonant perturbation method for capacitive sensing with composite right/left-handed transmission lines," in *Microwave Symposium Digest (MTT), 2010 IEEE MTT-S International*, 2010, pp. 481–484.

[26] J. Kim, A. Babajanyan, A. Hovsepyan, K. Lee, and B. Friedman, "Microwave dielectric resonator biosensor for aqueous glucose solution," *Rev. Sci. Instrum.*, vol. 79, no. 8, p. 86107, 2008.

[27] M. Puentes, M. Maasch, M. Schubler, and R. Jakoby, "Frequency multiplexed 2-dimensional sensor array based on split-ring resonators for organic tissue analysis," *IEEE Trans. Microw. Theory Tech.*, vol. 60, no. 6, pp. 1720–1727, 2012.

[28] M. Puentes, C. Weiß, M. Schüßler, and R. Jakoby, "Sensor array based on split ring resonators for analysis of organic tissues," in *Microwave Symposium Digest (MTT), 2011 IEEE MTT-S International*, 2011, pp. 1–4.

[29] A. P. O'Rourke, M. Lazebnik, J. M. Bertram, M. C. Converse, S. C. Hagness, J. G. Webster, and D. M. Mahvi, "Dielectric properties of human normal, malignant and cirrhotic liver tissue: in vivo and ex vivo measurements from 0.5 to 20 GHz using a precision open-ended coaxial probe," *Phys. Med. Biol.*, vol. 52, no. 15, p. 4707, 2007.

[30] M. Puentes, F. Bashir, M. Maasch, M. Schussler, and R. Jakoby, "Planar microwave sensor for thermal ablation of organic tissue," in *Microwave Conference (EuMC), 2013 European*, 2013, pp. 479–482.

[31] C. Reimann, M. Puentes, M. Maasch, F. Hübner, B. Bazrafshan, T. J. Vogl, C. Damm, and R. Jakoby, "Planar Microwave Sensor for Theranostic Therapy of Organic Tissue Based on Oval Split Ring Resonators," *Sensors*, vol. 16, no. 9, p. 1450, 2016.

[32] B. Bohunicky and S. A. Mousa, "Biosensors: the new wave in cancer diagnosis," *Nanotechnol. Sci. Appl.*, vol. 4, p. 1, 2011.

[33] L.-F. Chen, C. K. Ong, C. P. Neo, V. V Varadan, and V. K. Varadan, *Microwave electronics: measurement and materials characterization*. John Wiley & Sons, 2004.

[34] E. Nyfors, "Industrial microwave sensors—A review," *Subsurf. Sens. Technol. Appl.*, vol. 1, no. 1, pp. 23–43, 2000.

[35] P. Vainikainen, M. Tiuri, V. Kontra, and E. Nyfors, "Portable short range subsurface radar," in *Fourth International Conference on Ground Penetrating Radar*, 1992.

[36] A. P. Annan, "Electromagnetic principles of ground penetrating radar," *Gr. penetrating radar theory Appl. Amsterdam, Netherlands*, pp. 1–40, 2009.

[37] J. Naqui, M. Durán-Sindreu, and F. Martín, "Alignment and position sensors based on split ring resonators," *Sensors*, vol. 12, no. 9, pp. 11790–11797, 2012.

[38] R. Melik, E. Unal, N. K. Perkgoz, C. Puttlitz, and H. V. Demir, "Metamaterial-based wireless strain sensors," *Appl. Phys. Lett.*, vol. 95, no. 1, p. 11106, 2009.

[39] A. K. Horestani, J. Naqui, D. Abbott, C. Fumeaux, and F. Martín, "Two-dimensional displacement and alignment sensor based on reflection coefficients of open microstrip lines loaded with split ring resonators," *Electron. Lett.*, vol. 50, no. 8, pp. 620–622, 2014.

[40] C. Kummerow, W. S. Olson, and L. Giglio, "A simplified scheme for obtaining precipitation and vertical hydrometeor profiles from passive microwave sensors," *IEEE Trans. Geosci. Remote Sens.*, vol. 34, no. 5, pp. 1213–1232, 1996.

[41] Y. Nebiyeloul-Kifle and W. G. Woodington, "Automotive side object detection sensor blockage detection system and related techniques." Google Patents, 26-Aug-2003.

[42] K. Saeed, M. F. Shafique, M. B. Byrne, and I. C. Hunter, "Planar microwave sensors for complex permittivity characterization of materials and their applications," in *Applied Measurement Systems*, InTech, 2012.

[43] A. Note, "Basics of measuring the dielectric properties of materials," *Agil. Lit. Number*, 2006.

[44] W. Bolton, *Electrical and magnetic properties of materials*. Longman Scientific & Technical, 1992.

[45] P. Guillon, "Microwave techniques for measuring complex permittivity and permeability of materials," *MRS Online Proc. Libr. Arch.*, vol. 347, 1994.

[46] J. Baker-Jarvis, E. J. Vanzura, and W. A. Kissick, "Improved technique for determining complex permittivity with the transmission/reflection method," *IEEE Trans. Microw. Theory Tech.*, vol. 38, no. 8, pp. 1096–1103, 1990.

[47] T. W. Athey, M. A. Stuchly, and S. S. Stuchly, "Measurement of radio frequency permittivity of biological tissues with an open-ended coaxial line: Part I," *IEEE Trans. Microw. Theory Tech.*, vol. 30, no. 1, pp. 82–86, 1982.

[48] W. T. Joines, Y. Zhang, C. Li, and R. L. Jirtle, "The measured electrical properties of normal and malignant human tissues from 50 to 900 MHz," *Med. Phys.*, vol. 21, no. 4, pp. 547–550, 1994.

[49] D. Popovic, L. McCartney, C. Beasley, M. Lazebnik, M. Okoniewski, S. C. Hagness, and J. H. Booske, "Precision open-ended coaxial probes for in vivo and ex vivo dielectric spectroscopy of biological tissues at microwave frequencies," *IEEE Trans. Microw. Theory Tech.*, vol. 53, no. 5, pp. 1713–1722, 2005.

[50] M. Hofmann, G. Fischer, R. Weigel, and D. Kissinger, "Microwave-based noninvasive concentration measurements for biomedical applications," *IEEE Trans. Microw. Theory Tech.*, vol. 61, no. 5, pp. 2195–2204, 2013.

[51] S. N. Jha, K. Narsaiah, A. L. Basediya, R. Sharma, P. Jaiswal, R. Kumar, and R. Bhardwaj, "Measurement techniques and application of electrical properties for nondestructive quality evaluation of foods—a review," *J. Food Sci. Technol.*, vol. 48, no. 4, pp. 387–411, 2011.

[52] P. Piyasena, C. Dussault, T. Koutchma, H. S. Ramaswamy, and G. B. Awuah, "Radio frequency heating of foods: principles, applications and related properties—a review," *Crit. Rev. Food Sci. Nutr.*, vol. 43, no. 6, pp. 587–606, 2003.

[53] H. Feng, J. Tang, and R. P. Cavalieri, "Dielectric properties of dehydrated apples as affected by moisture and temperature," *Trans. ASAE*, vol. 45, no. 1, p. 129, 2002.

[54] A. M. Nicolson and G. F. Ross, "Measurement of the intrinsic properties of materials by time-domain techniques," *IEEE Trans. Instrum. Meas.*, vol. 19, no. 4, pp. 377–382, 1970.

[55] M. D. Janezic and J. A. Jargon, "Complex permittivity determination from propagation constant measurements," *IEEE Microw. Guid. Wave Lett.*, vol. 9, no. 2, pp. 76–78, 1999.

[56] D. F. Williams and R. B. Marks, "Accurate transmission line characterization," *IEEE Microw. Guid. Wave Lett.*, vol. 3, no. 8, pp. 247–249, 1993.

[57] M. S. Venkatesh and G. S. V Raghavan, "An overview of dielectric properties measuring techniques," *Can. Biosyst. Eng.*, vol. 47, no. 7, pp. 15–30, 2005.

[58] V. V Varadan, R. D. Hollinger, D. K. Ghodgaonkar, and V. K. Varadan, "Free-space, broadband measurements of high-temperature, complex dielectric properties at microwave frequencies," *IEEE Trans. Instrum. Meas.*, vol. 40, no. 5, pp. 842–846, 1991.

[59] U. Raveendranath, S. Bijukumar, and K. T. Mathew, "Broadband coaxial cavity resonator for complex permittivity measurements of liquids," *IEEE Trans. Instrum. Meas.*, vol. 49, no. 6, pp. 1305–1312, 2000.

[60] R. H. Johnson, J. L. Green, M. P. Robinson, A. W. Preece, and R. N. Clarke, "Resonant open ended coaxial line sensor for measuring complex permittivity," *IEE Proc. A (Science, Meas. Technol.*, vol. 139, no. 5, pp. 261–264, 1992.

[61] P. A. Bernard and J. M. Gautray, "Measurement of dielectric constant using a microstrip ring resonator," *IEEE Trans. Microw. Theory Tech.*, vol. 39, no. 3, pp. 592–595, 1991.

[62] N. Simons Rainee, "Coplanar waveguide circuits, components, and systems." John Wiley and Sons, Inc. ISBN, 2001.

[63] K. C. Gupta, R. Garg, I. Bahl, and P. Bhartia, "Microstrip Lines and Slotlines. 1996," *Arthech House*, 1996.

[64] B. C. Wadell, *Transmission line design handbook*. Artech House, 1991.

[65] D. M. Pozar, *Microwave engineering*. John Wiley & Sons, 2009.

[66] J. Naqui, M. Durán-Sindreu, and F. Martín, "Selective mode suppression in coplanar waveguides using metamaterial resonators," *Appl. Phys. A*, vol. 109, no. 4, pp. 1053–1058, 2012.

[67] F. Martín, *Artificial transmission lines for RF and microwave applications*. Wiley Online Library, 2015.

[68] R. Marqués, F. Martin, and M. Sorolla, *Metamaterials with negative parameters: theory, design and microwave applications*, vol. 183. John Wiley & Sons, 2011.

[69] J. B. Pendry, A. J. Holden, D. J. Robbins, and W. J. Stewart, "Magnetism from conductors and enhanced nonlinear phenomena," *IEEE Trans. Microw. Theory Tech.*, vol. 47, no. 11, pp. 2075–2084, 1999.

[70] D. R. Smith, W. J. Padilla, D. C. Vier, S. C. Nemat-Nasser, and S. Schultz, "Composite medium with simultaneously negative permeability and permittivity," *Phys. Rev. Lett.*, vol. 84, no. 18, p. 4184, 2000.

[71] J. D. Baena, J. Bonache, F. Martin, R. M. Sillero, F. Falcone, T. Lopetegi, M. A. G. Laso, J. Garcia-Garcia, I. Gil, and M. F. Portillo, "Equivalent-circuit models for split-ring resonators and complementary split-ring resonators coupled to planar transmission lines," *IEEE Trans. Microw. Theory Tech.*, vol. 53, no. 4, pp. 1451–1461, 2005.

[72] R. Marqués, F. Medina, and R. Rafii-El-Idrissi, "Role of bianisotropy in negative permeability and left-handed metamaterials," *Phys. Rev. B*, vol. 65, no. 14, p. 144440, 2002.

[73] W. N. Hardy and L. A. Whitehead, "Split ‐ ring resonator for use in magnetic resonance from 200–2000 MHz," *Rev. Sci. Instrum.*, vol. 52, no. 2, pp. 213–216, 1981.

[74] M. Shamonin, E. Shamonina, V. Kalinin, and L. Solymar, "Properties of a metamaterial element: Analytical solutions and numerical simulations for a singly split double ring," *J. Appl. Phys.*, vol. 95, no. 7, pp. 3778–3784, 2004.

[75] M. Shamonin, E. Shamonina, V. Kalinin, and L. Solymar, "Resonant frequencies of a split ‐ ring resonator: Analytical solutions and numerical simulations," *Microw. Opt. Technol. Lett.*, vol. 44, no. 2, pp. 133–136, 2005.

[76] J. Naqui, *Symmetry properties in transmission lines loaded with electrically small resonators: circuit modeling and applications*. Springer, 2015.

[77] H. G. Booker, "Slot aerials and their relation to complementary wire aerials (Babinet's principle)," *J. Inst. Electr. Eng. IIIA Radiolocation*, vol. 93, no. 4, pp. 620–626, 1946.

[78] R. King and G. H. Owyang, "Complementarity in the study of transmission lines," *IRE Trans. Microw. theory Tech.*, vol. 8, no. 2, pp. 172–181, 1960.

[79] F. Falcone, T. Lopetegi, M. A. G. Laso, J. D. Baena, J. Bonache, M. Beruete, R. Marqués, F. Martín, and M. Sorolla, "Babinet principle applied to the design of metasurfaces and metamaterials," *Phys. Rev. Lett.*, vol. 93, no. 19, p. 197401, 2004.

[80] A. Velez, F. Aznar, J. Bonache, M. C. Velazquez-Ahumada, J. Martel, and F. Martin, "Open complementary split ring resonators (OCSRRs) and their application to wideband CPW band pass filters," *IEEE Microw. Wirel. Components Lett.*, vol. 19, no. 4, pp. 197–199, 2009.

[81] W. J. Getsinger, "Circuit duals on planar transmission media," in *Microwave Symposium Digest, 1983 IEEE MTT-S International*, 1983, pp. 154–156.

[82] J. Bonache, M. Gil, I. Gil, J. Garcia-Garcia, and F. Martin, "On the electrical characteristics of complementary metamaterial resonators," *IEEE Microw. Wirel. Components Lett.*, vol. 16, no. 10, pp. 543–545, 2006.

[83] M. Makimoto and S. Yamashita, "Compact bandpass filters using stepped impedance resonators," *Proc. IEEE*, vol. 67, no. 1, pp. 16–19, 1979.

[84] Y.-C. Chiou, J.-T. Kuo, and E. Cheng, "Broadband quasi-Chebyshev bandpass filters with multimode stepped-impedance resonators (SIRs)," *IEEE Trans. Microw. Theory Tech.*, vol. 54, no. 8, pp. 3352–3358, 2006.

[85] I. J. Bahl, "Capacitively compensated high performance parallel coupled microstrip filters," in *Microwave Symposium Digest, 1989., IEEE MTT-S International*, 1989, pp. 679–682.

[86] M. Duran-Sindreu, J. Bonache, and F. Martin, "Compact elliptic-function coplanar waveguide low-pass filters using backside metallic patterns," *IEEE Microw. Wirel. Components Lett.*, vol. 20, no. 11, pp. 601–603, 2010.

[87] J. Naqui, M. Durán-Sindreu, and F. Martín, "On the symmetry properties of coplanar waveguides loaded with symmetric resonators: analysis and potential applications," in *Microwave Symposium Digest (MTT), 2012 IEEE MTT-S International*, 2012, pp. 1–3.

[88] J. Naqui, C. Damm, A. Wiens, R. Jakoby, L. Su, and F. Martin, "Transmission lines loaded with pairs of magnetically coupled stepped impedance resonators (SIRs): Modeling and application to microwave sensors," in *Microwave Symposium (IMS), 2014 IEEE MTT-S International*, 2014, pp. 1–4.

[89] G. E. Ponchak and A. N. Downey, "Characterization of thin film microstrip lines on polyimide," *IEEE Trans. Components, Packag. Manuf. Technol. Part B*, vol. 21, no. 2, pp. 171–176, 1998.

[90] M. D. Janezic, D. F. Williams, V. Blaschke, A. Karamcheti, and C. S. Chang, "Permittivity characterization of low-k thin films from transmission-line measurements," *IEEE Trans. Microw. Theory Tech.*, vol. 51, no. 1, pp. 132–136, 2003.

[91] A. K. Verma and A. S. Omar, "Microstrip resonator sensors for determination of complex permittivity of materials in sheet, liquid and paste forms," *IEE Proceedings-Microwaves, Antennas Propag.*, vol. 152, no. 1, pp. 47–54, 2005.

[92] E. Chen and S. Y. Chou, "Characteristics of coplanar transmission lines on multilayer substrates: Modeling and experiments," *IEEE Trans. Microw. Theory Tech.*, vol. 45, no. 6, pp. 939–945, 1997.

[93] L. Su, J. Mata-Contreras, P. Vélez, and F. Martín, "A Review of Sensing Strategies for Microwave Sensors Based on Metamaterial-Inspired Resonators: Dielectric Characterization, Displacement, and Angular Velocity Measurements for Health Diagnosis, Telecommunication, and Space Applications," *Int. J. Antennas Propag.*, vol. 2017, 2017.

[94] J. Naqui, M. Durán-Sindreu, and F. Martín, "Novel sensors based on the symmetry properties of split ring resonators (SRRs)," *Sensors*, vol. 11, no. 8, pp. 7545–7553, 2011.

[95] A. K. Horestani, C. Fumeaux, S. F. Al-Sarawi, and D. Abbott, "Displacement sensor based on diamond-shaped tapered split ring resonator," *IEEE Sens. J.*, vol. 13, no. 4, pp. 1153–1160, 2013.

[96] J. Naqui and F. Martín, "Application of broadside-coupled split ring resonator (BC-SRR) loaded transmission lines to the design of rotary encoders for space applications," in *Microwave Symposium (IMS), 2016 IEEE MTT-S International*, 2016, pp. 1–4.

[97] J. Naqui and F. Martı, "Transmission lines loaded with bisymmetric resonators and their application to angular displacement and velocity sensors," *IEEE Trans. Microw. Theory Tech.*, vol. 61, no. 12, pp. 4700–4713, 2013.

[98] J. Naqui and F. Martin, "Angular displacement and velocity sensors based on electric-LC (ELC) loaded microstrip lines," *IEEE Sens. J.*, vol. 14, no. 4, pp. 939–940, 2014.

[99] J. Naqui, J. Coromina, A. Karami-Horestani, C. Fumeaux, and F. Martín, "Angular displacement and velocity sensors based on coplanar waveguides (CPWs) loaded with S-shaped split ring resonators (S-SRR)," *Sensors*, vol. 15, no. 5, pp. 9628–9650, 2015.

[100] J. Naqui, M. Durán-Sindreu, and F. Martín, "Modeling split-ring resonator (SRR) and complementary split-ring resonator (CSRR) loaded transmission lines exhibiting cross-polarization effects," *IEEE Antennas Wirel. Propag. Lett.*, vol. 12, pp. 178–181, 2013.

[101] J. Naqui, A. Fernández-Prieto, F. Mesa, F. Medina, and F. Martín, "Effects of inter-resonator coupling in split ring resonator loaded metamaterial transmission lines," *J. Appl. Phys.*, vol. 115, no. 19, p. 194903, 2014.

[102] T. Tamir and A. A. Oliner, "Guided complex waves. Part 1: Fields at an interface," in *Proceedings of the Institution of Electrical Engineers*, 1963, vol. 110, no. 2, pp. 310–324.

[103] R. R. A. Syms and L. Solymar, "Effective permeability of a metamaterial: Against conventional wisdom," *Appl. Phys. Lett.*, vol. 100, no. 12, p. 124103, 2012.

[104] F. Aznar, J. Bonache, and F. Martín, "Improved circuit model for left-handed lines loaded with split ring resonators," *Appl. Phys. Lett.*, vol. 92, no. 4, p. 43512, 2008.

[105] L. Su, J. Naqui, J. Mata-Contreras, and F. Martín, "Modeling metamaterial transmission lines loaded with pairs of coupled split-ring resonators," *IEEE Antennas Wirel. Propag. Lett.*, vol. 14, pp. 68–71, 2015.

[106] L. Su, J. Naqui, J. Mata, and F. Martín, "Dual-band epsilon-negative (ENG) transmission line metamaterials based on microstrip lines loaded with pairs of coupled complementary split ring resonators (CSRRs): Modeling, analysis and applications," in *Advanced Electromagnetic Materials in Microwaves and Optics (METAMATERIALS), 2015 9th International Congress on*, 2015, pp. 298–300.

[107] J. S. Hong and M. J. Lancaster, "Microstrip Filters for RF/Microstrip Applications." New York: Wiley, 2001.

[108] L. Su, J. Naqui, J. Mata-Contreras, and F. Martín, "Analysis of coupled microstrip lines loaded with complementary split ring resonators (CSRRs) and applications," in *Microwave Conference (APMC), 2015 Asia-Pacific*, 2015, vol. 1, pp. 1–3.

[109] J.-S. Lim, C.-S. Kim, Y.-T. Lee, D. Ahn, and S. Nam, "A spiral-shaped defected ground structure for coplanar waveguide," *IEEE Microw. Wirel. Components Lett.*, vol. 12, no. 9, pp. 330–332, 2002.

[110] A. M. E. Safwat, F. Podevin, P. Ferrari, and A. Vilcot, "Tunable bandstop defected ground structure resonator using reconfigurable dumbbell-shaped coplanar waveguide," *IEEE Trans. Microw. Theory Tech.*, vol. 54, no. 9, pp. 3559–3564, 2006.

[111] A. M. E. Safwat, S. Tretyakov, and A. V Räisänen, "Defected ground and patch-loaded planar transmission lines," *IET microwaves, antennas Propag.*, vol. 3, no. 2, pp. 195–204, 2009.

[112] S. Wang and F. C. Lee, "Negative capacitance and its applications on parasitic cancellation for EMI noise suppression," in *Power Electronics Specialists Conference, 2007. PESC 2007. IEEE*, 2007, pp. 2887–2891.

[113] J. Naqui, L. Su, J. Mata, and F. Martín, "Recent advances in the modeling of transmission lines loaded with split ring resonators," *Int. J. Antennas Propag.*, vol. 2015, 2015.

[114] R. K. Mongia, J. Hong, P. Bhartia, and I. J. Bahl, *RF and microwave coupled-line circuits*. Artech house, 2007.

[115] J. Bonache, M. Gil, O. García ‐ Abad, and F. Martín, "Parametric analysis of microstrip lines loaded with complementary split ring resonators," *Microw. Opt. Technol. Lett.*, vol. 50, no. 8, pp. 2093–2096, 2008.

[116] J. Bonache, I. Gil, J. Garcia-Garcia, and F. Martín, "Complementary split ring resonators for microstrip diplexer design," *Electron. Lett.*, vol. 41, no. 14, pp. 810–811, 2005.

[117] J. Naqui, “Transmission Lines Loaded with Pairs of Magnetically Coupled Stepped Impedance Resonators (SIRs): Modeling and Application to Microwave Sensors,” in *IMS*, 2014, vol. 1, no. 1, pp. 2–4.

[118] C. Damm, M. Schüßler, M. Puentes, H. Maune, M. Maasch, and R. Jakoby, “Artificial transmission lines for high sensitive microwave sensors,” in *Sensors, 2009 IEEE*, 2009, pp. 755–758.

[119] C. Damm, *Artificial Transmission Line Structures for Tunable Microwave Components and Microwave Sensors*. Shaker, 2010.

[120] L. Su, J. Mata-Contreras, P. Vélez, and F. Martín, “Splitter/combiner microstrip sections loaded with pairs of complementary split ring resonators (CSRRs): modeling and optimization for differential sensing applications,” *IEEE Trans. Microw. Theory Tech.*, vol. 64, no. 12, pp. 4362–4370, 2016.

[121] M. Puentes, M. Schüßler, and R. Jakoby, “2D sensor array based on Split Ring Resonators for monitoring of organic tissue,” in *Sensors, 2011 IEEE*, 2011, pp. 272–275.

[122] E. Cubukcu, S. Zhang, Y.-S. Park, G. Bartal, and X. Zhang, “Split ring resonator sensors for infrared detection of single molecular monolayers,” *Appl. Phys. Lett.*, vol. 95, no. 4, p. 43113, 2009.

[123] C.-S. Lee and C.-L. Yang, “Complementary split-ring resonators for measuring dielectric constants and loss tangents,” *IEEE Microw. Wirel. Components Lett.*, vol. 24, no. 8, pp. 563–565, 2014.

[124] C.-L. Yang, C.-S. Lee, K.-W. Chen, and K.-Z. Chen, “Noncontact measurement of complex permittivity and thickness by using planar resonators,” *IEEE Trans. Microw. Theory Tech.*, vol. 64, no. 1, pp. 247–257, 2016.

[125] A. Ebrahimi, W. Withayachumnankul, S. Al-Sarawi, and D. Abbott, “High-sensitivity metamaterial-inspired sensor for microfluidic dielectric characterization,” *IEEE Sens. J.*, vol. 14, no. 5, pp. 1345–1351, 2014.

[126] A. K. Horestani, S. Member, C. Fumeaux, S. Member, S. F. Al-sarawi, and D. Abbott, “Displacement Sensor Based on Diamond-Shaped Tapered Split Ring Resonator,” vol. 13, no. 4, pp. 1153–1160, 2013.

[127] M. H. Zarifi and M. Daneshmand, “Wide dynamic range microwave planar coupled ring resonator for sensing applications,” *Appl. Phys. Lett.*, vol. 108, no. 23, p. 232906, 2016.

[128] M. S. Boybay and O. M. Ramahi, “Material characterization using complementary split-ring resonators,” *IEEE Trans. Instrum. Meas.*, vol. 61, no. 11, pp. 3039–3046, 2012.

[129] A. A. Abduljabar, D. J. Rowe, A. Porch, and D. A. Barrow, "Novel microwave microfluidic sensor using a microstrip split-ring resonator," *IEEE Trans. Microw. Theory Tech.*, vol. 62, no. 3, pp. 679–688, 2014.

[130] W. Withayachumnankul, K. Jaruwongrungsee, A. Tuantranont, C. Fumeaux, and D. Abbott, "Metamaterial-based microfluidic sensor for dielectric characterization," *Sensors Actuators A Phys.*, vol. 189, pp. 233–237, 2013.

[131] T. Chen, D. Dubuc, and K. Grenier, "Resonant-based microwave biosensor for physiological liquid identification," in *Microwave Conference (EuMC), 2012 42nd European*, 2012, pp. 448–450.

[132] T. Chretiennot, D. Dubuc, and K. Grenier, "Optimized electromagnetic interaction microwave resonator/microfluidic channel for enhanced liquid bio-sensor," in *Microwave Conference (EuMC), 2013 European*, 2013, pp. 464–467.

[133] T. Chretiennot, D. Dubuc, and K. Grenier, "Double stub resonant biosensor for glucose concentrations quantification of multiple aqueous solutions," in *Microwave Symposium (IMS), 2014 IEEE MTT-S International*, 2014, pp. 1–4.

[134] G. Galindo-Romera, F. J. Herraiz-Martínez, M. Gil, J. J. Martínez-Martínez, and D. Segovia-Vargas, "Submersible printed split-ring resonator-based sensor for thin-film detection and permittivity characterization," *IEEE Sens. J*, vol. 16, no. 10, pp. 3587–3596, 2016.

[135]U. Kaatze, "Complex permittivity of water as a function of frequency and temperature," *J. Chem. Eng. Data*, vol. 34, no. 4, pp. 371–374, 1989.

[136] B. L. Hayes, "Microwave Synthesis: Chemistry at the Speed of Light 2002," *CEM Matthews, NC*, 2006.

Publications by the Author

Journal Publications

[J1] **L. Su**, J. Mata-Contreras, P. Vélez, and F. Martín, "Configurations of splitter/combiner microstrip sections loaded with stepped impedance resonators (SIRs) for sensing applications," *Sensors*, vol. 16, no. 12, p. 2195, 2016.

[J2] **L. Su**, J. Mata-Contreras, P. Vélez, and F. Martín, "Splitter/combiner microstrip sections loaded with pairs of complementary split ring resonators (CSRRs): modeling and optimization for differential sensing applications," *IEEE Trans. Microw. Theory Tech.*, vol. 64, no. 12, pp. 4362–4370, 2016.

[J3] J. Naqui, C. Damm, A. Wiens, R. Jakoby, **L. Su**, J. Mata-Contreras, and F. Martín, "Transmission lines loaded with pairs of stepped impedance resonators: modeling and application to differential permittivity measurements," *IEEE Trans. Microw. Theory Tech.*, vol. 64, no. 11, pp. 3864–3877, 2016.

[J4] J. Naqui, **L. Su**, J. Mata, and F. Martín, "Coplanar waveguides loaded with symmetric and asymmetric pairs of slotted stepped impedance resonators: Modeling, applications, and comparison to SIR ‐ loaded CPWs," *Microw. Opt. Technol. Lett.*, vol. 58, no. 11, pp. 2741–2745, 2016.

[J5] **L. Su**, J. Naqui, J. Mata, and F. Martín, "Coplanar waveguides loaded with symmetric and asymmetric multisection stepped impedance resonators: Modeling and potential applications," *Microw. Opt. Technol. Lett.*, vol. 58, no. 3, pp. 722–726, 2016.

[J6] **L. Su**, J. Naqui, J. Mata-Contreras, and F. Martín, "Modeling and applications of metamaterial transmission lines loaded with pairs of coupled complementary split-ring resonators (CSRRs)," *IEEE Antennas Wirel. Propag. Lett.*, vol. 15, pp. 154–157, 2016.

[J7] P. Vélez, M. Valero, **L. Su**, J. Naqui, J. Mata ‐ Contreras, J. Bonache, and F. Martín, "Enhancing common ‐ mode suppression in microstrip differential lines by means of chirped and multi ‐ tuned electromagnetic bandgaps," *Microw. Opt. Technol. Lett.*, vol. 58, no. 2, pp. 328–332, 2016.

[J8] **L. Su**, J. Naqui, J. Mata-Contreras, and F. Martin, "Miniature Microwave Notch Filters and Comparators Based on Transmission Lines Loaded with Stepped Impedance Resonators (SIRs)," *Micromachines*, vol. 7, no. 1, p. 1, 2015.

[J9] J. Naqui, **L. Su**, J. Mata, and F. Martín, "Recent advances in the modeling of transmission lines loaded with split ring resonators," *Int. J. Antennas Propag.*, vol. 2015, 2015.

[J10] J. Naqui, **L. Su**, J. Mata, and F. Martín, "Analysis of transmission lines loaded with pairs of coupled resonant elements and application to sensors," *J. Magn. Magn. Mater.*, vol. 383, pp. 144–151, 2015.

[J11] J. Naqui, **L. Su**, J. Mata, and F. Martín, "Symmetry-related electromagnetic properties of resonator-loaded transmission lines and applications," *Appl. Sci.*, vol. 5, no. 2, pp. 88–113, 2015.

[J12] **L. Su**, J. Naqui, J. Mata-Contreras, and F. Martín, "Modeling metamaterial transmission lines loaded with pairs of coupled split-ring resonators," *IEEE Antennas Wirel. Propag. Lett.*, vol. 14, pp. 68–71, 2015.

Conference Contributions

[C1] **L. Su**, J. Mata-Contreras, P. Vélez, and F. Martín, "Estimation of Complex Permittivity of Liquids by means of Complementary Split Ring Resonator (CSRR) Loaded Transmission Lines," *IEEE MTT-S International Microwave Workshop Series on Advanced Materials and Process*, Pavia, Italy, September 2017. (Accepted)

[C2] **L. Su**, J. Mata-Contreras, P. Vélez, and F. Martín, "Estimation of Conductive Losses in Complementary Split Ring Resonator (CSRR) Loading an Embedded Microstrip Line and Applications," *IEEE MTT-S International Microwave Symposium*, Honolulu, Hawaii, USA, June 2017.

[C3] **L. Su**, J. Naqui, J. Mata-Contreras, and F. Martín, "Cascaded Splitter/Combiner Microstrip Sections Loaded with Complementary Split Ring Resonators (CSRRs): Modeling, Analysis and Applications," *IEEE MTT-S International Microwave Symposium*, San Francisco, USA, May 2016.

[C4] **L. Su**, J. Naqui, J. Mata-Contreras, and F. Martín, "Analysis of coupled microstrip lines loaded with complementary split ring resonators (CSRRs) and applications," in *Microwave Conference (APMC), 2015 Asia-Pacific*, 2015, vol. 1, pp. 1–3.

[C5] **L. Su**, J. Naqui, J. Mata, and F. Martín, "Dual-band epsilon-negative (ENG) transmission line metamaterials based on microstrip lines loaded with pairs of coupled complementary split ring resonators (CSRRs): Modeling, analysis and applications," in *Advanced Electromagnetic Materials in Microwaves and Optics (METAMATERIALS), 2015 9th International Congress*, 2015, pp. 298–300.

[C6] **L. Su**, J. Naqui, J. Mata-Contreras, P. Vélez, and F. Martín, "Transmission line metamaterials based on pairs of coupled split ring resonators (SRRs) and complementary split ring resonators (CSRR): A comparison to the light of the lumped element equivalent circuits," in *Electromagnetics in Advanced Applications (ICEAA)*, 2015 International Conference on, 2015, pp. 891–894.

[C7] P. Velez, M. Valero, **L. Su**, J. Naqui, J. Mata-Contreras, J. Bonache, and F. Martín, "Differential microstrip lines with wideband common-mode rejection based on chirped-EBGs," in *Electromagnetics in Advanced Applications (ICEAA)*, 2015 International Conference on, 2015, pp. 855–858.

[C8] **L. Su**, J. Naqui, J. Mata, and F. Martín, "Recent advances in modeling metamaterial transmission lines based on pairs of split ring resonators (SRRs): Coupling between the SRRs forming the pair," in *Advanced Electromagnetic Materials in Microwaves and Optics (METAMATERIALS), 2014 8th International Congress*, 2014, pp. 382–384.

[C9] J. Naqui, **L. Su**, J. Mata, and F. Martin, "Analysis of transmission lines loaded with pairs of coupled resonant elements and application to sensors," *Moscow International Symposium on Magnetism, Moscow (Rusia)*, 29 June – 3 July, 2014. Invited.

[C10] J. Naqui, C. Damm, A. Wiens, R. Jakoby, **L. Su**, and F. Martín, "Transmission Lines Loaded with Pairs of Magnetically Coupled Stepped Impedance Resonators (SIRs): Modeling and Application to Microwave Sensors," in *IMS*, 2014, vol. 1, no. 1, pp. 2–4.

Articles in the Ph.D. Thesis

Fundamental articles

AWPL15: L. Su, J. Naqui, J. Mata-Contreras, and F. Martín, "Modeling metamaterial transmission lines loaded with pairs of coupled split-ring resonators," *IEEE Antennas Wirel. Propag. Lett.*, vol. 14, pp. 68–71, 2015.

AWPL16: L. Su, J. Naqui, J. Mata-Contreras, and F. Martín, "Modeling and applications of metamaterial transmission lines loaded with pairs of coupled complementary split-ring resonators (CSRRs)," *IEEE Antennas Wirel. Propag. Lett.*, vol. 15, pp. 154–157, 2016.

MOTL16 (3): L. Su, J. Naqui, J. Mata, and F. Martín, "Coplanar waveguides loaded with symmetric and asymmetric multisection stepped impedance resonators: Modeling and potential applications," *Microw. Opt. Technol. Lett.*, vol. 58, no. 3, pp. 722–726, 2016.

TMTT16 December: L. Su, J. Mata-Contreras, P. Vélez, and F. Martín, "Splitter/combiner microstrip sections loaded with pairs of complementary split ring resonators (CSRRs): modeling and optimization for differential sensing applications," *IEEE Trans. Microw. Theory Tech.*, vol. 64, no. 12, pp. 4362–4370, 2016.

Sensors16: L. Su, J. Mata-Contreras, P. Vélez, and F. Martín, "Configurations of splitter/combiner microstrip sections loaded with stepped impedance resonators (SIRs) for sensing applications," *Sensors*, vol. 16, no. 12, p. 2195, 2016.

Non-fundamental articles*

Micromachines15: L. Su, J. Naqui, J. Mata-Contreras, and F. Martin, "Miniature Microwave Notch Filters and Comparators Based on Transmission Lines Loaded with Stepped Impedance Resonators (SIRs)," *Micromachines*, vol. 7, no. 1, p. 1, 2015.

MOTL16 (11): J. Naqui, L. Su, J. Mata, and F. Martín, "Coplanar waveguides loaded with symmetric and asymmetric pairs of slotted stepped impedance resonators: Modeling, applications, and comparison to SIR ‐ loaded CPWs," *Microw. Opt. Technol. Lett.*, vol. 58, no. 11, pp. 2741–2745, 2016.

* Note: the classification between fundamental and non-fundamental articles obeys the Doctoral Regulations of Universitat Autònoma de Barcelona to present the thesis as a compendium of publications. They are all important for this thesis. Conference articles[(C)] included in this thesis for completeness but cannot be officially part of the compendium of the articles of the Ph.D. thesis.

IMS16(C): L. Su, J. Naqui, J. Mata-Contreras, and F. Martín, "Cascaded Splitter/Combiner Microstrip Sections Loaded with Complementary Split Ring Resonators (CSRRs): Modeling, Analysis and Applications," *IEEE MTT-S International Microwave Symposium*, San Francisco, USA, May 2016.

TMTT16 November: J. Naqui, C. Damm, A. Wiens, R. Jakoby, L. Su, J. Mata-Contreras, and F. Martín, "Transmission lines loaded with pairs of stepped impedance resonators: modeling and application to differential permittivity measurements," *IEEE Trans. Microw. Theory Tech.*, vol. 64, no. 11, pp. 3864–3877, 2016.

IMS17(C): L. Su, J. Mata-Contreras, P. Vélez, and F. Martín, "Estimation of Conductive Losses in Complementary Split Ring Resonator (CSRR) Loading an Embedded Microstrip Line and Applications," *IEEE MTT-S International Microwave Symposium*, Honolulu, Hawaii, USA, June 2017.

Pavia17(C): L. Su, J. Mata-Contreras, P. Vélez, and F. Martín, "Estimation of Complex Permittivity of Liquids by means of Complementary Split Ring Resonator (CSRR) Loaded Transmission Lines," *IEEE MTT-S International Microwave Workshop Series on Advanced Materials and Process*, Pavia, Italy, September 2017. (Accepted)

Fundamental articles in the thesis

AWPL15

"Modeling metamaterial transmission lines loaded with pairs of coupled split-ring resonators"

Su, Lijuan, Jordi Naqui, Javier Mata-Contreras, and Ferran Martín

IEEE Antennas and Wireless Propagation Letters 14 (2015): 68-71

Pre-print of: Su, L. et al. “Modeling metamaterial transmission lines loaded with pairs of coupled split-ring resonators” in IEEE antennas and wireless propagation letters, vol. 14 (2015), p. 68-71. DOI 10.1109/LAWP.2014.2355035

Modeling Metamaterial Transmission Lines loaded with Pairs of Coupled Split Ring Resonators

Lijuan Su, Jordi Naqui, *Student Member, IEEE,* Javier Mata-Contreras, Ferran Martín, *Fellow, IEEE*

***Abstract*— A lumped element equivalent circuit model of the unit cell of metamaterial transmission lines loaded with pairs of coupled split ring resonators (SRRs) is presented. It is assumed that the dominant coupling mechanism between the SRRs forming the pair is magnetic, and that the distance between SRRs of adjacent cells is high enough to neglect such additional inter-resonator coupling. SRRs are oriented with their symmetry plane orthogonal to the line axis. Under these conditions, the line-to-SRR coupling is also magnetic, the electric coupling being negligible. The presented model accounts for the rupture of symmetry that can be caused, for instance, by asymmetric dielectric loading of the SRRs. Thus, the analysis is carried out on a general model where the SRRs of the pair have different inductance and capacitance. Then, different cases are studied, in particular a line with identical SRRs, and a line with different SRRs, but with the same resonance frequency. It is shown that coupling between SRRs tends to far or split the resonance frequencies of the loaded lines (transmission zeros), except for the symmetric case, where only one resonance (different to the one of uncoupled SRRs) appears. The model is validated by comparing circuit simulations using extracted parameters with electromagnetic simulations and experimental data.**

***Index Terms*– Electromagnetic metamaterials, metamaterial transmission lines, split ring resonators (SRRs).**

I. Introduction

Artificial transmission lines inspired by metamaterial concepts, also called metamaterial transmission lines, have been a subject of intensive research in the last years. These lines are implemented by loading a host line with reactive elements, including inductors, capacitors and/or resonators. The main relevant aspect of metamaterial transmission lines, as compared to ordinary lines, is the fact that, thanks to the presence of the reactive elements, there are more degrees of freedom for design purposes. It is thus possible to tailor both the characteristic impedance and the dispersion, opening the path to the implementation of microwave components with novel functionalities on the basis of impedance and dispersion engineering [1]. To a first order approximation, ordinary lines are dispersionless. Hence, dispersion engineering is the main differential (and genuine) aspect of metamaterial transmission lines as compared to their conventional counterparts. Enhanced bandwidth components [2]-[5], multiband components [6]-[8], and leaky wave antennas with end-fire to back-fire scanning capability [9]-[11] are some of the proposed microwave components where dispersion engineering plays a fundamental role in their designs.

Many of the previous metamaterial based components have been implemented by means of the so-called resonant-type approach [12], where the host line is loaded with split ring resonators (SRRs) [13] or with other related resonant particles (such as CSRRs [14],[15]). For design purposes, lumped element equivalent circuit models of the unit cells of these artificial lines are very useful. This paper is focused on the first approach for the implementation of resonant-type metamaterial transmission lines: coplanar waveguides loaded with pairs of SRRs [13]. These lines exhibit a stop band functionality that may be interpreted as due to the extreme effective permeability in the vicinity of the fundamental SRR resonance (positive below it and negative above it). By loading these lines with shunt inductive strips, the stop band is switched to a pair of pass bands with composite right/left handed (CRLH) behavior, namely, backward wave propagation at the lower transmission band (due to the combined effect of SRRs and shunt strips), and forward wave propagation at the upper transmission band (caused by the host CPW) [16].

The first model of these CPWs loaded with SRRs and shunt strips was reported in [13], and later revised in [16] to account for the effects of the inductive strips on the transmission zero frequency, present below the first transmission band. In these models, coupling between SRRs of adjacent cells was not included, and the orientation of the SRRs was considered to be with their symmetry plane orthogonal to the line axis. With such orientation, the single coupling mechanism between the line and the SRRs is magnetic. However, by rotating the SRRs electric coupling must also be accounted for in the model (giving rise to mixed coupling), and it explains the asymmetry in the reflection coefficients measured from the two ports, as demonstrated in [17]. Coupling between adjacent SRRs was considered in [18],[19]. In [19] it was demonstrated that stopband bandwidth enhancement in SRR-loaded CPW transmission lines is due to the presence of complex modes [20], which appear as conjugate pairs and do not carry net power.

In this paper we study the effects of coupling between the SRRs forming the pair for the first time, neglecting the coupling between adjacent SRRs. Moreover, orthogonal orientation between the symmetry plane of the CPW and the symmetry plane of the pair of SRRs is considered. The consideration of all the effects together is extremely complex. However, for many purposes, the orthogonal orientation is the convenient one (to avoid mixed coupling) and coupling

This work has been supported by MINECO (Spain) under projects TEC2010-17512, TEC2013-40600-R and CSD2008-00066, and AGAUR-Generalitat de Catalunya under projects 2009SGR-421 and 2014SGR-157. Jordi Naqui is in debt to MECD (Spain) for supporting his work through the FPU grant AP2010-0431. Ferran Martín is in debt to ICREA for supporting his work.

The authors are with GEMMA/CIMITEC, Departament d’Enginyeria Electrònica, Universitat Autònoma de Barcelona, 08193 Bellaterra, Spain (e-mail: Ferran.Martin@uab.es).

between adjacent (cascaded) resonators does not apply in single stage structures, or if the SRRs are distant enough. Moreover, although for the implementation of metamaterial transmission lines the pairs of SRRs are implemented with identical resonators, disruption of symmetry may be of interest in certain applications, such as sensors and comparators based on symmetry properties. Therefore, we will consider the more general case of CPWs with asymmetric SRR loading (i.e., with different SRRs forming the pair). This asymmetry, and the inclusion of magnetic coupling between the resonators forming the pair is the novel aspect of the present paper as compared to previous models. In section II, we present the circuit model of these SRR-loaded lines, including magnetic coupling between the SRRs forming the pair. From this model we will be able to obtain the SRR resonances (or zeros in the transmission coefficient), where different situations will be considered: symmetric loading (identical SRRs), asymmetric loading with identical resonance frequencies of the individual SRRs but different reactance slope, and asymmetric loading with different resonance frequencies of the individual SRRs. The model is then validated in section III through parameter extraction. Finally, the main conclusions are highlighted in section IV.

II. Circuit Model and Analysis

A typical topology of the considered lines (unit cell), with identical SRRs, is depicted in Fig. 1(a). Rupture of symmetry can be achieved, for instance, by using different SRRs, or by loading the SRRs with asymmetric dielectric loads (interesting for dielectric characterization by comparison to a reference load). The circuit model of the unit cell of these lines, that accounts for both magnetic couplings (line-to-resonator, through M_1 and M_2, and inter-resonator coupling, through M'), is depicted in Fig. 1(b). L and C are the per-unit-cell inductance and capacitance of the line, and the SRRs are described by the resonant tanks L_1-C_1 and L_2-C_2.

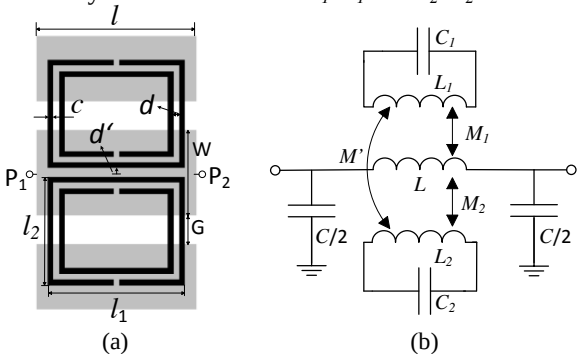

(a) (b)

Fig. 1. Typical topology of a CPW loaded with a pair of SRRs (a), and lumped element equivalent circuit model, considering magnetic coupling between SRRs (b). The SRRs (in black) are etched in the back substrate side of the CPW (depicted in grey). The model considers the general case of different SRRs, or identical SRRs with different dielectric loading.

The circuit of Fig. 1(b) is a π-circuit where the shunt branches are purely capacitive. Thus, the transmission zeros (or resonance frequencies of the coupled resonators) are given by the poles of the series reactance. From Kirchhoff's equations, including the different mutual couplings, applied to the series branch of the circuit of Fig. 1(b), the impedance of this branch is found to be:

$$Z_s(\omega) = j\omega L + j\omega^3 \times \left\{ \frac{C_1 M_1^2 \left(1-\frac{\omega^2}{\omega_2^2}\right) + C_2 M_2^2 \left(1-\frac{\omega^2}{\omega_1^2}\right) + 2\omega^2 M_1 M_2 M' C_1 C_2}{\left(1-\frac{\omega^2}{\omega_1^2}\right)\left(1-\frac{\omega^2}{\omega_2^2}\right) - \omega^4 M'^2 C_1 C_2} \right\} \quad (1)$$

where $\omega_1 = (L_1C_1)^{-1/2}$ and $\omega_2 = (L_2C_2)^{-1/2}$ are the resonance frequencies of the isolated resonators. By forcing the denominator of the last term to be zero, the notch (or transmission zero) frequencies can be derived, namely:

$$\omega_{\pm}^2 = \frac{\omega_1^2 + \omega_2^2 \pm \sqrt{(\omega_1^2 - \omega_2^2)^2 + 4M'^2 \omega_1^4 \omega_2^4 C_1 C_2}}{2[1 - M'^2 \omega_1^2 \omega_2^2 C_1 C_2]} \quad (2)$$

Note that these frequencies do not depend on the mutual couplings, M_1 and M_2, between the line and the SRRs, but on the mutual coupling, M', between the SRRs. If inter-resonator coupling is negligible ($M' = 0$), reasonable if the SRRs are separated enough, the solutions of (2) are simply ω_1 and ω_2. In this case, the equivalent circuit is formally identical to the one reported in [16], but with two different resonators in the series branch, due to the asymmetry of the unit cell. Let us now discuss three specific situations considering that $M' \neq 0$.

A. Symmetric case

The simplest one is the symmetric case, where $M_1 = M_2 = M$, $\omega_1 = \omega_2 = \omega_0$, $L_1 = L_2 = L_r$, and $C_1 = C_2 = C_r$. Under these conditions, the two solutions of (2) are (k_M is the magnetic coupling coefficient):

$$\omega_{\pm} = \frac{\omega_o}{\sqrt{1 \mp \frac{M'}{L_r}}} = \frac{\omega_o}{\sqrt{1 \mp k_M}} \quad (3)$$

However, one of the solutions, the one with the (−) sign in the radicand of (3) (ω_+), is not actually a transmission zero frequency. The reason is that this frequency also nulls the numerator of the last term in (1). By applying l'Hôpital's rule, it follows that the series impedance is finite at the frequency ω_+; hence, we can conclude that only one transmission zero, to the left of ω_0 (since $M' > 0$), appears in the transmission coefficient for symmetric structures with magnetically coupled SRRs.

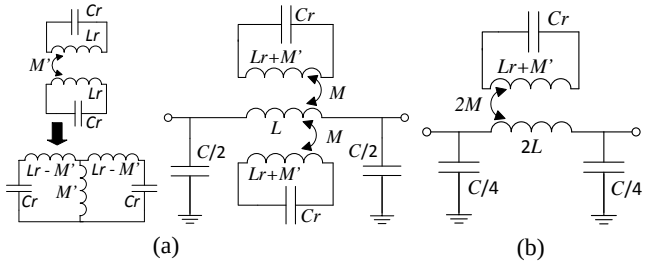

(a) (b)

Fig. 2. Circuit model of the structure of Fig. 1 for the symmetric case, with the inductive coupling between resonators transformed to the equivalent T-model (a), and circuit that results by applying the magnetic wall concept (b).

The transmission zero frequency for the symmetric case, ω_-, can alternatively be obtained by applying the magnetic wall concept to the circuit of Fig. 1(b). Before that, it is necessary to transform the magnetically coupled inductors L_r's of the

circuit of Fig. 1(b) to the equivalent T-circuit model (see Fig. 2) [21]. Notice that the inductance of each resonator at both sides of the symmetry plane (magnetic wall) is given by L_r+M', from which expression (3) with the (+) sign results. For the symmetric case, the model of [13],[16] provides the same results, but according to this new analysis the equivalent inductance of the resonators includes the effects of M', i.e., in [13],[16] M' is included in the SRR inductance.

B. Asymmetric case (different SRRs with same resonance)

The next analysis is for the asymmetric structure (different coupled SRRs), but considering that their fundamental resonance frequencies are identical, that is, $L_1 \neq L_2$, $C_1 \neq C_2$, $\omega_1 = \omega_2 = \omega_0$. In this case, expression (2) gives:

$$\omega_{\pm} = \frac{\omega_o}{\sqrt{1 \mp \dfrac{M'}{\sqrt{L_1 L_2}}}} = \frac{\omega_o}{\sqrt{1 \mp k_M}} \tag{4}$$

Note that (4) is formally identical to (3), but replacing the inductance L_r with the geometrical mean of the two inductances L_1 and L_2 (both expressions can be written in terms of the magnetic coupling coefficient, k_M). The two frequencies given by (4) null the denominator of the last term in (1), but, in general, none of them nulls the numerator. However, if the following condition is satisfied

$$C_1 M_1^2 + C_2 M_2^2 = 2 M_1 M_2 \sqrt{C_1 C_2} \tag{5}$$

then the numerator of the last term in (1) is also null at ω_+, and the impedance of the series branch is finite at this frequency (as the application of l'Hôpital's rule reveals). Expression (5) can be simplified to:

$$\frac{M_1}{M_2} = \sqrt{\frac{L_1}{L_2}} = \sqrt{\frac{C_2}{C_1}} \tag{6}$$

Thus, if condition (6) is satisfied, then only one transmission zero (at ω_-) is expected (notice that (6) represents a balance that forces the structure to behave similarly to the symmetric one). Otherwise, two transmission zeros at the frequencies given by (4), i.e., one above and the other below ω_0, are expected.

C. General case

The last analysis corresponds to the asymmetric case with arbitrary resonator frequencies ($L_1 \neq L_2$, $C_1 \neq C_2$, $\omega_1 \neq \omega_2$). In this case, the transmission zeros are given by the two solutions of (2), and the mutual coupling between resonators (M') enhances the distance between the transmission zeros, i.e.,

$$\omega_+^2 - \omega_-^2 = \frac{\sqrt{(\omega_1^2 - \omega_2^2)^2 + 4M'^2 \omega_1^4 \omega_2^4 C_1 C_2}}{[1 - M'^2 \omega_1^2 \omega_2^2 C_1 C_2]} > \omega_1^2 - \omega_2^2 \tag{7}$$

If the resonance frequencies of the isolated resonators (ω_1 and ω_2) are distant enough ($|\omega_1^2 - \omega_2^2| >> 0$) and M' is small (this later condition is very reasonable in the considered structures), the two solutions of (2) can be approximated by:

$$\omega_+ = \omega_1 \sqrt{\frac{1 + R \cdot k_M^2}{1 - k_M^2}} > \omega_1 \quad ; \quad \omega_- = \omega_2 \sqrt{\frac{1 - (1+R) \cdot k_M^2}{1 - k_M^2}} < \omega_2 \tag{8}$$

where we have considered that $\omega_1 > \omega_2$, and the positive dimensionless factor $R = (\omega_1^2/\omega_2^2 - 1)^{-1}$ has been introduced to simplify expressions (8). The validity of (8) is subjected to large values of $\omega_1^2 - \omega_2^2$ (small R) and small values of M' (or k_M), avoiding negative radicand in the square root of ω_- in (8).

III. VALIDATION

To validate the proposed model, we first consider the symmetric case, where SRR and CPW dimensions are set to l_1 = 4.8mm, l_2 = 3.8mm, $c = d$ = 0.2mm, l = 5.6mm, W = 3mm, and G = 1.01mm. The lossless electromagnetic simulations (inferred from *Agilent Momentum*) of the structure (S_{21}), considering different values of inter-resonator distance, d', are depicted in Fig. 3 (the considered substrate is *Rogers RO3010* with dielectric constant ε_r = 11.2 and thickness h = 1.27 mm). The circuit parameters for the four considered cases (extracted from the method reported in [22]) are shown in Table I (analytical models for the SRRs are reported in [12], [23],[24], but these models are not accurate enough with the presence of the CPW). As d' increases, the mutual coupling M' decreases, and the resonance frequency increases. Note that the other circuit parameters do not significantly vary, and the agreement between circuit and electromagnetic simulations in the region of interest is very good, pointing out the validity of the model. The measured responses (shown in Fig. 3) are also in good agreement (slight discrepancies are due to losses and fabrication related tolerances).

TABLE I. EXTRACTED CIRCUIT PARAMETERS (SYMMETRIC CASE) FOR DIFFERENT VALUES OF d'

d' (mm)	L (nH)	C (pF)	C_r (pF)	L_r (nH)	M (nH)	M' (nH)
0.105	1.82	1.58	0.44	6.85	0.82	1.74
0.305	1.86	1.58	0.44	6.85	0.82	1.29
0.505	1.84	1.57	0.43	6.85	0.81	1.02
0.755	1.85	1.55	0.43	6.85	0.80	0.80

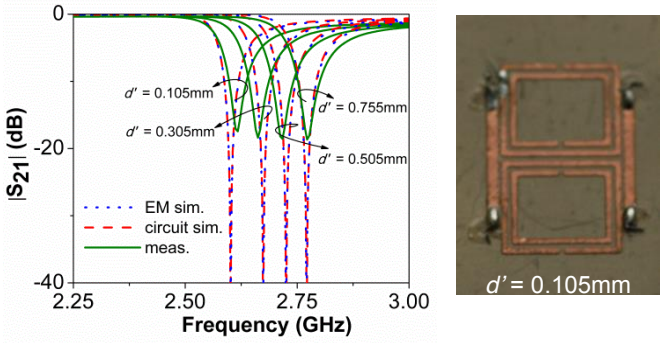

(a) (b)

Fig. 3. Frequency response (symmetric case) for different values of d' (a), and detail of one of the fabricated samples (bottom) where the ground planes have been connected through vias and strips to avoid the slot mode (b).

Let us now consider the asymmetric SRR-loaded line with identical resonance frequency for both SRRs ($\omega_1 = \omega_2 = \omega_0$). The considered geometrical parameters are: l = 5.6mm, W = 3mm, G = 1.01mm; upper (smaller) SRR: l_1 = 4mm, l_2 = 3mm, c = 0.2mm, d = 0.1mm, d' = 0.305mm; lower (larger) SRR: l_1 = 4.5mm, l_2 = 4.1mm, c = 0.2mm, d = 0.725mm, d' = 0.155mm. The extracted parameters are: L = 1.77nH, C = 1.6pF, L_1 = 5.0nH, C_1 = 0.42pF, L_2 = 7.2nH, C_2 = 0.29pF, M_1 = 0.513nH, M_2 = 0.774nH, M' = 0.96nH. As expected, two notches (one above and the other below ω_0) are present (the agreement between the circuit and electromagnetic simulation

is very good, according to Fig. 4). We have verified through circuit simulation that when condition (6) is satisfied, only one notch appears (see Fig. 4).

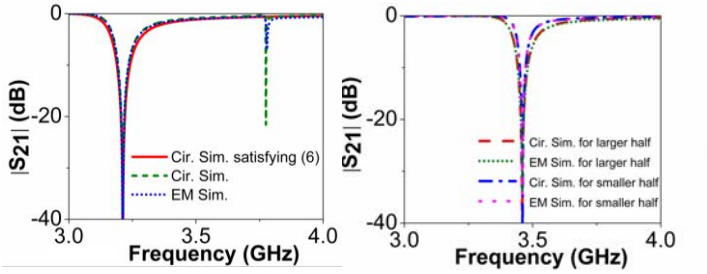

(a) (b)

Fig. 4. (a) Frequency response for the considered asymmetric case with identical SRRs resonance frequencies, and circuit simulation corresponding to L_1 = 5nH, L_2 = 7.2nH, M_2 = 0.774nH, M_1 = 0.645nH, i.e., satisfying (6); (b) responses of the CPW loaded with only the larger or smaller SRR.

Finally, we have considered an asymmetric structure with different SRR resonance frequencies. The geometry is as follows: l = 5.6mm, W = 3mm, G = 1.01mm; upper SRR: l_1= 4.8mm, l_2 = 4.6mm, c = d = 0.2mm; lower SRRs: l_1 = 4.8mm, l_2 = 3.8mm, c = d = 0.2mm. We have obtained the frequency response and the circuit parameters for four different values of d'. The pair of notches (at f_- = $\omega_-/2\pi$ and f_+ = $\omega_+/2\pi$) are depicted in Fig. 5, and verify that their distance increases as d' decreases, and $f_- < f_2$ and $f_+ > f_1$, in agreement to (8).

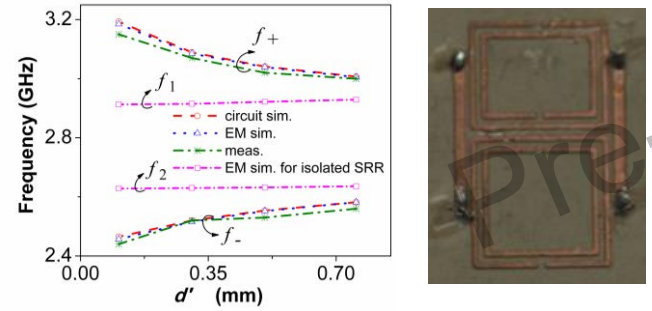

(a) (b)

Fig. 5. Variation of the notch frequencies as a function of d' for the asymmetric SRR-loaded CPW (a), and detail of the fabricated sample (bottom face) for d' = 0.105 mm (b).

IV. Conclusion

We have proposed and validated a circuit model for CPWs loaded with pairs of magnetically coupled SRRs. The model is valid for both symmetric and asymmetric structures. In the former case, only one notch in the transmission coefficient appears. For asymmetric structures, two notches are present and their separation increases as the distance between resonators decreases. However, there is a particular case of asymmetry, representing a balance condition between circuit parameters, where only one notch appears. The agreement between circuit, electromagnetic simulations and experiment is good in all the cases, supporting the validity of the model.

References

[1] M. Durán-Sindreu, A. Vélez, G. Sisó, J. Selga, P. Vélez, J. Bonache, and F. Martín "Recent advances in metamaterial transmission lines based on split rings", *Proc. IEEE*, vol. 99, pp. 1701-1710, Oct. 2011.

[2] H. Okabe, C. Caloz, T. Itoh, "A compact enhanced bandwidth hybrid ring using an artificial lumped element left handed transmission line section", *IEEE Trans. Microw. Theory Techn.*, vol. 52, pp. 798-804, Mar. 2004.

[3] M.A. Antoniades and G.V. Eleftheriades, "A broadband series power divider using zero-degree metamaterial phase shifting lines", *IEEE Microw. Wirel. Comp. Lett.*, vol. 15, pp. 808-810, Nov. 2005.

[4] M.A. Antoniades, and G.V. Eleftheriades, "A broadband Wilkinson balun using microstrip metamaterial lines", *IEEE Ant. Wirel. Propag. Lett.*, vol. 4, pp. 209–212 , 2005.

[5] G. Sisó, J. Bonache, M. Gil and F. Martín, "Application of resonant-type metamaterial transmission lines to the design of enhanced bandwidth components with compact dimensions", *Microw. Opt. Techn. Lett.*, vol. 50, pp. 127-134, Jan. 2008.

[6] I-H. Lin, M. DeVincentis, C. Caloz, and T. Itoh, "Arbitrary dual-band components using composite right/left-handed transmission lines", *IEEE Trans. Microw. Theory Techn.*, vol. 52, pp. 1142-1149, Apr. 2004.

[7] A.C. Papanastasiou, G.E. Georghiou, G.V. Eleftheriades, "A quad-band wilkinson power divider using generalized NRI transmission lines", *IEEE Microw. Wirel. Comp. Lett.*, vol. 18, pp. 521-523, Aug. 2008.

[8] M. Durán-Sindreu, G. Sisó, J. Bonache, F. Martín, "Planar multi-band microwave components based on the generalized composite right/left handed transmission line concept", *IEEE Trans. Microw. Theory Techn.*, vol. 58, no 12, pp. 3882-3891, Dec. 2010.

[9] S. Lim, C. Caloz, T. Itoh," Electronically Scanned Composite Right/Left Handed Microstrip Leaky-Wave Antenna", *IEEE Microw. Wirel. Comp. Lett.*, vol. 14, pp. 277-279, Jun. 2004.

[10] M.A. Antoniades, G.V. Eleftheriades, "A CPS leaky-wave antenna with reduced beam squinting using NRI-TL metamaterials," *IEEE Trans. Antennas Propag.*, vol. 56, no. 3, pp. 708-721, Mar. 2008.

[11] G. Zamora, S. Zuffanelli, F. Paredes, F. Javier Herraiz-Martínez, F. Martín, J. Bonache, "Fundamental mode leaky-wave-antenna (LWA) using slot line and split-ring-resonator (SRR) based metamaterials", *IEEE Ant. Wirel. Prop. Lett.*, vol. 12, pp. 1424-1427, 2013.

[12] R. Marqués, F. Martín and M. Sorolla, *Metamaterials with Negative Parameters: Theory, Design and Microwave Applications*, John Wiley & Sons Inc., New York, 2007.

[13] F. Martín, F. Falcone, J. Bonache, R. Marqués and M. Sorolla, "Split ring resonator based left handed coplanar waveguide", *Appl. Phys. Lett.*, vol. 83, pp. 4652-4654, December 2003.

[14] F. Falcone, T. Lopetegi, J.D. Baena, R. Marqués, F. Martín and M. Sorolla, "Effective negative-ε stop-band microstrip lines based on complementary split ring resonators", *IEEE Microw. Wirel. Comp. Lett.*, vol. 14, pp. 280-282, Jun. 2004.

[15] J.D. Baena, J. Bonache, F. Martín, R. Marqués, F. Falcone, T. Lopetegi, M.A.G. Laso, J. García, I Gil, M. Flores-Portillo and M. Sorolla, "Equivalent circuit models for split ring resonators and complementary split rings resonators coupled to planar transmission lines", *IEEE Trans. Microw. Theory Techn.*, vol. 53, pp. 1451-1461, Apr. 2005.

[16] F. Aznar, J. Bonache and F. Martín, "Improved circuit model for left handed lines loaded with split ring resonators", *Appl. Phys. Lett.*, vol. 92, paper 043512, February 2008.

[17] J. Naqui, M. Durán-Sindreu, and F. Martín, "Modeling Split Ring Resonator (SRR) and Complementary Split Ring Resonator (CSRR) Loaded Transmission Lines Exhibiting Cross Polarization Effects", *IEEE Ant. Wirel. Propag. Lett.*, vol. 12, pp. 178-181, 2013.

[18] R. R. A. Syms, and L. Solymar, "Effective permeability of a metamaterial: against conventional wisdom", *App. Phys. Lett.* vol. 100, paper 124103 (2012).

[19] J. Naqui, A. Fernández-Prieto, F. Mesa, F. Medina and F. Martín, "Effects of inter-resonator coupling in split ring resonator (SRR) loaded metamaterial transmission lines", *J. Appl. Phys.*, vol. 115, paper 194903, 2014.

[20] T. Tamir and A. A. Oliner, "Guided complex waves," *Proc. Inst. Elect. Eng.*, vol. 110, pp. 310–334, 1963.

[21] J-S. Hong and M.J. Lancaster, *Microstrip filters for RF/microwave applications*, John Wiley, New Jersey, 2001.

[22] F. Aznar, M. Gil, J. Bonache, J.D. Baena, L. Jelinek, R. Marqués, F. Martín, "Characterization of miniaturized metamaterial resonators coupled to planar transmission lines" *J. Appl. Phys.*, vol. 104, paper 114501-1-8, Dec. 2008.

[23] F. Bilotti, A. Toscano, L. Vegni, K. Aydin, K. Alici, and E. Ozbay, "Equivalent-circuit models for the design of metamaterials based on artificial magnetic inclusions", *IEEE Trans. Microw. Theory Techn.*, vol. 55, no. 12, pp. 2865 – 2873, Dec. 2007.

[24] D. Ramaccia, L. Di Palma, D. Ates, E. Ozbay, A. Toscano, and F. Bilotti, "Analytical model of connected bi-omega: robust particle for the selective power transmission through sub-wavelength apertures", *IEEE Trans. Ant. Prop.*, vol. 62, no. 4, pp. 2093-2101, Apr. 2014.

AWPL16

"Modeling and applications of metamaterial transmission lines loaded with pairs of coupled complementary split-ring resonators (CSRRs)"

Su, Lijuan, Jordi Naqui, Javier Mata-Contreras, and Ferran Martín

IEEE Antennas and Wireless Propagation Letters 15 (2016): 154-157

Post-print of: Su, L. et al. "Modeling and applications of metamaterial transmission lines loaded with pairs of coupled complementary split ring resonators (CSRRs) " in IEEE antennas and wireless propagation letters, vol. 15 (2016), p. 154-157. DOI 10.1109/LAWP.2015.2435656

Modeling and Applications of Metamaterial Transmission Lines loaded with Pairs of Coupled Complementary Split Ring Resonators (CSRRs)

Lijuan Su, Jordi Naqui, *Member*, *IEEE*, Javier Mata-Contreras, Ferran Martín, *Fellow*, *IEEE*

***Abstract*— This paper is focused on the modeling, analysis and applications of microstrip lines loaded with pairs of electrically coupled complementary split ring resonators (CSRRs). Typically, these epsilon negative (ENG) metamaterial transmission lines are implemented by loading the line with a single CSRR (etched beneath the conductor strip) in the unit cell. This provides a stop band in the vicinity of the CSRR resonance. However, by loading the line with a pair of CSRRs per unit cell, it is possible to either implement a dual-band ENG transmission line (useful, for instance, as a dual-band notch filter), provided the CSRRs are tuned at different frequencies, or to design microwave sensors and comparators based on symmetry disruption (in this case by using identical CSRRs and by truncating symmetry by different means, e.g., asymmetric dielectric loading). The design of these CSRR-based structures requires an accurate circuit model able to describe the line, the resonators and the different coupling mechanisms (i.e., line-to-resonator and inter-resonator coupling). Thus, a lumped element equivalent circuit is proposed and analyzed in detail. The model is validated by comparison to electromagnetic simulations and measurements. A proof-of-concept of a differential sensor for dielectric characterization is proposed. Finally, the similarities of these structures with coplanar waveguide transmission lines loaded with pairs of SRRs are pointed out.**

***Index Terms*– Electromagnetic metamaterials, metamaterial transmission lines, complementary split ring resonators (CSRRs).**

I. Introduction

Metamaterial transmission lines based on complementary split ring resonators (CSRRs), first proposed in [1],[2], have found many applications in RF/microwave engineering, including filters [3]-[6], multiband components [7], enhanced bandwidth components [8], leaky wave antennas [9], etc. Typically, these lines are implemented by loading a microstrip line with the CSRRs etched in the ground plane, beneath the conductor strip, and with their symmetry plane orthogonal to the line axis. Under these conditions, line-to-resonator coupling is purely electric, and the lumped element circuit model (including only electric coupling) was first proposed in [10]. The effects of CSRR rotation (i.e., mixed electric and magnetic coupling) and coupling between CSRRs of adjacent cells (bandwidth enhancement), not included in the former model, were studied in [11] and [12], respectively.

In these previous studies and in the reported applications of CSRR-loaded lines, only one CSRR in the unit cell was considered. However, in microstrip lines loaded with two CSRRs per unit cell interesting possibilities arise. Specifically, by loading the line with different CSRRs, a dual-band epsilon negative (ENG) metamaterial transmission line results. These lines can be useful, for instance, as dual-band bandstop or notched filters. Conversely, by loading the line with identical CSRR in the unit cell, and by considering a single unit cell in the structure, the resulting (single) transmission zero splits into two notches if symmetry is truncated, e.g., by an asymmetric dielectric load. Thus, these symmetric CSRR-pair-loaded lines have potential applications as differential sensors or comparators.

Necessarily, the distance between the CSRRs forming the pair must be small (otherwise the coupling between the line and the CSRRs would be negligible). Hence, the circuit model of these lines should account not only for the line, CSRRs, and coupling between the line and the resonators (as usual [10]), but also for inter-resonator coupling. In this paper, the lumped element equivalent circuit model of these microstrip lines loaded with pairs of CSRRs is reported and analyzed in detail, and a proof-of-concept of a comparator to detect differences between a sample and a reference is proposed. In Section II, the model is presented and analyzed, and it is compared to the model of coplanar waveguides (CPWs) loaded with pairs of SRRs [13]. Model validation through parameter extraction is carried out in Section III, whereas the use of a symmetric structure as a comparator is demonstrated in Section IV. Finally, the main conclusions are highlighted in Section V.

II. Circuit Model and Analysis

The topology and the proposed lumped element equivalent circuit model of the considered structures (unit cell) are depicted in Fig. 1(a) and (b), respectively. The line is modeled by the inductance L and the capacitance C. C_{c1} and C_{c2} account for the electric coupling between the line and the CSRRs, described by the resonant tanks L_1-C_1 and L_2-C_2, and C_M accounts for their mutual electric coupling. The model, valid as long as the CSRRs are electrically small, considers the general case of a microstrip line loaded with different CSRRs (asymmetric structure). Besides the fact that there are two coupled CSRRs per unit cell, there is a significant

This work has been supported by MINECO (Spain) under project TEC2013-40600-R, by AGAUR-Generalitat de Catalunya under project 2014SGR-157, and by FEDER funds. Ferran Martín is in debt to ICREA for supporting his work. Lijuan Su thanks CSC (China scholarship council) Grant for supporting her work in UAB.

The authors are with GEMMA/CIMITEC, Departament d'Enginyeria Electrònica, Universitat Autònoma de Barcelona, 08193 Bellaterra, Spain (e-mail: Ferran.Martin@uab.es).

difference between the model of Fig. 1(b) and the model of the microstrip line loaded with a single CSRR [10]. In [10], the capacitance of the line was considered to be the coupling capacitance between the line and the CSRR. The reason is that if the single CSRR is etched in the ground plane with its center aligned with the line axis, the conductor strip is located above the inner metallic region of the CSRR, and the electric field lines generated by the line entirely penetrate (at least to a first order approximation) the inner metallic region of the CSRRs (this is valid provided the conductor strip -unit cell- does not extend significantly beyond the extremes of the CSRR). However, in the structure of Fig. 1(a) not all the electric field lines penetrate the inner metallic regions of the CSRRs, hence being necessary to include a capacitor, C, between the conductor strip and ground. Strictly speaking, this is not the line capacitance, but the capacitance between the inter-resonator metallic region and the conductor strip (note that this capacitance should increase by increasing the distance between CSRRs, at the expense of a decrease in C_{c1} and C_{c2}).

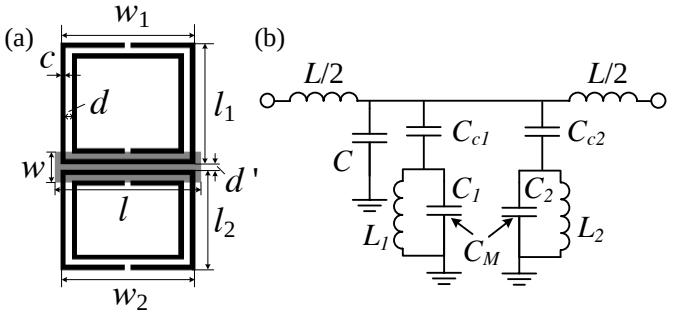

Fig. 1. Typical topology of a microstrip line loaded with a pair of CSRRs (a) and lumped element circuit model (b). The CSRRs (etched in the ground plane) are depicted in black and the conductor strip (upper metal) is depicted in grey.

In order to find the transmission zeros in the circuit of Fig. 1(b), the reactance of the shunt branch is forced to be zero (note that C has not any influence on this calculation). This leads us (by using the equivalence shown in Fig. 2 [14] and the Δ-T transform, and after some tedious calculations) to the following bi-quadratic equation:

$$A\omega^4 + B\omega^2 + D = 0 \tag{1}$$

where ω is the angular frequency and

$$A = L_1L_2\left\{C_M(C_{c1}+C_{c2})(C_{c1}+C_1)(C_{c2}+C_2) - C_{c1}C_{c2}C_M^2\right\} +$$
$$+ L_1L_2\left\{C_{c1}C_{c2}(C_{c1}+C_1)(C_{c2}+C_2) - (C_{c1}+C_{c2})C_M^3\right\} =$$
$$= D\cdot L_1L_2\left\{(C_{c1}+C_1)(C_{c2}+C_2) - C_M^2\right\}$$
$$B = -D\cdot\left\{L_1(C_{c1}+C_1) + L_2(C_{c2}+C_2)\right\}$$
$$D = C_{c1}C_M + C_{c2}C_M + C_{c1}C_{c2}$$

Since $D > 0$, the solution of (1) is equivalent to the solution of

$$L_1L_2\left\{(C_{c1}+C_1)(C_{c2}+C_2) - C_M^2\right\}\omega^4 -$$
$$-\left\{L_1(C_{c1}+C_1) + L_2(C_{c2}+C_2)\right\}\omega^2 + 1 = 0 \tag{2}$$

namely,

$$\omega_{\pm}^2 = \frac{\omega_1^2 + \omega_2^2 \pm \sqrt{(\omega_1^2-\omega_2^2)^2 + 4C_M^2\omega_1^4\omega_2^4L_1L_2}}{2[1-C_M^2\omega_1^2\omega_2^2L_1L_2]} \tag{3}$$

where

$$\omega_i = \frac{1}{\sqrt{L_i(C_i + C_{ci})}} \tag{4}$$

with i = 1,2, are the transmission zero frequencies of the isolated resonators (i.e., without inter-resonator coupling).

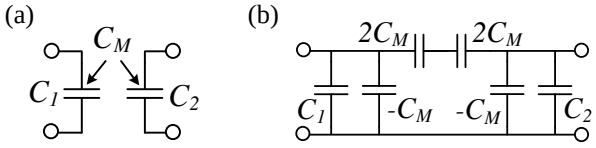

Fig. 2. Two-port with mutual capacitive coupling (a) and its equivalent π-circuit (b).

Note that if inter-resonator coupling is zero (C_M = 0), the two solutions of (3) are simply ω_1 and ω_2, an expected result since at these frequencies one of the two (uncoupled) parallel branches of the circuit of Fig. 1(b) is shorted to ground. Let us now discuss three specific situations considering that $C_M \neq 0$.

A. Symmetric case

If the structure is symmetric with regard to the line axis, then $C_{c1} = C_{c2} = C_c$, $L_1 = L_2 = L_r$, and $C_1 = C_2 = C_r$ (giving also $\omega_1 = \omega_2 = \omega_0$), and the two solutions of (3) are:

$$\omega_{\pm} = \frac{\omega_o}{\sqrt{1 \mp \dfrac{C_M}{C_r + C_c}}} \tag{5}$$

However, ω_- is not actually a physical solution, since the shunt branch reactance presents a pole at this frequency, resulting in a finite reactance. Indeed, the single transmission zero frequency (ω_+) that arises when the CSRR-loaded line is symmetric can be easily inferred by direct inspection of the circuit of Fig. 1(b) and the equivalence of Fig. 2. Note that the coupling between CSRRs, for this symmetric case, has the effect of increasing the transmission zero frequency.

B. Asymmetric case (different CSRRs with same resonance frequency)

Let us now consider an asymmetric structure (i.e., with different coupled CSRRs, or $L_1 \neq L_2$, $C_1 \neq C_2$), but satisfying the condition $\omega_1 = \omega_2 = \omega_0$. In this case, expression (3) gives:

$$\omega_{\pm} = \frac{\omega_o}{\sqrt{1 \mp \dfrac{C_M}{\sqrt{(C_1 + C_{c1})(C_2 + C_{c2})}}}} \tag{6}$$

namely, an expression formally identical to (5). In general the two mathematical solutions given by (6) are both physical solutions (none of them correspond to poles of the shunt reactance), and the corresponding transmission zeros are located to the left (ω_-) and right (ω_+) of ω_0. However, if the following balance condition is satisfied

$$\frac{C_{c1}}{C_{c2}} = \sqrt{\frac{C_1 + C_{c1}}{C_2 + C_{c2}}} = \sqrt{\frac{L_2}{L_1}} \tag{7}$$

then only one transmission zero (at ω_+) is expected, since the reactance exhibits a pole at ω_-.

C. General case

For the general case, i.e., an asymmetric structure with arbitrary resonator frequencies ($L_1 \neq L_2$, $C_1 \neq C_2$) and $\omega_1 \neq \omega_2$, the transmission zeros are given by the two solutions of (3). The coupling capacitance C_M enhances the distance between the transmission zeros, i.e.,

$$\omega_+^2 - \omega_-^2 = \frac{\sqrt{(\omega_1^2 - \omega_2^2)^2 + 4C_M^2\omega_1^4\omega_2^4 L_1 L_2}}{[1 - C_M^2\omega_1^2\omega_2^2 L_1 L_2]} > \omega_1^2 - \omega_2^2 \quad (8)$$

Moreover, $\omega_+ > \omega_1$ and $\omega_- < \omega_2$, where it is assumed that $\omega_1 > \omega_2$.

D. Comparison to the model of SRR-loaded CPW transmission lines

Despite the fact that CPW structures loaded with pairs of magnetically coupled split ring resonators (SRRs) are described by a circuit model completely different from the one of Fig. 1(b) [13], the behavior of these SRR- and CSRR-loaded lines, inferred from the circuit models, is very similar (although not identical). Indeed, the general solution (3), as well as the mathematical solutions corresponding to the considered particular cases (expressions 5, 6 and condition 7) are identical to the equivalent solutions in SRR-loaded lines, provided the following mapping holds:

$$C_M \leftrightarrow M' \quad (9a)$$

$$L_{1,2} \leftrightarrow C_{1,2} \quad (9b)$$

$$C_{1,2} + C_{c1,2} \leftrightarrow L_{1,2} \quad (9c)$$

where the left and right hand sides refer to the elements of the circuit model of the CSRR-loaded microstrip line [Fig. 1(b)] and SRR-loaded CPW [13], respectively.

One difference between both models concerns the single transmission zero for the symmetric case or for the asymmetric case subjected to the balance condition. As mentioned above, for CSRR-loaded lines the physical solution is the upper frequency, whereas it is the lower frequency for SRR-loaded lines. Thus, for microstrip lines loaded with pairs of identical and symmetrically etched CSRRs, the transmission zero appears to the right of ω_0, whereas it appears to the left of ω_0 in symmetric SRR-loaded CPW transmission lines. Note, however that ω_0, ω_1 and ω_2 are defined by (4) in this work, whereas in [13], these angular frequencies are the intrinsic resonator (SRR) frequencies.

It is also worth to mention that, whereas in SRR-loaded CPWs the position of the transmission zeros does not depend on the mutual coupling between the line and the resonators, this does not hold in microstrip lines loaded with pairs of CSRRs, where the coupling capacitors C_{c1} and C_{c2} (or C_c for the symmetric case) have influence on the location of the transmission zeros (through ω_1 and ω_2).

III. Validation

To validate the model we have considered three different structures. Two of them are symmetric, the unique difference being the lengths $l_1 = l_2$ [see Fig. 1(a)],which are set to $l_1 = l_2 =$ 3.8 mm in one case (A), and to $l_1 = l_2 =$ 4.6 mm in the other case (B). The asymmetric structure (case C) is implemented by considering the two previous CSRRs (i.e., $l_1 =$ 4.6 mm and $l_2 =$ 3.8 mm). The other parameters, in reference to Fig. 1(a), are $W =$ 1.18 mm, $l =$ 5.2 mm, $c = d =$ 0.2 mm, $w_1 = w_2 =$ 4.8 mm, and $d' =$ 0.2 mm. The considered substrate is *Rogers RO3010* with thickness $h =$ 1.27 mm and dielectric constant ε_r =10.2. The simulated (without losses) frequency responses of these structures, inferred from the *Keysight Momentum* commercial software, are depicted in Fig. 3. Parameter extraction has been done following the procedure explained in the next paragraph.

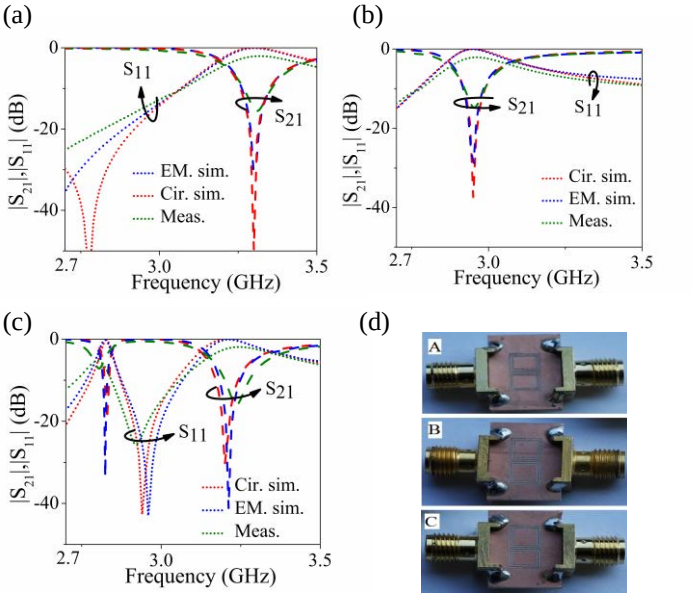

Fig. 3. Electromagnetic simulation, circuit simulation and measured responses of the three considered CSRR-loaded microstrip structures. (a) symmetric case A; (b) symmetric case B; (c) asymmetric case C; (d) photographs of symmetric case A, symmetric case B and asymmetric case C.

For the symmetric structures, the equivalent circuit model can be reduced to the one depicted in Fig. 4, and parameter extraction is realized following the procedure first published in [15]. Note, however, that the fact that there is an additional reactive element in the model (the capacitor C) forces us to include an additional condition for parameter extraction. However, since there are two frequencies where the phase of S_{21} is -90^o, the condition $Z_s(\omega) = -Z_p(\omega)$ is used twice, and the five parameters of the model can be determined, i.e., L, C, C_c, L_r and $C_r - C_M$. Following this procedure, it is not possible to independently infer C_r and C_M. However, by repeating this procedure for the other symmetric structure, we can obtain the corresponding set of parameters. Finally, C_M is used as fitting parameter in the asymmetric structure, to adjust the position of the transmission zeros, and once C_M is known, C_r for each symmetric structure (or C_1 and C_2 in the asymmetric one) can be inferred. The extracted parameters for the three structures are shown in table I.

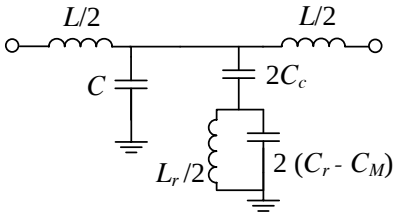

Fig. 4. Lumped element circuit model for the symmetric CSRR-loaded line.

TABLE I. EXTRACTED CIRCUIT PARAMETERS

	L (nH)	C (pF)	C_1-C_2 (pF)	L_1-L_2 (nH)	$C_{c1,2}$ (pF)	C_M (pF)
A	3.47	0.086	1.96	1.10	0.336	0.177
B	3.53	0.092	2.27	1.18	0.360	0.177
C	3.50	0.085	1.96-2.27	1.10-1.18	0.347	0.177

The circuit simulations for the three considered cases are also depicted in Fig. 3, where it can be appreciated the good agreement with the lossless electromagnetic simulations. The three structures have been fabricated and the measured responses (inferred from the *Agilent Technologies N5221A* vector network analyzer) are also depicted in Fig. 3. The slight discrepancies with the circuit and electromagnetic simulations are due to fabrication related tolerances and to the fact that losses have been excluded in the simulations. Nevertheless, with the results of Fig. 3, it is clear that the proposed model [Fig. 1(b)] is validated.

We would like to mention that in SRR-loaded CPWs, the increase in frequency splitting (asymmetric structures) caused by shortening the distance between SRRs (hence enhancing their coupling) was confirmed through electromagnetic simulation and experiment. In microstrip lines loaded with pairs of CSRRs, this effect has also been corroborated, but by varying the inter-CSRR space *d'*, not only C_M experiences changes (as expected), but also C_{c1}, C_{c2}, C, L_1, L_2, C_1 and C_2 are modified. This means that when *d'* is reduced, the effects (increase of frequency splitting) cannot be merely attributed to inter-CSRR coupling enhancement.

IV. PROOF OF CONCEPT OF A COMPARATOR

According to Fig. 3(c), it is clear that the asymmetric structures can be used as dual-band notched filters. However, an alternative interesting application concerns differential sensors and comparators on the basis of disruption of symmetry. Namely, if a symmetric CSRR-loaded microstrip line is loaded with an asymmetric load, this asymmetry will cause a frequency splitting that can be easily detected. Thus, it is possible, for instance, to compare dielectric loads to a reference, in order to detect defects, abnormalities, etc. As a proof of concept, we report here the frequency response of the symmetric structure (case A), where one of the CSRR has been loaded with a dielectric slab of permittivity identical to that of the substrate (10.2), thickness 1.27 mm and dimensions 7.5 mm × 6.6 mm. As can be appreciated, two notches, indicative of the asymmetric loading of the structure, appear.

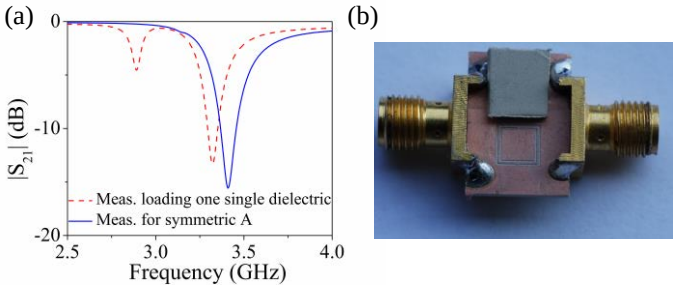

Fig. 5. (a) Measured frequency response of the symmetric CSRR-loaded microstrip structure corresponding to case A, loaded with a dielectric slab, placed on top of one of the CSRRs; (b) photograph of the symmetric case A loaded with a dielectric slab in the upper CSRR.

V. CONCLUSION

We have proposed and validated a circuit model for microstrip lines loaded with pairs of electrically coupled CSRRs. The model, valid for both symmetric and asymmetric structures, has been analyzed in detail, and the similarities with CPW transmission lines loaded with pairs of magnetically coupled SRRs have been pointed out. The model has been validated by parameter extraction and comparison to electromagnetic simulations and experimental data, by considering two symmetric and one asymmetric structures. Finally, a proof of concept of a comparator has been reported.

REFERENCES

[1] F. Falcone, T. Lopetegi, J.D. Baena, R. Marqués, F. Martín and M. Sorolla, "Effective negative-ε stop-band microstrip lines based on complementary split ring resonators", *IEEE Microw. Wirel. Comp. Lett.*, vol. 14, pp. 280-282, Jun. 2004.

[2] F. Falcone, T. Lopetegi, M.A.G. Laso, J.D. Baena, J. Bonache, R. Marqués, F. Martín, M. Sorolla, "Babinet principle applied to the design of metasurfaces and metamaterials", *Phys. Rev. Lett.*, vol. 93, paper 197401, Nov. 2004.

[3] J. Bonache, F. Martín, I. Gil, J. García-García, R. Marqués and M. Sorolla, "Microstrip bandpass filters with wide bandwidth and compact dimensions", *Microw. Opt. Technol. Lett.*, vol. 46, pp. 343-346, Aug. 2005.

[4] J. Bonache, F. Martín, J. García-García, I. Gil, R. Marqués and M. Sorolla, "Ultra wide band pass filtres (UWBPF) based on complementary split rings resonators", *Microw. Opt. Technol. Lett.*, vol. 46, pp.283-286, Aug. 2005.

[5] P. Mondal, M.K. Mandal, A. Chaktabarty, S. Sanyal, "Compact bandpass filters with wide controllable fractional bandwidth", *IEEE Microw. Wireless Compon. Lett.*, vol. 16, pp, 540–542, Oct. 2006.

[6] J. Bonache, I. Gil, J. García-García, F. Martín, "Novel Microstrip Band Pass Filters Based on Complementary Split Rings Resonators", *IEEE Trans. Microw. Theory Techn.*, vol. 54, pp. 265-271, Jan. 2006.

[7] J. Bonache, G. Sisó, M. Gil, A. Iniesta, J. García-Rincón and F. Martín, "Application of composite right/left handed (CRLH) transmission lines based on complementary split ring resonators (CSRRs) to the design of dual band microwave components", *IEEE Microw. Wirel. Compon. Lett.*, vol. 18, pp. 524-526, Aug. 2008.

[8] G. Sisó, J. Bonache, M. Gil and F. Martín, "Application of resonant-type metamaterial transmission lines to the design of enhanced bandwidth components with compact dimensions", *Microw. Opt. Technol. Lett.*, vol. 50, pp. 127-134, Jan. 2008.

[9] S. Eggermont, I. Huynen, "Leaky wave radiation phenomena in metamaterial transmission lines based on complementary split ring resonators," *Microw. Opt. Techn. Lett.*, vol. 53, pp. 2025-2029, Sep. 2011.

[10] J.D. Baena, J. Bonache, F. Martín, R. Marqués, F. Falcone, T. Lopetegi, M.A.G. Laso, J. García, I Gil, M. Flores-Portillo and M. Sorolla, "Equivalent circuit models for split ring resonators and complementary split rings resonators coupled to planar transmission lines", *IEEE Trans. Microw. Theory Techn.*, vol. 53, pp. 1451-1461, Apr. 2005.

[11] J. Naqui, M. Durán-Sindreu, and F. Martín, "Modeling split ring resonator (SRR) and complementary split ring resonator (CSRR) loaded transmission lines exhibiting cross polarization effects", *IEEE Ant. Wirel. Propag. Lett.*, vol. 12, pp. 178-181, 2013.

[12] J. Naqui, M. Durán-Sindreu, A. Fernández-Prieto, F. Mesa, F. Medina, and F. Martín, "Multimode propagation and complex waves in CSRR-based transmission line metamaterials", *IEEE Ant. Wirel. Propag. Lett.*, vol. 11, pp. 1024-1027, 2012.

[13] L. Su, J. Naqui, J. Mata-Contreras and F. Martín "Modeling metamaterial transmission lines loaded with pairs of coupled split ring resonators", *IEEE Ant. Wirel. Propag. Lett.*, vol. 14, pp. 68-71, 2015.

[14] J-S. Hong and M.J. Lancaster, *Microstrip filters for RF/microwave applications*, John Wiley, New Jersey, 2001.

[15] J. Bonache, M. Gil, I. Gil, J. Garcia-García and F. Martín, "On the electrical characteristics of complementary metamaterial resonators", *IEEE Microw. Wirel. Compon. Lett.*, vol. 16, pp. 543.545, Oct. 2006.

MOTL16 (3)

"Coplanar waveguides loaded with symmetric and asymmetric multisection stepped impedance resonators: Modeling and potential applications"

Su, Lijuan, Jordi Naqui, Javier Mata-Contreras, and Ferran Martín

Microwave and Optical Technology Letters 58, no. 3 (2016): 722-726

Coplanar Waveguides Loaded with Symmetric and Asymmetric Multi-Section Stepped Impedance Resonators (SIRs): Modeling and Potential Applications

Lijuan Su, Jordi Naqui, Javier Mata, and Ferran Martín

CIMITEC, Departament d'Enginyeria Electrònica
Universitat Autònoma de Barcelona, 08193 Bellaterra (Barcelona), Spain
Corresponding author: Ferran.Martin@uab.es

Abstract

This paper is focused on the analysis and modeling of coplanar waveguide (CPW) transmission lines loaded with multi-section stepped impedance resonators (MS-SIRs), transversely etched on the back substrate side. The considered structure consists of a CPW loaded with a 5-section SIR (5S-SIR) with wide (capacitive) central and external sections cascaded with narrow (inductive) sections. The general case of a 5S-SIR with arbitrary lengths and widths of the different sections is considered. The structure is described by a pair of inductively coupled grounded series resonators coupled to the line through the capacitance of the central 5S-SIR section. If the structure is symmetric, the transmission coefficient exhibits a single transmission zero. Hence, these structures can be used as notch filters exhibiting wide bandwidths, provided the inductance of the 5S-SIR can be made small, and the capacitance can be enhanced by virtue of the broadside coupling. However, if symmetry is broken, two notches separated a distance that depends on the level of asymmetry and inductive coupling appear. Therefore, these structures are also useful for the implementation of differential sensors and comparators. The proposed model is validated through parameter extraction and experiment, and a proof-of-concept of a comparator is reported.

KEYWORDS: Microwave sensors, circuit modeling, stepped impedance resonator (SIR), CPW technology.

1. Introduction

Stepped impedance resonators (SIRs) are electrically small resonators useful for the implementation of planar filters [1-3]. Coupled to planar transmission lines, such resonators have found applications in the design of elliptic lowpass filters [4], or frequency-domain (spectral signature) barcodes [5], due to the transmission zeros that appear at their fundamental resonance frequency. Although SIRs are usually implemented as metallic resonators, the complementary counterparts (slotted SIRs, also called dumbbell defected ground structures) are also of interest for microwave circuit design [6].

In this paper, we study in detail the electromagnetic behavior of CPW transmission lines loaded with multi-section stepped impedance resonators (MS-SIRs), transversely etched on the back substrate side, and we propose a lumped element equivalent circuit model of the structure. Such model accounts not only for the different semi-lumped planar (inductive and capacitive) elements of the MS-SIR, but also for the main coupling mechanisms between the line and the resonator and between the resonator elements, essential for an accurate model. The specific MS-SIR considered is a 5-section resonator (5S-SIR) with wide (capacitive) central and external sections cascaded with narrow (inductive) sections. The central section is placed below the central strip of the CPW transmission line, whereas the external sections are allocated below the ground planes. This provides a large resonator capacitance that makes the particle electrically small. The inductive sections are etched beneath the slot region. All the sections must be electrically short for a correct description of the structure by means of a lumped element circuit.

In the modeling, the general case of a 5S-SIR with arbitrary lengths and widths of the different sections is considered. Although for the application of these structures as wideband notch filters, or as part of elliptic filters, there is no reason to choose asymmetric 5S-SIRs (note that by using symmetric resonators the slot mode is prevented and air bridges or backside strips and vias are avoided), the fact that disruption of symmetry in the 5S-SIR gives rise to two transmission zero frequencies (frequency splitting [7]), opens the path to the implementation of differential sensors or comparators (e.g., for analysis of biological cells and tissues, defects or abnormalities in materials, etc. [8]). These sensors based on frequency splitting are robust against variable environmental conditions. Hence, the modeling of the 5S-SIR-loaded CPW with asymmetric resonators is of interest. To the best authors' knowledge, it is the first time that a lumped element circuit model describing a CPW transmission line loaded with an arbitrary 5S-SIR, including inductive coupling between resonator elements (the two 5S-SIR inductances), is proposed. Nevertheless, a microstrip structure loaded with pairs of coupled SIRs was recently investigated as a potential candidate for differential sensing [8], and a prototype sensor (implemented in CPW technology) operative at Q-band was presented. As compared to the structures of that work, the 5S-SIR-loaded CPW structure presented in this paper exhibits more design flexibility as long as it is described by a circuit model where the resonant element (5S-SIR) is electrically coupled to the line (by contrast, in the structure reported in [8] the pair of SIRs are in direct contact with the line).

This work, dedicated to the analysis and modeling of CPWs loaded with MS-SIRs, represents a clear progress on the topic of transmission lines loaded with resonant elements, and points out the potential of these structures as notch filters (symmetric case) and microwave sensors and comparators based on frequency splitting (asymmetric case).

2. Topology and equivalent circuit model

In this section, the 5S-SIR-loaded CPW topology and its lumped element equivalent circuit model are presented, and the resonance frequencies (transmission zeros) for the general asymmetric case are calculated analytically. Model validation through parameter extraction and comparison to electromagnetically simulated and measured responses is left for next sections.

Fig. 1(a) shows the typical topology of a CPW loaded with a 5S-SIR. The equivalent circuit model is depicted in Fig. 1(b), where L and C are the inductance and capacitance of the CPW line section, and L_i and C_i (with i = 1,2) describe the inductances and capacitances of the narrow (inductive) and external sections, respectively, of the 5S-SIR. Two coupling mechanisms are considered: (i) electric coupling between the 5S-SIR and the line, through C_c (the broadside capacitance between the central strip of the CPW and the central section of the 5S-SIR), and (ii) magnetic coupling between the two inductances of the resonator, through M (such coupling is negative because the currents in the inductances flow in opposite directions). Losses are not considered in the model.

Although for sensing purposes the structure should be symmetric and symmetry disruption would modify the element values of the equivalent circuit, we directly consider the more general case of a circuit model corresponding to an arbitrary asymmetric structure. Note that the considered structure is electrically short and hence it is reasonable to assume, to a first order approximation, that the slot mode is not generated (the ports in the electromagnetic simulation and the connectors in the measurement act as air bridges effectively connecting the two ground plane regions).

From the analysis of the circuit model of Fig. 1(b), it follows that the transmission zeros, given by those frequencies that null the reactance of the shunt branch, are:

$$\omega_{\pm}^2 = \frac{A \pm \sqrt{B}}{D} \tag{1}$$

with

$$A = C_1 C_2 (L_1 + L_2 - 2M) + C_c (L_1 C_1 + L_2 C_2)$$

$$B = C_1^2 C_2^2 (L_1 + L_2 - 2M)^2 + C_c^2 (L_1 C_1 - L_2 C_2)^2 + 2C_c C_1 C_2 \times$$

$$\left\{ L_1 C_1 (L_1 - L_2 - 2M) + L_2 C_2 (L_2 - L_1 - 2M) + 2M^2 (C_1 + C_2 + C_c) \right\}$$

$$D = 2C_c C_1 C_2 (L_1 L_2 - M^2)$$

If the structure is symmetric (i.e., $L_1 = L_2 \equiv L_r$ and $C_1 = C_2 \equiv C_r$), the mathematical solutions of (1) are:

$$\omega_{+} = \frac{1}{\sqrt{(L_r + M) \cdot \dfrac{C_c C_r}{C_c + 2C_r}}} \tag{2a}$$

$$\omega_{-} = \frac{1}{\sqrt{(L_r - M) \cdot C_r}} \tag{2b}$$

However, ω_{-} is not actually a physical solution since it nulls the denominator of the reactance. Thus, the mutual coupling between the two inductors of two SIRs has the effect of increasing the notch frequency (symmetric case).

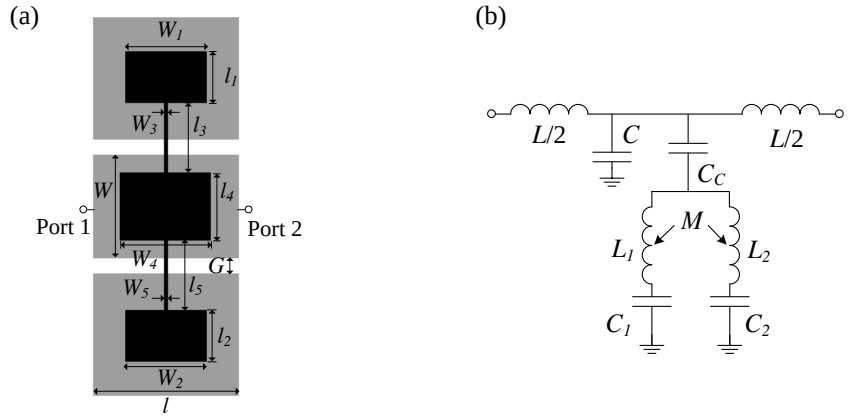

Fig. 1. (a) CPW loaded with a 5S-SIRs and (b) circuit model. Relevant dimensions are indicated.

3. Model validation through parameter extraction

Let us now demonstrate the validity of the proposed circuit model by providing a method to extract the parameters of that model and by comparison of the lossless electromagnetic simulation with the circuit simulation of the model with the extracted parameters. As a case example we will consider a set of three 5S-SIR-loaded CPWs, one symmetric and the other two asymmetric, where the two asymmetric structures are derived from the symmetric one by increasing or decreasing the area of one of the external patch capacitors, while the other external patch capacitors for these two asymmetric structures keep the same dimensions as in the symmetric one. The corresponding layouts are depicted in Fig. 2 (dimensions and substrate parameters are indicated in the caption).

Due to the large number of elements in the circuit model, parameter extraction is a multi-step process. First of all, one of the capacitances and inductances of the 5S-SIR (one half) is removed, and the resulting central patch is short circuited to ground by means of vias, as indicated in Fig. 3(a). The corresponding model, indicated in Fig. 3(b), has a reduced number of parameters (i.e., four) that can be inferred by means of the following four conditions. The first one is the transmission zero frequency, given by:

$$\omega_z = 2\pi f_z = \frac{1}{\sqrt{L_r C_r}} \tag{3}$$

A pair of additional conditions are derived from the frequency that opens the shunt branch, i.e.,

$$\omega_0 = 2\pi f_0 = \frac{1}{\sqrt{L_r \cdot \dfrac{CC_r}{C+C}}} \tag{4}$$

which can be inferred from the intercept of S_{11} with the unit resistance circle in Smith chart. From this intercept, the reactance of the series branch, χ_s, can be directly obtained, and hence L, i.e.,

$$\chi_s = L\omega_0 \tag{5}$$

Finally, the fourth condition is given by the frequency where the phase of S_{21} is -90^{o}. At this frequency, $\omega_{-\pi/2}$, the series and shunt reactances verify [9]:

$$\chi_s(\omega_{-\pi/2}) = -\chi_p(\omega_{-\pi/2}) \tag{6}$$

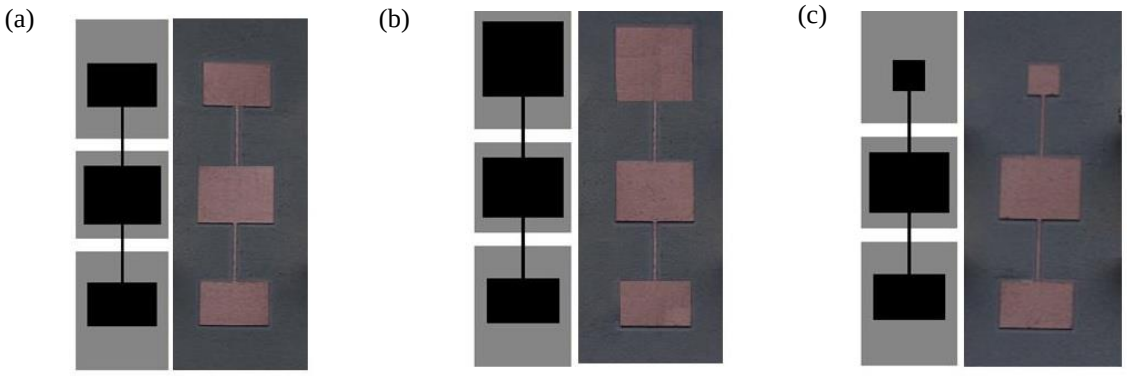

Fig. 2. Considered 5S-SIR-loaded CPWs: (a) symmetric; (b) asymmetric with one external patch capacitor larger; (c) asymmetric with one external patch capacitor smaller. Dimensions are (in reference to Fig. 1): for CPW lines: l = 6 mm, W = 6 mm and G= 0.96 mm, corresponding to 50 Ω. For 5S-SIRs: (a) $W_1 = W_2 = 4.5$ mm, $l_1 = l_2 = 3$ mm, $W_3 = W_5 = 0.2$ mm, $l_3 = l_5 = 4$ mm, $W_4 = 5$ mm, $l_4 = 4$ mm. For (b) $W_1 = l_1 = 5$ mm and (c) $W_1 = l_1 = 2$ mm, with the other dimensions the same as in (a). The considered substrate (*Rogers RO3010*) has thickness of h = 0.635 mm and dielectric constant of $\varepsilon_r = 11.2$.

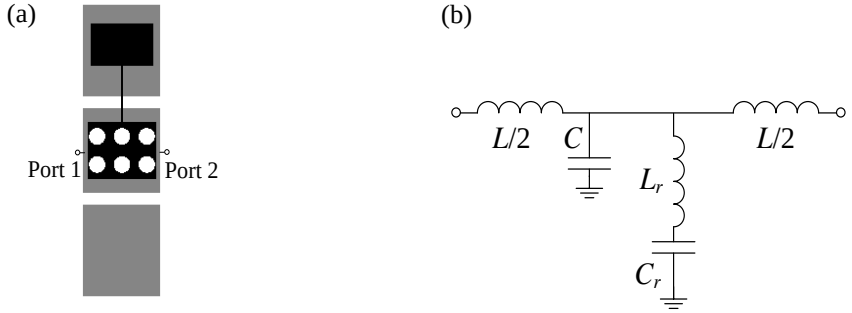

Fig. 3. Layout and circuit model of the symmetric structure of Fig. 2(a) after removing one of the halves of the 5S-SIR and adding vias to the resulting central patch (a), and equivalent circuit model (b).

Using (3)-(6), the parameters of the model of Fig. 3(b) are extracted, namely, L = 3.49 nH, C = 1.21 pF, L_r = 4.20 nH, C_r = 2.65 pF. Once the inductance and capacitance of the halved 5S-SIR and the line parameters are known, the next step is to determine the mutual coupling between the two inductors of the SIRs, M, and the capacitance of the central patch in Fig. 2(a). For the extraction of M, we add vias in the central patch capacitor and short it to ground (see Fig. 4). Then, from this model we can determine M by curve fitting, i.e., M = −1.08 nH. Finally, we remove the vias in the central patch capacitor, the whole symmetric structure is simulated, and C_c, the remaining parameter, is determined by curve fitting, i.e., C_c = 3.62 pF. The comparison of the electromagnetic simulation (using *Keysight Technologies*) with the circuit simulation of the symmetric structure is shown in Fig. 5 (the measurement data is included as well), where good agreement can be appreciated, pointing out the validity of the proposed model.

To determine the modified patch capacitances of the two considered asymmetric cases, the procedure is as simple as removing the opposite half of the 5S-SIR. From the resulting transmission zero frequency, the capacitance and inductance of the halved 5S-SIR can be obtained. Then, by simulating the whole structure with and without vias respectively, the mutual inductance M and the middle patch capacitance C_c can be inferred.

By means of this procedure, the small external patch capacitor and narrow inductive section of 5S-SIR have been found to be 0.97 pF and 4.30, and the big external patch capacitor and narrow inductive section of 5S-SIR have been found to be 4.53 pF and 4.26 nH. The mutual inductances for these two asymmetric cases, i.e., in Fig. 2 (b) and Fig. 2(c), have been found to be −1.16 nH and −1.10 nH respectively, i.e., similar values, and also similar to the value corresponding to the symmetric structure. This indicates that *M* is scarcely dependent on the dimensions of the patch capacitances of the 5S-SIR, as expected. The agreement among the electromagnetic simulation, circuit simulation and measurement for the two asymmetric cases (Figs. 6 and 7) is reasonable.

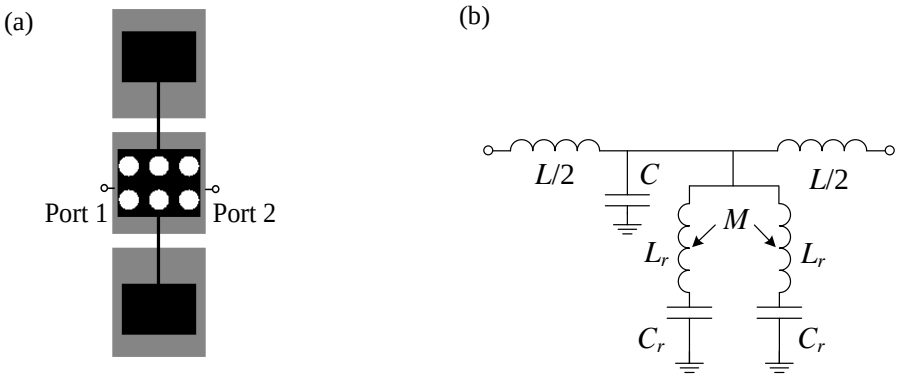

Fig. 4. Layout and circuit model of the symmetric structure of Fig. 2(a) after adding vias to the central patch of the 5S-SIR (a), and equivalent circuit model (b).

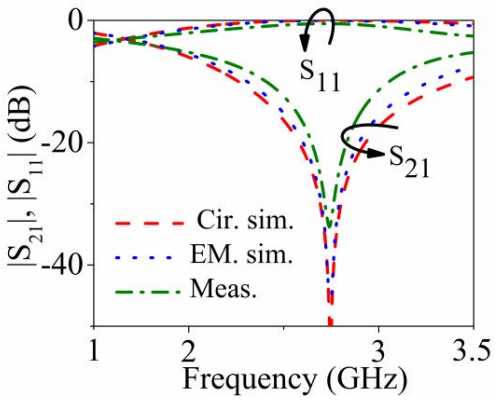

Fig. 5. Electromagnetic simulation, circuit simulation and measurement response for the symmetric structure of Fig.2(a).

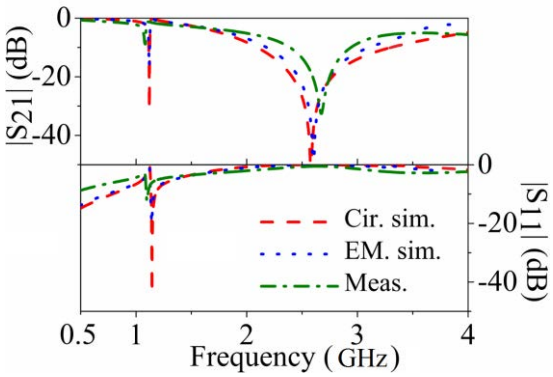

Fig. 6. Electromagnetic simulation, circuit simulation and measurement response for the asymmetric structure of Fig.2(b).

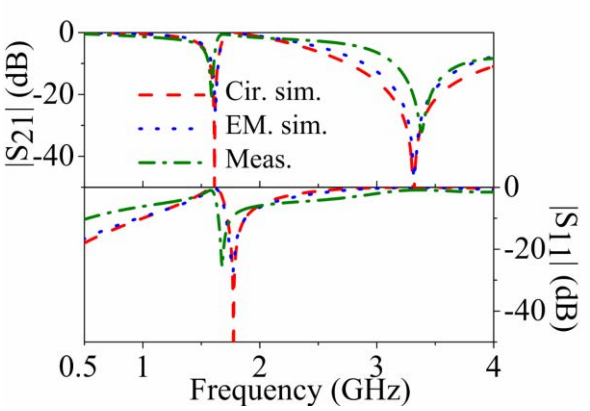

Fig. 7. Electromagnetic simulation, circuit simulation and measurement response for the asymmetric structure of Fig.2(c).

4. Experimental validation

The structures of Fig. 2 have been fabricated by means of a milling machine *LPKF HF100*, and have been measured by means of the *Keysight N5221A* vector network analyzer. The measured responses are depicted in Figs. 5, 6 and 7, where it can be appreciated that the asymmetry splits and modifies the position of the main transmission zero, shifting it to the left and right, respectively, for the big and small patch capacitances, in agreement with the theory. There is some shift between the simulated responses and the measured responses, which is attributed to fabrication related tolerances. Nevertheless, it is experimentally verified that the asymmetry produces two notches, and the structure can be used for sensing purposes, as demonstrated in the next section.

5. Demonstration of the sensing principle

A proof-of-concept of the sensing principle is reported in this section. To this end, we have loaded the symmetric structure of Fig. 2(a) with a dielectric load (consisting of a small piece of *Rogers RO3010* substrate with the copper removed from both substrate sides) placed on top of one of the patch capacitances. The measured response, shown in Fig. 8, exhibits two notches, indicative of the asymmetric loading. Then, we have repeated the experiment by using the same piece of substrate but keeping the metal layers (metallic loading). The measured response is also included in Fig. 8, where it can be seen that the depth of the first notch is superior (as compared to dielectric loading), since the structure is more sensitive to the effects of a metallic layer placed on top of one of the patch capacitances.

6. Conclusion

In conclusion, the modeling of CPW transmission lines loaded with multi-section (specifically 5-section) SIRs of arbitrary dimensions (including thus asymmetric structures) has been carried out for the first time. The model takes into account the negative magnetic coupling between the two inductive elements of the 5S-SIR. A parameter extraction procedure, able to provide the element parameters of the proposed circuit model, considering both symmetric and asymmetric structures, has been reported and explained in detail. The validity of the model has been verified by comparing the electromagnetic responses of the considered structures with circuit simulations. Furthermore, we have validated the model through experiment. Finally, the sensing

principle has been demonstrated by asymmetrically loading a symmetric 5S-SIR-loaded CPW with dielectric and metallic loads.

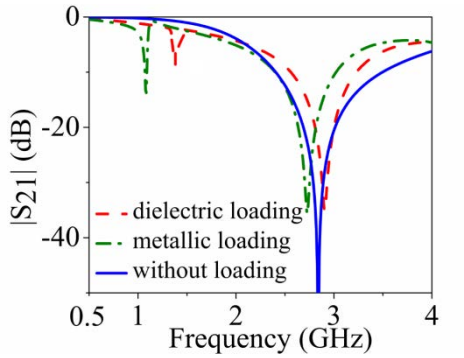

Fig. 8. Measured responses of the structure of Fig. 2(a) with asymmetric dielectric loading and metallic loading.

Acknowledgements

This work has been supported by MINECO (Spain) under project TEC2013-40600-R, by AGAUR-Generalitat de Catalunya under project 2014SGR-157, and by FEDER funds. Ferran Martín is in debt to Institució Catalana de Recerca i Estudis Avançats (ICREA) for supporting his work. Lijuan Su thanks China Scholarship Council (CSC) for supporting her work in UAB through the grant No. 201306950011.

References

[1] M. Makimoto and S. Yamashita, "Compact bandpass filters using stepped impedance resonators", *Proc. IEEE*, vol. 67, pp. 16-19, Jan. 1979.

[2] H. Zhang and K.J. Chen, "Miniaturized coplanar waveguide bandpass filters using multisection stepped-impedance resonators", *IEEE Trans. Microw. Theory. Techn.*, vol. 54, pp. 1090-1095, March 2006.

[3] J. Shi, and Q. Xue, "Novel balanced dual-band bandpass filter using coupled stepped-impedance resonators," *IEEE Microw. Wireless Compon. Lett.*, vol. 20, pp. 19-21, Jan. 2010.

[4] M. Durán-Sindreu, J. Bonache, F. Martín, "Compact elliptic-function coplanar waveguide low-pass filters using backside metallic patterns", *IEEE Microw. Wireless Compon. Lett.*, vol. 20, pp. 601-603, Nov. 2010.

[5] J. Naqui, M. Durán-Sindreu and F. Martín, "On the symmetry properties of coplanar waveguides loaded with symmetric resonators: analysis and potential applications", *IEEE MTT-S Int. Microwave Symp.*, June 2012, Montreal (Canada).

[6] D. Ahn, J-S. Park, C-S. Kim, J. Kim, Y. Qian, T. Itoh, "A design of the low-pass filter using the novel microstrip defected ground structure", *IEEE Trans. Microw. Theory Techn.*, vol. 49, pp. 86-93, Jan. 2001.

[7] A. K. Horestani, J. Naqui, Z. Shaterian, D. Abbott, C. Fumeaux, and F. Martín, "Two-dimensional alignment and displacement sensor based on movable broadside-coupled split ring resonators", *Sensors and Actuators A*, vol. 210, pp. 18-24, April 2014.

[8] J. Naqui, C. Damm, A. Wiens, R. Jakoby, L. Su, F. Martín, "Transmission lines loaded with pairs of magnetically coupled stepped impedance resonators (SIRs): modeling and application to microwave sensors", *IEEE MTT-S Int. Microwave Symp.*, June 2014, Tampa, FL (USA).

[9] J. Bonache, M. Gil, I. Gil, J. Garcia-García and F. Martín, "On the electrical characteristics of complementary metamaterial resonators", *IEEE Microw. Wireless Compon. Lett.*, vol. 16, pp. 543.545, Oct. 2006.

TMTT16 December

"Splitter/combiner microstrip sections loaded with pairs of complementary split ring resonators (CSRRs): modeling and optimization for differential sensing applications."

Su, Lijuan, Javier Mata-Contreras, Paris Vélez, and Ferran Martín

IEEE Transactions on Microwave Theory and Techniques 64, no. 12 (2016): 4362-4370

Splitter/Combiner Microstrip Sections Loaded with Pairs of Complementary Split Ring Resonators (CSRRs): Modeling and Optimization for Differential Sensing Applications

Lijuan Su, *Student Member IEEE*, Javier Mata-Contreras, Paris Vélez, *Member IEEE*, and Ferran Martín, *Fellow IEEE*

***Abstract*— This paper focuses on the analysis of splitter/combiner microstrip sections where each branch is loaded with a complementary split ring resonator (CSRR). The distance between CSRRs is high, and hence their coupling can be neglected. If the structure exhibits perfect symmetry with regard to the axial plane, a single transmission zero (notch) at the fundamental resonance of the CSRR, arises. Conversely, two notches (i.e., frequency splitting) appear if symmetry is disrupted, and their positions are determined not only by the characteristics of the CSRRs but also by the length of the splitter/combiner sections. A model that includes lumped elements (accounting for the CSRR-loaded line sections) and distributed components (corresponding to the transmission lines) is proposed and used to infer the position of the transmission zeros. Frequency splitting is useful for the implementation of differential sensors and comparators based on symmetry disruption. Using the model, the length of the splitter/combiner sections necessary to optimize the sensitivity of the structures as sensing elements is determined. Parameter extraction and comparison to electromagnetic simulations and measurements in several symmetric and asymmetric structures is used to validate the model. Finally, a prototype device sensor/comparator based on the proposed CSRR-loaded splitter/combiner microstrip sections is presented.**

***Index Terms*– Complementary split ring resonators (CSRRs), microstrip technology, circuit modeling, microwave sensors.**

I. INTRODUCTION

Many electromagnetic sensors are based on the variation of the resonance frequency, phase or quality factor of resonant elements, caused by the physical variable of interest (measurand) [1]-[18]. Among them, microwave sensors consisting of transmission lines loaded with planar resonators have been the subject of an intensive research activity in the last years [8],[9],[12],[18]. These structures are not exempt from a general drawback of sensors that limits their performance: cross sensitivity. Namely, the electrical variables are not only sensitive to the measurand, but also to other physical quantities. For instance, in resonance-based permittivity sensors, variations in temperature or moisture (environmental factors) may cause unintentional frequency shifts [15],[19], which in turn may produce systematic sensing errors. One solution to partially alleviate the effects of cross sensitivity, particularly those derived from changing environmental conditions, is differential sensing. Differential sensors are robust against variations in the ambient factors since such changes are seen as common-mode perturbations [16]-[18],[20],[21].

Differential sensors are typically implemented by means of two sensing elements, e.g., two loaded transmission lines, one of them acting as reference [16]. Nevertheless, it is possible to implement sensors scarcely sensitive to environmental factors by means of a single sensing element [22]-[24]. This can be achieved, for instance, by symmetrically loading a transmission line with a planar symmetric resonator [22],[25]-[32]. The sensing principle of these sensors is based on symmetry disruption. As pointed out in [22]-[24], by symmetrically loading a line with a resonator exhibiting symmetry plane of different electromagnetic nature (at the fundamental resonance) from the symmetry plane of the line (typically a magnetic wall, at least in microstrip or coplanar waveguide technology), the structure is transparent since coupling is prevented under these conditions. However, by truncating the symmetry, either electric or magnetic coupling (or both) between the line and the resonator may arise, with the result of a frequency notch (transmission zero) at the fundamental resonance frequency. Moreover, the magnitude of the notch (related to the coupling level) is determined by the level of asymmetry. Note, however, that in these coupling-modulated resonance sensors [24], environmental conditions do not produce misalignment between the line and the resonator or any other type of symmetry disruption. Therefore, these sensors are similar to differential sensors in terms of robustness against environmental factors.

Another type of sensors also exhibiting small cross sensitivity to environmental conditions is based on the symmetric loading (or coupling) of a transmission line with a pair of resonant elements [33]-[38]. Such sensors, referred to as frequency-splitting sensors [24], are true differential sensors with two sensing elements (the resonators). In this case, the sensing principle is also related to symmetry, but different than the one for coupling-modulated resonance sensors. In brief, under perfect symmetry, the structure exhibits a single transmission zero (provided the resonant elements are coupled to the line or in contact with it); however, by truncating symmetry, e.g., by loading the

This paper is an expanded version from the 2016 International Microwave Conference, San Francisco, CA, May 22-27, 2016. This work was supported by MINECO-Spain (project TEC2013-40600-R), *Generalitat de Catalunya* (project 2014SGR-157), *Institució Catalana de Recerca i Estudis Avançats* (who awarded Ferran Martín), and by FEDER funds. Lijuan Su acknowledges the China Scholarship Council (CSC) for the grant 201306950011.

The authors are with GEMMA/CIMITEC, Departament d'Enginyeria Electrònica, Universitat Autònoma de Barcelona, 08193 Bellaterra, Spain. E-mail: Ferran.Martin@uab.es.

resonators with unbalanced dielectric loads, two notches arise, and the frequency difference depends on the level of asymmetry. One limitation of these frequency-splitting sensors may be caused by the possible coupling between resonant elements (unavoidable if such elements are close enough). Such coupling, if present, severely degrades the sensitivity for small perturbations [34]. Inter-resonator coupling can be prevented by considering two resonant elements separated enough, each one coupled to (or in contact with) a different transmission line in a splitter/combiner configuration as the one proposed in [39] (an alternative is a cascaded configuration, as reported in [40], where the authors consider stepped impedance resonators). However, in this case, the sensitivity is degraded by the length of the lines, and sensing, also related to symmetry disruption and based on the separation between transmission zeros (the output variable), is influenced by the interference between the pair of resonator-loaded lines. In other words, the transmission zeros are not only dictated by the intrinsic resonance frequency of the resonators, but also by the length of the lines, and such transmission zeros occur, in general, at those frequencies where the signals at the end of each loaded line exactly cancel.

This paper is focused on the analysis of frequency-splitting sensors based on splitter/combiner microstrip sections loaded with complementary split ring resonators (CSRRs), first presented in [39]. The main aim is to optimize the sensitivity to unbalanced loads or, more specifically, to obtain the necessary conditions (length of the splitter/combiner sections) to achieve such optimization. The analysis, based on a mixed distributed/lumped model of the considered structures is presented in Section II. This section, supported by the two appendixes, constitutes the main contribution of the paper, as compared to [39]. It is clearly pointed out that one of the transmission zeros may be given by the resonance of the CSRRs, if a suitable electrical length between the position of the CSRR and the T junctions is chosen. Validation of the model, including sensitivity optimization, is discussed in Section III, where it is clearly pointed out that sensitivity is optimized if such electrical length is selected. In Section IV, a prototype device acting as a differential sensor and comparator, i.e., a device able to detect differences between a sample under test (SUT) and a reference sample and useful for differential measurements of dielectric constant, is presented (this includes measurement of the dielectric constant of a known substrate –to demonstrate the potential of the approach– and estimation of the effective dielectric constant of a sample with defects). Finally, the main conclusions are highlighted in section V.

II. TOPOLOGY, CIRCUIT MODEL AND ANALYSIS

The typical topology (including relevant dimensions) of the considered power splitter/combiner microstrip structure with CSRRs etched in the ground plane is shown in Fig. 1(a). Each branch consists of a 50 Ω line loaded with a CSRR, etched in the ground plane. To match the structure to the 50 Ω ports, impedance inverters implemented by means of 35.35 Ω quarter wavelength transmission line sections are cascaded between the ports and the T-junctions. The circuit schematic, with distributed and lumped elements, is shown in Fig. 1(b). An asymmetric structure is considered as general case, but asymmetry refers to the dimensions of the CSRR, rather than the transmission line sections. The lumped elements account for the CSRR-loaded microstrip line sections. Thus, L_u (L_l) and C_u (C_l) model the inductance and capacitance of the microstrip line, respectively, above the CSRR in the upper (lower) parallel branch, and the resonators (CSRRs) are accounted for by the tanks L_{Cu}-C_{Cu} (upper CSRR) and L_{Cl}-C_{Cl} (lower CSRR) [41]. The distributed elements account for the transmission line sections which are not located on top of the CSRRs. The line impedance Z_i and the electrical length θ_i (with i = 1,2) define such line sections.

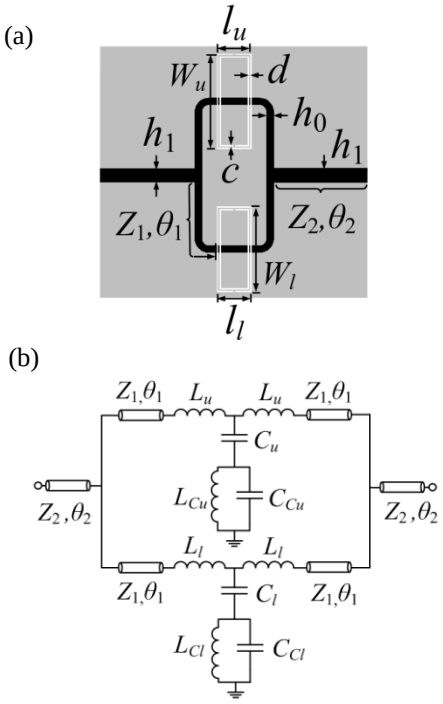

Fig. 1. (a) Typical topology of the power splitter/combiner loaded with two CSRRs and (b) circuit schematic.

Note that to predict the transmission zero frequencies through the schematic of Fig. 1(b), the input and output transmission line sections can be neglected (such sections do not have influence on the position of the notches). The two-port network then contains two parallel branches. Thus, for analysis purposes, it is convenient to deal with the admittance matrix. Let us now center on the two-port network of Fig. 2, where the output port is terminated with the reference impedance Z_0. A transmission zero (i.e., total reflection) results if the current at the output port is zero (I_2 = 0) and $I_1 \neq 0$. From the admittance matrix equation, considering the indicated load at port 2, the following results are obtained:

$$I_1 = Y_{11}V_1 + Y_{12}Z_0 I_2 \quad (1a)$$

$$I_2 = Y_{21}V_1 + Y_{22}Z_0 I_2 \quad (1b)$$

and from these equations, I_2 can be isolated, that is

$$I_2 = \frac{Y_{21}}{Y_{11}(1-Y_{22}Z_0)+Y_{21}Y_{12}Z_0} I_1 \quad (2)$$

Therefore, $Y_{21} = 0$ with the denominator of (2) different than zero), or $Y_{11} = \infty$ with $Y_{21} \neq \infty$ are sufficient conditions to obtain a transmission zero. It follows from reciprocity that $Y_{12} = 0$, or $Y_{22} = \infty$ are also sufficient conditions to obtain total reflection. Indeed, since the considered structure is symmetric with regard to the mid-plane between the input and output ports, the transmission zero frequencies should simply satisfy $Y_{21} = Y_{12} = 0$, and/or $Y_{11} = Y_{22} = \infty$.

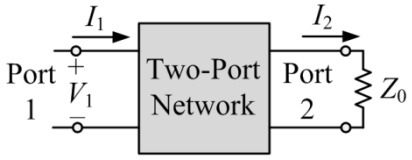

Fig. 2. Two-port network loaded with the impedance Z_0 at the output port.

Let us distinguish the anti-diagonal elements of the admittance matrices of the upper and lower branches of the structure of Fig. 1 by the sub-indexes *u* and *l*. Thus, Y_{21} is given by

$$Y_{21} = Y_{21,u} + Y_{21,l} \tag{3}$$

and $Y_{21,u}$ and $Y_{21,l}$ can be determined by first obtaining the *ABCD* matrix of each branch. This is given by the matrix product of the matrices corresponding to the three cascaded two-port networks, that is, the pair of transmission line sections with characteristic impedance Z_1, and the sandwiched lumped two-port network. From the *ABCD* matrices for each branch, the elements of the right-hand side in (3) are given by $Y_{21,u} = -1/B_u$ and $Y_{21,l} = -1/B_l$, where B_u and B_l are the *B* elements of the *ABCD* matrix for the upper and lower branches, respectively [42]. Thus, the transmission zeros related to $Y_{21} = Y_{12} = 0$ are given by:

$$\frac{1}{B_u} + \frac{1}{B_l} = 0 \tag{4}$$

with

$$B_u = j(Z_1 \sin 2\theta_1 + 2\omega L_u \cos^2\theta_1) + j\frac{\left(Z_1 \sin\theta_1 + \omega L_u \cos\theta_1\right)^2}{\dfrac{\omega L_{Cu}}{1-\dfrac{\omega^2}{\omega_{Cu}^2}} - \dfrac{1}{\omega C_u}} \tag{5a}$$

$$B_l = j(Z_1 \sin 2\theta_1 + 2\omega L_l \cos^2\theta_1) + j\frac{\left(Z_1 \sin\theta_1 + \omega L_l \cos\theta_1\right)^2}{\dfrac{\omega L_{Cl}}{1-\dfrac{\omega^2}{\omega_{Cl}^2}} - \dfrac{1}{\omega C_l}} \tag{5b}$$

with $\omega_{Cu} = (L_{Cu} \cdot C_{Cu})^{-1/2}$ and $\omega_{Cl} = (L_{Cl} \cdot C_{Cl})^{-1/2}$. The general solution of (4) is not simple. However, it is possible to obtain the pair of transmission zeros numerically. Also, we can obtain the influence of the element values on the position of such transmission zeros. Particularly, the effects of the asymmetry produced by the CSRRs can be studied. If two identical CSRRs are considered, (4) gives a unique solution (transmission zero) with angular frequency given by

$$\omega_z = \frac{1}{\sqrt{L_r (C_r + C)}} \tag{6}$$

where $L_{Cu} = L_{Cl} = L_r$, $C_{Cu} = C_{Cl} = C_r$, and $C_u = C_l = C$. Note that (6) is the frequency that shorts to ground the reactance of the identical shunt branches of the lumped two-port T-networks of Fig. 1(b), as expected.

Except for the symmetric case, where the single transmission zero is simply given by the characteristics of the resonators and their coupling to the line, the two transmission zeros of the general case are consequence of an interfering phenomenon between the parallel CSRR-loaded line sections.

Let us now consider the alternative situation providing transmission zeros, that is, $Y_{11} = Y_{22} = \infty$ with $Y_{21} = Y_{12} \neq \infty$. In this case, we can analyze each branch independently. The reason is that $Y_{11,u} = \infty$ and/or $Y_{11,l} = \infty$ (where the sub-indexes *u* and *l* have been defined before) suffices to guarantee that $Y_{11} = Y_{11,u} + Y_{11,l} = \infty$. Therefore, let us calculate, e.g., $Y_{11,u}$. This parameter can be inferred from the elements of the *ABCD* matrix as $Y_{11,u} = D_u/B_u$ [42]. Even though B_u has been calculated before, this element can be simplified by designating by Y_u the admittance of the shunt branch (formed by C_u, L_{cu}, C_{cu}). We can proceed similarly in order to calculate D_u. Once B_u and D_u have been inferred, $Y_{11,u}$ can be expressed as a function of Y_u, i.e.,

$$Y_{11,u} = \frac{\cos 2\theta_1 - \dfrac{\omega L_u}{Z_1}\sin 2\theta_1 + jY_u\left(\omega L_u \cos 2\theta_1 + Z_1 \dfrac{\sin 2\theta_1}{2} - \omega^2 L_u^2 \dfrac{\sin 2\theta_1}{2Z_1}\right)}{j\left(2\omega L_u \cos^2\theta_1 + Z_1 \sin 2\theta_1\right) - Y_u\left(Z_1 \sin\theta_1 + \omega L_u \cos\theta_1\right)^2} \tag{7}$$

Inspection of (7) reveals that $Y_u = \infty$ (corresponding to a short circuit) may provide $Y_{11,u} = \infty$. However, this is not a sufficient condition. To verify this, let us calculate $Y_{11,u}$ in the limit when $Y_u \to \infty$. The result is as follows:

$$Y_{11,u} = -j\frac{\left(\omega L_u \cos 2\theta_1 + Z_1 \dfrac{\sin 2\theta_1}{2} - \omega^2 L_u^2 \dfrac{\sin 2\theta_1}{2Z_1}\right)}{\left(Z_1 \sin\theta_1 + \omega L_u \cos\theta_1\right)^2} \tag{8}$$

and this result is in general finite, unless the following condition is satisfied

$$Z_1 \sin\theta_1 + \omega_0 L_u \cos\theta_1 = 0 \tag{9}$$

In (9), ω_0 is the frequency where $Y_u = \infty$. From (9), the following result is inferred

$$\theta_1 = \arctan\left(-\frac{\omega_0 L_u}{Z_1}\right) = \pi - \arctan\left(\frac{\omega_0 L_u}{Z_1}\right) \equiv \theta_{1,\infty} \tag{10}$$

(10) gives the electrical length at ω_0 that is necessary to obtain $Y_{11,u} = \infty$ and hence $Y_{11} = \infty$. However, note that in view of (2), $Y_{11} = \infty$ does not guarantee $I_2 = 0$, as required to obtain a transmission zero. We can however express (2), for the upper branch, in terms of the *ABCD* matrix as follows:

$$I_2 = \frac{B_u}{D_u B_u - D_u^2 Z_0 + Z_0} I_1 \tag{11}$$

With the condition (9), $B_u = 0$ and $D \neq 1$ (see Appendix I). Therefore, it is demonstrated that $Y_u = \infty$ and (9) are sufficient conditions to obtain a transmission zero.

The physical interpretation of this transmission zero is very clear. The solution of θ_1 provided by (9) corresponds to the electrical length of the line necessary to translate the shunt branch to the input or output port. Note that if $L_u = 0$, such electrical length is simply $\theta_1 = \pi$, as expected. Thus, if the frequency that nulls the reactance of the shunt branch satisfies (9), a short is present in the input and output ports of the upper branch, hence providing a transmission zero to the whole structure. Note that such transmission zero frequency does not depend on the characteristics of the other (lower) branch, and hence it is not associated to an interfering phenomenon, contrary to the other transmission zero (assuming asymmetry) which is still related to the destructive interference of the two branches.

It is interesting to mention that since condition (9) translates to the input and output ports the shunt reactance, such condition should also be derived by forcing the electrical length of the whole upper branch to be 2π (by excluding the shunt reactance and by considering this branch as the unit cell of a periodic structure). This is demonstrated in Appendix II.

III. Model Validation and Optimization for Sensing Purposes

Model validation has been carried out by comparing lossless electromagnetic simulations of different structures with circuit simulations. To this end, it has been necessary to extract the circuit elements describing the transmission line sections loaded with CSRRs following the procedure described in [43]. For that purpose, we have first independently simulated the considered CSRR-loaded microstrip sections.

We have first considered the symmetric CSRR-loaded splitter/combiner section as depicted in Fig. 1(a). The frequency response (magnitude of the transmission coefficient) inferred from electromagnetic simulation, using the *Keysight Momentum* commercial software, is depicted in Fig. 3(a). This figure also depicts the response resulting from circuit simulation by using the extracted element values, indicated in the caption. Then, we have considered two asymmetric structures where we have modified only the dimensions of the lower CSRR, specifically W_l, by increasing or decreasing ΔW_l, leaving the upper CSRR unaltered. In one case this dimension has been increased and in the other one it has been decreased. The responses (electromagnetic and circuit simulations) are depicted in Figs. 3(b) and (c), where the corresponding sets of extracted parameters are indicated (see caption). In all the cases, there is very good agreement between the electromagnetic and circuit simulations, pointing out the validity of the model. Fig. 3 also includes the measured responses, inferred from the *Agilent N5221A* vector network analyzer [see the picture of the experimental set-up in Fig. 3(d)].

We have carried out further electromagnetic simulations with different values of W_l. The pairs of transmission zeros as a function of $\Delta W_l/W_l$ are depicted in Fig. 4(a). As ΔW_l tends to be zero, corresponding to the symmetric structure, the separation between the transmission zeros decreases. However, it can be appreciated in Fig. 4(a) that both transmission zeros do not converge (a sudden jump occurs when the structure is symmetric, with only one transmission zero, as anticipated before).

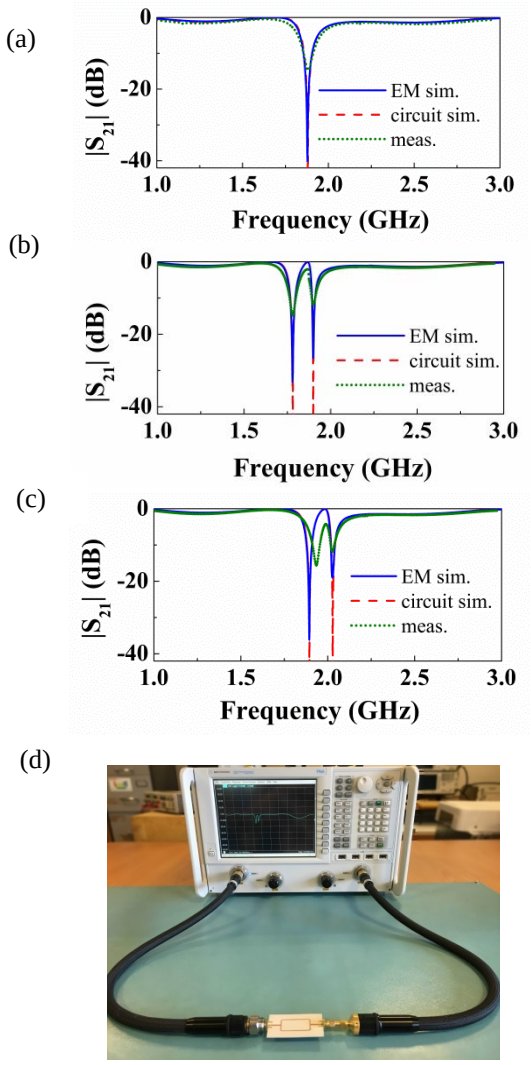

Fig. 3. (a) Magnitude of the transmission coefficient corresponding to the symmetric structure of Fig 1(a) by considering the *Rogers RO3010* substrate with thickness h = 1.27 mm and dielectric constant ε_r = 10.2, and with geometrical parameters as follows: h_0 =1.15 mm, h_1 =2.22 mm, c = 0.2 mm, d = 0.2 mm, $W_u = W_l$ = 7.86 mm, $l_u = l_l$ = 4.8 mm; (b) Magnitude of the transmission coefficient obtained by increasing the length of the lower CSRR with $\Delta W_l = 0.1W_u$ = 0.786 mm; (c) Magnitude of the transmission coefficient obtained by decreasing the length of the lower CSRR with $\Delta W_l = -0.1W_u = -0.786$ mm; (d) Photograph of the experimental set-up. The extracted parameters are: (a) $L_u = L_l$ = 2.18 nH, $C_u = C_l$ = 0.82 pF, $L_{Cu} = L_{Cl}$ = 1.91 nH, and $C_{Cu} = C_{Cl}$ = 2.94 pF; (b) L_l = 2.30 nH, C_l = 0.82 pF, L_{Cl} = 2.08 nH, and C_{Cl} = 3.09 pF; (c) L_l = 2.07 nH, C_l = 0.82 pF, L_{Cl} = 1.70 nH, and C_{Cl} = 2.84 pF. For both (b) and (c), the rest of extracted element values are the same as (a).

In the structure of Fig. 1(a), giving the responses of Fig. 3 and the pairs of transmission zeros of Fig. 4(a) for different values of W_l, the electrical length of the transmission line sections between the T-junctions and the position of the CSRRs, θ_l, does not satisfy (10). Particularly, in Fig. 1(a) $\theta_1 < \theta_{1,\infty}$, where $\theta_{1,\infty}$ is the phase that satisfies (10). We have repeated the electromagnetic simulations of the structures considered in Fig. 4(a), but by considering $\theta_1 > \theta_{1,\infty}$. The pairs of transmission zeros that result by varying W_l are depicted in Fig. 4(b). The behaviour is very similar to the one observed in Fig. 4(a). However, the single transmission zero for the symmetric structure belongs now to the opposite curve.

Finally, we have considered the case with $\theta_1 = \theta_{1,\infty}$ [Fig. 4(c)]. In this case, the pair of transmission zeros merge when the structure is symmetric, and the two curves cross. This is an expected result since it was demonstrated in the previous section that when condition (10) is satisfied one of the transmission zeros is given by the frequency that nulls the reactance of the upper shunt branch, regardless of the dimensions of the CSRR present at the other (lower) branch. Concerning the frequency response, a typical characteristic when $\theta_1 = \theta_{1,\infty}$ is the similarity between the two notches (depth and width) for asymmetric structures, as it can be appreciated in Fig. 5.

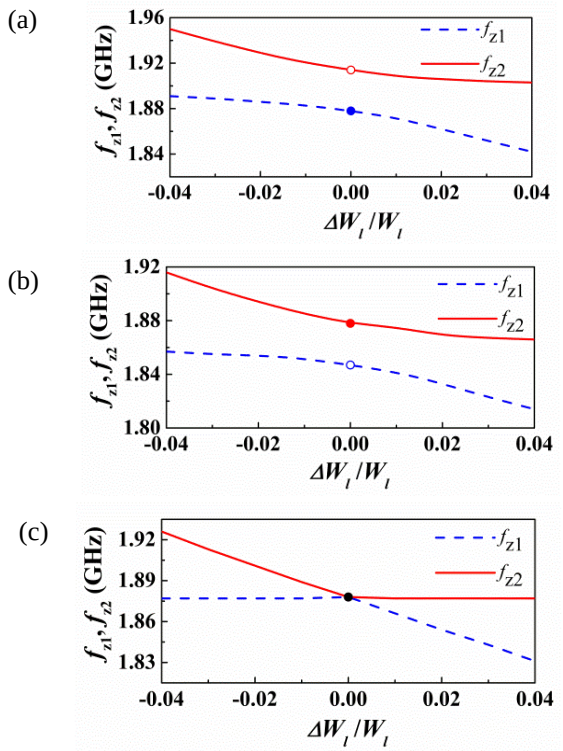

Fig. 4. Variation of the transmission zeros as a function of the variation of the width of one of the CSRRs ($\Delta W_l / W_l$) for different electrical lengths of the transmission lines: (a) $\theta_1 = 0.672\pi < \theta_{1,\infty}$; (b) $\theta_1 = 1.008\pi > \theta_{1,\infty}$; (c) $\theta_1 = 0.84\pi = \theta_{1,\infty}$.

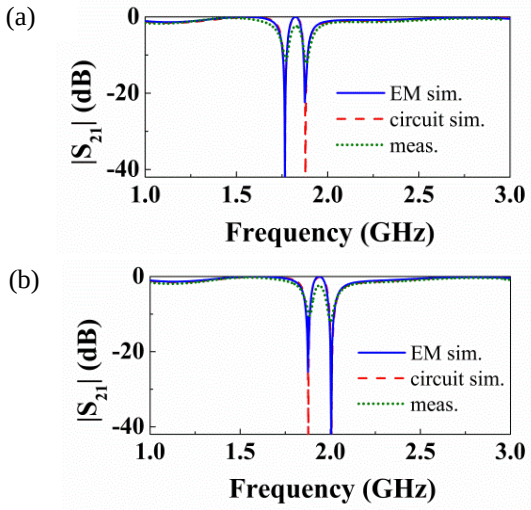

Fig. 5. Response of the CSRR-loaded combiner/splitter structure with $\theta_1 = \theta_{1,\infty}$ for two asymmetric structures. (a) $W_l = 8.65$ mm, by increasing $\Delta W_l = 0.1$ $W_u = 0.786$ mm; (b) $W_l = 7.07$ mm, by decreasing $-\Delta W_l = -0.1$ $W_u = -0.786$ mm.

If we use the CSRR-loaded splitter/combiner structures as sensors or comparators based on frequency splitting, where the sensitivity is defined as the variation of the frequency difference between the two transmission zeros (f_{z1} and f_{z2}) with the variable that generates the asymmetry (typically a difference in dielectric constant between two samples), it follows that the optimum structure in terms of sensitivity is the one satisfying (10), i.e., the one giving the transmission zeros of Fig. 4(c). In Fig. 4, the asymmetries are caused by varying the dimensions of one of the CSRRs, but this behaviour (the dependence of the transmission zero curves with θ_1) does not depend on the cause of the asymmetry, and it is general for unbalanced loads. Thus, without loss of generality, we can define the sensitivity as

$$S = \frac{\partial \Delta f_z}{\partial \Delta W_l} \tag{12}$$

where $\Delta f_z = f_{z1} - f_{z2}$. The sensitivity for the three considered cases is depicted in Fig. 6, where it can be appreciated that the sensitivity for small unbalanced perturbations is clearly optimized when $\theta_1 = \theta_{1,\infty}$ (note that if the optimum electrical length, 0.84π in our case, is not considered, but it is very close to this value, the sensitivity is expected to approach the optimum value for practical unbalanced loads).

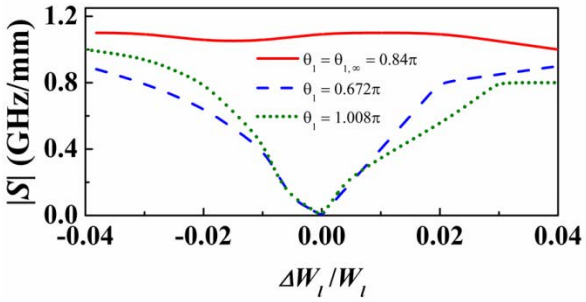

Fig. 6. Sensitivity as a function of $\Delta W_l/W_l$ for different values of the electrical length of the transmission lines.

IV. PROTOTYPE DEVICE SENSOR AND COMPARATOR

To demonstrate the potential of the structure with $\theta_1 = \theta_{1,\infty}$ as sensor and comparator, we have first loaded it (i.e., the lower CSRR, acting as the active sensor region) with small dielectric slabs with different dielectric constant (the other CSRR is kept unloaded). Specifically, we have cut square-shaped pieces of un-metalized commercial microwave substrates with dielectric constants of 10.2 (*Rogers RO3010*), 3.55 (*Rogers RO4003C*) and 2.43 (*Arlon CuClad 250*). The measured responses are depicted in Fig. 7(a), whereas the variation of frequency splitting, Δf_z, with the dielectric constant, exhibiting roughly a linear variation, is shown in Fig. 7(b). This curve can be used to determine the dielectric constant of unknown substrates/samples from the measurement of the resulting frequency splitting. The dielectric constant of the SUT can in principle be arbitrarily small. Nevertheless, as the dielectric constant of the sample approaches unity, the two notches may merge in a single one by the effect of losses of the device (metallic and dielectric). Therefore, the discrimination is limited by this effect. Considering SUTs with large dielectric constant would force us to consider additional samples with known large dielectric constant in order to extend the span of the calibration curve. Apart from that, the curve of Fig. 7(b)

reveals a significant variation of Δf_z with the dielectric constant. If we assume that frequency differences (for different samples) of the order of 0.01 GHz can be distinguished (reasonable on account of the peaked responses at the notches), then differences in dielectric constants of the order of 0.35 or even less, can be detected.

As a test example, we have loaded the device with a square slab of un-cladded *FR4* substrate (with nominal dielectric constant 4.5). The resulting frequency splitting is Δf_z = 0.112 GHz, providing a dielectric constant of 4.56, according to the curve of Fig. 7(b), i.e., in close agreement to the nominal value.

It is worth mentioning that the SUT is assumed to be a dielectric slab larger than the dimensions of the CSRRs. The relative position of the SUT with regard to the CSRR is not relevant as long as the SUT limits are beyond those of the CSRRs. Otherwise, the notch frequency will depend on the relative position between the SUT and the CSRR, situation that must be avoided. In principle, the proposed sensor system is useful for dielectric slabs, not for samples with arbitrary geometry. The reason is that the CSRR slots must be surrounded by the SUT material under consideration. Concerning the potentiality of this approach for the characterization of the dielectric constant of liquids, the system may be useful as long as the experimental set up is able to guarantee sealing. Obviously this needs further work, which is out of the scope of this paper. The main aim of the paper is the determination of the dielectric constant in low-loss dielectric samples.

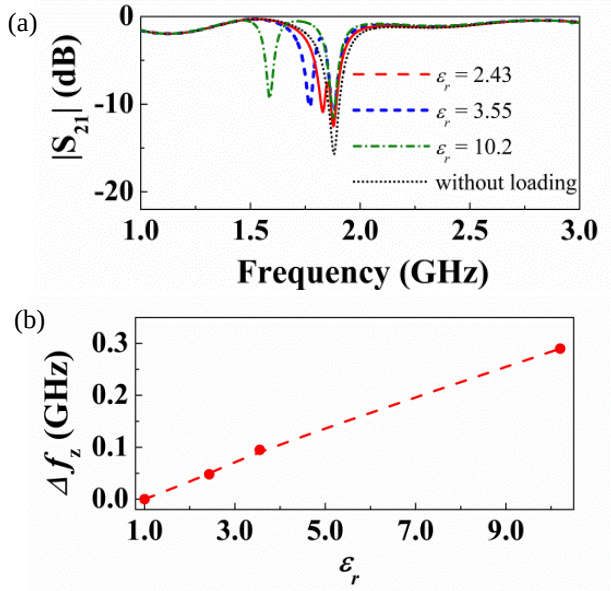

Fig. 7. (a) Response of the CSRR-loaded combiner/splitter structure with $\theta_1 = \theta_{1,\infty}$ to different dielectric loads and (b) variation of Δf_z with the dielectric constant of the considered load.

To demonstrate its use as comparator, we have loaded the structure with two square-shaped pieces of un-metalized *Rogers RO3010* substrate (with dielectric constant 10.2), but with defects in one of the samples (the SUT) in the form of a square array of vertical cylindrical holes with radius 0.2 mm and separated 0.8 mm (see Fig. 8). This reduces the effective dielectric constant. The measured response (Fig. 9) gives two notches, indicative of the difference between the two samples, the SUT and the reference sample (unaltered piece of substrate).

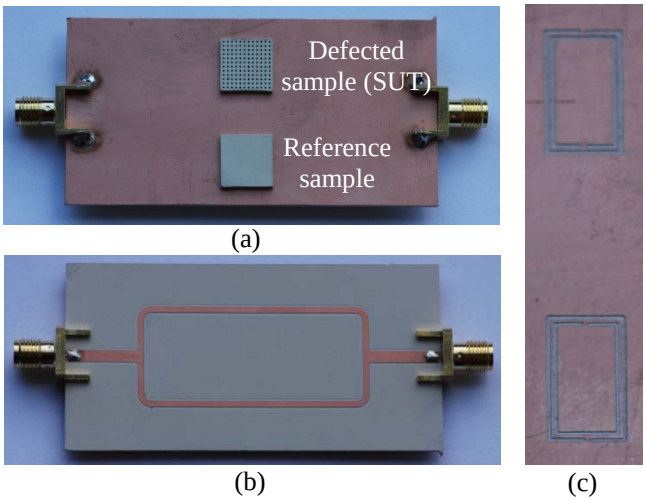

Fig. 8. Photograph of the splitter/combiner loaded with the reference sample and the SUT. (a) Bottom view; (b) top view. The detail of the CSRRs, not shown in (a) by the presence of the slabs, is shown in (c).

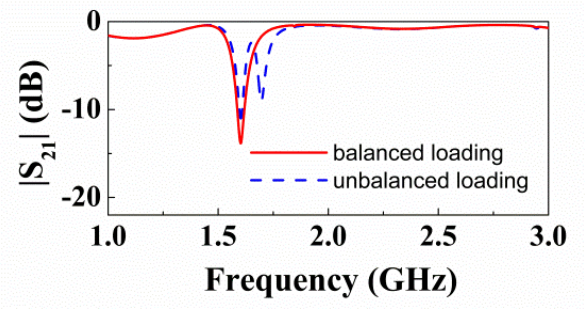

Fig. 9. Response of the CSRR-loaded combiner/splitter structure to two unbalanced loads, i.e., a reference sample and the same sample with defects (SUT). The response with both CSRRs loaded with the reference sample (balanced loading) is also included for comparison.

The SUT has been also measured with the other CSRR unloaded (similar to the experiment carried out in Fig. 7). The resulting frequency splitting, Δf_z = 0.204 GHz, indicates that the effective dielectric constant of the sample is in the vicinity of 7.4, according to the curve in Fig. 7(b). This is a reasonable value on account of the perforated cylindrical holes across the sample.

Another interesting aspect concerns the effects of pressure applied to the SUT, related to the presence of an air gap between the CSRRs and the samples. In our case, we have simply left the samples to rest on top of the CSRRs. By putting pressure, the notch positions certainly change. However, the device will work both as sensor and as comparator as long as the pressure is the same in the SUT and reference sample (comparator), or in the considered SUT as compared to the samples used for calibration (sensor).

V. CONCLUSIONS

In conclusion, splitter/combiner microstrip sections loaded with pairs of CSRRs have been studied in detail. These structures are useful as sensors and comparators, and their working principle is based on frequency splitting caused by symmetry disruption on the CSRR pair. Thus, the structures are especially suitable for the measurement of the dielectric constant of samples (sensor functionality) and for the detection of defects or anomalies in a sample under test, as compared to a reference sample (comparator functionality). We have proposed a mixed

distributed/lumped circuit model of the structures, which has been validated by comparison between the circuit responses obtained from circuit simulation (with extracted parameters) and those inferred from electromagnetic simulation and experiment. From the circuit model, we have obtained the necessary conditions, relative to the electrical length of the transmission line sections of the splitter/combiner, to optimize the sensitivity of the structures as sensing elements and the discrimination as comparators. Finally, we have demonstrated the potential of the reported CSRR-based structures as sensors and comparators by considering different dielectric loads, located in the active region of the sensor (one of the CSRRs), and by obtaining the resulting frequency splitting, and by comparing a defected sample under test (SUT) with a reference (unaltered) sample. In the latter case, the presence of two notches in the frequency response indicates the difference between the two samples. The reported approach solves the limitation of previous sensing structures based on pairs of CSRRs loading a single line, where coupling between resonators degrades the sensitivity and discrimination. As pointed out in [39], several samples can be sensed/compared simultaneously by cascading several splitter/combiner sections, each one loaded with a different pair of CSRRs. Nevertheless, up to three samples can be also measured with a single splitter/combiner, by adequately locating three pairs of CSRRs in the structure: two of them in the input/output access lines, two of them in the parallel microstrip lines, at a distance given by (10) from the input T-junction, and the remaining two CSRRs also in the parallel microstrip lines at a distance given by (10) from the T-junction adjacent to the output port.

APPENDIX I

B_u, the denominator of (7), can be expressed as

$$B_u = j2\cos\theta_1\left(\omega L_u\cos\theta_1 + Z_1\sin\theta_1\right) - \\ -Y_u\left(Z_1\sin\theta_1 + \omega L_u\cos\theta_1\right)^2 \qquad \text{(AI.1)}$$

Since the condition (9) is a common factor in the previous equation, it follows that $B_u = 0$ if (9) is satisfied. Actually, from a mathematical viewpoint, the second term in the right-hand side can be null, infinite or finite, depending on the variation of Y_u with frequency in the limit when $\omega \to \omega_0$. However, for any shunt admittance, Y_u, it can be demonstrated that such term is null. To this end, let us calculate this term in the indicated limit, i.e.,

$$\lim_{\omega\to\omega_0}\frac{\left(Z_1\sin\theta_1 + \omega L_u\cos\theta_1\right)^2}{Z_u} \qquad \text{(AI.2)}$$

where $Z_u = 1/Y_u$ is the impedance of the shunt branch, which nulls at ω_0. Since both the numerator and the denominator of (AI.2) are zero in the indicated limit, it is necessary to apply the L'Hôpital rule. However, for simplicity, let us take the derivatives with θ_1, rather than with the angular frequency, that is

$$\lim_{\theta_1\to\theta_{1,0}}\frac{2\left(Z_1\sin\theta_1 + \omega L_u\cos\theta_1\right)\left[\left(Z_1 + \frac{L_u v_p}{l_1}\right)\cos\theta_1 - L_u\frac{\theta_1 v_p}{l_1}\sin\theta_1\right]}{Z_u'} \qquad \text{(AI.3)}$$

where $\theta_{1,0}$ is the electrical length of the lines at ω_0, v_p is the phase velocity of the lines, l_1 is their physical length, and Z_u' is the derivative of the shunt impedance with θ_1 (proportional to the derivative with ω). Inspection of (AI.3) reveals that the numerator is null since the left-hand term is null (condition 9), whereas the right-hand term is finite. However, the denominator is finite, as corresponds to the derivative of any reactance with frequency at resonance. Therefore, the previous limit is null, and hence $B_u = 0$.

For which concerns D, the numerator of (7), it can be expressed as follows:

$$D_u = 1 - \frac{2\sin\theta_1}{Z_1}\left(\omega L_u\cos\theta_1 + Z_1\sin\theta_1\right) + \\ + jY_u\left(\omega L_u\cos\theta_1 + Z_1\sin\theta_1\right)\left(\cos\theta_1 + \frac{\omega L_u\sin\theta_1}{Z_1}\right) \qquad \text{(AI.4)}$$

According to the previous equation, if (9) is satisfied, the second term is null. The third term is also null, unless $Y_u \to \infty$. Hence, if Y_u is finite, $D_u = 1$, I_2 given by (11) is not null, and therefore a transmission zero does not occur (as one expects since a transmission zero requires that $Y_u \to \infty$). If $Y_u \to \infty$, the third term in (AI.4) is neither null nor infinite, but finite. The reason is that, in this case, application of the L'Hôpital rule, by considering $Z_u = 1/Y_u$, provides a finite value of both the numerator and the denominator. According to these words, if follows that $D \neq 1$.

APPENDIX II

By excluding the shunt reactance of the upper branch in the circuit of Fig. 1(b), the elements of the *ABCD* matrix can be calculated. In particular, the diagonal elements are given by

$$A = D = \cos^2\theta_1 - \sin^2\theta_1 - \frac{2\omega_0 L_u\sin\theta_1\cos\theta_1}{Z_1} \qquad \text{(AII.1)}$$

Since the electrical length, ϕ, of the unit cell of a periodic structure in the allowed bands is given by [23]

$$\cos\phi = \frac{A+D}{2}\ , \qquad \text{(AII.2)}$$

by forcing $\phi = 2\pi$, it follows that $A = 1$, which is equivalent to (9).

REFERENCES

[1] T. Driscoll, G.O. Andreev, D.N. Basov, S. Palit, S.Y. Cho, N.M. Jokerst, and D.R. Smith, "Tuned permeability in terahertz split ring resonators for devices and sensors," *Appl. Phys. Lett*., vol 91, paper 062511-1-3, 2007.

[2] R. Melik, E. Unal, N.K. Perkgoz, C. Puttlitz, and H.V. Demir, "Metamaterial-based wíreles strain sensors," *Appl. Phys. Lett.*, vol. 95, paper 011106-1-3, 2009.

[3] R.A. Yogi, R.S. Parolia, R.N. Karekar, and R.C. Aiyer, "Microwave microstrip ring resonador as a paper moisture sensor: study with different grammage," *Meas. Sci. Technol*. vol *13*, pp. 1558−1562, 2002.

[4] X-J. He, Y. Wang, J-M. Wang, and T-L. Gui, "Thin film sensor based tip-shaped splits ring resonator metamaterial for microwave application," *Microsystems Technology*, vol. 16, pp. 1735−1739, 2010.

[5] M. S. Boybay and O. M. Ramahi, "Material characterization using complementary split-ring resonators," *IEEE Trans. Instrum. Meas*., vol. 61, no. 11, pp. 3039−3046, Nov. 2012.

[6] C.-S. Lee and C.-L. Yang, "Complementary split-ring resonators for measuring dielectric constants and loss tangents," *IEEE Microw. Wireless Compon. Lett.*, vol. 24, no. 8, pp. 563−565, Aug. 2014.

[7] C.-L. Yang, C.-S. Lee, K.-W. Chen, and K.-Z. Chen, "Noncontact measurement of complex permittivity and thickness by using planar resonators," *IEEE Trans. Microw. Theory Techn*., vol. 64, no.1, pp. 247−257, Jan. 2016.

[8] M. Puentes, C. Weiß, M. Schüßler, and R. Jakoby, "Sensor array based on split ring resonators for analysis of organic tissues," in *IEEE MTT-S Int. Microw. Symp.*, Baltimore, MD, USA, Jun. 2011, pp. 1−4.
[9] M. Puentes, *Planar Metamaterial Based Microwave Sensor Arrays for Biomedical Analysis and Treatment*. Springer, Heidelberg, Germany, 2014.
[10] T. Chretiennot, D. Dubuc, and K. Grenier, "A microwave and microfluidic planar resonator for efficient and accurate complex permittivity characterization of aqueous solutions," *IEEE Trans. Microw. Theory Techn.*, vol. 61, no. 2, pp. 972−978, Feb. 2013.
[11] A. Abduljabar, D. Rowe, A. Porch, and D. Barrow, "Novel microwave microuidic sensor using a microstrip split-ring resonator," *IEEE Trans. Microw. Theory Techn.*, vol. 62, no. 3, pp. 679−688, Mar. 2014.
[12] A. Ebrahimi, W. Withayachumnankul, S. Al-Sarawi, D. Abbott, "High-sensitivity metamaterial-inspired sensor for microfluidic dielectric characterization," *IEEE Sensors J.*, vol. 14, no. 5, pp. 1345−1351, May 2014.
[13] W. Withayachumnankul, K. Jaruwongrungsee, A. Tuantranont, C. Fumeaux, and D. Abbott, "Metamaterial-based microfluidic sensor for dielectric characterization," *Sensor Actuat. A Phys.*, vol. 189, pp. 233−237, Jan. 2013
[14] H.-J. Lee and J.-G. Yook, "Biosensing using split-ring resonators at microwave regime," *App. Phys. Lett.*, vol. 92, no. 25, p. 254103, 2008.
[15] E. Ekmekci and G. Turhan-Sayan, "Multi-functional metamaterial sensor based on a broad-side coupled SRR topology with a multi-layer substrate," *App. Phys. A* , vol. 110, no. 1, pp. 189−197, Jan. 2013.
[16] C. Damm, M. Schussler, M. Puentes, H. Maune, M. Maasch, and R. Jakoby, "Artificial transmission lines for high sensitive microwave sensors," *IEEE Sensors Conf.*, Christchurch, New Zealand, pp. 755−758, Oct. 2009.
[17] C. Damm, *Artificial Transmission Line Structures for Tunable Microwave Components and Microwave Sensors*, Shaker Verlag, Aachen, Germany, 2011.
[18] M. Schueler, C. Mandel, M. Puentes, and R. Jakoby, "Metamaterial inspired microwave sensors," *IEEE Microw. Mag.*, vol. 13, no. 2, pp. 57–68, Mar. 2012.
[19] M. Tiuri, "Microwave Sensor Applications in Industry," in *Europ. Microw. Conf.*, pp. 25−32, Sep. 1987.
[20] J. G. Webster, *The Measurement Instrumentation and Sensors Handbook*. Boca Raton, FL, USA: CRC, 1999.
[21] J. Fraden, *Handbook of Modern Sensors: Physics, Design, and Applications*, 3rd ed. New York, NY, USA, Springer, 2004.
[22] J. Naqui, M. Durán-Sindreu and F. Martín, "Novel Sensors Based on the Symmetry Properties of Split Ring Resonators (SRRs)," *Sensors*, vol 11, pp. 7545−7553, 2011.
[23] F. Martín, *Artificial Transmission Lines for RF and Microwave Applications*, John Wiley, Hoboken, NJ, 2015.
[24] J. Naqui, *Symmetry properties in transmission lines loaded with electrically small resonators: circuit modeling and applications*, Springer, Heidelberg, Germany, 2016.
[25] J. Naqui, M. Durán-Sindreu, and F. Martín, "Alignment and Position Sensors Based on Split Ring Resonators," *Sensors*, vol. 12, pp. 11790−11797, 2012.
[26] A.K. Horestani, C. Fumeaux, S.F. Al-Sarawi, and D. Abbott, "Displacement sensor based on diamond-shaped tapered split ring resonator," *IEEE Sens. J.*, vol. 13, pp. 1153–1160, 2013.
[27] A.K. Horestani, D. Abbott, and C. Fumeaux, "Rotation sensor based on horn-shaped split ring resonator," *IEEE Sens. J.*, vol. 13, pp. 3014–3015, 2013.
[28] J. Naqui and F. Martín, "Transmission Lines Loaded with Bisymmetric Resonators and Their Application to Angular Displacement and Velocity Sensors," *IEEE Trans. Microw. Theory Techn.*, vol. 61, no. 12, pp. 4700–4713, Dec. 2013.
[29] J. Naqui and F. Martín, "Angular displacement and velocity sensors based on electric-LC (ELC) loaded microstrip lines," *IEEE Sensors J.*, vol. 14, no. 4, pp. 939–940, Apr. 2014.
[30] A.K. Horestani, J. Naqui, D. Abbott, C. Fumeaux, and F. Martín, "Two-dimensional displacement and alignment sensor based on reflection coefficients of open microstrip lines loaded with split ring resonators," *Elec. Lett.*, vol. 50, pp. 620–622, Apr. 2014.
[31] J. Naqui and F. Martín, "Microwave sensors based on symmetry properties of resonator-loaded transmission lines: a review," *Journal of Sensors*, vol. 2015, Article ID 741853, 10 pages, 2015.
[32] J. Naqui, J. Coromina, A. Karami-Horestani, C. Fumeaux, and F. Martín, "Angular displacement and velocity sensors based on coplanar waveguides (CPWs) loaded with S-shaped split ring resonator (S-SRR)," *Sensors*, vol. 15, pp. 9628–9650, 2015.
[33] A. K. Horestani, J. Naqui, Z. Shaterian, D. Abbott, C. Fumeaux, and F. Martín, "Two-Dimensional Alignment and Displacement Sensor based on Movable Broadside-coupled Split Ring Resonators," *Sensors and Actuators A*, vol. 210, pp. 18–24, April 2014.
[34] J. Naqui, C. Damm, A. Wiens, R. Jakoby, L. Su, and F. Martín, "Transmission lines loaded with pairs of magnetically coupled stepped impedance resonators (SIRs): modeling and application to microwave sensors," *IEEE MTT-S Int. Microwave Symp.*, Tampa, FL, USA, June 2014, pp. 1–4.
[35] L. Su, J. Naqui, J. Mata-Contreras, and F. Martín "Modeling metamaterial transmission lines loaded with pairs of coupled split ring resonators," *IEEE Ant. Wireless Propag. Lett.*, vol. 14, pp. 68–71, 2015.
[36] L. Su, J. Naqui, J. Mata, and F. Martín, "Dual-band epsilon-negative (ENG) transmission line metamaterials based on microstrip lines loaded with pairs of coupled complementary split ring resonators (CSRRs): modeling, analysis and applications," *9th International Congress on Advanced Electromagnetic Materials in Microwaves and Optics*, Metamaterials 2015, Oxford, UK, Sep., 7-12, 2015.
[37] L. Su, J. Naqui, J. Mata-Contreras, P. Vélez, and F. Martín, "Transmission line metamaterials based on pairs of coupled split ring resonators (SRRs) and complementary split ring resonators (CSRR): a comparison to the light of the lumped element equivalent circuits," *International Conference on Electromagnetics for Advanced Applications*, ICEAA 2015, Torino, Italy, 7-11 Sep. 2015.
[38] L. Su, J. Naqui, J. Mata-Contreras, and F. Martín, "Modeling and applications of metamaterial transmission lines loaded with pairs of coupled complementary split ring resonators (CSRRs)," *IEEE Ant. Wireless Propag. Lett.*, vol. 15, pp. 154–157, 2016.
[39] L. Su, J. Naqui, J. Mata-Contreras, and F. Martín, "Cascaded Splitter/Combiner Microstrip Sections Loaded with Complementary Split Ring Resonators (CSRRs): Modeling, Analysis and Applications," *IEEE MTT-S Int. Microwave Symp.* (IMS'16), San Francisco, CA, USA, May 2016, pp. 1–4.
[40] J. Naqui, C. Damm, A. Wiens, R. Jakoby, L. Su, and F. Martín, "Transmission Lines Loaded with Pairs of Stepped Impedance Resonators: Modeling and Application to Differential Permittivity Measurements," *IEEE Trans. Microw. Theory Techn.*, published online, DOI: 10.1109/TMTT.2016.2610423.
[41] J.D. Baena, J. Bonache, F. Martín, R. Marqués, F. Falcone, T. Lopetegi, M.A.G. Laso, J. García, I Gil, M. Flores-Portillo and M. Sorolla, "Equivalent circuit models for split ring resonators and complementary split rings resonators coupled to planar transmission lines," *IEEE Trans. Microw. Theory Techn.*, vol. 53, no. 4, pp. 1451−1461, Apr. 2005.
[42] D.M. Pozar, *Microwave Engineering*, 3rd ed. John Wiley, Hoboken, NJ, USA, 2005.
[43] J. Bonache, M. Gil, I. Gil, J. Garcia-García, and F. Martín, "On the electrical characteristics of complementary metamaterial resonators," *IEEE Microw. Wireless Compon. Lett.*, vol. 16, no. 10, pp. 543−545, Oct. 2006.

Lijuan Su (S'15) was born in Qianjiang, Hubei, China, in 1983. She received the Bachelor's degree in Communication Engineering and the M.E. degree in Circuits and Systems from Wuhan University of Technology, Wuhan, China, in 2005 and 2013, respectively. She is currently pursuing the Ph.D. degree in metamaterials applied to RF/microwave sensors at the Universitat Autonoma de Barcelona, Barcelona, Spain.
From 2005 to 2009, she was an Engineer with China Telecom Corporation Ltd.

Javier Mata-Contreras was born in 1976 in Málaga (Spain). He received the Ingeniería de Telecomunicación Degree from the Universidad de Málaga (UMA) in 2000 and the PhD degree from the same university in 2010, with the Thesis "Distributed Amplifiers and Mixers with Transmission Lines based on Metamaterials".
In 2000, he joined the UMA Department of Ingeniería de Comunicaciones UMA as Assistant Professor.
He is currently working at CIMITEC and the Universitat Autònoma de Barcelona as Visitant Professor. His research interests include active and

passive microwave devices and active distributed circuits based on metamaterials, among others.

Paris Vélez (S'10-M'14) was born in Barcelona (Spain) in 1982. He received the degree in Telecommunications Engineering, specializing in Electronics in 2008 and the Electronics Engineering degree in 2010 from the Universitat Autònoma de Barcelona. In 2014 he received his PhD in Electrical Engineering from the UAB with a thesis entitled "Common mode suppression differential microwave circuits based on Metamaterial concepts and semilumped resonators". During the PhD he was awarded with a predoctoral teaching and research fellowship by the Spanish Government from 2011 to 2014.

Dr. Vélez is a reviewer of the IEEE T-MTT and of other journals. Actually, his scientific activity is focused on the miniaturization of passive circuits RF / microwave and sensors based Metamaterials. He is currently working in subjects related to Metamaterials sensors for fluidics detection at LAAS-CNRS through TECNIOSpring fellowship cofounded by Mari Curie program.

Ferran Martín (M'04-SM'08-F'12) was born in Barakaldo, Vizcaya, Spain, in 1965. He received the B.S. Degree in Physics from the Universitat Autònoma de Barcelona (UAB) in 1988 and the PhD degree in 1992.

From 1994 to 2006, he was Associate Professor in Electronics at the Departament d'Enginyeria Electrònica (Universitat Autònoma de Barcelona), and since 2007 he is Full Professor of Electronics. In recent years, he has been involved in different research activities including modelling and simulation of electron devices for high frequency applications, millimeter wave and THz generation systems, and the application of electromagnetic bandgaps to microwave and millimeter wave circuits. He is now very active in the field of metamaterials and their application to the miniaturization and optimization of microwave circuits and antennas. He is the head of the Microwave Engineering, Metamaterials and Antennas Group (GEMMA Group) at UAB, and director of CIMITEC, a research Center on Metamaterials supported by TECNIO (Generalitat de Catalunya). He has organized several international events related to metamaterials, including Workshops at the IEEE International Microwave Symposium (years 2005 and 2007) and European Microwave Conference (2009), and the Fifth International Congress on Advanced Electromagnetic Materials in Microwaves and Optics (Metamaterials 2011), where he has acted as chair of the Local Organizing Committee. He has acted as Guest Editor for three Special Issues on Metamaterials in three International Journals. He has authored and co-authored over 500 technical conference, letter, journal papers and book chapters, he is co-author of the book on Metamaterials entitled *Metamaterials with Negative Parameters: Theory, Design and Microwave Applications* (John Wiley & Sons Inc. 2008), author of the book *Artificial Transmission Lines for RF and Microwave Applications* (John Wiley & Sons Inc. 2015), and he has generated 15 PhDs. Ferran Martín has filed several patents on metamaterials and has headed several Development Contracts.

Prof. Martín is a member of the IEEE Microwave Theory and Techniques Society (IEEE MTT-S). He is reviewer of the IEEE Transactions on Microwave Theory and Techniques and IEEE Microwave and Wireless Components Letters, among many other journals, and he serves as member of the Editorial Board of IET Microwaves, Antennas and Propagation and International Journal of RF and Microwave Computer-Aided Engineering. He is also a member of the Technical Committees of the European Microwave Conference (EuMC) and International Congress on Advanced Electromagnetic Materials in Microwaves and Optics (Metamaterials). Among his distinctions, Ferran Martín has received the 2006 Duran Farell Prize for Technological Research, he holds the *Parc de Recerca UAB – Santander* Technology Transfer Chair, he has been the recipient of two ICREA ACADEMIA Awards (calls 2008 and 2013) and recipient of the Ingeniero Comerma Prize in 2015. He is Fellow of the IEEE since 2012 and Fellow of the IET since 2016.

Sensors16

"Configurations of splitter/combiner microstrip sections loaded with stepped impedance resonators (SIRs) for sensing applications"

Su, Lijuan, Jordi Naqui, Javier Mata-Contreras, and Ferran Martín

Sensors 16, no. 12 (2016): 2195

sensors

MDPI

Article

Configurations of Splitter/Combiner Microstrip Sections Loaded with Stepped Impedance Resonators (SIRs) for Sensing Applications

Lijuan Su, Javier Mata-Contreras, Paris Vélez and Ferran Martín *

CIMITEC, Departament d'Enginyeria Electrònica, Universitat Autònoma de Barcelona, Bellaterra, 08193 Barcelona, Spain; Lijuan.Su@uab.cat (L.S.); Franciscojavier.Mata@uab.cat (J.M.-C.); Paris.Velez@uab.cat (P.V.)

* Correspondence: Ferran.Martin@uab.cat; Tel.: +34-93-581-3522; Fax: +34-93-581-2600

Academic Editor: Vittorio M. N. Passaro

Received: 14 November 2016; Accepted: 16 December 2016; Published: 20 December 2016

Abstract: In this paper, several configurations of splitter/combiner microstrip sections loaded with stepped impedance resonators (SIRs) are analyzed. Such structures are useful as sensors and comparators, and the main aim of the paper is to show that the proposed configurations are useful for the optimization of sensitivity and discrimination. Specifically, for comparison purposes, i.e., to determine anomalies, abnormalities or defects of a sample under test (SUT) in comparison to a reference sample, it is shown that up to three samples can be simultaneously tested. Simple models of the proposed structures are presented, and these models are validated through electromagnetic simulation and experiment. Finally, the principle of operation is validated through a proof-of-concept demonstrator.

Keywords: stepped impedance resonator (SIR); microstrip technology; microwave sensors; differential sensors

1. Introduction

In recent years, there has been an increasing interest in microwave sensors. Many of these sensors are based on the variation of the resonance frequency, phase or quality factor of a resonant element, caused by the variable to be sensed [1–9]. Among them, there are sensors implemented by loading a transmission line with planar resonators coupled to it [8,9]. One limitation of these sensors is caused by the so-called cross sensitivity, i.e., the sensitivity of the sensing element to other variables. Particularly critical are the effects of changing environmental conditions, such as temperature or humidity, which may cause erroneous readouts and/or may force the sensing system to continuously calibrate the sensor in order to obtain reliable measurements. One possible solution to these limitations is differential sensing. The reason is that in differential sensors, the environmental factors are seen as common-mode stimulus. Therefore, their effects can be minimized and hence differential sensors are more robust in the face of variations in ambient factors.

Typically, differential sensors are based on two sensing elements, e.g., two transmission lines loaded with reactive elements or with resonators [10]. However, differential sensors can be also implemented by means of a single transmission line loaded with a pair of resonant elements [11,12], or with a pair of resonators coupled to it [13–15]. In this latter type of sensors, the sensing principle is based on frequency splitting. Namely, under a common-mode stimulus, e.g., identical dielectric loading in both resonators, a single transmission zero at the fundamental resonance frequency of the resonant elements arises. However, if the resonators are unequally loaded, two transmission zeros appear, and the distance between them is related to the difference in the loads.

It is also possible to implement sensors robust in the face of variations in ambient conditions by loading a transmission line with a single symmetric resonator. In this case, the sensing principle is based on symmetry properties, and specifically on the controllability of line-to-resonator coupling [16–18]. That is, by symmetrically loading a line with a symmetric resonator with its symmetry plane (aligned with the one of the line) being of different electromagnetic nature from the symmetry plane of the line (one an electric wall and the other one a magnetic wall), the resonator is not effectively coupled to the line. Under these conditions, resonance is prevented and the loaded line is transparent. However, if symmetry is truncated (e.g., by means of an asymmetric dielectric load, or by a relative displacement between the resonator and the line), the electric or magnetic field lines in the resonator area no longer cancelled, and line-to-resonator coupling appears, with the result of a frequency notch at resonance. Moreover, the notch depth, determined by the magnitude of coupling, is related to the level of asymmetry. Even though these sensors are not true differential sensors, they are scarcely affected by environmental factors, since such factors do not modify the symmetry conditions. Coupling-modulated resonance sensors have been applied to the implementation of linear and angular displacement sensors [16,19–25].

This work is focused on frequency splitting sensors/comparators based on pairs of stepped impedance resonators (SIRs) [26,27] (other recently reported sensors based on pairs of resonant elements are reported in [28–31]). The first implementation of such sensors was presented in [11], where the sensing element consisted of a microstrip line loaded with a pair of SIRs placed at the same position in the line (parallel configuration, see Figure 1a). In this configuration, the SIRs are inductively coupled, and this causes sensitivity degradation at small perturbations, as discussed in [11,12]. One solution to prevent inter-resonator coupling is to place the SIRs at different positions along the line (cascade connection, see Figure 1b [12]). In this case, the transmission zeros are given by the intrinsic resonances of both resonators, and it was argued in [12] that by spacing the SIRs $\lambda/2$, where λ is the guided wavelength at SIR resonance, the equivalent circuit model is the one of the parallel configuration but without inter-resonator coupling.

In this paper, we discuss an alternative solution to avoid the coupling between SIRs: splitter/combiner microstrip sections, where each parallel line is loaded with a SIR (see Figure 1c). Nevertheless, various configurations for multi-sensing purposes, involving further number of SIRs and also based on parallel microstrip lines, are discussed in the paper.

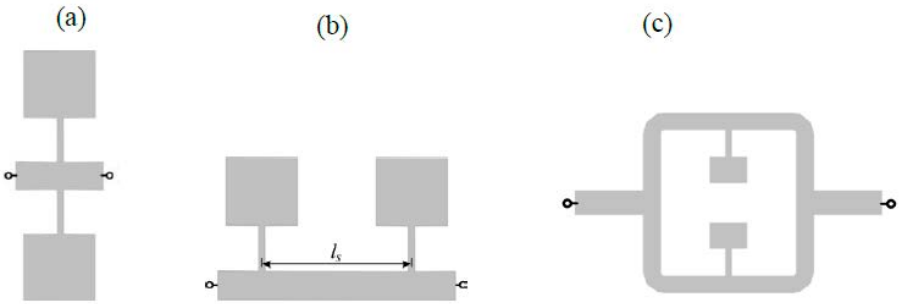

Figure 1. Various topologies of sensors based on microstrip lines loaded with SIRs. (**a**) Parallel configuration; (**b**) cascaded configuration; (**c**) splitter/combiner configuration.

2. Circuit Model and Analysis of SIR-Based Splitter/Combiner Sensors

The typical topology (including relevant dimensions) of the considered SIR-loaded power splitter/combiner microstrip structure is depicted in Figure 2a. Each branch consists of a 50 Ω line loaded with a SIR. To match the structure to the 50 Ω ports, impedance inverters implemented by means of 35.35 Ω quarter wavelength transmission line sections are cascaded between the ports and the T-junctions. The circuit schematic, including distributed and lumped elements, is shown in Figure 2b, where the general case of an asymmetric structure is considered. However, asymmetry

Sensors **2016**, *16*, 2195 3 of 11

concerns SIR dimensions, rather than the distributed elements (transmission line sections). The lumped element circuit for the SIRs, L_u-C_u and L_l-C_l model the upper and lower SIR, respectively. The distributed elements model the different transmission line sections, and are characterized by the impedance Z_i and electrical length θ_i (with $\theta_i = \theta$, $i = 1, 2$).

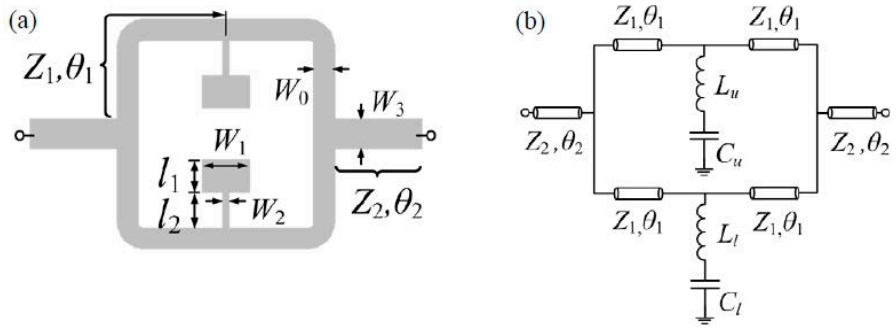

Figure 2. Topology and relevant dimensions of the SIR-loaded power splitter/combiner microstrip structure (**a**) and circuit schematic (**b**).

It is assumed in the model that the SIRs are separated enough so as to neglect coupling between them. Nevertheless, note that unless the resonators are identical, situation that provides a single transmission zero at the fundamental SIR resonance, the two transmission zeros that should appear for asymmetric resonators (or unbalanced perturbations) are not given, in general, by the resonance frequencies of the SIRs. The reason is that in this splitter/combiner structure, a short in one of the parallel microstrip lines does not guarantee a transmission zero in the whole structure since the power can be transmitted through the other line. Indeed, for asymmetric SIRs, the transmission zeros are in general consequence of an interfering phenomenon. To gain insight on this, let us calculate the transmission zeros of the structure of Figure 2b. Such transmission zeros are given by the frequencies satisfying $Y_{21} = Y_{12} = 0$ [32], where $Y_{21} = Y_{12}$ are the anti-diagonal elements of the admittance matrix (identical due to symmetry, with regard to the midplane between the ports, and reciprocity). Such element is given by:

$$Y_{21} = Y_{21,u} + Y_{21,l} \quad (1)$$

where $Y_{21,u}$ and $Y_{21,l}$ are the anti-diagonal elements of the admittance matrix corresponding to the upper and lower SIR-loaded transmission lines. Such elements can be determined by first obtaining the $ABCD$ matrix of each branch. It is simply given by the product of the matrices of the three cascaded two-port networks, including the two transmission line sections with impedance Z_1, and the shunt connected series resonator (accounting for the SIR) in between. Once the $ABCD$ matrices for each branch have been determined, the elements of the right-hand side in Equation (1) are given by $Y_{21,u} = -1/B_u$ and $Y_{21,l} = -1/B_l$, where B_u and B_l are the B elements of the $ABCD$ matrix for the upper and lower parallel branches, respectively [32]. Thus, the transmission zeros are given by:

$$\frac{1}{B_u} + \frac{1}{B_l} = 0 \quad (2)$$

with:

$$B_u = jZ_1 \sin 2\theta_1 - \frac{Z_1^2 \sin^2 \theta_1}{Z_u} \quad (3a)$$

$$B_l = jZ_1 \sin 2\theta_1 - \frac{Z_1^2 \sin^2 \theta_1}{Z_l} \quad (3b)$$

Z_u and Z_l being the impedance of the SIR of the upper and lower branch, respectively. i.e.,:

Sensors **2016**, *16*, 2195 4 of 11

Z_u and Z_l being the impedance of the SIR of the upper and lower branch, respectively. i.e.,:

$$Z_u = j\left(\omega L_u - \frac{1}{\omega C_u}\right) \quad (4a)$$

$$Z_l = j\left(\omega L_l - \frac{1}{\omega C_l}\right) \quad (4b)$$

Inspection of Equations (2) and (3) reveals that if either Z_u or Z_l are zero (both cannot be zero simultaneously unless the resonance frequencies of both resonators are identical), a transmission zero does not arise. If the resonators are different and exhibit different resonance frequencies, the transmission zeros appear at those frequencies where $B_u = -B_l$, and are consequence of signal interference. There is, however, a particular situation not accounted for by Equation (2). It corresponds to the case where the distance between the T-junction and one of the SIRs is $\lambda/2$, or $\theta_1 = \pi$. In this case, one of the transmission zeros is given by the resonance frequency of the corresponding SIR, whereas the other one is given by the solution of Equation (2). Note that if $\theta_1 = \pi$, the shunt reactance is translated to the T-junction, providing a short at this point and hence a transmission zero regardless of the characteristics of the other branch. In this case, $Y11 = \infty$ and $Y21 \neq \infty$.

Inspection of Equations (2) and (3) reveals that if either Z_u or Z_l are zero (both cannot be zero simultaneously unless the resonance frequencies of both resonators are identical), a transmission zero does not arise. If the resonators are different and exhibit different resonance frequencies, the transmission zeros appear at those frequencies where $B_u = -B_l$, and are consequence of signal interference. There is, however, a particular situation not accounted for by Equation (2). It corresponds to the case where the distance between the T-junction and one of the SIRs is $\lambda/2$, or $\theta_1 = \pi$. In this case, one of the transmission zeros is given by the resonance frequency of the corresponding SIR, whereas the other one is given by the solution of Equation (2). Note that if $\theta_1 = \pi$, the shunt reactance is translated to the T-junction, providing a short at this point and hence a transmission zero regardless of the characteristics of the other branch. In this case, $Y11 = \infty$ and $Y21 \neq \infty$.

3. Model Validation and Sensitivity Optimization

3. Model Validation and Sensitivity Optimization

For the validation of the model of the SIR-based structures under study, let us consider the topology of Figure 2 with the geometric parameters indicated in the caption of Figure 3, and the RO4003C substrate (Rogers, CT, USA) with thickness h = 812.8 μm and dielectric constant ε_r = 3.38. The insertion losses inferred from electromagnetic simulation (using the Momentum software, Keysight, Santa Rosa, CA, USA) are depicted in Figure 3a.

For the validation of the model of the SIR-based structures under study, let us consider the topology of Figure 2 with the geometric parameters indicated in the caption of Figure 3, and the RO4003C substrate (Rogers, CT, USA) with thickness h = 812.8 μm and dielectric constant ε_r = 3.38. The insertion losses inferred from electromagnetic simulation (using the Momentum software, Keysight, Santa Rosa, CA, USA) are depicted in Figure 3a.

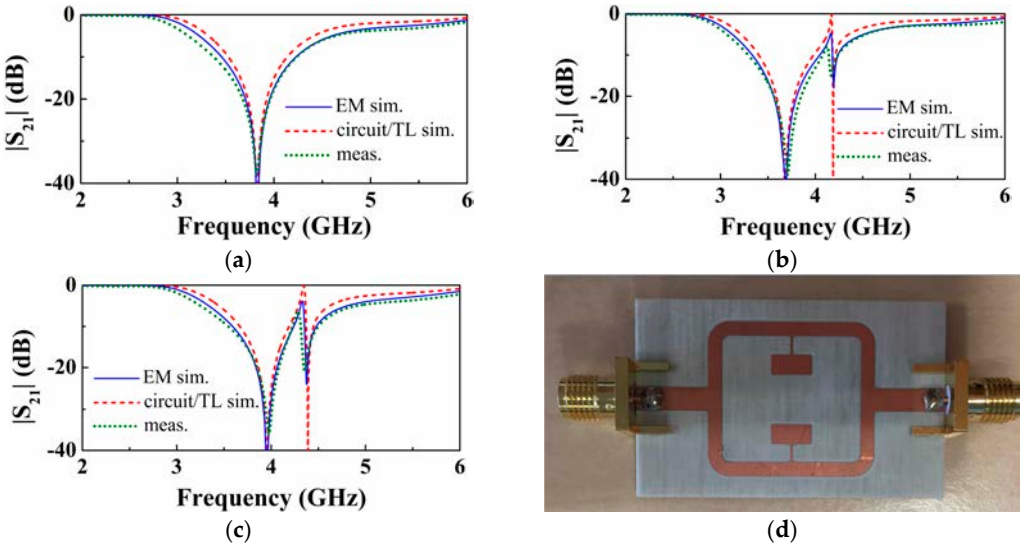

Figure 3. Insertion losses for the structure of Figure 2. (**a**) For the symmetric structure with both SIRs identical to the upper SIR of Figure 2, with $l_{1,u} = l_{1,l}$ = 2.6 mm; (**b**) for the asymmetric structure with lower SIR having bigger capacitance (increasing 0.494 mm or $\Delta l_{1,l} = 0.19 l_{1,l}$) and (**c**) for the asymmetric structure with lower SIR having smaller capacitance (decreasing 0.494 mm or $\Delta l_{1,l} = 0.19 l_{1,l}$). For all three cases, the dimensions of the others are the same: $W_{1,u} = W_{1,l}$ = 0.5 mm, $W_{2,u} = W_{2,l}$ = 0.25 mm, $l_{2,u} = l_{2,l}$ = 2.6 mm, W_0 = 1.84 mm, W_3 = 0.1 mm, $\theta_1 = \theta_2$ = 0.5π. The reactive parameters are: (**a**) $L_u = L_l$ = 2.59 nH, $C_u = C_l$ = 0.67 pF; for (**b**), C_l = 0.77 pF and for (**c**), C_l = 0.56 pF, with the other parameters the same as in (**a**). The photograph of the fabricated structure corresponding to the symmetric case is depicted in (**d**).

Figure 3. Insertion losses for the structure of Figure 2. (**a**) For the symmetric structure with both SIRs identical to the upper SIR of Figure 2, with $l_{1,u} = l_{1,l}$ = 2.6 mm; (**b**) for the asymmetric structure with lower SIR having bigger capacitance (increasing 0.494 mm or $\Delta l_{1,l} = 0.19 l_{1,l}$) and (**c**) for the asymmetric structure with lower SIR having smaller capacitance (decreasing 0.494 mm or $\Delta l_{1,l} = 0.19 l_{1,l}$). For all three cases, the dimensions of the others are the same: $W_{1,u} = W_{1,l}$ = 0.5 mm, $W_{2,u} = W_{2,l}$ = 0.25 mm, $l_{2,u} = l_{2,l}$ = 2.6 mm, W_0 = 1.84 mm, W_3 = 0.1 mm, $\theta_1 = \theta_2$ = 0.5π. The reactive parameters are: (**a**) $L_u = L_l$ = 2.59 nH, $C_u = C_l$ = 0.67 pF; for (**b**), C_l = 0.77 pF and for (**c**), C_l = 0.56 pF, with the other parameters the same as in (**a**). The photograph of the fabricated structure corresponding to the symmetric case is depicted in (**d**).

Sensors **2016**, *16*, 2195 5 of 11

The reactive parameters of the two resonators can be easily inferred from independent simulations of single SIR-loaded transmission lines. From the resonance frequency (transmission zero) and reactance slope, L_u, C_u and L_l, C_l can be obtained. The circuit response obtained from the extracted element values (indicated in the caption of Figure 3), is also depicted in Figure 3a, where the good agreement with the electromagnetic response can be appreciated. Finally, we have fabricated the structure of Figure 2, and we have experimentally obtained the insertion losses, also included in Figure 3a, by means of the N5221 vector network analyzer (Agilent, Santa Clara, CA, USA). Again, the agreement with the electromagnetic and circuit response is reasonable (small discrepancies are due to fabrication related tolerances and to some uncertainties in the nominal value of the dielectric constant of the considered substrate).

We have repeated the previous procedure by varying the dimensions of one of the SIRs (particularly the dimensions of the capacitive patch of the lower SIR). Specifically, we have considered asymmetric structures with the patch capacitances of the lower SIR smaller or larger than the one of the upper SIR (contrary to the symmetric case described in the previous paragraph). The frequency responses of these two asymmetric cases are depicted in Figure 3b,c, and the agreement between the simulated and experimental responses is good as well. Therefore, with these results, corresponding to different situations, the model is validated.

We have considered further asymmetric structures resulting by further increasing or decreasing the length of the patch capacitance of the lower SIR. In all the cases, we have obtained the transmission zeros as a function of this length (Figure 4a). As can be seen, the transmission zeros tend to separate as the asymmetry increases. However, such zeros do not cross in the limit of small asymmetries (emulating small asymmetric perturbations or loads). Hence, the sensitivity, defined as the variation of the differential output with the differential input, is degraded in this limit. Note that the differential output is the difference between the transmission zeros, whereas the differential input can be, for instance, the difference in the capacitances of the SIRs. This phenomenology is also present in structures consisting of single transmission lines loaded with parallel SIRs [11].

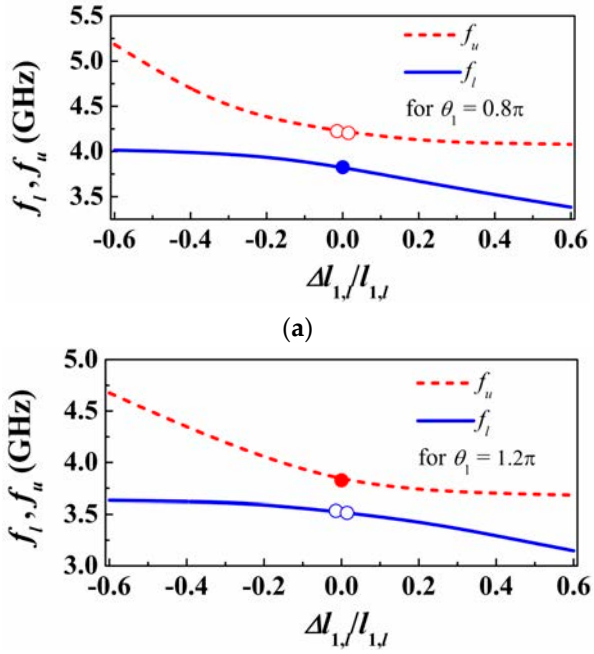

Figure 4. *Cont.*

Sensors **2016**, *16*, 2195 6 of 11

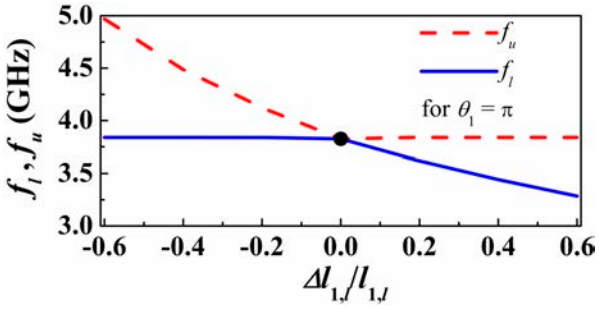

(**c**)

Figure 4. Variation of the transmission zeros as a function of the length of one of the SIR capacitive patch, for different electrical length of the transmission lines: (**a**) $\theta_1 = 0.8\pi$; (**b**) $\theta_1 = 1.2\pi$; (**c**) $\theta_1 = \pi$.
Figure 4. Variation of the transmission zeros as a function of the length of one of the SIR capacitive patch, for different electrical length of the transmission lines: (**a**) $\theta_1 = 0.8\pi$; (**b**) $\theta_1 = 1.2\pi$; (**c**) $\theta_1 = \pi$.

In the structures corresponding to Figure 4a, the electrical length of the lines satisfies $\theta_1 < \pi$, specifically $\theta_1 = 0.8\pi$. Let us now repeat the previous procedure by considering $\theta_1 = 1.2\pi > \pi$. The resonance frequencies are depicted in Figure 4b. A similar phenomenology arises, but now the single resonance frequency corresponding to the symmetric structure appears on the opposite curve. Finally, let us consider the situation with $\theta_1 = \pi$. In this case, the curves giving the two transmission zeros cross (Figure 4c), and one of the transmission zeros does not vary with the level of asymmetry, as anticipated before. This latter case is the preferred one in terms of sensitivity optimization. By choosing $\theta_1 = \pi$ we achieve a similar performance as the one of the cascaded configuration [12].
In the structures corresponding to Figure 4a, the electrical length of the lines satisfies $\theta_1 < \pi$, specifically $\theta_1 = 0.8\pi$. Let us now repeat the previous procedure by considering $\theta_1 = 1.2\pi > \pi$. The resonance frequencies are depicted in Figure 4b. A similar phenomenology arises, but now the single resonance frequency corresponding to the symmetric structure appears on the opposite curve. Finally, let us consider the situation with $\theta_1 = \pi$. In this case, the curves giving the two transmission zeros cross (Figure 4c), and one of the transmission zeros does not vary with the level of asymmetry, as anticipated before. This latter case is the preferred one in terms of sensitivity optimization. By choosing $\theta_1 = \pi$ we achieve a similar performance as the one of the cascaded configuration [12].

4. Multi-Sensing Structure
4. Multi-Sensing Structure

The structure of Figure 2 can be useful as a sensor for permittivity measurement or as comparator, where a single sample (sample under test -SUT) can be tested. In order to simultaneously characterize multiple samples, several splitter/combiner sections like the one shown in Figure 2, each one loaded with a pair of SIRs tuned at different frequencies, can be cascaded (Figure 5). With this configuration, in absence of loading or with balanced loads in each pair of SIRs, three transmission zeros (each one at the resonance frequency of the SIRs) are expected. However, with an unbalanced perturbation in a pair of SIRs, it is expected that the corresponding frequency splits. By the placement of the pairs of SIRs at a distance of $\lambda/2$ from the T-junctions, sensitivity and discrimination for small unbalanced perturbations is optimized, as discussed before. This is corroborated in Figure 6, where the split frequencies for each pair of SIRs, achieved by varying the patch dimensions of one of the SIRs of the pair, are depicted. As can be seen, the transmission zero frequencies cross, this being indicative of sensitivity and discrimination optimization. In Figure 6, only one pair of SIRs is unbalanced (the others are kept unaltered). However, by inferring the split frequencies (transmission zeros) by considering the other two pairs unbalanced as well, similar results are obtained, as corroborated in Figure 7.
The structure of Figure 2 can be useful as a sensor for permittivity measurement or as comparator, where a single sample (sample under test -SUT) can be tested. In order to simultaneously characterize multiple samples, several splitter/combiner sections like the one shown in Figure 2, each one loaded with a pair of SIRs tuned at different frequencies, can be cascaded (Figure 5). With this configuration, in absence of loading or with balanced loads in each pair of SIRs, three transmission zeros (each one at the resonance frequency of the SIRs) are expected. However, with an unbalanced perturbation in a pair of SIRs, it is expected that the corresponding frequency splits. By the placement of the pairs of SIRs at a distance of $\lambda/2$ from the T-junctions, sensitivity and discrimination for small unbalanced perturbations is optimized, as discussed before. This is corroborated in Figure 6, where the split frequencies for each pair of SIRs, achieved by varying the patch dimensions of one of the SIRs of the pair, are depicted. As can be seen, the transmission zero frequencies cross, this being indicative of sensitivity and discrimination optimization. In Figure 6, only one pair of SIRs is unbalanced (the others are kept unaltered). However, by inferring the split frequencies (transmission zeros) by considering the other two pairs unbalanced as well, similar results are obtained, as corroborated in Figure 7.

Sensors **2016**, *16*, 2195 7 of 11
Sensors **2016**, *16*, 2195 7 of 11

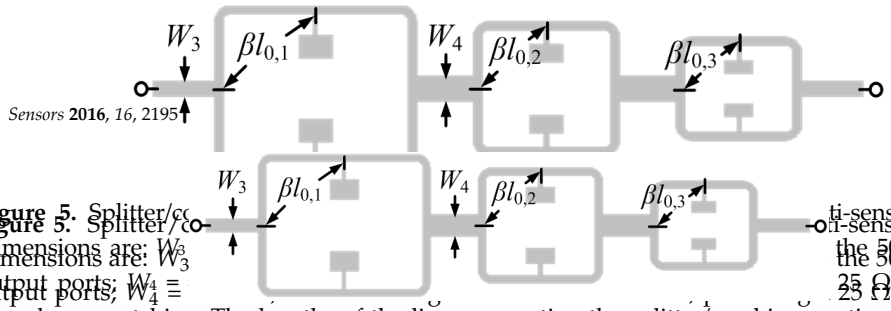

Figure 5. Splitter/combiner circuit loaded with three pairs of SIR for monitoring purposes. Dimensions are: W_3 = 0.25 Ω line for good impedance matching. The lengths of the lines connecting the splitter/combiner sections and the lines adjacent to the ports are 12.1901 mm and 12.4495 mm, given at the center frequency of the working frequency range (3.6 GHz). For each sub-section, $l_{0,1}$ = 32.2192 mm, given at intrinsic resonant frequency of the first sub-section's SIR (2.852 GHz) with electric length of π, $l_{0,2}$ = 25.9817 mm, given at intrinsic resonant frequency of the middle sub-section's SIR (3.826) GHz with electric length of π, $l_{0,3}$ = 24.1571 mm, given at intrinsic resonant frequency of the third sub-section's SIR (4.807 GHz) with electric length of π. SIR dimensions are: the first section with W_1 = 5.5 mm, l_1 = 3.5 mm, W_2 = 0.25 mm, l_2 = 3.8 mm; the middle sub-section with W_1 = 5.5 mm, l_1 = 2.6 mm, W_2 = 0.25 mm, l_2 = 2.6 mm; the third sub-section with W_1 = 4.5 mm, l_1 = 1.8 mm, W_2 = 0.25 mm, l_2 = 2.6 mm (each sub-section is symmetric, so the SIRs have the same dimension as mentioned above). The substrate is identical to the one of Figure 2.

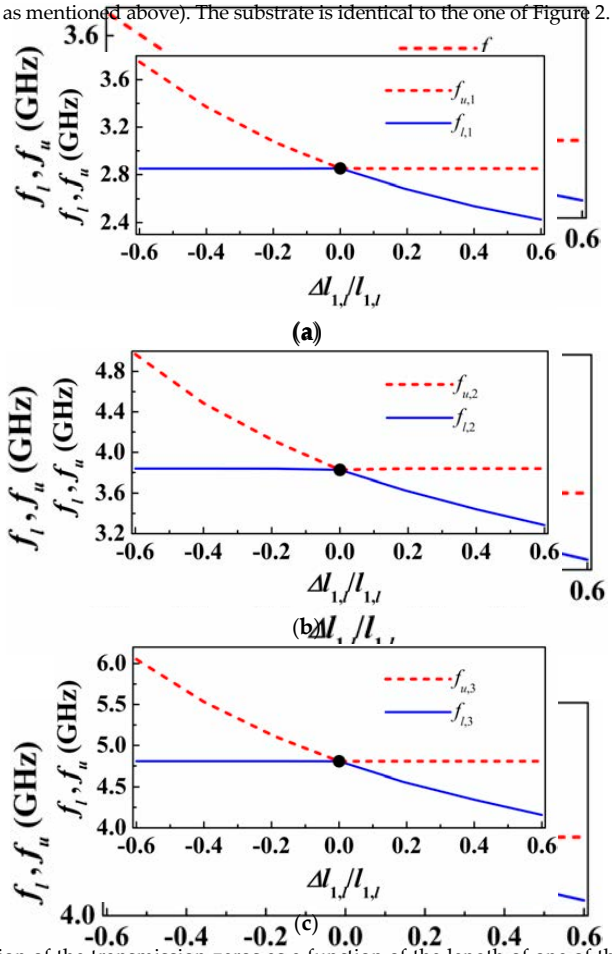

Figure 6. Variation of the transmission zeros as a function of the length of one of the SIR capacitive patch. (**a**) the first sub-section; (**b**) the middle sub-section; (**c**) the third sub-section. For each figure, only one pair of SIRs is unbalanced ($f_{u,i}$ and $f_{l,i}$ – i corresponding for three different sub-sections).

Figure 6. Variation of the transmission zeros as a function of the length of one of the SIR capacitive patch. (**a**) the first sub-section; (**b**) the middle sub-section; (**c**) the third sub-section. For each figure, only one pair of SIRs is unbalanced ($f_{u,i}$ and $f_{l,i}$ – i corresponding for three different sub-sections).

Sensors **2016**, *16*, 2195 8 of 11

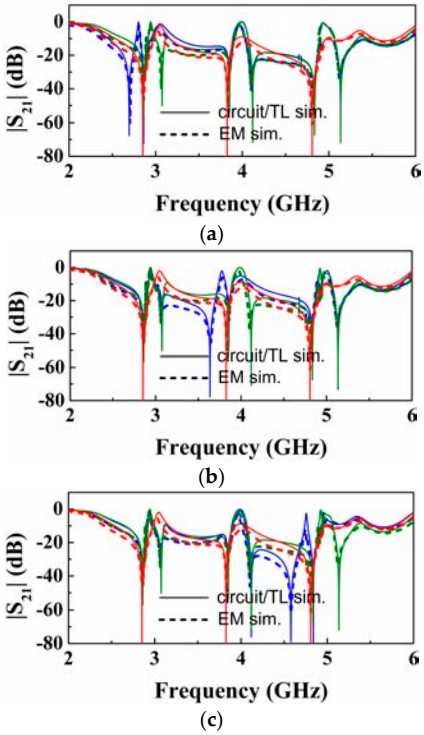

Figure 7. Magnitude of the transmission coefficient obtained from lossless electromagnetic and circuit simulations. In all three cases, red curve is for symmetric case, where blue and olive curves correspond to asymmetric cases, respectively (as the capacitor patch length of the lower SIR for the first sub-section increased/decreased 0.665 mm ($\Delta\ l_{1,l} = \pm 0.19$, $l_{1,l} = \pm 0.665$ mm), while the second and third sub-sections being asymmetric by decreasing the length of the lower capacitive patch 0.19 $l_{1,l}$ for each SIR patch length individually; (**b**) the capacitor patch length of the lower SIR for the second sub-section increased/decreased 0.494 mm ($\Delta\ l_{1,l} = \pm 0.19$, $l_{1,l} = \pm 0.494$ mm), while the first and third sub-sections being asymmetric by decreasing the length of the lower capacitive patch 0.19 $l_{1,l}$ for each SIR patch length individually; (**c**) the capacitor patch length of the lower SIR for the third sub-section increased/decreased 0.342 mm ($\Delta\ l_{1,l} = \pm 0.19$, $l_{1,l} = \pm 0.342$ mm), while the first and second sub-sections being asymmetric by decreasing the length for the lower capacitive patch 0.19 $l_{1,l}$ of each SIR patch length individually.

5. Proof-of-Concept Demonstrator

We have fabricated the structure of Figure 5. The measured response, depicted in Figure 8, exhibits three transmission zeros, as anticipated before. To demonstrate the potential of this structure as multi-sensor based on frequency splitting, we have asymmetrically loaded the three pairs of SIRs. To this end, we have simply added a dielectric slab (a square-shaped piece of un-metalized Rogers RO3010 substrate with thickness h = 1.27 mm and dielectric constant ε_r = 10.2) on top of one of the SIRs of each pair. With these unbalanced loads, frequency splitting of the three resonance frequencies of the SIRs is expected, and this is confirmed from the measured response, also included in Figure 8. Note that one of the notches for each split resonance coincides with the one of the symmetric structure. The reason is that asymmetry has been achieved by keeping one of the SIRs of each pair unaltered (i.e., without dielectric on top of it).

Then we have considered another experiment, where each pair of SIRs has been loaded with unbalanced loads, but in this case considering dielectric slabs with different dielectric constants (i.e., square-shaped pieces of un-metalized substrate with thickness h = 1.27 mm and dielectric constants ε_r = 10.2 and Arlon CuClad 250 LX with ε_r = 2.43 and h = 0.49 mm).

Again, frequency splitting (see Figure 8) points out the difference in the dielectric constants of both slabs loading the different pairs of SIRs. In this case, however, the two notches are shifted to lower frequencies, as compared to the resonance positions for the symmetric case. It is interesting to highlight that the notch positions for the structure with two different slabs for each pair are a result of an interfering phenomenon. For that reason the pair of notches generated by each splitter/combiner section does not coincide with those for the previous case.

Note that the experiment of Figure 8 is simply a proof of concept to demonstrate the possibility of performing multi-sensing measurements simultaneously. The transmission zeros are in general dependent on the size and thickness of the samples, but if size and thickness are high enough, so that the electromagnetic field in the SIR region (patches) is within the sample and substrate, then the transmission zeros depend only on the dielectric constant of the material. This means that in order to carry out accurate measurements this condition is necessary. In our case, the considered samples have an area much larger than the patches of the SIRs. The thickness may not be sufficient to guarantee the previous condition, but, as mentioned, our aim was simply to demonstrate the possibilities of the approach for multi-sensing. Note, however, that for comparison purposes, i.e., to evaluate if two apparently identical samples have differences, the thickness of the samples could be small if it is identical in both samples. It can be appreciated in Figure 8 that the samples in each pair are tiny separated; however, the SIRs are separated enough so that coupling between them can be discarded.

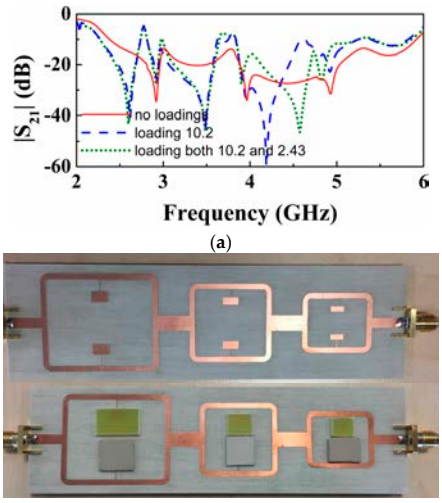

(**a**)

(**b**)

Figure 8. (**a**) Measured response (insertion loss) of the structure of Figure 5, compared with the response that results by loading one of the SIRs of every pair with a dielectric slab of dielectric constant 10.2, and by loading both SIRs of each pair with dielectric slabs of different dielectric constant (10.2 and 2.43); (**b**) The photograph of the fabricated structure corresponding to the symmetric case and when it is loaded with two different dielectric slabs for each pair of every section. The considered dimensions of the slabs are: for un-metalized *Rogers RO3010* (the bottom three loading slabs in Figure 2b), the average dimension is around 10 mm × 10 mm, and for Arlon CuClad 250 LX (the upper three loading pieces of slabs in Figure 2b), the biggest slab with 15.5 mm × 9.6 mm, the middle slab with 10 mm × 10 mm and the smallest slab with 9.3 mm × 8.0 mm, which is obvious that all slabs are much more bigger than the SIRs.

6. Conclusions

In conclusion, sensing structures based on splitter/combiner microstrip sections loaded with pairs of stepped impedance resonators (SIRs) have been studied in detail. First of all, we have considered a splitter/combiner loaded with a pair of SIRs situated in the mid-plane between the input and the output port. We have proposed a circuit schematic of the structure, which has been

validated by comparison of the circuit response with extracted parameters with electromagnetic and measured responses, where both symmetric and asymmetric configurations have been considered. It has been shown that by placing the SIRs at a distance of half wavelength from the T-junctions of the splitter/combiner section, the sensitivity and discrimination of the structure as sensor or comparator is optimized. Finally, a configuration, based on three splitter/combiner sections, able to simultaneously sense or compare three samples, has been proposed. We have also demonstrated the potential of this multi-sensing structure by asymmetrically loading the pairs of SIRs and measuring the frequency response, where frequency splitting reveals the presence of unbalanced loads.

Acknowledgments: This work has been supported by MINECO-Spain (project TEC2013-40600-R COM-SEN-RFID), by Generalitat de Catalunya (project 2014SGR-157). Ferran Martín has been awarded with an ICREA Academia Award. The work has been also supported by FEDER funds. Lijuan Su acknowledges the China Scholarship Council (CSC) for the grant 201306950011.

Author Contributions: Lijuan Su has executed the simulations and experimental work and all the authors have participated in the discussions to conceive the main idea of this paper. The paper has been mainly written by Lijuan Su and Ferran Martín, who is the director of the research.

Conflicts of Interest: The authors declare no conflict of interest.

References

1. He, X.-J.; Wang, Y.; Wang, J.-M.; Gui, T.-L. Thin film sensor based tip-shaped splits ring resonator metamaterial for microwave application. *Microsyst. Technol.* **2010**, *16*, 1735–1739. [CrossRef]
2. Cubukcu, E.; Zhang, S.; Park, Y.-S.; Bartal, G.; Zhang, X. Split ring resonator sensors for infrared detection of single molecular monolayers. *Appl. Phys. Lett.* **2009**, *95*, 043113. [CrossRef]
3. Driscoll, T.; Andreev, G.O.; Basov, D.N.; Palit, S.; Cho, S.Y.; Jokerst, N.M.; Smith, D.R. Tuned permeability in terahertz split ring resonators for devices and sensors. *Appl. Phys. Lett.* **2007**, *91*, 062511. [CrossRef]
4. Melik, R.; Unal, E.; Perkgoz, N.K.; Puttlitz, C.; Demir, H.V. Metamaterial-based wíreles strain sensors. *Appl. Phys. Lett.* **2009**, *95*, 011106. [CrossRef]
5. Yogi, R.A.; Parolia, R.S.; Karekar, R.N.; Aiyer, R.C. Microwave Microstrip ring resonador as a paper moisture sensor: Study with different grammage. *Meas. Sci. Technol.* **2002**, *13*, 1558–1562. [CrossRef]
6. Pattnaik, P.K.; Vijayaaditja, B.; Srinivas, T.; Selvarajan, A. Optical MEMS pressure sensor using ring resonador on a circular diaphragm. In Proceedings of the 2005 International Conference on MEMS, NANO and Smart Systems (ICMENS'05), Banff, AB, Canada, 24–27 July 2015.
7. Liu, X.; Xue, C.; Yan, S.; Xiong, J.; Zhang, W. Integrated high sensitivity displacement sensor based on micro ring resonador. In Proceedings of the 2009 4th IEEE International Conference Nano/Micro Engineered and Molecular Systems, Shenzhen, China, 5–8 January, 2009; pp. 1000–1003.
8. Mandel, C.; Kubina, B.; Schüßler, M.; Jakoby, R. Passive chipless wireless sensor for two-dimensional displacement measurement. In Proceedings of the 41st European Microwave Conference, Manchester, UK, 10–14 October 2011; pp. 79–82.
9. Puentes, M.; Weiss, C.; Schüßler, M.; Jakoby, R. Sensor array based on split ring resonators for analysis of organic tissues. In Proceedings of the IEEE MTT-S International Microwave Symposium Digest, Baltimore, MD, USA, 5–10 June 2011.
10. Damm, C.; Schussler, M.; Puentes, M.; Maune, H.; Maasch, M.; Jakoby, R. Artificial transmission lines for high sensitive microwave sensors. In Proceedings of the IEEE Sensors Conference, Christchurch, New Zealand, 25–28 October 2009; pp. 755–758.
11. Naqui, J.; Damm, C.; Wiens, A.; Jakoby, R.; Su, L.; Martín, F. Transmission lines loaded with pairs of magnetically coupled stepped impedance resonators (SIRs): Modeling and application to microwave sensors. In Proceedings of the IEEE MTT-S International Microwave Symposium (IMS), Tampa, FL, USA, 1–4 June 2014.
12. Naqui, J.; Damm, C.; Wiens, A.; Jakoby, R.; Su, L.; Mata-Contreras, J.; Martín, F. Transmission lines loaded with pairs of stepped impedance resonators: modeling and application to differential permittivity measurements. *IEEE Trans. Microw. Theory Tech.* **2016**, *64*, 3864–3877. [CrossRef]

13. Horestani, A.K.; Naqui, J.; Shaterian, Z.; Abbott, D.; Fumeaux, C.; Martín, F. Two-Dimensional Alignment and Displacement Sensor based on Movable Broadside-Coupled Split Ring Resonators. *Sens. Actuators A Phys.* **2014**, *210*, 18–24. [CrossRef]
14. Su, L.; Naqui, J.; Mata-Contreras, J.; Martín, F. Modeling metamaterial transmission lines loaded with pairs of coupled split ring resonators. *IEEE Ant. Wirel. Propag. Lett.* **2015**, *14*, 68–71. [CrossRef]
15. Su, L.; Naqui, J.; Mata-Contreras, J.; Martín, F. Modeling and applications of metamaterial transmission lines loaded with pairs of coupled complementary split ring resonators (CSRRs). *IEEE Ant. Wirel. Propag. Lett.* **2016**, *15*, 154–157. [CrossRef]
16. Naqui, J.; Durán-Sindreu, M.; Martín, F. Novel sensors based on the symmetry properties of split ring resonators (SRRs). *Sensors* **2011**, *11*, 7545–7553. [CrossRef] [PubMed]
17. Martín, F. *Artificial Transmission Lines for RF and Microwave Applications*; John Wiley: Hoboken, NI, USA, 2015.
18. Naqui, J. *Symmetry Properties in Transmission Lines Loaded with Electrically Small Resonators: Circuit Modeling and Applications*; Springer: Berlin/Heidelberg, Germany, 2016.
19. Naqui, J.; Durán-Sindreu, M.; Martín, F. Alignment and position sensors based on split ring resonators. *Sensors* **2012**, *12*, 11790–11797. [CrossRef]
20. Horestani, A.K.; Fumeaux, C.; Al-Sarawi, S.F.; Abbott, D. Displacement sensor based on diamond-shaped tapered split ring resonator. *IEEE Sens. J.* **2013**, *13*, 1153–1160. [CrossRef]
21. Horestani, A.K.; Abbott, D.; Fumeaux, C. Rotation sensor based on horn-shaped split ring resonator. *IEEE Sens. J.* **2013**, *13*, 3014–3015. [CrossRef]
22. Naqui, J.; Durán-Sindreu, M.; Martín, F. Transmission Lines Loaded with Bisymmetric Resonators and Applications. In Proceedings of the IEEE MTT-S International Microwave Symposium, Seattle, WA, USA, 2–7 June 2013.
23. Naqui, J.; Martín, F. Transmission lines loaded with bisymmetric resonators and their application to angular displacement and velocity sensors. *IEEE Trans. Microw. Theory Tech.* **2013**, *61*, 4700–4713. [CrossRef]
24. Naqui, J.; Martín, F. Angular displacement and velocity sensors based on electric-LC (ELC) loaded microstrip lines. *IEEE Sens. J.* **2014**, *14*, 939–940. [CrossRef]
25. Horestani, A.K.; Naqui, J.; Abbott, D.; Fumeaux, C.; Martín, F. Two-dimensional displacement and alignment sensor based on reflection coefficients of open microstrip lines loaded with split ring resonators. *Electron. Lett.* **2014**, *50*, 620–622. [CrossRef]
26. Makimoto, M.; Yamashita, S. Compact bandpass filters using stepped impedance resonators. *Proc. IEEE* **1979**, *67*, 16–19. [CrossRef]
27. Naqui, J.; Durán-Sindreu, M.; Bonache, J.; Martín, F. Implementation of shunt connected series resonators through stepped-impedance shunt stubs: Analysis and limitations. *IET Microw. Antennas Propag.* **2011**, *5*, 1336–1342. [CrossRef]
28. Choi, H.; Naylon, J.; Luzio, S.; Beutler, J.; Birchall, J.; Martin, C.; Porch, A. Design and in vitro interference test of microwave noninvasive blood glucose monitoring sensor. *IEEE Trans. Microw. Theory Tech.* **2015**, *63*, 3016–3025. [CrossRef] [PubMed]
29. Choi, H.; Naylon, J.; Luzio, S.; Beutler, J.; Porch, A. Design of continuous non-invasive blood glucose monitoring sensor based on a microwave split ring resonator. In Proceedings of the 2014 IEEE MTT-S International Microwave Workshop Series on RF and Wireless Technologies for Biomedical and Healthcare Applications (IMWS-Bio), London, UK, 8–10 December 2014.
30. Zarifi, M.H.; Farsinezhad, S.; Wiltshire, B.D.; Abdorrazaghi, M.; Mahdi, N.; Karl, P.; Daneshmand, M.; Shankar, K. Effect of phosphonate monolayer adsorbate on the microwave photoresponse of TiO2 nanotube membranes mounted on a planar double ring resonator. *Nanotechnology* **2016**, *27*, 375201. [CrossRef] [PubMed]
31. Zarifi, M.H.; Daneshmand, M. Wide dynamic range microwave planar coupled ring resonator for sensing applications. *Appl. Phys. Lett.* **2016**, *108*, 232906. [CrossRef]
32. Pozar, D.M. *Microwave Engineering*, 3rd ed.; John Wiley: Hoboken, NJ, USA, 2005.

Non-fundamental articles in the thesis

Micromachines15

"Miniature Microwave Notch Filters and Comparators Based on Transmission Lines Loaded with Stepped Impedance Resonators (SIRs)"

Su, Lijuan, Jordi Naqui, Javier Mata-Contreras, and Ferran Martín

Micromachines 7, no. 1 (2015): 1

micromachines

MDPI

Review

Miniature Microwave Notch Filters and Comparators Based on Transmission Lines Loaded with Stepped Impedance Resonators (SIRs)

Lijuan Su *,†, Jordi Naqui †, Javier Mata-Contreras and Ferran Martín

Received: 9 November 2015; Accepted: 19 December 2015; Published: 23 December 2015
Academic Editor: Behraad Bahreyni

Centre d'Investigació en Metamaterials per a la Innovació en Tecnologies Electrònica i de Comunicacions (CIMITEC), Departament d'Enginyeria Electrònica, Universitat Autònoma de Barcelona, 08193 Bellaterra (Barcelona), Spain; jordi.naqui@uab.cat (J.N.); franciscojavier.mata@uab.cat (J.M.-C.); ferran.martin@uab.cat (F.M.)

* Correspondence: lijuan.su@uab.cat; Tel.: +34-93-581-3522; Fax: +34-93-581-2600

† These authors contributed equally to this work.

Abstract: In this paper, different configurations of transmission lines loaded with stepped impedance resonators (SIRs) are reviewed. This includes microstrip lines loaded with pairs of SIRs, and coplanar waveguides (CPW) loaded with multi-section SIRs. Due to the high electric coupling between the line and the resonant elements, the structures are electrically small, *i.e.*, dimensions are small as compared to the wavelength at the fundamental resonance. The circuit models describing these structures are discussed and validated, and the potential applications as notch filters and comparators are highlighted.

Keywords: stepped impedance resonator (SIR); microstrip lines; coplanar waveguides; microwave notch filter; microwave comparator

1. Introduction

Stepped impedance resonators (SIRs) were proposed in the late 1970s as electrically small semi-lumped (planar) resonant elements useful for the realization of microwave filters [1–3]. These resonators are typically (although not exclusively) implemented by means of a tri-section structure where a narrow strip (high impedance section) is sandwiched between two wide (and hence low impedance) sections. The typical topology is depicted in Figure 1a, whereas Figure 1b shows the topology of the folded-SIR. At the fundamental resonance, both topologies exhibit an electric wall at the bi-section plane of the resonator (indicated in the figures), and there is an electric dipole moment orthogonal to this plane at such resonance frequency. Thus, both structures can be excited by means of a time-varying electric field, with a non-negligible component in the direction of the electric dipole moment. The folded-SIR, however, can be driven not only electrically, but also by means of a time-varying magnetic field applied orthogonal to the plane of the resonator, since there is also a magnetic dipole moment in that direction [4]. Folded SIRs are electrically small and can be useful as an alternative to split ring resonators (SRRs) [5] for the implementation of negative effective permeability metamaterials [4]. SIRs (including meandered SIRs and multi-section SIRs) and folded-SIRs have found numerous applications in microwave engineering, where size reduction has been a due [1–3,6,7].

In most of the previous applications, the resonators are coupled or attached to a host transmission line. A high level of miniaturization has been achieved in SIR-based coplanar waveguide (CPW) structures, where elliptic filters [6] and radiofrequency (RF) barcodes (or spectral

Micromachines **2015**, *6*, page–page

signature barcodes) [7] have been demonstrated. In microstrip technology, the so-called stepped impedance shunt stubs (SISS), consisting of half of the structure of Figure 1a directly in contact with a host microstrip line (Figure 1c), can be used for the implementation of notch filters, and a detailed analysis is reported in [8]. To a first order approximation the SISS can be modeled as a shunt connected series LC (inductance and capacitance) resonator.

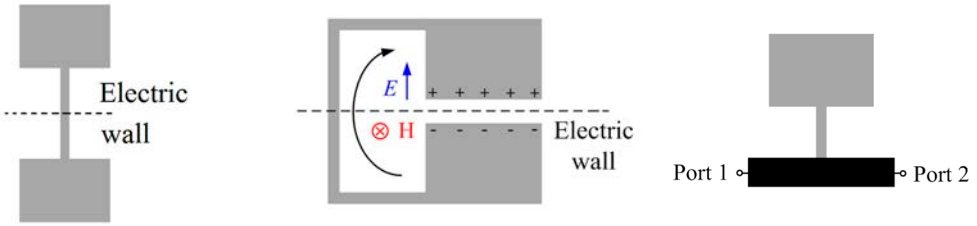

(**a**) (**b**) (**c**)

Figure 1. Typical topology of a tri-section stepped impedance resonators (SIR) (**a**), folded-SIR (**b**) and stepped impedance shunt stubs (SISS) attached to a microstrip line (depicted in black color) (**c**). The symmetry planes (for **a** and **b**), corresponding to an electric wall at the fundamental resonance, are indicated.

In this paper, we will review some of the applications of transmission lines loaded with SIRs. Specifically, the focus is on asymmetric structures, or symmetric structures that can be made asymmetric by appropriately loading the SIRs. We will consider both microstrip and CPW transmission lines loaded with SIRs, and the applications include dual-band microwave notch filters and comparators (*i.e.*, structures able to detect defects or abnormalities in samples, as compared to a reference). In Section 2, the microstrip line loaded with a pair of SISS is analyzed and modeled, and the model is validated experimentally. Section 3 deals with SIR-loaded CPWs, where two different structures are considered: A 5-section SIR-loaded CPW, where the central (wide) section of the 5-SIR is capacitively coupled to the CPW, and the same structure (5-SIR) but directly connected to the central strip of the CPW through metallic vias. In both cases, the 5-SIR is etched in the back substrate side of the CPW transmission line. The models of both structures are also presented and validated. In Section 4, the applicability of these SIR-based structures to dual-band notch filters and comparators is demonstrated. Finally, the main conclusions are highlighted in Section 5.

2. Microstrip Line Loaded with Pairs of SISSs

Figure 2a depicts a microstrip line section loaded with a pair of SISS. Assuming that the microstrip line is electrically short, and that there is a high impedance contrast between the narrow and wide sections of the SISS, the structure can be described by the lumped-element equivalent circuit shown in Figure 2b [9]. The model considers the general case of an asymmetric structure, where the SISS are modeled by the inductances L_1 and L_2, and the capacitances C_1 and C_2, and the microstrip line section is accounted for by the capacitance C and the inductance L. The coupling (magnetic) between the two SISS cannot be neglected and is modeled through the mutual inductance $-|M|$ (such coupling is negative because the currents in the inductances flow in opposite directions). Losses are not considered in the model.

The transmission zeros of the structure are given by those frequencies that null the reactance of the series branch, that is:

$$\omega_{\pm}^2 = \frac{A \pm \sqrt{B}}{LD} \tag{1}$$

with

$$A = L_1C_1 + L_2C_2$$

$$B = (L_1C_1 - L_2C_2)^2 + 4C_1C_2M^2$$

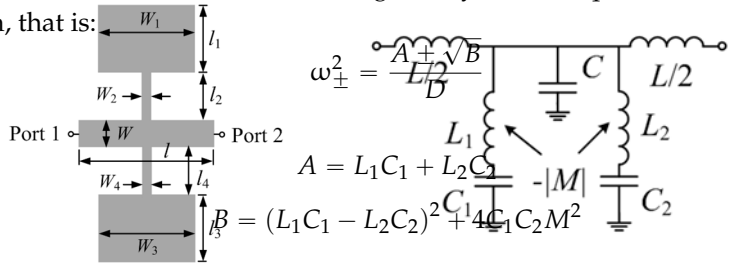

(**a**) (**b**)

Figure 2. (**a**) Microstrip line section loaded with a pair of SISS; (**b**) lumped element equivalent circuit model.

structures are considered: A 5-section SIR-loaded CPW, where the central (wide) section of the 5-SIR is capacitively coupled to the CPW, and the same structure (5-SIR) but directly connected to the central strip of the CPW through metallic vias. In both cases, the 5-SIR is etched in the back substrate side of the CPW transmission line. The models of both structures are also presented and validated. In Section 4, the applicability of these SIR-based structures to dual-band notch filters and comparators is demonstrated. Finally, the main conclusions are highlighted in Section 5.

2. Microstrip Lines Loaded with Pairs of SISSs

The transmission zeros of these structures are given by those frequencies that null the reactance of the series branch. That is, Equation (1) can be easily inferred from the transformed model of Figure 2b, depicted in Figure 3a. If the structure is symmetric (*i.e.*, $L_1 = L_2 \equiv L_r$ and $C_1 = C_2 \equiv C_r$), the mathematical solutions of Equation (1) are:

$$\omega_{\pm}^2 = \frac{A \pm \sqrt{B}}{D} \quad (1)$$

$$\omega_{\pm} = \frac{1}{\sqrt{(L_r \mp |M|) \cdot C_r}} \quad (2)$$

with

$$A = L_1 C_1 + L_2 C_2$$

$$B = (L_1 C_1 + L_2 C_2)^2 - 4C_1 C_2 (L_1 L_2 - M^2)$$

$$D = 2C_1 C_2 (L_1 L_2 - M^2)$$

Figure 2a depicts a microstrip line section loaded with a pair of SISS. Assuming that the microstrip line is electrically short, and that there is a high impedance contrast between the narrow and wide sections of the SISS, the structure can be described by the lumped element equivalent circuit shown in Figure 2b [9]. The model considers the general case of an asymmetric structure (two SISS can be symmetric and only one through the fundamental frequency of the SISS is negative because the currents in the coupled lines are opposite, the mutual coupling between the two inductors of two SISSs has the effect of increasing the notch frequency (symmetric case).

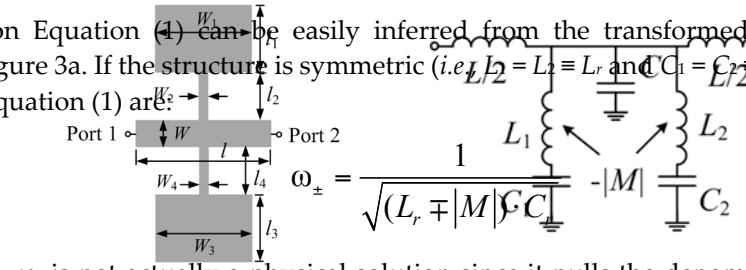

(a) (b)

Figure 2. (a) Microstrip line section loaded with a pair of SISS; (b) lumped element equivalent circuit model.

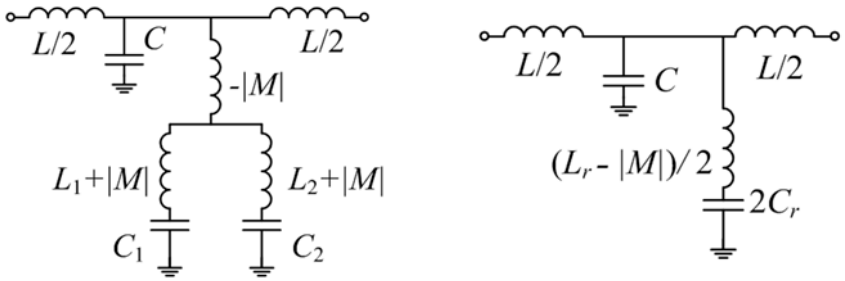

(a) (b)

Figure 3. (a) Equivalent circuit model to that of Figure 2b; (b) Equivalent circuit model for the symmetric case.

The validation of the model has been done by comparing full wave electromagnetic simulations with circuit simulations with extracted parameters of different structures. To extract the parameters, we have first considered microstrip lines loaded with a single SISS, following a procedure reported in [9], and similar to that reported in [10]. Then M has been obtained in the structures loaded with pairs of SISS by curve fitting. The agreement is good, as depicted in Figure 4, where the responses of three different structures are presented. One of such structures is symmetric, whereas the other two are obtained from the first one by increasing or decreasing one of the capacitances, as indicated. The responses of the microstrip lines loaded with single SISS are also indicated, so that the positive shift of the transmission zero for the symmetric structure can be appreciated. Note also that the agreement with the responses of the fabricated structures is also good (except by the effect of losses, not considered in the model, and fabrication related tolerances).

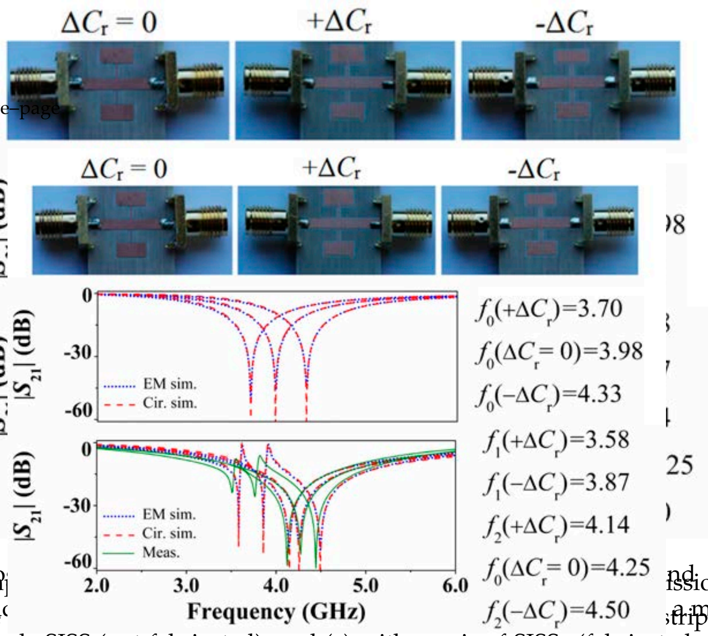

Figure 4. (**a**) Photograph of the fabricated SISS-loaded transmission lines, and transmission coefficient corresponding to the lossless electromagnetic and circuit simulations for a microstrip line loaded (**b**) with a single SISS (not fabricated), and (**c**) with a pair of SISSs (fabricated and shown in Figure 4a). In (**c**), measurements are included. The dimensions (in reference to Figure 2a) are $W = 1.83$ mm, $l = 15.9$ mm, $l_1 = l_2 = l_3 = l_4 = 2.6$ mm, $\Delta l = \pm 0.5$ mm, $W_1 = W_2 = 5.5$ mm, $W_3 = W_4 = 250$ μm. The substrate is *Rogers RO4003C* with considered dielectric constant $\varepsilon_r = 3.1$, thickness $h = 812.8$ μm, and loss tangent $\tan\delta = 0.0021$. The circuit values are $L = 1.80$ nH, $C = 0.57$ pF, $L_r = 2.46$ nH, $C_r = 0.65$ pF, $\pm\Delta C_r = \pm 0.15$ pF, and $M = -0.31$ nH. Reprinted with permission from [9].

3. CPW Loaded with 5-SIRs

Figure 5a depicts a CPW line section loaded with a 5S-SIR, etched in the back substrate side. The equivalent circuit model is depicted in Figure 5b [11], where L and C are the inductance and capacitance of the CPW line section, and L_1, L_2 and C_1, C_2 describe the inductances and capacitances of the middle and external sections, respectively, of the 5S-SIR. The 5-SIR is electrically coupled to the line through C_C, the broadside capacitance between the central strip of the CPW and the central section of the 5S-SIR. Finally, the magnetic coupling between the two inductances of the resonator is accounted for by M (negative, for the reasons explained in reference to the SISS-loaded microstrip line of the previous section). Since the considered structure is electrically short, it is reasonable to assume, to a first order approximation, that the slot mode is not generated (the ports in the electromagnetic simulation and the connectors in the measurement act as air bridges, effectively connecting the two ground plane regions).

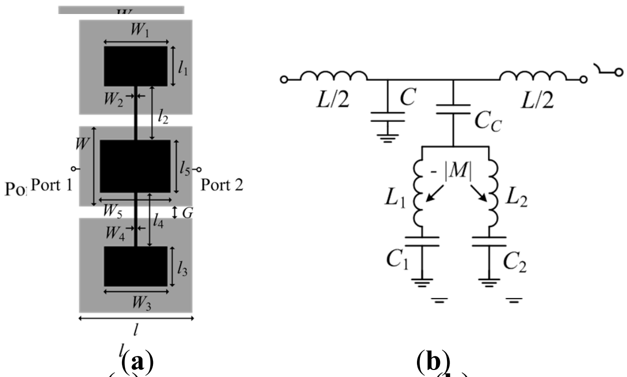

(**a**) (**b**)

Figure 5. (**a**) Coplanar waveguide (CPW) loaded with a 5S-SIR and (**b**) circuit model. Relevant dimensions are indicated.

In this case, the transmission zero frequencies are given by Equation (1) with:

$$A = C_1C_2(L_1 + L_2 - 2M) + C_c(L_1C_1 + L_2C_2)$$

In this case, the transmission zero frequencies are given by Equation (1) with:

$$A = C_1C_2(L_1 + L_2 - 2M) + C_c(L_1C_1 + L_2C_2)$$

$$B = C_1^2C_2^2(L_1 + L_2 - 2M)^2 + C_c^2(L_1C_1 - L_2C_2)^2 + 2C_cC_1C_2 \times \left\{L_1C_1(L_1 - L_2 - 2M) + L_2C_2(L_2 - L_1 - 2M) + 2M^2(C_1 + C_2 + C_c)\right\}$$

$$D = 2C_cC_1C_2(L_1L_2 - M^2)$$

If the structure is symmetric (*i.e.*, $L_1 = L_2 \equiv L_r$ and $C_1 = C_2 \equiv C_r$), the mathematical solutions are of the form:

$$\omega_+ = \frac{1}{\sqrt{(L_r - |M|)\dfrac{C_cC_r}{C_c + 2C_r}}} \quad (3a)$$

$$\omega_- = \frac{1}{\sqrt{(L_r + |M|)\cdot C_r}} \quad (3b)$$

However, ω_- is not actually a physical solution since it nulls the denominator of the reactance. Thus, the mutual coupling between the two inductors of the two 5-SIR has the effect of increasing the notch frequency for the symmetric case, *i.e.*, a behavior identical to the one of the microstrip line loaded with a pair of SIRs.

A variation of the previous CPW structure consists of a direct connection (through vias) of the 5-SIR to the central strip of the CPW, as depicted in Figure 6. This effectively shorts the capacitance C_c and the resulting circuit model is identical to the one depicted in Figure 2b.

The validation of the models of these CPW loaded structures has been also carried out by comparison between the frequency responses inferred from full-wave electromagnetic simulation and the responses derived from circuit simulation with the parameters conveniently extracted. For the structure of Figure 5 the parameter extraction method is more complex (as compared to the one of the previous section) since we have an additional parameter, namely, C_c (the details can be found in [11]). Indeed, the procedure first considers the structure with vias, so that all the parameters, except C_c, are determined; then C_c is determined by curve fitting.

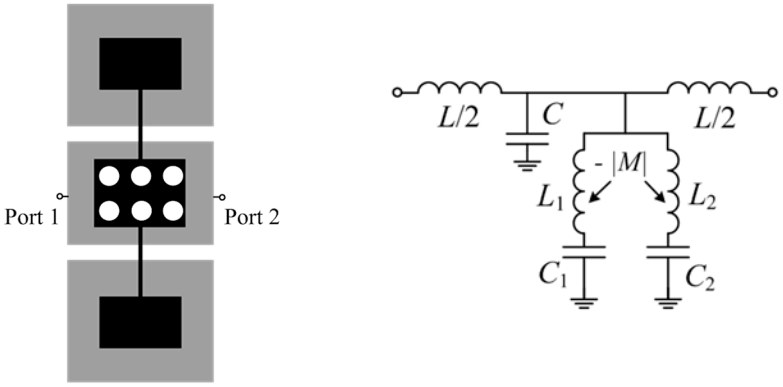

Figure 6. (**a**) CPW loaded with a 5S-SIR directly in contact to the central strip of the CPW through metallic vias, and (**b**) circuit model.

The three considered structures: For model validation are depicted in Figure 7 (dimensions and substrate parameters are indicated in the caption). One is symmetric and the other two asymmetric, where the two asymmetric structures are derived from the symmetric one by increasing or decreasing the area of one of the external patch capacitors, while the other external patch capacitors for these two asymmetric structures keeps the same dimensions as in the symmetric one. The element values of the

Micromachines **2015**, *6*, 6491–6501

decreasing the area of one of the external patch capacitors, while the other external patch capacitors for these two asymmetric structures keeps the same dimensions as in the symmetric one. The element values of the circuit model for the symmetric structure are L = 3.49 nH, C = 1.21 pF, L_r = 4.20 nH, C_r = 2.65 pF, M = −1.08 nH, and C_c = 3.62 pF. The comparison of the electromagnetic simulation (using Keysight Technologies Momentum, Keysight Technologies Inc., Santa Rosa, CA, USA) and circuit simulation of the symmetric structure is shown in Figure 8 (the measurement data is included as well), where good agreement can be appreciated, pointing out the validity of the proposed model.

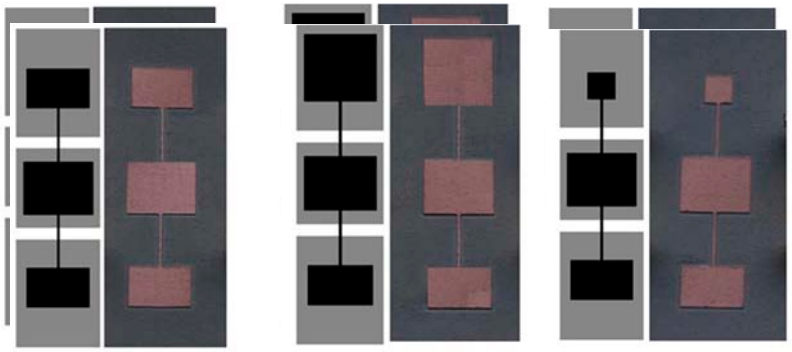

Figure 7. Considered 5S-SIR-loaded CPWs: **(a)** symmetric; **(b)** asymmetric with one capacitance larger; **(c)** asymmetric with one capacitance smaller. Dimensions are (in reference to Figure 5): for CPW lines: l_1 = 4.5 mm, W = 6 mm and G = 0.96 mm, corresponding to 50 Ω. For 5S-SIR: (**a**) W_1 = 4.5 mm, l_1 = 3 mm, W_2 = 4.5 mm, l_2 = 3 mm, W_3 = 4.5 mm, l_3 = 4 mm. For (**b**) W_1 = 7.5 mm and for (**c**) W_1 = 2 mm, with the other dimensions the same as in (**a**). The considered substrate (*Rogers RO3010*) has thickness of h = 0.635 mm and dielectric constant of ε_r = 11.2.

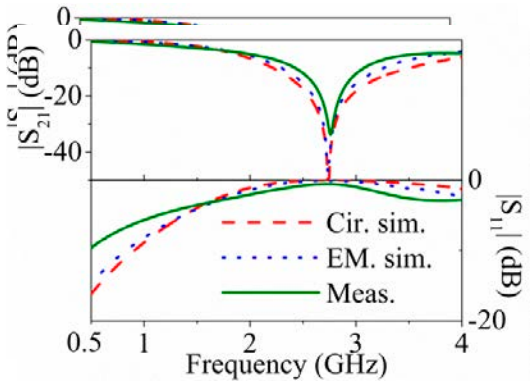

Figure 8. Electromagnetic simulation, circuit simulation and measurement response for the symmetric structure of Figure 7a. Reprinted with permission from [11].

For the asymmetric cases, the small external patch inductance and capacitance of the 5-SIR have been found to be 4.30 nH and 0.97 pF, and the big external patch inductance and capacitance of 5-SIR have been found to be 4.26 nH and 4.53 pF, whereas the mutual inductances for these two cases have been found to be −1.19 nH and −1.06 nH respectively, *i.e.*, very similar values, and also similar to the value corresponding to the symmetric structure. This indicates that M is scarcely dependent on the dimensions of the patch capacitances of the 5S-SIR, as expected. The resulting middle patch capacitances of small and big structures are 3.61 pF and 3.75 pF respectively. The agreement between the electromagnetic simulation, circuit simulation and measurement for the two asymmetric cases (Figures 9 and 10) is reasonable.

For the structures with vias, good agreement between circuit and electromagnetic simulation has been also obtained, as Figure 11 reveals (these structures have not been fabricated).

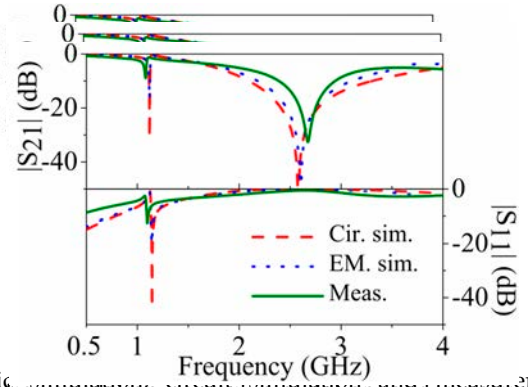

Figure 9. Electromagnetic simulation, circuit simulation and measurement response for the asymmetric structure of Figure 7b. Reprinted with permission from [11].

Figure 9. Electromagnetic simulation, circuit simulation and measurement response for the asymmetric structure of Figure 7b. Reprinted with permission from [11].
Figure 9. Electromagnetic simulation, circuit simulation and measurement response for the asymmetric structure of Figure 7b. Reprinted with permission from [11].

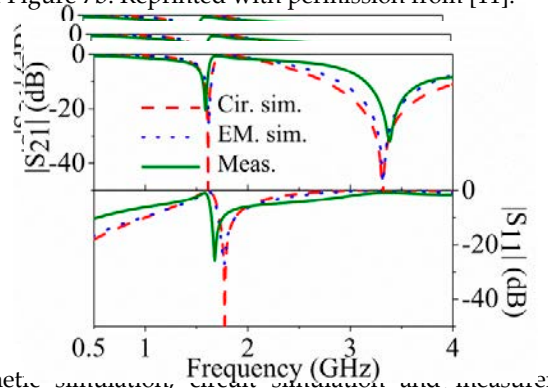

Figure 10. Electromagnetic simulation, circuit simulation and measurement response for the asymmetric structure of Figure 7c. Reprinted with permission from [11].

Figure 10. Electromagnetic simulation, circuit simulation and measurement response for the asymmetric structure of Figure 7c. Reprinted with permission from [11].
Figure 10. Electromagnetic simulation, circuit simulation and measurement response for the asymmetric structure of Figure 7c. Reprinted with permission from [11].

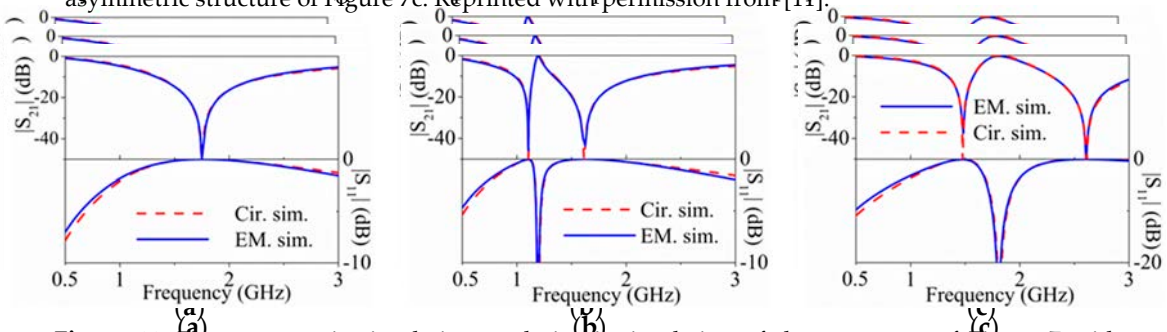

Figure 11. Electromagnetic simulation, and circuit simulation of the structures of Figure 7 with varying the central patch of the SIR and the location of the vias connecting the central strip of the CPW transmission line: (**a**) symmetric; (**b**) asymmetric with one capacitance larger; (**c**) asymmetric with one capacitance smaller.

Figure 11. Electromagnetic simulation, and circuit simulation of the structures of Figure 7 with varying the central patch of the SIR and the location of the vias connecting the central strip of the CPW transmission line: (**a**) symmetric; (**b**) asymmetric with one capacitance larger; (**c**) asymmetric with one capacitance smaller.
Figure 11. Electromagnetic simulation, and circuit simulation of the structures of Figure 7 with varying the central patch of the SIR and the location of the vias connecting the central strip of the CPW transmission line: (**a**) symmetric; (**b**) asymmetric with one capacitance larger; (**c**) asymmetric with one capacitance smaller.

4. Application to Microwave Notch Filters and Comparators

4. Application to Microwave Notch Filters and Comparators
4. Application to Microwave Notch Filters and Comparators
4. Application to Microwave Notch Filters and Comparators

According to the results of the previous subsections, the symmetric structures can be used as single broadband notch filters. Dual-band functionality is achieved by asymmetrically loading the single broadband notch filters. Dual-band functionality is achieved by asymmetrically loading the SISS-loaded microstrip line and the SIR-loaded CPW without vias, exhibiting both notches a very narrow notch, whereas for the SIR-loaded CPW without vias, exhibiting both notches as comparable. The reason is that for the CPW with vias there is not a coupling capacitance (C_c) in the shunt branch. Therefore, the CPW is not influenced by the mutual capacitance (C_c). Thus, depending on the application (*i.e.*, notch width requirement), one structure or the other may be more convenient.

According to the results of the previous subsections, the symmetric structures can be used as single broadband notch filters. Dual-band functionality is achieved by asymmetrically loading the SISS-loaded microstrip line and the SIR-loaded CPW without vias, exhibiting both notches as very narrow notch, whereas for the SIR-loaded CPW without vias, exhibiting both notches as comparable. The reason is that for the CPW with vias there is not a coupling capacitance (C_c) in the shunt branch. Therefore, the CPW is not influenced by the mutual capacitance (C_c). Thus, depending on the application (*i.e.*, notch width requirement), one structure or the other may be more convenient.
According to the results of the previous subsections, the symmetric structures can be used as single broadband notch filters. Dual-band functionality is achieved by asymmetrically loading the SISS-loaded microstrip line and the SIR-loaded CPW without vias, exhibiting both notches as very narrow notch, whereas for the SIR-loaded CPW without vias, exhibiting both notches as comparable. The reason is that for the CPW with vias there is not a coupling capacitance (C_c) in the shunt branch. Therefore, the CPW is not influenced by the mutual capacitance (C_c). Thus, depending on the application (*i.e.*, notch width requirement), one structure or the other may be more convenient.

In order to use the structures as microwave comparators, the SIR or SISS loaded lines must be symmetric. If line loading (dielectric or metallic) is symmetric, then the structure is expected to exhibit a single notch in the frequency response, whereas if the loading is asymmetric, two notches

In order to use the structures as microwave comparators, the SIR or SISS loaded lines must be symmetric. If line loading (dielectric or metallic) is symmetric, then the structure is expected to exhibit a single notch in the frequency response, whereas if the loading is asymmetric, two notches
In order to use the structures as microwave comparators, the SIR or SISS loaded lines must be symmetric. If line loading (dielectric or metallic) is symmetric, then the structure is expected to exhibit a single notch in the frequency response, whereas if the loading is asymmetric, two notches

depending on the application (*i.e.*, notch width requirement), one structure or the other may be more convenient.

In order to use the structures as microwave comparators, the SIR or SISS loaded lines must be symmetric. If line loading (dielectric or metallic) is symmetric, then the structure is expected to exhibit a single notch in the frequency response, whereas if the loading is asymmetric, two notches separated a distance depending on the level of asymmetry are expected. Thus, the reported structures are useful to determine differences between a sample under test (SUT) and a reference sample (*i.e.*, compare the two samples). To demonstrate the potential of these structures as comparators, the symmetric structure of Figure 7a has been loaded with a dielectric load (consisting of a small piece of Rogers RO3010 substrate with the copper removed from both substrate sides) placed on top of one of the patch capacitances. The measured response, shown in Figure 12, exhibits two notches, indicative of the asymmetric loading. Then, we have repeated the experiment by using the same piece of substrate but keeping the metal layers (metallic loading). The measured response is also included in Figure 12, where it can be seen that the depth of the first notch is superior (as compared to dielectric loading), since the structure is more sensitive to the effects of a metallic layer placed on top of one of the patch capacitances. The reason is that adding a metal increases more effectively the capacitance of the patch, as compared to dielectric loading.

As sensors, the SIR based structures discussed in this paper belong to the category of resonance frequency splitting sensors. However, there is also another type of sensing structures based on symmetry properties: Coupling modulated resonance based sensors [12]. In this case, the sensor is based on a transmission line loaded with a single (symmetric) resonant element, the symmetry plane of the line and resonator are aligned, and these planes are of different electromagnetic nature. One of them is a magnetic wall, and the other one is an electric wall. Under these conditions, the resonator is not coupled to the line. However, by truncating symmetry line to resonator coupling arises, producing a notch in the transmission coefficient, and the depth of this notch depends on the level of asymmetry, since it determines the coupling level. Several sensing strategies based on these principles have been proposed (several of them by the authors) [13–17]. For instance, split ring resonant elements or complementary split rings have been used for sensing purposes. By using SIRs, the sensors are small (this extends also to notch filters), since the coupling with the host line is broadside. This is the main advantage over other sensors of this type based on other resonant elements. Also, ground plane etching is avoided (contrary to sensors based on complementary resonant elements).

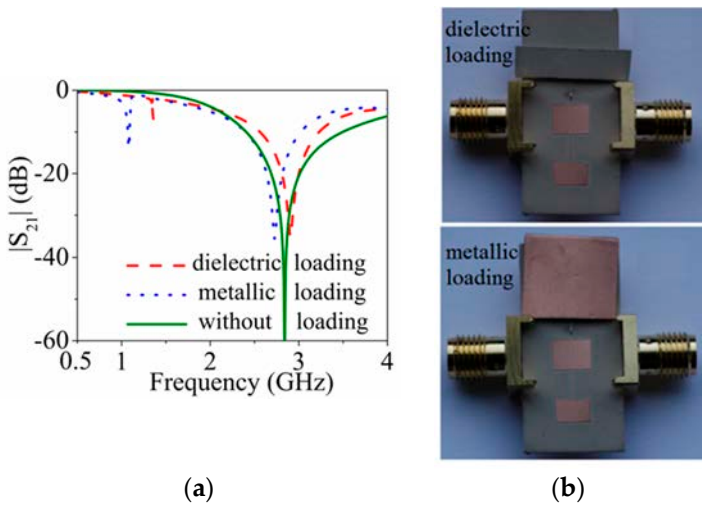

(**a**) (**b**)

Figure 12. (**a**) Measured responses of the structure of Figure 7a with asymmetric dielectric loading and metallic loading; (**b**) fabricated prototypes loaded with dielectric loading and metallic loading, respectively. Reprinted with permission from [11].

Concerning the demand of SIR based sensors or comparators in microwaves, applications include sensors for dielectric characterization, quality control, and microfluidics, among others. In the paper, proof-of-concept demonstrators are presented. Since the electric field below the patches is high, significant sensitivity can be potentially achieved by using multilayer structures and arrangement of the structures under test in those regions.

Concerning the demand of SIR based sensors or comparators in microwaves, applications include sensors for dielectric characterization, quality control, and microfluidics, among others. In the paper, proof-of-concept demonstrators are presented. Since the electric field below the patches is high, significant sensitivity can be potentially achieved by using multilayer structures and arrangement of the structures under test in those regions.

5. Conclusions

In summary, it has been shown that miniature microwave notch filters and comparators can be implemented by means of transmission lines loaded with stepped impedance resonators (SIRs), including stepped impedance shunt stubs (SISS) in microstrip technology, and 5-section SIRs (5-SIRs) in coplanar waveguide (CPW) technology. The lumped element equivalent circuit models of these electrically small planar structures have been proposed and validated, and an analysis that has lead us to find the position of the transmission zero frequencies has been carried out. Finally, a proof of concept of microwave comparators has been presented.

Acknowledgments: This work has been supported by MINECO (Spain) under project TEC2013-40600-R, by AGAUR-Generalitat de Catalunya under project 2014SGR-157, and by FEDER funds. Ferran Martín is in debt to Institució Catalana de Recerca i Estudis Avançats (ICREA) for supporting his work. Lijuan Su thanks China Scholarship Council (CSC) for supporting her work in UAB through the grant No. 201306950011.

Author Contributions: Lijuan Su has designed and analyzed the CPW structures, Jordi Naqui has designed and analyzed the microstrip structures, Javier Mata has carried out several calculations of the analysis carried out in the CPW structures, and Ferran Martín has acted as director of the research and has written the present manuscript.

Conflicts of Interest: The authors declare no conflict of interest.

References

1. Makimoto, M.; Sadahilo, Y. Compact bandpass filters using stepped impedance resonators. *IEEE Proc.* **1979**, *67*, 16–19. [CrossRef]
2. Hualiang, Z.; Chen, K.J. Miniaturized coplanar waveguide bandpass filters using multisection stepped-impedance resonators. *IEEE Trans. Microw. Theory Tech.* **2006**, *54*, 1090–1095. [CrossRef]
3. Shi, J.; Quan, X. Novel balanced dual-band bandpass filter using coupled stepped-impedance resonators. *IEEE Microw. Wirel. Compon. Lett.* **2010**, *20*, 19–21.
4. Ferran, M. *Artificial Transmission Lines for RF and Microwave Applications*; John Wiley & Sons: Hoboken, NJ, USA, 2015.
5. Pendry, J.B.; Holden, A.J.; Robbins, D.J.; Stewart, W.J. Magnetism from conductors and enhanced nonlinear phenomena. *IEEE Trans. Microw. Theory. Tech.* **1999**, *47*, 2075–2084. [CrossRef]
6. Durán-Sindreu, M.; Bonache, J.; Martín, F. Compact elliptic-function coplanar waveguide low-pass filters using backside metallic patterns. *IEEE Microw. Wirel. Compon. Lett.* **2010**, *20*, 601–603. [CrossRef]
7. Naqui, J.; Durán-Sindreu, M.; Martín, F. On the symmetry properties of coplanar waveguides loaded with symmetric resonators: Analysis and potential applications. In Proceedings of the IEEE MTT-S International Microwave Symposium Digest (MTT), Montreal, QC, Canada, 17–22 June 2012.
8. Naqui, J.; Durán-Sindreu, M.; Bonache, J.; Martín, F. Implementation of shunt connected series resonators through stepped-impedance shunt stubs: Analysis and limitations. *IET Microw. Antennas Propag.* **2011**, *5*, 1336–1342. [CrossRef]
9. Naqui, J.; Damm, C.; Wein, A.; Jakoby, R.; Su, L.; Martín, F. Transmission lines loaded with pairs of magnetically coupled stepped impedance resonators (SIRs): Modeling and application to microwave sensors. In Proceedings of the IEEE MTT-S International Microwave Symposium (IMS), Tampa, FL, USA, 1–6 June 2014.
10. Bonache, J.; Gil, M.; Gil, I.; Garcia, J.; Martín, F. On the electrical characteristics of complementary metamaterial resonators. *IEEE Microw. Wirel. Compon. Lett.* **2006**, *16*, 543–545. [CrossRef]

11. Su, L.; Naqui, J.; Mata, J.; Martín, F. Coplanar Waveguides Loaded with Symmetric and Asymmetric Multi-Section Stepped Impedance Resonators (SIRs): Modeling and Potential Applications. *Microw. Opt. Technol. Lett.* **2016**, in press.
12. Naqui, J. *Symmery Properties in Transmission Lines Loaded with Electrically Small Resonators: Circuit Modeling and Applications*; Springer: New York, NY, USA, 2016.
13. Naqui, J.; Durán-Sindreu, M.; Martín, F. Novel sensors based on the symmetry properties of split ring resonators (SRRs). *Sensors* **2011**, *11*, 7545–7553. [CrossRef] [PubMed]
14. Naqui, J.; Durán-Sindreu, M.; Martín, F. Alignment and position sensors based on split ring resonators. *Sensors* **2012**, *12*, 11790–11797. [CrossRef]
15. Horestani, A.K.; Fumeaux, C.; Al-Sarawi, S.; Abbott, D. Displacement sensor based on diamond-shaped tapered split ring resonator. *IEEE Sens. J.* **2013**, *13*, 1153–1160. [CrossRef]
16. Horestani, A.K.; Abbott, D.; Fumeaux, C. Rotation sensor based on horn-shaped split ring resonator. *IEEE Sens. J.* **2013**, *13*, 3014–3015. [CrossRef]
17. Horestani, A.K.; Naqui, J.; Shaterian, Z.; Abbott, D.; Fumeaux, C.; Martín, F. Two-dimensional alignment and displacement sensor based on movable broadside-coupled split ring resonators. *Sens. Actuators A* **2014**, *210*, 18–24. [CrossRef]

MOTL16 (11)

"Coplanar waveguides loaded with symmetric and asymmetric pairs of slotted stepped impedance resonators: Modeling, applications, and comparison to SIR - loaded CPWs"

Naqui, Jordi, Lijuan Su, Javier Mata, and Ferran Martín

Microwave and Optical Technology Letters 58, no. 11 (2016): 2741-2745

Coplanar Waveguides (CPWs) Loaded with Symmetric and Asymmetric Pairs of Slotted Stepped Impedance Resonators (S-SIRs): Modeling, Applications and Comparison to SIR-loaded CPWs

Jordi Naqui, Lijuan Su, Javier Mata, and Ferran Martín

CIMITEC, Departament d'Enginyeria Electrònica
Universitat Autònoma de Barcelona, 08193 Bellaterra (Barcelona), Spain
Corresponding author: Ferran.Martin@uab.es
Fax: 34 93 581 26 00

Abstract

This paper is focused on the analysis and modeling of coplanar waveguide (CPW) transmission lines loaded with pairs of slotted stepped impedance resonators (S-SIRs), etched in the ground planes. These structures may be described by a pair of parallel-connected transmission lines, each one loaded with a series-connected parallel resonator, and with mutual capacitive coupling between such resonators. If the structures are symmetric, the transmission coefficient exhibits a single transmission zero, related to the fundamental resonance of the SIRs, though perturbed by the effects of mutual coupling. However, if symmetry is disrupted, two notches appear, separated a distance that depends on the level of asymmetry, coupling, and CPW length. Therefore, these structures may be useful for the implementation of differential sensors and comparators. It is shown that if the S-SIR-loaded CPWs are electrically small, the structures can be modeled by a lumped element equivalent circuit. Using this model, the resonance frequencies are obtained analytically. The proposed lumped element model is validated through electromagnetic simulation and experiment, and a prototype comparator loaded with dielectric samples is fabricated and measured. Finally, the circuit model of the structure is compared to that of SIR-loaded CPW transmission lines. Despite the fact that the lumped element equivalent circuits of these structures are completely different, the equations providing the transmission zeros are formally identical.

KEYWORDS: Coplanar waveguide (CPW), stepped impedance resonators (SIRs), slot resonators, lumped element equivalent circuits.

1. Introduction

Stepped impedance resonators (SIRs) are electrically small resonators useful for the implementation of planar filters in microstrip and coplanar waveguide (CPW) technology [1]. Although SIRs are usually implemented as metallic resonators, the complementary counterparts (slotted SIRs –S-SIRs) are also of interest for microwave circuit design. In particular, dumbbell-shaped slotted SIRs symmetrically etched in the ground plane of a microstrip line are useful to create notches in the frequency response, and have been modeled as parallel resonant tanks series-connected to the line [2].

In this paper, we investigate the behavior of CPW transmission lines loaded with pairs of coupled S-SIRs for the implementation of differential microwave sensors and comparators. Such CPW structures can be an alternative to state-of-the-art microwave sensors and comparators for dielectric characterization of materials (organic tissue and biological sample analysis, defects or abnormalities in materials, etc.) [3], [4]. The main advantage of the proposed CPW structures is the major robustness against variable environmental conditions provided by a differential measurement.

Recently, a microstrip structure loaded with pairs of coupled metallic SIRs was investigated as a potential candidate for differential sensing [5], and a preliminary prototype sensor operative at the V-band was presented. As compared to the structures therein, the S-SIR-loaded CPW structures presented in this paper may take advantage of a superior sensitivity, as well as a simpler fabrication complexity due to the uni-planar metallic configuration of the CPW structure. The sensing principle is based on the relative variation of the edge capacitance of one of the slotted SIRs with regard to the other, experienced when a pair of samples under test (SUT) is located on top of them. It is expected that the effects of the SUT are more pronounced when they are placed on top of edge capacitances than on top of broad-side capacitances (as in SIR-loaded microstrip lines), and this explains the sensitivity enhancement expected for the structures studied in this paper. The sensing principle is thus based on symmetry disruption, causing the presence of two notches in the transmission coefficient separated a distance that depends (although not exclusively) on the level of asymmetry. A frequency-splitting sensing principle was proposed for the design of spatial sensors based on microstrip lines loaded with split ring resonators in [6].

The analysis and modeling of these CPW structures loaded with symmetric and asymmetric S-SIR pairs is necessary for design purposes. This is the actual challenge of this work, where electric coupling between the two S-SIRs is included for an accurate modeling. The proposed lumped element equivalent circuit model is validated through parameter extraction and comparison of the circuit response (for both symmetric and asymmetric configurations) to electromagnetic simulations and measurements. The viability of the proposed structure as comparator is then demonstrated. Finally, these S-SIR-loaded CPWs are compared to CPWs loaded with SIRs (indeed 5-section SIRs – 5S-SIRs) etched in the back substrate side [7], where it will be shown that, subjected to certain element mapping, the equations giving the pair of transmission zero frequencies (asymmetric case) in both structures (inferred from the corresponding models) are identical. An explanation of this fact is also given at the end of the paper.

2. Topology and model of the S-SIR-loaded CPW

Fig. 1 (a) shows the typical topology of a CPW loaded with a pair of S-SIRs. Although the topology shown in Fig. 1(a) is symmetric with regard to the line axis, the analysis will be carried out by considering the general case of arbitrary S-SIR dimensions. The modeling of CPWs loaded with slotted patterns (not necessarily S-SIRs), has been performed in several works [8]-[10]. However, in these publications the analysis corresponds to symmetric structures. Exceptionally, asymmetric structures providing more than one notch in the transmission coefficient are reported in [9]. Nevertheless, the reported model in [9] does not account for the effects of asymmetry in frequency splitting, and coupling between resonant elements is not modeled. In [11], a circuit model for a CPW-slotline cross was presented. The model accounts for the effects of asymmetry in the slotlines (generating the slot mode in the CPW structure), but this model is based on the decomposition of the two fundamental CPW modes (even and odd) into different ports, resulting in a complex 6-port circuit model, accurate but complex for design purposes.

The proposed model for the structure of Fig. 1(a) is depicted in Fig. 1(b). It is assumed that the structure can be described as a pair of split transmission lines (the central strip being a common conductor), each one loaded with a series-connected parallel resonant tank (L_{si}-C_{si} with i = 1,2). The electrical length and characteristic impedance of the transmission line sections are θ and $2Z_c$ (where Z_c is the CPW characteristic impedance), respectively. It has been found that for reasonable widths of the CPW central strip, electric coupling between the resonators arises, and this effect is accounted for by including a mutual capacitance, C_m, in the model [12],[13]. Except for the symmetric case, the analytical solution for the transmission zero frequencies (resonance frequencies from now on) in the circuit of Fig. 1(b) is not straightforward. However, if the CPW transmission line is electrically short, we can describe it by its inductance, L, and capacitance, C, resulting in the model depicted in Fig. 1(c). It is apparent that a necessary condition to connect capacitively the resonators (by C_m) is a non-zero potential difference between the two lateral metallic planes. Accordingly, the slot mode must propagate through the structure, and this occurs only when the structure is asymmetric. By contrast, for a symmetric structure (i.e. $L_{s1} = L_{s2} \equiv L_s$ and $C_{s1} = C_{s2} \equiv C_s$), the circuit model can be simplified to that shown in Fig. 1(d). Indeed, this is the typical circuit model of S-SIR-loaded transmission lines reported in the literature (where inter-resonator coupling only shifts the resonance frequency according to the proposed circuit model). Note that losses are not considered in the models.

The analytical calculation of the resonance frequencies in the circuit of Fig. 1(c) is cumbersome, but such frequencies can be expressed in a relatively closed form. To this end, we have obtained the reactance of the series branch in the π-model of Fig 1(c). By calculating such reactance and the corresponding poles, a bi-quadratic equation results,

$$A\omega^4 + B\omega^2 + D = 0 \tag{1}$$

where the coefficients are:

$$A = 4LL_{s1}L_{s2}(C_{s1}C_{s2} - C_m^2) \tag{2a}$$

$$B = -\left[L_{s1}L_{s2}(C_{s1} + C_{s2}) - 2L_{s1}L_{s2}C_m + 4L(C_{s1}L_{s1} + C_{s2}L_{s2})\right] \tag{2b}$$

$$D = L_{s1} + L_{s2} + 4L \tag{2c}$$

and the solutions are of the form

$$\omega_{\pm}^{2} = \frac{A' \pm \sqrt{B'}}{D'} \tag{3}$$

with

$$A' = L_{s1}L_{s2}(C_{s1} + C_{s2} - 2C_m) + 4L(L_{s1}C_{s1} + L_{s2}C_{s2}) \tag{4a}$$

$$\begin{aligned} B' = {} & L_{s1}^2 L_{s2}^2 (C_{s1} + C_{s2} - 2C_m)^2 + 16L^2 (L_{s1}C_{s1} - L_{s2}C_{s2})^2 + 8LL_{s1}L_{s2} \times \\ & \left\{ L_{s1}C_{s1}(C_{s1} - C_{s2} - 2C_m) + L_{s2}C_{s2}(C_{s2} - C_{s1} - 2C_m) + 2C_m^2 (L_{s1} + L_{s2} + 4L) \right\} \end{aligned} \tag{4b}$$

$$D' = 8LL_{s1}L_{s2}(C_{s1}C_{s2} - C_m^2) \tag{4c}$$

If the structure is symmetric (i.e., $L_{s1} = L_{s2} \equiv L_s$ and $C_{s1} = C_{s2} \equiv C_s$), the mathematical solutions are:

$$\omega_{+} = \frac{1}{\sqrt{(C_s + C_m)\dfrac{2LL_s}{2L + L_s}}} \tag{5a}$$

$$\omega_{-} = \frac{1}{\sqrt{L_s(C_s - C_m)}} = \frac{\omega_0}{\sqrt{1 - k_e}} \tag{5b}$$

where $\omega_0 = (L_s C_s)^{-1}$ and $k_e = C_m/C_s$ is the electric coupling coefficient. However, ω_+ is not actually a solution since it nulls the numerator of the reactance. This can also be derived by inspection of the circuit in Fig. 1(d).

3. Validation of the model

The models of Fig. 1 have been validated by considering three CPW structures loaded with different pairs of S-SIRs (see Fig. 2): a symmetric pair, and two asymmetric pairs where the width w_2 of one of the resonators is modified (this width changes both C_s and L_s of the corresponding resonator). First, the lumped element values of the circuit in Fig. 1(d) have been obtained assuming symmetric pairs with l = 7 mm. Thereby, for each w_2, the inductance, L_s, and the capacitance in the presence of coupling, $C_{seff} = C_s - C_m$, is obtained for each resonator. The parameters have been extracted from electromagnetic simulation (conductor and substrate losses are not considered) using the method reported in [14], [15]. Next, for the asymmetric structures, modeled by the circuit in Fig. 1(c), we have determined C_m by curve fitting. The extracted parameters are indicated in the caption of Fig. 3. Finally, since the fabricated CPW structures are not electrically small, we have included four transmission line sections like those represented in Fig. 1(b). It should be noted that the resonance frequencies depend on the CPW length, l. All the frequency responses are plotted in Fig. 3, revealing that there is good agreement between simulations and measurements.

A potential application of these structures is related to differential sensors and comparators based on frequency-splitting, since two split resonance frequencies appear when symmetry is broken. Particularly, Fig. 4 shows the response of the symmetric structure of Fig. 2(a) when it is symmetrically loaded with a pair of dielectric slabs of dielectric constant 3.38, and when it is asymmetrically loaded with a single slab (see inset). In the latter case, the asymmetry is clearly manifested by the presence of two notches. Note that for the asymmetric case, the response overall shifts to the right since subtracting one slab is equivalent to reduce one of the S-SIR capacitances.

4. Comparison to SIR-loaded CPWs

In [7], CPW transmission lines loaded with 5-section SIRs etched in the back substrate side were studied, and a circuit model for these lines was proposed. It is interesting to highlight that the bi-quadratic equation providing the transmission zeros in the SIR-loaded CPW is identical to equation (1) with the coefficients given by (2), provided the following mapping is satisfied: $C_c \leftrightarrow 4L$; $C_{1,2} \leftrightarrow L_{s1,2}$; $L_{1,2} \leftrightarrow C_{s1,2}$; $M \leftrightarrow C_m$, where C_c, $C_{1,2}$, $L_{1,2}$ and M are the reactive elements of the circuit model of the SIR-loaded CPW [7]. Thus, with this mapping, the pair of transmission zero frequencies of the two structures, given by (3) using (4) for S-SIR-loaded CPWs of the present paper, are also identical. Note, however, that the degenerate (and hence single) solutions for the symmetric cases occur at different frequencies (i.e., the upper frequency for the SIR-loaded CPW and the lower frequency for the S-SIR-loaded CPW). This fact explains that for the 5-SIR-loaded CPW, when symmetry is disrupted, the two resulting notches are either located at both sides of the single notch corresponding to the symmetric case, or below it [7], whereas for the S-SIR-loaded CPW, when symmetry is disrupted, the two resulting notches are either located at both sides of the single notch corresponding to the symmetric case, or above it (see Fig. 3).

Interestingly, despite the fact that the SIR- and S-SIR-loaded CPW transmission lines are significantly different, with the previous indicated mapping the expressions providing the resonance frequencies are identical for both structures. Neither these structures are dual, nor are the equivalent circuits circuit duals [16]. However, the poles of the dual circuit of the resonant shunt branch of the SIR-loaded CPW, depicted in Fig. 5, are identical to those of the circuit of Fig. 3(c), and this explains the formal coincidence of the two equations providing the transmission zero frequencies.

5. Conclusion

In this work, we have analyzed asymmetric CPW-based structures where the CPW central strip is kept unaltered whereas S-SIRs are etched on the lateral metallic planes (ground planes in conventional CPW implementations). A novel strategy for modeling symmetric/asymmetric configurations is reported, where the structures are viewed as two parallel-connected loaded transmission lines. A lumped element equivalent circuit of the structure has been proposed, and from this model the pair of transmission zeros have been analytically inferred. The model has been experimentally validated and the potential of the structure as differential sensor or comparator has been pointed out by means of a proof-of-concept device comparator. Finally, it has been demonstrated that the analytical expressions for the pair of transmission zeros in these S-SIR-loaded CPW structures are identical to those of the SIR-loaded CPWs, provided a simple mapping between elements is applied.

Acknowledgements

This work has been supported by MINECO (Spain) under project TEC2013-40600-R and FEDER Funds. Thanks are also given to AGAUR-Generalitat de Catalunya for partially funding this research activity through the project 2014SGR-157. Ferran Martín is in debt to ICREA for supporting his work. Lijuan Su thanks China Scholarship Council (CSC) for supporting her work in UAB through the grant No. 201306950011.

References

[1] M. Makimoto and S. Yamashita, Compact bandpass filters using stepped impedance resonators, Proc. IEEE, vol. 67, pp. 16-19, Jan. 1979.

[2] D. Ahn, J-S. Park, C-S. Kim, J. Kim, Y. Qian, and T. Itoh, A design of the low-pass filter using the novel microstrip defected ground structure, IEEE Trans. Microw. Theory Techn., vol. 49, pp. 86-93, Jan. 2001.

[3] M. Puentes, C. Weiß, M. Schüßler, and R. Jakoby, Sensor array based on split ring resonators for analysis of organic tissues, IEEE MTT-S International Microwave Symposium Digest, Baltimore, USA, June 2011.

[4] T. Chretiennot, D. Dubuc and K. Grenier, Optimized electromagnetic interaction microwave resonator/microfluidic channel for enhanced liquid bio-sensor, Proc. European Microwave Conference, Nuremberg, Germany, October 2013.

[5] J. Naqui, C. Damm, A. Wiens, R. Jakoby, L. Su, and F. Martín, Transmission lines loaded with pairs of magnetically coupled stepped impedance resonators (SIRs): modeling and application to microwave sensors, IEEE MTT-S Int. Microwave Symp., Jun. 2014, Tampa, FL (USA).

[6] A. K. Horestani, J. Naqui, Z. Shaterian, D. Abbott, C. Fumeaux, and F. Martín, Two-dimensional alignment and displacement sensor based on movable broadside-coupled split ring resonators, Sens. Act. A, vol. 210, pp. 18-24, Apr. 2014.

[7] L. Su, J. Naqui, J. Mata-Contreras, and F. Martín, Coplanar waveguides loaded with symmetric and asymmetric multisection stepped impedance resonators: modeling and potential applications, Microw. Opt. Technol. Lett., vol 58, pp. 722–726, Mar. 2016.

[8] J.-S. Lim, C.-S. Kim, Y-T. Lee, D. Ahn, and S. Nam, A Spiral-Shaped Defected Ground Structure for Coplanar Waveguide, IEEE Microw. Wirel. Compon. Lett., vol. 12, pp. 330-332, Sep. 2002.

[9] A.M.E. Safwat, F. Podevin, P. Ferrari, and A. Vilcot, Tunable bandstop defected ground structure resonator using reconfigurable dumbbell-shaped coplanar waveguide, IEEE Trans. Microw. Theory Techn., vol. 54, pp. 3559-3564, Sep. 2006.

[10] A.M.E. Safwat, S. Tretyakov, and A.V. Räisänen, Defected ground and patch-loaded planar transmission lines, IET Microw. Antennas Propag., vol. 3, pp. 195-204, 2009.

[11] M. Ribó and L. Pradell, Circuit model for a coplanar-slotline cross, IEEE Microw. Guided Wave Lett., vol. 10, pp. 511-513, Dec. 2000.

[12] J.-S. Hong, and M. J. Lancaster, Microstrip Filters for RF/Microwave Applications, John Wiley & Sons, 2001.

[13] Shuo Wang and F.C. Lee, Negative capacitance and its applications on parasitic cancellation for EMI Noise Suppression, IEEE PESC 2007, pp.2887-2891, Jun. 2007.

[14] J. Bonache, M. Gil, I. Gil, J. Garcia-García and F. Martín, On the electrical characteristics of complementary metamaterial resonators, IEEE Microw. Wireless Compon. Lett., vol. 16, pp. 543.545, Oct. 2006.

[15] F. Aznar, M. Gil, J. Bonache, L. Jelinek, J. D. Baena, R. Marqués and F. Martín, Characterization of miniaturized metamaterial resonators coupled to planar transmission lines through parameter extraction, J. Appl. Phys., vol. 104, pp. 114501, Dec. 2008.

[16] W.J. Getsinger, Circuit duals on planar transmission media, IEEE MTT-S Int. Microwave Symp. Dig., May-June 1983, pp. 154-156, Boston, MA (USA).

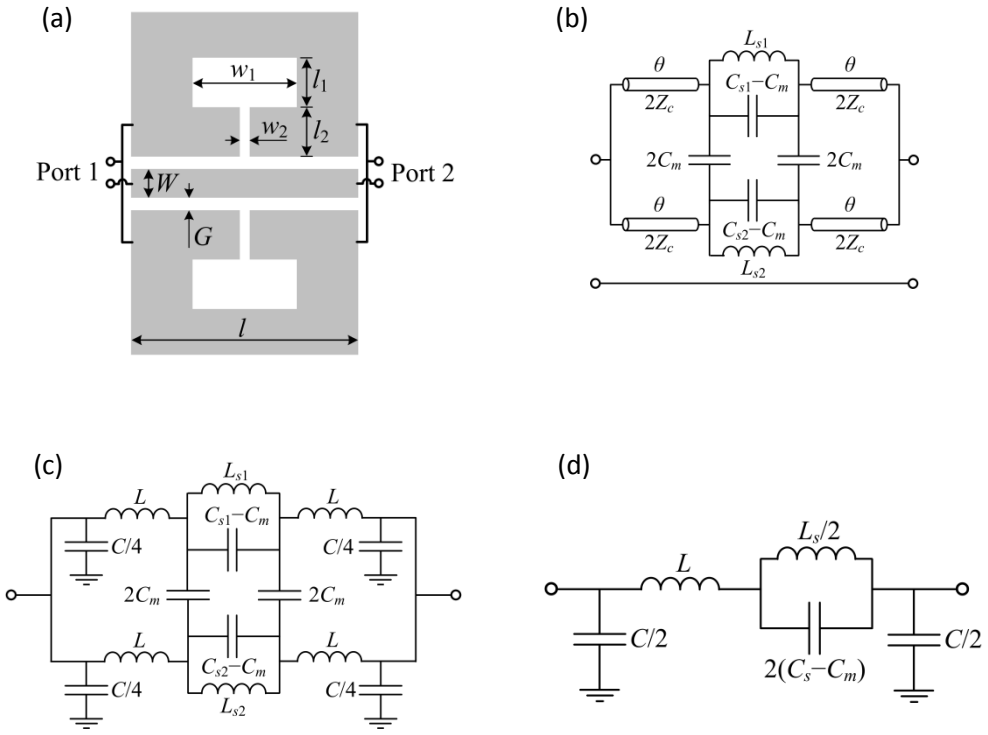

Fig. 1. (a) CPW loaded with a pair of coupled slotted SIRs; (b) hybrid lumped-distributed model; (c) lumped model; and (d) simplified lumped model for a symmetric pair of resonators

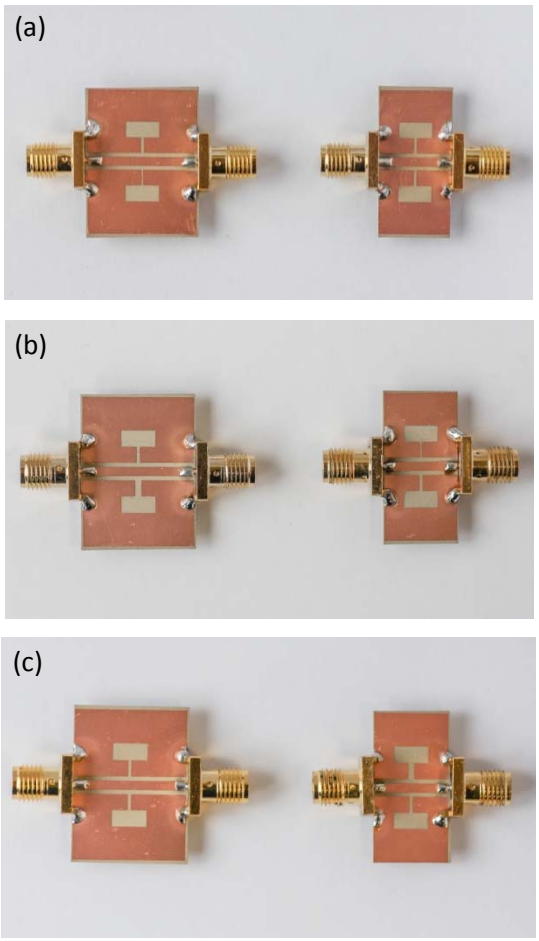

Fig. 2. Photograph of the fabricated 50-Ω CPWs loaded with pairs of S-SIRs. The substrate is *Rogers RO3010* with thickness h = 1.27 mm and dielectric constant ε_r = 11.2. Dimensions are: W = 1.5 mm, G = 0.65 mm, l =12 mm, $l_1 = l_2$ = 2.6 mm, w_1 = 5.5 mm, and for the lower fixed resonator w_2 = 0.5 mm. For the upper resonator, w_2 is (a) 0.5 mm, (b) 0.25 mm, and (c) 1 mm.

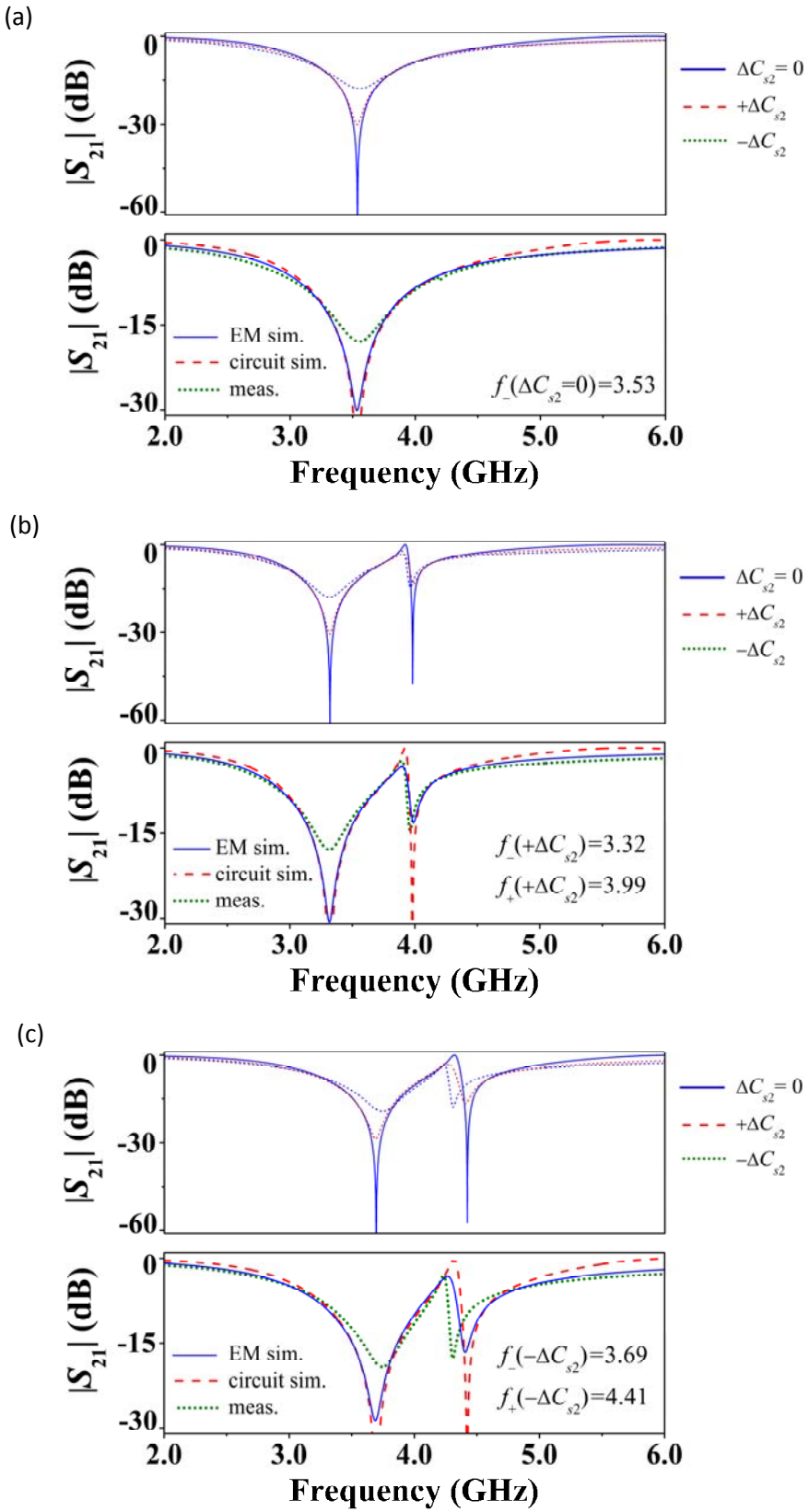

Fig. 3. Transmission coefficient magnitude for the structures in Fig. 2. The lumped parameters are: L = 2.36 nH, C = 1.28 pF; for w_2 = 0.25 mm, L_s = 3.77 nH, C_{seff} = 0.66 pF; for w_2 = 0.5 mm, L_s = 3.63 nH and C_{seff} = 0.56 pF; for w_2 = 1 mm, L_s = 3.39 nH and C_{seff} = 0.46 pF; $C_m(+\Delta C_{s2})$ = −0.09 pF and $C_m(-\Delta C_{s2})$ = −0.08 pF ($C_{seff} = C_s - C_m$ where C_s is the capacitance for a symmetric case). The indicated resonance frequencies correspond to simulation.

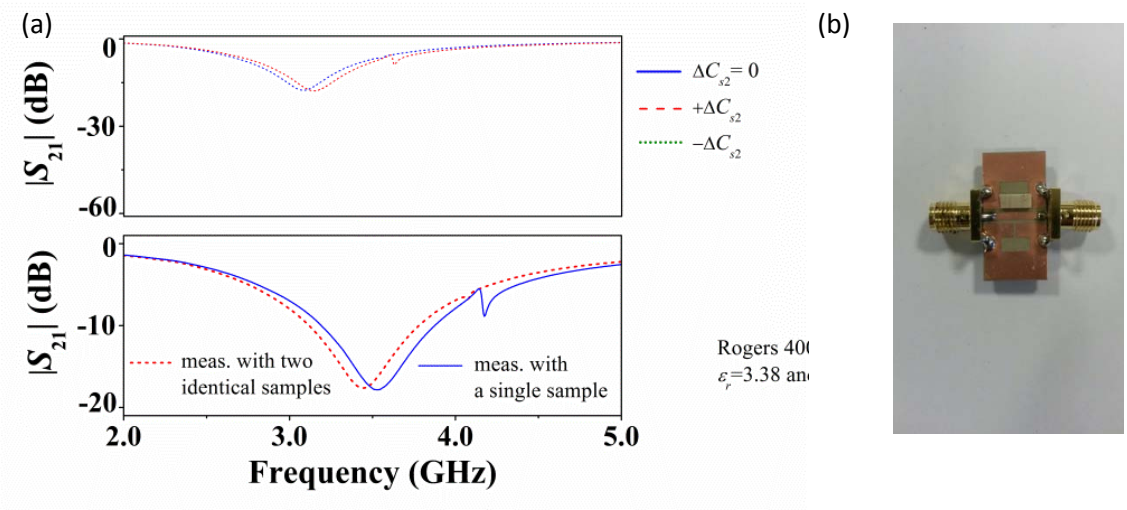

Fig. 4. Symmetric and asymmetric dielectric loading onto the structure of Fig. 2(a) by means of a pair and a single dielectric sample ($\varepsilon_r = 3.38$ and $h = 0.8128$ mm), respectively.

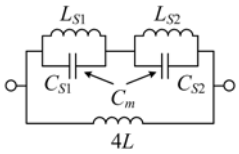

Fig. 5. Circuit dual of the resonant shunt branch of the equivalent circuit of the 5-SIR-loaded CPW of [7]. Note that the reactive elements have been designated according to the mapping.

IMS16(C)*

"Cascaded Splitter/Combiner Microstrip Sections Loaded with Complementary Split Ring Resonators (CSRRs): Modeling, Analysis and Applications"

Su, Lijuan, Jordi Naqui, Javier Mata-Contreras, and Ferran Martín

IEEE MTT-S International Microwave Symposium (IMS'16), San Francisco, May 2016

* Conference articles(C) included in this thesis for completeness but cannot be officially part of the compendium of the articles of the Ph.D. thesis.

Cascaded Splitter/Combiner Microstrip Sections Loaded with Complementary Split Ring Resonators (CSRRs): Modeling, Analysis and Applications

Lijuan Su, Jordi Naqui, Javier Mata-Contreras, and Ferran Martín

CIMITEC, Departament d'Enginyeria Electrònica, Universitat Autònoma de Barcelona

08193 Bellaterra, Barcelona, Spain

E-mail: Ferran.Martin@uab.es

Abstract — This paper is focused on the study of splitter/ combiner microstrip sections where each branch is loaded with a complementary split ring resonator (CSRR). If the structure is symmetric with regard to the axial plane, only one transmission zero (notch) in the transmission coefficient arises. Conversely, two notches appear if symmetry is disrupted. A model that combines lumped elements (describing the CSRR-loaded line sections) and distributed components (accounting for the transmission lines) is proposed and used to obtain the position of the transmission zeros. The model is validated through parameter extraction and comparison to electromagnetic simulations and measurements, where up to three cascaded splitter/combiner sections (symmetric and asymmetric) are considered. Finally, the three-section symmetric structure is asymmetrically loaded to demonstrate the possibility of using the proposed device as a microwave sensor/detector able to identify defects or abnormalities between a sample under test (SUT) and a reference sample. With this technique, as many samples as splitter/combiner sections can be sensed simultaneously.

Index Terms — Complementary split ring resonators (CSRRs), microstrip technology, circuit modeling, microwave sensors.

I. Introduction

The use of slot resonant elements in combination with transmission lines for sensing purposes has been recently reported [1,2]. These sensors offer good sensitivity for dielectric characterization due to the high confinement of the electric field in the slot regions, and have been particularly used for the implementation of microfluidic sensors operating at microwaves. Most of these microwave sensors are based on the variation of resonance frequency, phase or quality factor, caused by the variable to be sensed. Therefore, these sensors are subject to drift problems caused by environmental conditions (temperature, humidity, etc.).

Another sensing approach is based on symmetry disruption in symmetric resonator loaded lines. In this case, the variable to be sensed (position, angle, dielectric permittivity, etc.) causes an asymmetry in the (symmetric) sensing structure that may be detected by the appearance of a notch in the transmission coefficient (coupling-modulated sensors) [3], or by the splitting of the resonance frequency (frequency splitting sensors) [4]. In the later case, two resonant elements are needed, and disruption of symmetry produces two notches separated a distance that depends on the level of asymmetry. These structures are useful to compare a sample with a reference, where differences are manifested by the presence of two notches in the frequency response. In this paper, we propose a frequency splitting sensor able to simultaneously analyze three samples. The sensors consists of three cascaded splitter/combiner microstrip sections loaded with pairs of complementary split ring resonators (CSRRs) tuned at different frequencies. The main aim of the paper is the analysis of the splitter/combiner section on the basis of a circuit schematic able to predict the position of the transmission zeros. In this analysis, the general case of an asymmetric structure is considered. Then the model is validated through parameter extraction, and comparison to electromagnetic simulations and experimental data. Finally, the sensing principle is demonstrated through a proof-of-concept.

II. Topology, circuit model and analysis

The typical topology of a cascaded three-section CSRR-loaded power splitter/combiner microstrip structure is depicted in Fig. 1 (a). Each section consists of a pair of 50 Ω microstrip lines, where each line is loaded with a CSRR. The loaded microstrip line pairs are cascaded between quarter wavelength transmission line sections (at roughly the average frequency of the considered frequency range interval) with the required characteristic impedance to ensure a good matching (35.35 Ω and 25 Ω for the external and central sections, respectively).

The topology of the power splitter/combiner section and relevant dimensions are depicted in Fig. 1(b), whereas the circuit schematic, including distributed and lumped elements, is shown in Fig. (2). The model considers the general case of an asymmetric structure, but the asymmetry concerns the CSRR dimensions only, not the distributed elements. The lumped elements model the microstrip line sections loaded with CSRRs. Thus, L_u/L_l and C_u/C_l account for the microstrip line inductance and capacitance corresponding to the line

section above the CSRR region in upper and lower parallel branches respectively, and the CSRRs are described by the resonant tanks L_{Cu}/L_{Cl}-C_{Cu}/C_{Cl}. The distributed elements describe the different transmission line sections that do not lie on top of the CSRRs, and are characterized by the line impedance Z_i and electrical length θ_i (with i = 1,2,3).

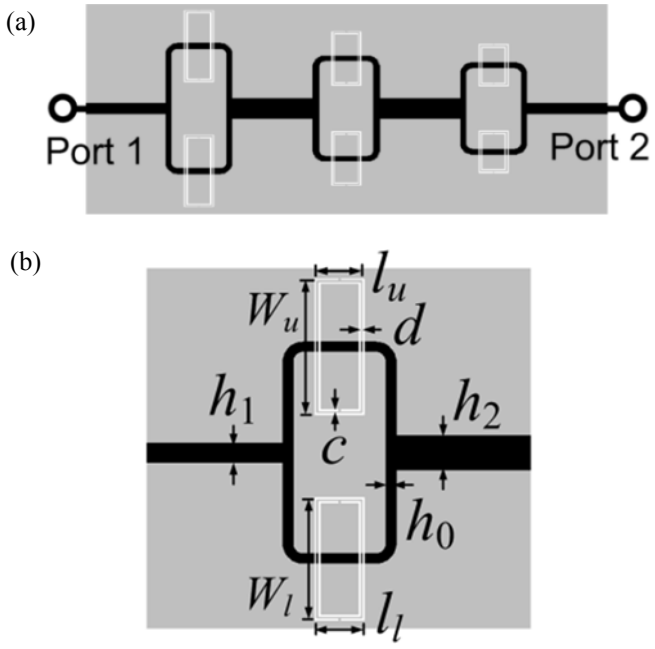

Fig. 1. Topology of a cascaded three-section CSRR-loaded splitter/combiner (a); and details of one section with relevant dimensions indicated (b).

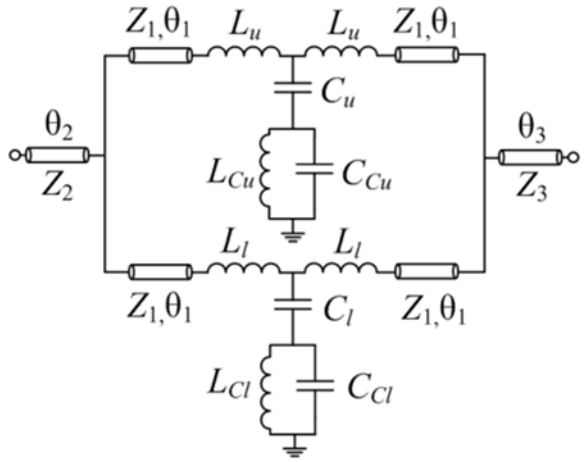

Fig. 2. Equivalent circuit schematic of the splitter/combiner.

Note that the transmission zeros (or notches) of the considered three-section splitter/combiner structure are given by the transmission zeros of each individual splitter/combiner, provided these elements are cascaded. Thus, we can use the schematic of Fig. 2 to predict the position of such transmission zeros for each section. For that purpose, we can neglect the input and output transmission line sections since their presence do not affect the notch positions. The resulting two-port network exhibits transmission zeros at those frequencies satisfying $Y_{12} = Y_{21} = 0$, where Y_{12} and Y_{21} are the anti-diagonal elements of the admittance matrix. Since this two-port consists of two parallel connected two-ports (i.e., the upper and the lower CSRR-loaded branches of the splitter/combiner), Y_{21} is simply given by

$$Y_{21} = Y_{21,u} + Y_{21,l} \tag{1}$$

and $Y_{21,u}$ and $Y_{21,l}$ can be determined by first obtaining the *ABCD* matrix of each branch. It is simply given by the product of the matrices of the three cascaded two-ports, including the two transmission line sections with impedance Z_1, and the lumped two-port network in between. Once the *ABCD* matrices for each branch have been determined, the elements of the right-hand side in (1) are given by $Y_{21,u} = -1/B_u$ and $Y_{21,l} = -1/B_l$, where B_u and B_l are the B elements of the *ABCD* matrix for the upper and lower branches, respectively. Thus, the transmission zeros are given by:

$$\frac{1}{B_u} + \frac{1}{B_l} = 0 \tag{2}$$

with

$$B_u = \mathrm{j}\left[Z_1 \sin(2\theta_1) + \frac{Z_1 \omega L_u \sin(2\theta_1)}{\frac{\omega L_{Cu}}{1-\frac{\omega^2}{\omega_{Cu}^2}} - \frac{1}{\omega C_u}} + \frac{\omega^2 L_u^2 \cos^2(\theta_1)}{\frac{\omega L_{Cu}}{1-\frac{\omega^2}{\omega_{Cu}^2}} - \frac{1}{\omega C_u}} + 2\omega L_u \cos^2(\theta_1) + \frac{Z_1^2 \sin^2(\theta_1)}{\frac{\omega L_{Cu}}{1-\frac{\omega^2}{\omega_{Cu}^2}} - \frac{1}{\omega C_u}}\right] \tag{3a}$$

$$B_l = \mathrm{j}\left[Z_1 \sin(2\theta_1) + \frac{Z_1 \omega L_l \sin(2\theta_1)}{\frac{\omega L_{Cl}}{1-\frac{\omega^2}{\omega_{Cl}^2}} - \frac{1}{\omega C_l}} + \frac{\omega^2 L_l^2 \cos^2(\theta_1)}{\frac{\omega L_{Cl}}{1-\frac{\omega^2}{\omega_{Cl}^2}} - \frac{1}{\omega C_l}} + 2\omega L_l \cos^2(\theta_1) + \frac{Z_1^2 \sin^2(\theta_1)}{\frac{\omega L_{Cl}}{1-\frac{\omega^2}{\omega_{Cl}^2}} - \frac{1}{\omega C_l}}\right] \tag{3b}$$

with $\omega_{Cu} = (L_{Cu} \cdot C_{Cu})^{-1/2}$ and $\omega_{Cl} = (L_{Cl} \cdot C_{Cl})^{-1/2}$. The general solution of (2) is not straightforward. Nevertheless, it can be numerically solved in order to obtain the pair of transmission zeros and the effects of the different element values on their position. Particularly, we can study the effects of the asymmetry caused by the CSRRs, or determine the optimum conditions to enhance sensitivity. If the CSRRs are identical, the structure is symmetric, and expression (2) provides a single solution (transmission zero) with angular frequency given by

$$\omega_z = \frac{1}{\sqrt{L_r (C_r + C)}} \tag{4}$$

where $L_r = L_{Cu} = L_{Cl}$, $C_r = C_{Cu} = C_{Cl}$, and $C = C_u = C_l$. Note that expression (4) corresponds to the angular frequency that nulls the reactance of the identical shunt branches of the lumped two-port T-networks of Fig. 2, as expected.

III. Model Validation and Results

To validate the model, we have considered three structures consisting of three sections loaded with three different pairs of CSRRs: one of such structures is symmetric, whereas the other two are asymmetric, and the asymmetry is achieved by considering different dimensions in the pairs of CSRRs (the dimensions are shown in the caption of Fig. 3). The width of the transmission lines on top of the CSRRs is h_0 = 1.04 mm [as indicated in Fig. 1(b)], corresponding to 50Ω line in the considered substrate (*Rogers RO*3010 with dielectric constant ε_r = 10.2 and thickness h = 1.27 mm), whereas h_1 = 2.06 mm and h_2 = 3.58 mm, providing the required 35.35Ω and 25Ω line impedances.

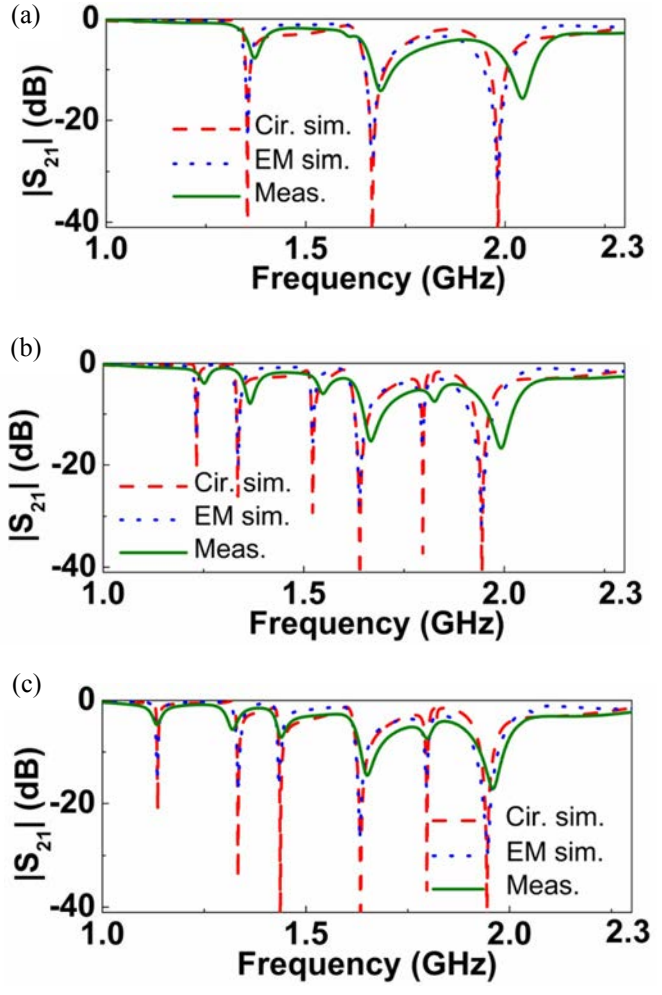

Fig. 3. Transmission coefficient corresponding to the structure of Fig. 1 (a). Symmetric (a); asymmetric I (b); and asymmetric Π (c). The dimensions are: $c = d$ = 0.2 mm, $l_u = l_l$ = 4.8 mm (for all the CSRRs, the longitudinal length is the same). For (a) $W_{u,1} = W_{l,1}$ = 12.5 mm, $W_{u,2} = W_{l,2}$ = 9.36 mm, $W_{u,3} = W_{l,3}$ = 7.24 mm (numerical subindex indicates the section); For (b) $W_{u,1}$ = 13.9 mm, $W_{u,2}$ = 10.28 mm, $W_{u,3}$ = 7.86 mm and (c) $W_{u,1}$ = 15.57 mm, $W_{u,2}$ = 11.29 mm, $W_{u,3}$ = 7.24 mm, both with the other parameters the same as symmetric structure. The extracted parameters are (a) $L_{u,1} = L_{l,1}$ = 2.833 nH, $C_{u,1} = C_{l,1}$ = 0.824 pF, $L_{Cu,1} = L_{Cl,1}$ = 2.878 nH, $C_{Cu,1} = C_{Cl,1}$ = 4.383 pF, $\theta_{1,1}$ = 87.69º; $L_{u,2} = L_{l,2}$ =2.477 nH, $C_{u,2} = C_{l,2}$ = 0.832 pF, $L_{Cu,2} = L_{Cl,2}$ = 2.23 nH, $C_{Cu,2} = C_{Cl,2}$= 3.606 pF, $\theta_{1,2}$ = 61.71º ; $L_{u,3} = L_{l,3}$ = 2.172 nH, $C_{u,3} = C_{l,3}$ = 0.827 pF, $L_{Cu,3} = L_{Cl,3}$ = 1.775 nH, $C_{Cu,3} = C_{Cl,3}$= 3.122 pF, $\theta_{1,3}$ = 55.21º and with $\theta_2 = \theta_3$ = 90º in all three sections (the electrical lengths are given at 1.8 GHz); (b) $L_{u,1}$ = 2.957 nH, $C_{u,1}$ = 0.788 pF, $L_{Cu,1}$ = 3.302 nH, $C_{Cu,1}$ = 4.539 pF, $L_{u,2}$ = 2.594 nH, $C_{u,2}$ = 0.998 pF, $L_{Cu,2}$ = 1.906 nH, $C_{Cu,2}$ = 4.87 pF, $L_{u,3}$ = 2.266 nH, $C_{u,3}$ = 0.822 pF, $L_{Cu,3}$ = 1.933 nH, $C_{Cu,3}$ = 3.217 pF; (c) $L_{u,1}$ = 3.081 nH, $C_{u,1}$ = 0.829 pF, $L_{Cu,1}$ = 3.418 nH, $C_{Cu,1}$ = 5.295 pF, $L_{u,2}$ = 2.71 nH, $C_{u,2}$ = 0.787 pF, $L_{Cu,2}$ = 2.781 nH, $C_{Cu,2}$ = 3.861 pF.

For parameter extraction, we have firstly extracted the circuit element values for each CSRR, using a single CSRR-loaded microstrip line, following the procedure reported in [5]. Then the electrical lengths of the different microstrip lines in the parallel CSRR-loaded branches have been adjusted by curve fitting the circuit simulation of the model (by cascading three sections of the model shown in Fig. 2) to the electromagnetic simulation of the cascade connection of three sections. For the asymmetric structures, the only change concerns the transverse dimensions of the CSRRs. Hence, it is assumed that the coupling between the CSRR and the microstrip line is the same in both branches. Obviously, modification of this CSRR transverse dimension does not affect the distributed elements. The extracted parameters have been used to obtain the circuit simulation, which is compared with the lossless electromagnetic simulation and measurement in Fig. 3. The agreement between the circuit simulation results and electromagnetic simulations is very good, thus validating the circuit model. Discrepancies in measurement are due to fabrication related tolerances and the effect of losses, not taken into account in the circuit schematic and electromagnetic simulations.

IV. Proof-of-Concept of Sensor

As proof of concept we have considered the symmetric structure asymmetrically loaded in the splitter/combiner sections closer to port 1 (those with larger CSRRs). The result, depicted in Fig. 4, shows that frequency splitting caused by asymmetry arises (to achieve the asymmetry we have loaded only the upper CSRR of the first two sections with two dielectric slabs with dielectric constant 10.2 and 3.38).

V. Conclusion

In conclusion, a circuit schematic for splitter/combiner microstrip sections loaded with complementary split ring resonators (CSRRs) has been proposed and validated. With such model, the transmission zeros of cascaded CSRR-loaded splitter/combiner sections can be predicted. These multi-

section structures can be useful for sensors able to measure several samples simultaneously.

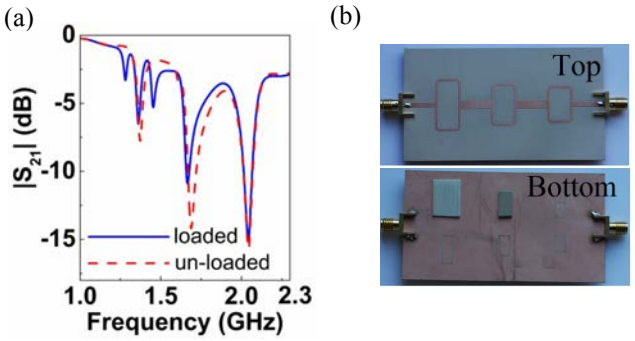

Fig. 4. Measured response of the sensing structure loaded with two slabs (a), and photograph of the proof-of-concept demonstrator (b). The response of the un-loaded structure is also depicted.

ACKNOWLEDGEMENT

This work has been supported by MINECO (Spain) under project TEC2013-40600-R and FEDER Funds. Thanks are also given to AGAUR-Generalitat de Catalunya for partially funding this research activity through the project 2014SGR-157. Ferran Martín is in debt to ICREA for supporting his work. Lijuan Su thanks China Scholarship Council (CSC) for supporting her work in UAB through the grant No. 201306950011.

REFERENCES

[1] A. Ebrahimi, W. Withayachumnankul, S. Al-Sarawi, and D. Abbott, "High-sensitivity metamaterial-inspired sensor for microfluidic dielectric characterization", *IEEE Sensors J*., vol. 14, pp. 1345-1351, May 2014.

[2] A. Ebrahimi, W. Withayachumnankul, S. Al-Sarawi, and D. Abbott, "Microwave microfluidic sensor for determination of glucose concentration in water", *Mediterranean Microwave Symposium* (MMS'15), Nov. 30 – Dec. 2, 2015, Lecce, Italy.

[3] J. Naqui, M. Durán-Sindreu and F. Martín, "Novel sensors based on the symmetry properties of split ring resonators (SRRs)", *Sensors*, vol 11, pp. 7545-7553, 2011.

[4] J. Naqui, C. Damm, A. Wiens, R. Jakoby, L. Su, F. Martín, "Transmission lines loaded with pairs of magnetically coupled stepped impedance resonators (SIRs): modeling and application to microwave sensors", *IEEE MTT-S Int. Microwave Symp*., June 2014, Tampa, FL (USA).

[5] J. Bonache, M. Gil, I. Gil, J. Garcia-García and F. Martín, "On the electrical characteristics of complementary metamaterial resonators", *IEEE Microw. Wireless Compon. Lett*., vol. 16, pp. 543.545, Oct. 2006.

TMTT16 November

"Transmission lines loaded with pairs of stepped impedance resonators: modeling and application to differential permittivity measurements"

Naqui, Jordi, Christian Damm, Alex Wiens, Rolf Jakoby, Lijuan Su, Javier Mata-Contreras, and Ferran Martín

IEEE Transactions on Microwave Theory and Techniques 64, no. 11 (2016): 3864-3877

Transmission Lines Loaded with Pairs of Stepped Impedance Resonators: Modeling and Application to Differential Permittivity Measurements

Jordi Naqui, *Member, IEEE*, Christian Damm, *Member, IEEE*, Alex Wiens, *Student Member, IEEE*, Rolf Jakoby, *Member, IEEE*, Lijuan Su, *Student Member, IEEE*, Javier Mata-Contreras, and Ferran Martín, *Fellow, IEEE*

***Abstract*—Differential techniques are widely used in communication and sensor systems, as these techniques have been shown to improve the performance. This paper shows how differential sensing of permittivity can be conducted in a simple way. For that purpose, a microstrip line loaded with a pair of stepped impedance resonators is used in two different resonator connections: parallel and cascade. Each resonator is individually perturbed dielectrically so that: (*i*) when the two individual permittivities are identical, the structure exhibits a single resonance frequency; (*ii*) when the permittivities are different, resonance frequency splitting occurs, giving rise to two resonances (all these resonances are seen in the form of transmission zeros). The two sensing approaches are successfully validated through electromagnetic simulations and experiments. By virtue of a differential measurement, robustness against changing ambient factors that may produce sensor miscalibration is expected.**

***Index Terms*— differential measurement, dual-mode resonator, microstrip, microwave sensor, stepped-impedance resonator.**

I. Introduction

Permittivity sensors are prominent electromagnetic sensors whose development began in the mid-twentieth century [1],[2]. These sensors are highly versatile, as the measurand (the physical quantity of interest) can be either the permittivity or another physical variable directly related to it.

Nowadays, there are multiple technologies available to implement permittivity sensors. Nevertheless, the focus here is restricted to sensors consisting of passive planar transmission lines and/or resonators. In the last few years, many planar resonator-based permittivity sensors, where frequency shift is typically the electrical sensing variable, have been reported. These permittivity sensors are aimed at many topics, including material characterization [3]-[5] (this is indeed the context of the sensors proposed in this work), analysis of organic tissue [6][7], microfluidics [8]-[11], biosensing [12]-[16], or environmental factors [17]. Other planar permittivity sensors implemented by means of artificial transmission-lines have also been proposed [18]-[20].

A general drawback of resonance-based sensors is that, as permittivity depends on environmental conditions (e.g., temperature), the resonance frequency can be unintentionally shifted by spurious effects [2],[17]. As is well known, ideal sensors are designed to be linear or linear to some simple mathematical function with the measurand. However, sensors may be sensitive to other physical quantities, an effect designated as cross-sensitivity that entails measurement errors (miscalibration). Common cross-sensitivities are those derived from ambient factors; in sensor design, environmental stability is usually a key point and cannot be ignored [21],[22]. Regarding permittivity sensors, it can be argued that environmental drifts should be defined in terms of sensitivity rather than cross sensitivities. Nevertheless, if ambient factors are uncontrolled, the drifts should be indeed categorized into cross sensitivities. Additionally, the resonance frequency is generally dependent not only on the permittivity of interest, but also on the permittivity of the substrate/s necessary to support the resonant element [3]-[17]; this dependency is clearly a cross sensitivity.

In order to prevent or reduce systematic errors due to cross sensitivities as much as possible, several strategies can be utilized, such as compensation techniques, or the use of environmentally stable materials. Another typical solution to deal with changing environmental factors is through differential measurements, the one considered here. Differential measurements are robust against variable ambient conditions provided that these conditions perturb in the form of a common-mode stimulus. Generally, two sensors are used

This work was supported by MINECO-Spain (project TEC2013-40600-R), *Generalitat de Catalunya* (project 2014SGR-157), *Institució Catalana de Recerca i Estudis Avançats* (who awarded Ferran Martín), and by FEDER funds. Lijuan Su acknowledges the China Scholarship Council (CSC) for the grant 201306950011. This work was also partly supported by LOEWE STT.

J. Naqui, L. Su, J. Mata-Contreras and F. Martín are with GEMMA/CIMITEC, Departament d'Enginyeria Electrònica, Universitat Autònoma de Barcelona, 08193 Bellaterra, Spain (e-mail: Ferran.Martin@uab.es).

C. Damm, A. Wiens, and R. Jakoby are with the Institute for Microwave Engineering and Photonics. Technische Universitaet Darmstadt, Merckstrasse 25, 64283 Darmstadt, Germany.

to construct a differential sensor, both of them being subjected to the same external factors [18]-[22]; an ideal sensor should be capable of conducting measurements regardless of the surrounding ambient factors.

Depending on the application, differential measurements can be used with sensing or comparison purposes. A differential sensor measures the difference in permittivity (or one of the two permittivities, provided that the other one is known), whereas a comparator (differential by definition) can be used to inquire about whether two permittivities are the same or not. Permittivity comparators may be of interest, for instance, for the detection of defects or alteration of a SUT (sample under test) by comparing it to a well-known reference.

A differential permittivity sensor based on amplitude levels by means of an interferometer setup was reported in [18]-[20]. In [23] the authors presented a differential sensor/comparator consisting of a transmission line loaded with a pair of identical shunt-connected stepped-impedance resonators (SIRs) connected to the same junction. Instead of duplicating and combining sensors in pairs to construct a differential sensor, pairs of resonators connected to a single signal interface (a single transmission line) were employed. Because of the SIR semi-lumped behavior, the size was compact, and electric energy was concentrated in a small region allowing for small SUTs and for low cross sensitivities (if present) related to substrate/s. Due to the SIR high *Q*-factor, high frequency discrimination was expected. The sensing principle, experimentally validated in the vicinity of 60 GHz, is based on resonance frequency splitting derived from symmetry perturbation [23]-[25]; there is one or two transmission zeros depending on whether the two permittivities are the same or not, respectively. However, the inter-resonator coupling was seen to degrade considerably the sensitivity and discrimination for small differential inputs.

This work is aimed at expanding the preliminary research work conducted in [23], with a view to performing real-time differential permittivity measurements. Further analysis for the topology proposed in [23] is carried out, and an alternative topology based on a transmission line loaded with a cascade connection of SIRs to face with the drawback of the original topology is proposed. Equivalent circuit models are proposed and validated, from which the theoretical sensitivity is inferred. Experimental data applying material permittivity perturbation is reported to validate the potentiality of the proposed approaches. As will be proven, the new proposed structure exhibits significant benefits against the original one when the individual permittivities attain close values; higher sensitivity, higher discrimination, and narrower bandwidth of operation.

This paper is organized as follows. Section II is devoted to show the two considered physical sensing topologies, and to their modeling by equivalent circuits. In Section III, the capabilities of these structures to operate as a differential sensor or a comparator are investigated by analyzing the sensitivity and the discrimination, respectively. Next, Section IV reports experimental verifications of the sensing approaches. Finally, the main conclusions are drawn in Section V.

II. Topologies and Equivalent Circuit Models

This section analyzes transmission lines loaded with a pair of shunt-connected stepped impedance resonators (SIRs) in two different topologies; one with the SIRs loaded at the same junction, and the other one by cascading the SIRs. Two SIRs are used to perform a real-time (i.e., through a single measurement) differential measurement. Furthermore, the two SIRs are identical with the purpose of rejecting as much as possible common-mode stimulus. Equivalent circuit models including independent and arbitrary capacitive variations in the SIRs are presented and validated. Without loss of generality, we use microstrip implementation. Losses are disregarded throughout this work, eligible approximation when dealing with low-loss substrates and SUTs. Nevertheless, a method to estimate the loss factor is included in the last section.

A. Microstrip Line Loaded with a pair of parallel SIRs

The SIR in Fig. 1(a), in shunt connection to a microstrip line section, is a semi-lumped resonator [26]. Provided that the two sections are electrically small, the behavior of a shunt-connected SIR may be approximated to that of a shunt-connected lumped *LC* resonator. The inductance/capacitance of the SIR is essentially determined by the inductance/capacitance of the high/low impedance section. Consequently, the circuit model depicted in Fig. 1(b) may describe accurately a microstrip line loaded with a single SIR. The inductance and capacitance of the main host transmission line are L and C, respectively, whereas the SIR inductance and capacitance are L_s and C_s, respectively. Additionally, for sensing purposes, the model takes into account a capacitive perturbation, ΔC_s, applied to the SIR. According to the circuit model of Fig. 1(b), a transmission zero (or notch) appears at the angular resonance frequency given by

$$\omega_0 = \frac{1}{\sqrt{L_s\left(C_s \pm |\Delta C_s|\right)}}. \tag{1}$$

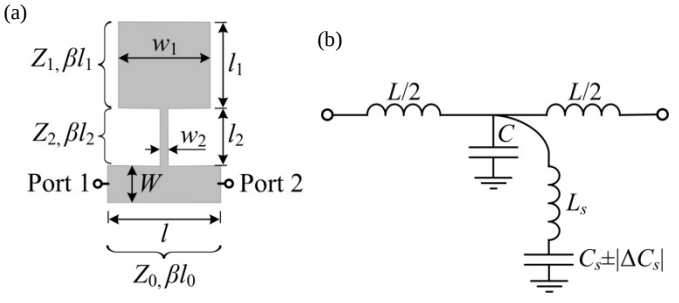

Fig. 1. (a) Typical topology of a SIR-loaded microstrip line, where geometrical and electrical parameters are indicated. (b) Equivalent circuit model with a capacitive perturbation applied to the SIR.

As a case study a single SIR-loaded line with dimensions W = 1.83 mm, l = 6 mm, $l_1 = l_2$ = 2.6 mm, w_1 = 5.5 mm, and w_2 = 250 μm and substrate *Rogers RO4003C* with relative

permittivity $\varepsilon_r = 3.38$, thickness $h = 812.8$ μm, and loss tangent $\tan\delta = 0.0021$, was considered in [23]. The model was validated by circuit simulation of extracted parameters, inferred following the systematic procedure reported in [27], which is based on a mapping of the scattering parameters obtained from full-wave electromagnetic simulation, adapted to the considered circuit. The resulting circuit parameters, characteristic impedances and electrical lengths were found to be: $Z_0 = 50\ \Omega$, $Z_1 = 23\ \Omega$ and $Z_2 = 120\ \Omega$, electrical lengths at $f_0 = 3.83$ GHz were $\beta l_0 = 45°$, $\beta l_1 = 21°$ and $\beta l_2 = 18°$, and the circuit elements were $L = 1.81$ nH, $C = 0.57$ pF, $L_s = 2.45$ nH, and $C_s = 0.70$ pF ($\Delta C_s = 0$).

In order to verify the modeling of an alteration in the resonator capacitance, a shape perturbation was produced in [23]. Namely, the length of the wide section of the reference resonator was enlarged ($+|\Delta l_1|$) or shortened ($-|\Delta l_1|$), with $\Delta l_1 = \pm 0.5$ mm $= \pm 0.19 l_1$, to increase ($+|\Delta C_s|$) or decrease ($-|\Delta C_s|$) its associated capacitance, respectively. The circuit values of these perturbations ($\pm|\Delta C_s|$), with $\Delta C_s = \pm 0.11$ pF $= \pm 0.15 C_s$, were obtained from (1) and the transmission zero frequencies inferred from electromagnetic simulations. The transmission coefficient of these structures, confirmed that the circuit simulations were in good accordance with those inferred from electromagnetic solvers in [23].

As expected from (1), any capacitive perturbation may be sensed by monitoring the change in the resonance frequency. However, a real-time differential measurement of two capacitive perturbations cannot be performed by loading a transmission line with a single SIR. Therefore, transmission lines loaded with pairs of SIRs are necessary.

Fig. 2(a) shows a microstrip line loaded with a pair of identical shunt-connected SIRs placed at the same junction, and on opposite sides of the line (parallel configuration). In this topology, as was already considered in [23], it is assumed that both resonators are individually and simultaneously capacitively-perturbed by ΔC_{si} ($i = 1, 2$). The lumped element equivalent circuit model that was proposed in [23] is represented in Fig. 2(b). The SIRs are close together, and magnetic coupling between them is modeled, such a coupling being negative since the currents in the mirrored SIRs flow in opposite directions (i.e., the currents are anti-parallel at the junction of the SIRs). This coupling is accounted for by the mutual inductance $-|M|$, the magnetic coupling coefficient being [26]

$$k_m = -\frac{|M|}{L_s}. \tag{2}$$

From the equivalent T-circuit model of a two-port network consisting of a pair of coupled inductors, the circuit model shown in Fig. 2(c) is inferred. If the capacitive perturbations are identical ($\Delta C_{s1} = \Delta C_{s2} = \Delta C_s$), the simpler circuit depicted in Fig. 2(d) results.

For balanced (i.e., identical) perturbations, according to the circuit of Fig. 2(d), it can be readily noticed that the structure exhibits a single transmission zero at

$$\omega_e = \frac{1}{\sqrt{\left(L_s - |M|\right)\left(C_s \pm |\Delta C_s|\right)}} = \frac{\omega_0}{\sqrt{1-|k_m|}}. \tag{3}$$

In the presence of coupling, the transmission zero simply shifts upwards. The resonance frequency in (3) is denoted by ω_e, in agreement to the nomenclature used in [26] to emphasize the presence of an open circuit, under even mode excitation, at the symmetry plane of two identical coupled resonators.

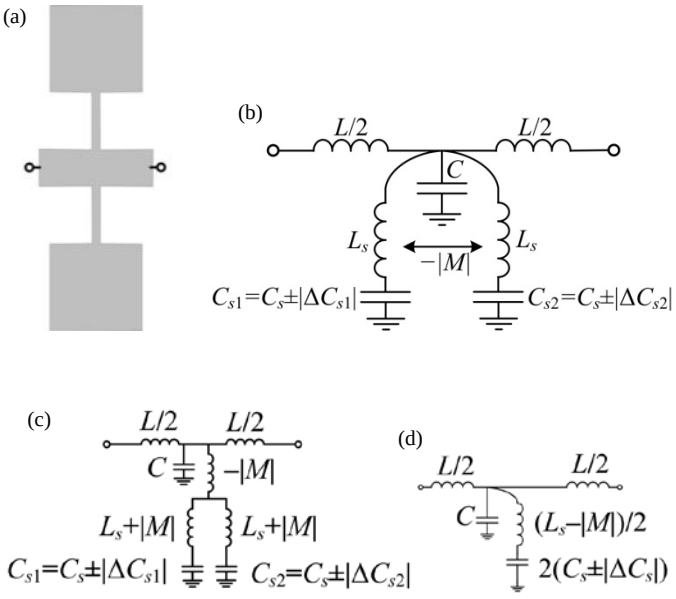

Fig. 2. (a) Microstrip line loaded with a pair of identical SIRs at the same junction and on opposite sides. (b) Equivalent circuit model with arbitrary capacitive perturbations in the two SIRs. (c) Transformed equivalent circuit model. (d) Transformed and simplified equivalent circuit model with balanced perturbations.

In the case with different perturbations ($\Delta C_{s1} \neq \Delta C_{s2}$), the symmetry in the shunt branch of the circuit model is disrupted. Although the resulting circuit model is not as simple as with balanced perturbations, the resonance condition can be easily obtained by setting the shunt branch impedance to zero. This gives the resonance frequencies of a circuit network composed of two magnetically coupled resonators, given by [26]

$$\omega_{l,u} = \sqrt{\frac{L_s\left(C_{s1}+C_{s2}\right) \pm \sqrt{\left[L_s\left(C_{s1}-C_{s2}\right)\right]^2 + 4C_{s1}C_{s2}M^2}}{2C_{s1}C_{s2}\left(L_s^2 - M^2\right)}}, \tag{4}$$

where ω_l and ω_u denote the lower and upper resonance frequencies, respectively. Therefore, a jump discontinuity arises due to unbalanced perturbations giving rise to two split resonance frequencies. The most relevant aspect is the fact that, because of coupling, the two resonances depend on the two perturbations, i.e., $\omega_{l,u} = f(\Delta C_{s1}, \Delta C_{s2})$. Accordingly, each resonance frequency cannot be independently tuned by its corresponding perturbation. In other words, when one of the resonators is perturbed, the two resonance frequencies change (the more similar the perturbations, the higher the cross-dependence). It turns out that a parallel combination of shunt-connected SIRs can be viewed as a dual-mode tri-section

(wide-narrow-wide) SIR [28]-[32], where symmetry disruption is necessary to invoke the dual-mode behavior [33]. Note that multimode resonators are usually utilized to reduce the size of circuits, but in the present work a dual resonant behavior is used to conduct a differential measurement.

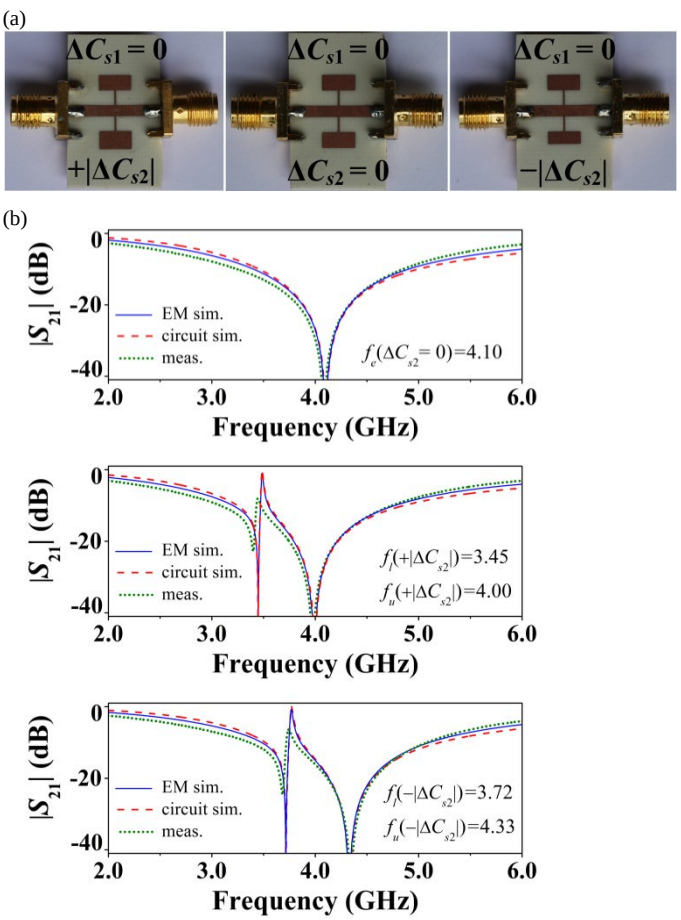

Fig. 3. (a) Photograph of the considered microstrip lines loaded with pairs of parallel SIRs. The lower SIR is perturbed by $\pm|\Delta C_{s2}|$, whereas the upper SIR is unperturbed ($\Delta C_{s1} = 0$). The dimensions and substrate are those indicated in the text in reference to the single SIR-loaded line of [23] (except l = 15.9 mm to solder the connectors). (b) Magnitude of the transmission coefficient obtained from lossless electromagnetic and circuit simulations, and measurements. The circuit parameters are those indicated in the text for the single SIR-loaded line of [23], with $M = -0.31$ nH ($k_m = -0.13$), as the additional host line length produces a phase shift only. The indicated resonance frequencies correspond to those obtained by simulation.

In order to demonstrate the validity and usefulness of the models in Fig. 2, in [23] three different pairs of SIRs loading a microstrip line were considered, as can be seen in Fig. 3(a): a symmetric pair, an asymmetric pair derived by increasing l_1 in one of the SIRs ($+|\Delta C_{s2}|$), and another asymmetric pair derived by decreasing l_1 ($-|\Delta C_{s2}|$). These structures were already fabricated (using a drilling machine) and measured in [23], but some fabrication-related tolerances and uncertainties were observed. For this reason, we have fabricated them again (using a photo-etching process) to fit better the measurements with the simulations. As the considered structures are built up from those of single SIR loaded line, the only circuit parameter that needs to be obtained is the mutual inductance. This parameter has been obtained by curve fitting the circuit simulation to the electromagnetic simulation in the case of the host line loaded with symmetric SIRs. Analytically, (3) can be used alternatively. The extracted value is $M = -0.31$ nH ($k_m = -0.13$). As proven in Fig. 3(b), the circuit simulations are consistent with both electromagnetic simulations and measurements, verifying that losses omission is a reasonable approximation using low-loss substrates.

It should be noted from Fig. 3 that the resonance frequency at f_u resembles that at f_e, while an additional narrowband lower resonance frequency at f_l appears. When symmetry (in regard to the line axis) is broken, the bandwidth at f_l is narrower than that at f_u. The smaller the difference in the perturbations, the narrower the lower notch. As a result, the discrimination to detect small differences between the perturbations is expected to be degraded by losses.

B. Microstrip Line Loaded with a Pair of Cascaded SIRs

This subsection deals with an alternative topology presented in this paper to perform differential capacitive measurements in such a way that inter-resonator coupling is prevented. The proposed topology is illustrated in Fig. 4(a), and consists of a transmission line loaded with a cascade connection of two identical SIRs which are spaced apart by a transmission line section of length l_s. If the SIRs are loaded on the same side of the line, as is considered, the resonators may be coupled not only magnetically, but also electrically. However, the resonators are placed sufficiently separated so that we may assume that the total coupling is negligible.

The proposed circuit model is that represented in Fig. 4(b). Regardless of the length of the transmission line section between resonators, l_s, the transmission zero frequencies are given by

$$\omega_l = \min\left(\frac{1}{\sqrt{L_s\left(C_s \pm |\Delta C_{s1}|\right)}}, \frac{1}{\sqrt{L_s\left(C_s \pm |\Delta C_{s2}|\right)}}\right), \quad (5a)$$

$$\omega_u = \max\left(\frac{1}{\sqrt{L_s\left(C_s \pm |\Delta C_{s1}|\right)}}, \frac{1}{\sqrt{L_s\left(C_s \pm |\Delta C_{s2}|\right)}}\right), \quad (5b)$$

where ω_l and ω_u denote again the lower and upper resonance frequencies, respectively. According to the previous expressions, the two resonances can be shifted independently like using single SIRs, even for unbalanced perturbations. Clearly, the resonance frequency splitting phenomenon, which emerges from unbalanced perturbations, is of different nature in the two configurations under study. In cascaded SIRs, splitting occurs as a mere result of frequency shifting, whereas in parallel SIR there is a combination of frequency shifting and inter-resonator coupling.

Let us now assume the particular case where the in-between transmission line section is half-wavelength long ($l_s = \lambda/2$, where λ is the guided wavelength). As the input impedance of a load seen through a $\lambda/2$ line is unchanged, the circuit in Fig. 4(b) is equivalent to that shown in Fig. 4(c). Note that the SIRs are virtually connected at the same junction so that the structure behaves like if the SIRs were physically located at

the same junction (due to periodicity, this holds at integer multiples of $\lambda/2$). Indeed, the latter circuit is the ideal one which we would like to implement. The problems to implement this idealized circuit are: (*i*) in parallel SIRs, there is inter-resonator coupling (Section II-B); (*ii*) in cascaded SIRs, $l_s = \lambda/2$ is satisfied at one frequency only (this condition is designed to be satisfied at the resonance frequency of the unperturbed resonators). However, the latter issue is not dramatic, since the resonance frequencies in (5) do not depend on the inter-resonator distance (as long as inter-resonator coupling can be ignored). Therefore, the resonance frequencies of the model in Fig. 4(c) always coincide with those of the model in Fig. 4(b).

The last simplification makes the assumption that the perturbations are identical ($\omega_l = \omega_u = \omega_0$). In this circumstance, the circuit in Fig. 4(c) derives to the one in Fig. 4(d), which is formally identical to that with parallel SIRs depicted in Fig. 2(d).

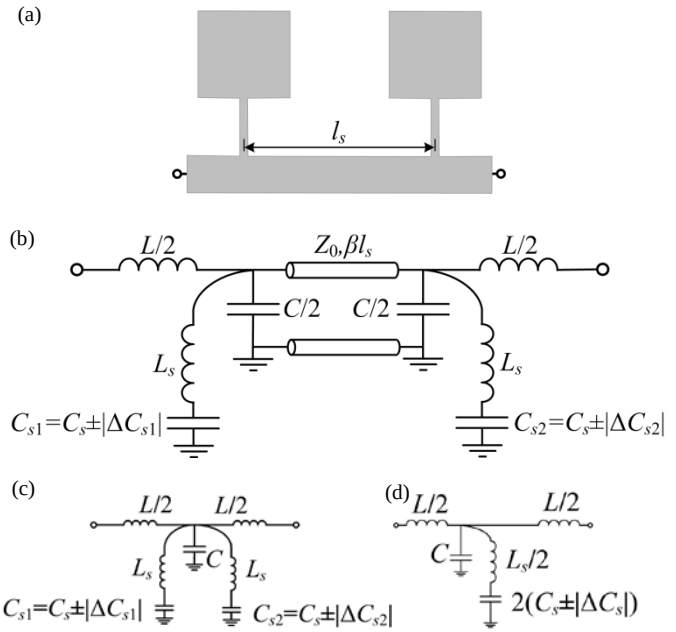

Fig. 4. (a) Microstrip line loaded with a pair of identical SIRs in cascade connection. (b) Equivalent hybrid circuit/TL model including arbitrary capacitive perturbations. (c) Simplified equivalent circuit model when the resonators are spaced half-wavelength apart, i.e., the in-between transmission line section has an electrical length of $\beta l_s = 180°$. (d) Simplified equivalent circuit model for $\beta l_s = 180°$ in the case of balanced perturbations.

To demonstrate the usefulness of the cascaded approach, we have considered the same three previous scenarios in line with the parallel connection [see Fig. 5(a)]. Accordingly, the same circuit elements have been used to validate the equivalent circuit models. As can be seen in Fig. 5(b), the agreement between the circuit/TL simulations, the electromagnetic simulations, and measurements is quite good. It deserves mentioning that a small ripple can be noticed from measurements in the symmetric structure, owing to the fact that the in-between transmission line is not exactly half-wavelength at the corresponding resonance frequency. Importantly, the notch frequencies are the same as those using single SIRs. Another relevant result is that the bandwidth of both notches is not narrow by nature, in contrast to what occurs at the lower resonance frequency employing parallel SIRs.

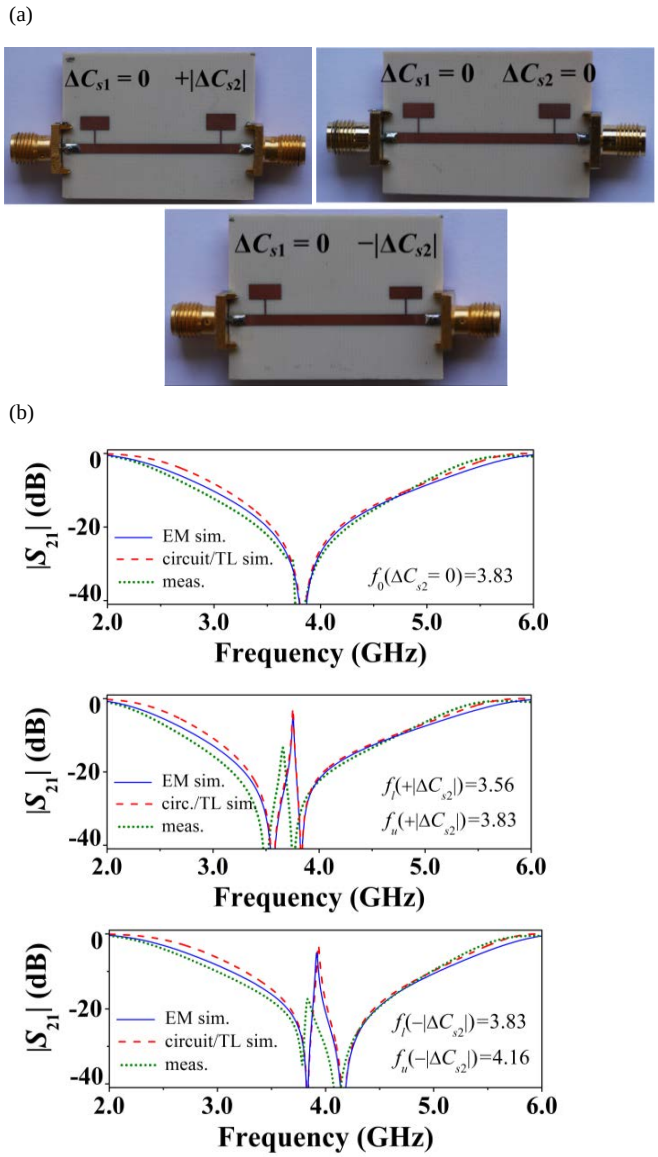

Fig. 5. (a) Photograph of the considered microstrip lines loaded with pairs of cascaded SIRs. The right SIR is perturbed by $\pm|\Delta C_{s2}|$, whereas the left SIR is unperturbed ($\Delta C_{s1} = 0$). The dimensions, substrate, and circuit parameters are those of the single SIR-loaded line (except $l_s = 23.9$ mm and $l = 35.9$ mm). (b) Transmission coefficient magnitude obtained from lossless electromagnetic and circuit/TL simulations, and measurements. The indicated resonance frequencies correspond to simulations.

C. Comparison between the Topologies

To end this section, we compare the transmission zero frequencies given by the two considered configurations, namely, those depicted in Figs. 3(a) and 5(a).

The results for the three considered scenarios with different perturbations [Figs. 3(b) and 5(b), as well as the single SIR] are plotted in Fig. 6 for comparison purposes. In the light of this figure, it is clear that the two concerning topologies

manifest a strongly different behavior caused by the presence or absence of inter-resonator coupling.

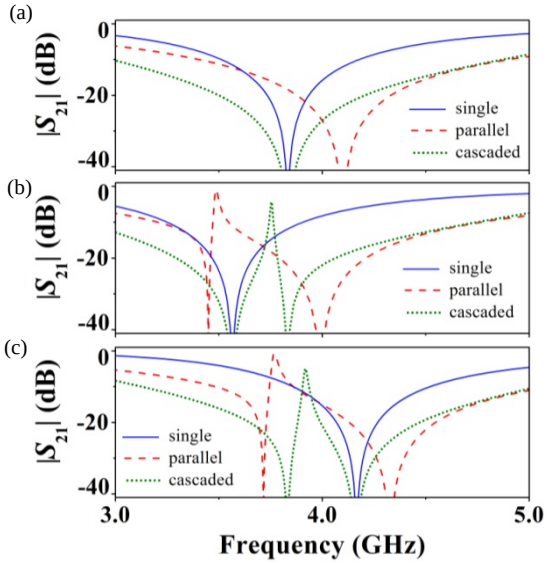

Fig.6. Transmission coefficient magnitude (lossless electromagnetic simulation) of the considered microstrip lines loaded with parallel or cascaded SIRs for $\Delta C_{s1} = 0$, and (a) $\Delta C_{s2} = 0$, (b) $+|\Delta C_{s2}|$, and (c) $-|\Delta C_{s2}|$. For comparison purposes, the response using a single SIR [23] applying to it ΔC_{s2} is also plotted.

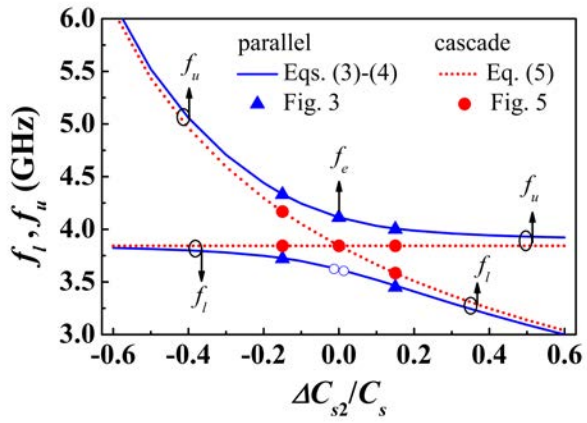

Fig. 7. Resonance frequencies predicted by (3)−(4) and (5) versus a capacitive perturbation ($\Delta C_{s1} = 0$ and $-0.6 \le \Delta C_{s2} / C_s \le 0.6$) for the considered reference microstrip lines loaded with parallel and cascaded SIRs, respectively. The circuit parameters of the reference structures are: $L = 1.81$ nH, $C = 0.57$ pF, $L_s = 2.45$ nH, $C_s = 0.70$ pF, and $M = -0.31$ nH. The resonance frequencies of the three basic scenarios of Figs. 3 and 5, which correspond to particular perturbations, are mapped.

Fig. 7 plots the resonance frequencies predicted by (3)−(4) and (5) in the case where a capacitive perturbation is applied to one of the SIRs ($\Delta C_{s1} = 0$ and $\Delta C_{s2} \neq 0$). The considered circuit parameters of the unperturbed structures are those obtained previously. Additionally, the resonances for the particular perturbed structures are also mapped to the curves. It is especially visible that, when one of the resonators is perturbed ($\Delta C_{s2} \neq 0$), the frequency splitting in parallel SIRs is characterized by a shift in the two resonances. On the contrary, for cascaded SIRs only the resonance frequency of the perturbed resonator is shifted.

In conclusion, it can be drawn that a cascade connection of SIRs provides a good solution to prevent coupling between them. Moreover, significant advantages arise, particularly, the resonances are independent to each other (enhancing the sensitivity, as will be shown in Subsection III-C), their bandwidth is moderately wide by nature (improving the discrimination), the spectral separation between the resonance frequencies is not enhanced by coupling (requiring a narrower bandwidth of operation), and unknown perturbations can be physically identified. As will be shown, these advantages hold as long as the perturbations are similar.

III. Sensitivity Analysis

Thus far, capacitive perturbations have been produced by changing the physical dimensions of the resonators. Evidently, in practice, the capacitive perturbations in a permittivity sensor must be due to permittivity perturbations of samples under test (SUTs). We use the term *sample* in order not to lose generality, meaning that the sample can be a material, liquid, organic tissue, and so forth. Furthermore, the SUT may also refer to a functional layer that enhances the measurand-to-permittivity relationship for sensing purposes (e.g., in environmental sensors based on functional layers, a material highly sensitive to the environmental factor of interest is used).

This section evaluates the sensitivity in differential permittivity measurements, for both capacitive and permittivity perturbations. The study is conducted on the basis of the proposed equivalent circuit models, together with analytical expressions of capacitances, and on electromagnetic simulations.

A. Analytical Sensitivity in terms of Capacitance

With a view to performing differential sensing of capacitances in the considered approach based on frequency splitting, the differential input is the difference between the capacitances, that is

$$C_{sd} = C_{s2} - C_{s1}. \tag{6}$$

The output electrical variable to be monitored is frequency, and the differential output is defined as the difference between the upper and lower resonance frequencies, that is

$$f_d = f_u - f_l. \tag{7}$$

Obviously, despite the fact that the resonance for balanced perturbations is denoted by f_e or f_0, when a single resonance is monitored, implicitly results $f_l = f_u$. The curve that relates the output and input quantities, namely $f_d(C_{sd})$, is named transfer function, whose slope is the sensitivity. Hence, the sensitivity is defined as the variation in the difference between the resonance frequencies divided by the variation in the difference between the capacitances. Mathematically, the sensitivity can be written as

$$S = \frac{df_d}{dC_{sd}} = \lim_{\Delta C_{s2} - \Delta C_{s1} \to 0} \frac{\Delta f_u - \Delta f_l}{\Delta C_{s2} - \Delta C_{s1}}, \tag{8}$$

where ΔC_{si} ($i = 1,\ 2$) and $\Delta f_{l,u}$ stand for individual incremental/decremental changes in capacitance and resonance frequency, respectively. For simplicity, if one of the SIRs is not perturbed and considered to be a reference (so that $\Delta C_{s1} = 0$) then (8) reduces to

$$S = \frac{df_d}{dC_{s2}} = \lim_{\Delta C_{s2}\to 0} \frac{\Delta(f_u - f_l)}{\Delta C_{s2}}. \tag{9}$$

In addition, in the cascade configuration, the magnitude of the analytical sensitivity for null perturbation (y-axis) becomes

$$|S| = \frac{f_0}{2C_{s2}}. \tag{10}$$

The sensitivity should be as high as possible and constant values of it are preferred. In order to gain insight into the sensitivity, instead of analyzing (9), that is cumbersome when the resonance frequencies are governed by (4), numerical solutions will be given. The resonance frequencies determined by (3)−(4) for two different coupling coefficients and by (5) are plotted in Fig. 8(a) assuming $\Delta C_{s1} = 0$. It is evident that the output is null in the case of a perfect balance of perturbations ($\Delta C_{s1} = \Delta C_{s2} = 0$). On the other hand, unbalanced perturbations have been introduced by a capacitive variation in one of the SIRs ($\Delta C_{s1} = 0$, $\Delta C_{s2} \neq 0$). As expected, when $k_m \neq 0$, corresponding to the case with parallel SIRs, f_u is more sensitive to $-|\Delta C_{s2}|$ than f_l, and complementarily f_l is more sensitive to $+|\Delta C_{s2}|$. Both frequencies tend to the frequencies without coupling as the capacitive perturbation increases.

Fig. 8(b) shows the corresponding transfer function from which it is apparent that, as $|k_m|$ increases, the frequency splitting, f_d, strengthens. It turns out that the sensitivity, shown in Fig. 8(c), worsens as $|k_m|$ increases. Indeed, the maximum sensitivity corresponds to the case of (uncoupled) cascaded SIRs, and is given by (10). Specifically, a significant degradation in the sensitivity results for small perturbations. As was stressed earlier, even for loose coupling coefficients, coupling cannot be neglected for similar perturbations. Nevertheless, the parallel configuration can be useful when the perturbations differ from each other significantly. In these situations, coupling plays an insignificant role.

The results in Fig. 8 were already published in [23], where using parallel SIRs with $k_m = 0$ was assumed to be fictitious. Here, $k_m = 0$ is no longer fictitious, as is implemented employing cascaded SIRs. For small inputs, since the inter-resonator coupling in parallel SIRs decreases the sensitivity, parallel-connected SIRs are apparently not much appropriate to properly operate as a sensor. Additionally, this topology working as a comparator between two capacitively-perturbed SIRs is not very promising. As mentioned before, the discrimination for small differential inputs is expected to be rather limited due to the narrowband nature of the lower resonance. Conversely, SIRs in cascade connection are expected to achieve high sensitivities and discriminations.

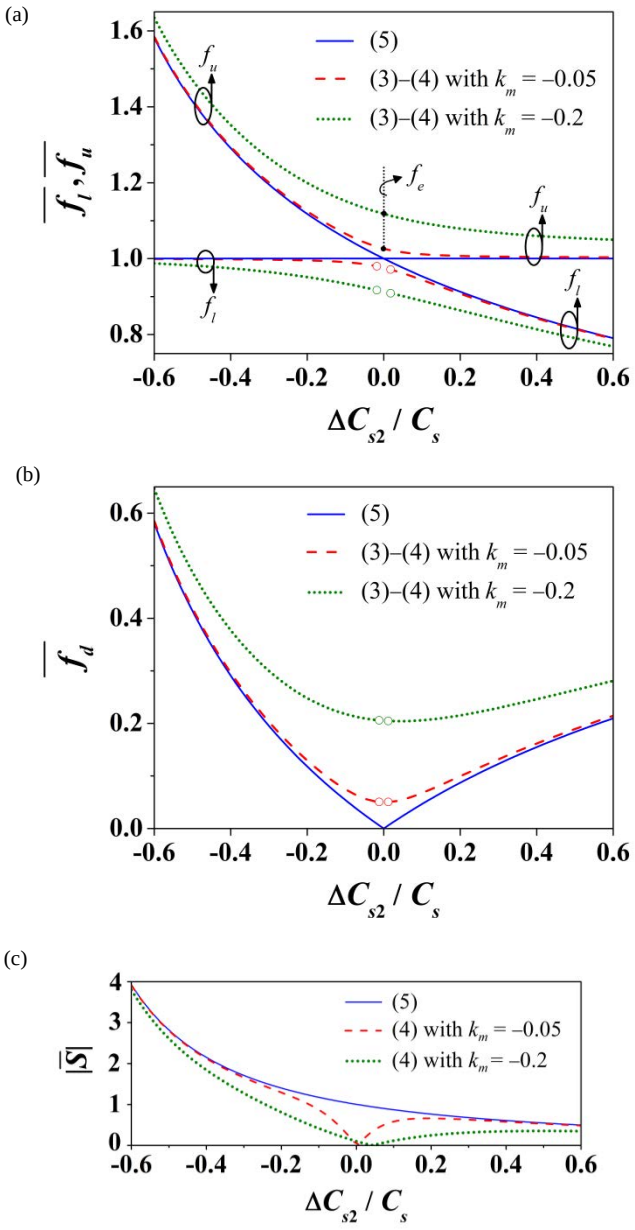

Fig. 8. (a) Resonance frequencies given by (3)−(4) for different k_m and (5) normalized to the constant resonance frequency of the non-perturbed uncoupled SIR determined by (5). The capacitive perturbations are $\Delta C_{s1} = 0$ and $-0.6 \le \Delta C_{s2} / C_s \le 0.6$. (b) Normalized transfer function. (c) Sensitivity magnitude normalized to the case of balanced perturbations ($\Delta C_{s2} = 0$) in the cascaded configuration. For the parallel arrangement, sensitivity is calculated using (4) solely, disregarding (3) in order not to calculate the sensitivity across the jump discontinuity.

It should be mentioned that the dynamic range of measurement is not limited to the considered one ($|\Delta C_{s2}| \le 0.6 C_s$). This relatively small dynamic range, however, allows for illustrating properly the handicap of the parallel configuration, i.e., low performance under small inputs. Finally, it is also important to highlight that the sensitivity is not constant due to the fact that the transfer function is not linear [this is indeed evident from the simplest form of the sensitivity given by (10)]. Moreover, sensitivity is

not a symmetric function with respect to the *y*-axis, i.e., $S(+|\Delta C_{sd}|) \neq S(-|\Delta C_{sd}|)$. Instead, the sensitivity magnitude increases or decreases as the input capacitance is increasingly lower or higher, respectively.

B. Analytical Sensitivity in terms of Permittivity

In the previous subsection we considered a capacitive input as a generalization. Capacitive variations can be produced by several means, e.g., by changing the physical dimensions of the resonators (i.e., shape perturbation as done in Section II) or by changing dielectric properties (i.e., material perturbation, as it must be in practice). Therefore, in a real sensor the differential input is the difference in the relative permittivity of the SUTs, defined here as

$$\varepsilon_{rd} = \varepsilon_{r2} - \varepsilon_{r1}. \tag{11}$$

It should be noted that the sensor measures a difference between two permittivities. Provided that one of the two permittivities is known, the other permittivity can be inferred.

The sensitivity in terms of the relative permittivity becomes

$$S = \frac{\partial f_d}{\partial \varepsilon_{rd}} = \lim_{\Delta\varepsilon_{r2}-\Delta\varepsilon_{r1}\to 0} \frac{\Delta f_u - \Delta f_l}{\Delta\varepsilon_{r2} - \Delta\varepsilon_{r1}}, \tag{12}$$

where $\Delta\varepsilon_{ri}$ (i = 1, 2) stands for changes in relative permittivity. The partial derivatives indicate that the output differential frequency may be influenced by other physical variables related to cross sensitivities, as will be illustrated before ending this subsection. By assuming a linear dependence of the capacitance with the permittivity (with proportionality constant k), and letting $\Delta\varepsilon_{r1} = 0$ and $k_m = 0$ once again, the sensitivity magnitude becomes

$$|S| = \frac{f_0}{2\varepsilon_{r2}}. \tag{13}$$

To establish analytically the transfer function and sensitivity above, the SIR capacitance was approximated by the parallel-plate capacitance of its wide section, namely

$$C_p = \frac{\varepsilon_0 \varepsilon_{r2} w_1 l_1}{h} = k\varepsilon_{r2}, \tag{14}$$

where ε_0 is the vacuum permittivity. In (14), the substrate in the vicinity of the wide section is supposed to be replaced with one SUT. The most relevant aspect in this approximation is that the SIR capacitance is linearly dependent on the permittivity. The corresponding capacitance for the reference SIR is C_p = 0.53 pF. However, (14) must be considered as a first-order approximation as mentioned above, where $l_1, w_1 >> h$ are required for accurate results. Likewise, C_s is neither exactly proportional to l_1; $\Delta l_1 = \pm 0.19 l_1$ produces $\Delta C_s = \pm 0.15 C_s$.

Finally, to illustrate the robustness of differential measurements against cross sensitivities, let us assume that we compare two identical materials ($\Delta C_s = \Delta C_{s1} = \Delta C_{s2}$). Using a two-step process with a single SIR, the resulting resonance frequencies are

$$\omega_0 = \frac{1}{\sqrt{L_s\left(C_s + \Delta C_s\right)}}. \tag{15}$$

Let us now introduce a spurious change in the capacitance related to a cross sensitivity, denoted by ΔC_{xi} (i = 1,2). As the effect of cross sensitivities may change over time, one may assume $\Delta C_{x1} \neq \Delta C_{x2}$ (neither a compensation technique nor recalibration is considered). Hence, in the presence of cross sensitivities, the different drifts shift the resonance frequencies to

$$\omega_{01} = \frac{1}{\sqrt{L_s\left(C_s + \Delta C_s + \Delta C_{x1}\right)}}, \tag{16a}$$

$$\omega_{02} = \frac{1}{\sqrt{L_s\left(C_s + \Delta C_s + \Delta C_{x2}\right)}}. \tag{16b}$$

Therefore, $f_d \neq 0$ and the readout is going to be wrong. By contrast, performing the proposed real-time differential measurement, using the cascaded configuration, the resulting single resonance frequency is

$$\omega_l = \omega_u = \omega_0 = \frac{1}{\sqrt{L_s\left(C_s + \Delta C_s\right)}}. \tag{17}$$

Since the two materials are the same and affected by cross sensitivities at the same time, it is reasonable to assume that $\Delta C_x = \Delta C_{x1} = \Delta C_{x2}$, so that

$$\omega_l = \omega_u = \omega_0 = \frac{1}{\sqrt{L_s\left(C_s + \Delta C_s + \Delta C_x\right)}}. \tag{18}$$

Consequently, $f_d = 0$, indicating that there is no difference between the materials. Note, however, that a comparison between identical materials is the most favorable case to reject cross sensitivities, this case being theoretically totally immune to them, as indicated by (18). In a differential sensing, some degree of robustness is expected, as different materials may respond in a different way to the same stimulus. Particularly, if we compare f_d for different materials (characterized by $\Delta C_{s1} = 0$, $\Delta C_{s2} = \Delta C_s$), and the same quantity under the presence of a common mode stimulus f_d', the difference is found to be:

$$f_d\,' - f_d = -f_u \frac{\Delta C_x}{2(C + \Delta C_s)} + f_l \frac{\Delta C_x}{2C}. \tag{19}$$

i.e., not exactly null if $\Delta C_x \neq 0$, but small (and identical to zero if $\Delta C_s = 0$).

C. Simulated Sensitivity in terms of Permittivity

It is apparent that the optimum position (i.e., the most sensitive region) where the SUTs must be loaded depends on the technology of implementation. In microstrip technology, as is well known, most of the electric field is concentrated in the substrate. Therefore, the SUTs should be located between the SIR and the ground plane, like filling a parallel-plate structure. Otherwise, the sensitivity will be decreased. Figure 9 shows a 2D cut of the electric field amplitude simulated with C*ST Microwave Studio*, confirming that most of the electric field confinement lies below the wide section of the SIR (i.e., the electric field is dominated by the capacitance effect of the resonator). Moreover, since the field is roughly uniformly distributed, the wide section behaves approximately like a parallel-plate capacitance.

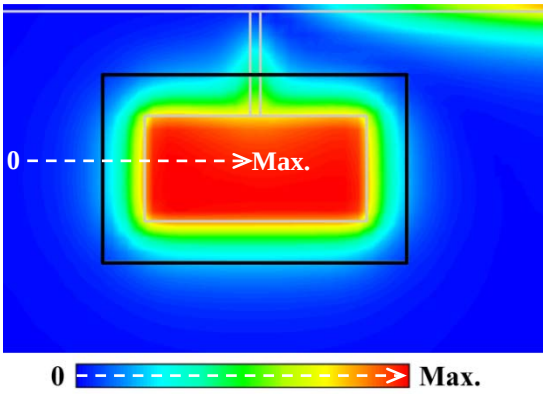

Fig. 9. Electric field amplitude at the SIR resonance frequency of the reference structure (single SIR) over the mid-plane between the SIR and the ground plane. The SUT height is set to $h-2t$ where t = 35 μm, and its length and width extend 1 mm beyond the wide section of the SIR, as depicted. The SUT size is 4.6 mm x 7.5 mm x 812.8 μm.

In order to characterize the sensitivity in terms of permittivity perturbations, we have considered the same reference structures as in Section II [Figs. 3(a) and 5(a)], and we have introduced a bulk dielectric SUT in one of the SIRs as illustrated in Fig. 9. The structures have been simulated with different values of the SUT relative permittivity, ε_{r2}, and the resulting resonance frequencies are plotted in Fig. 10. The resulting sensitivity derived from the results in Fig. 10 is plotted in Fig. 11. Clearly, for small perturbations, the sensitivity in cascaded SIRs is superior to that obtained using parallel SIRs.

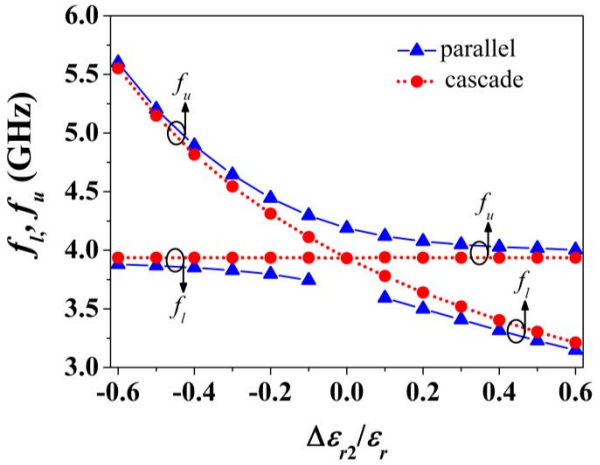

Fig. 10. Resonance frequencies for parallel and cascaded SIRs, obtained by electromagnetic simulation, versus a perturbation in the relative permittivity of a SUT loaded to one of the SIRs. The relative permittivity is perturbed by steps of ±10% so that $1.352 \le \varepsilon_{r2} \le 5.408$ ($-0.6 \le \Delta\varepsilon_{r2}/\varepsilon_r \le 0.6$) where ε_r = 3.38. Losses are considered.

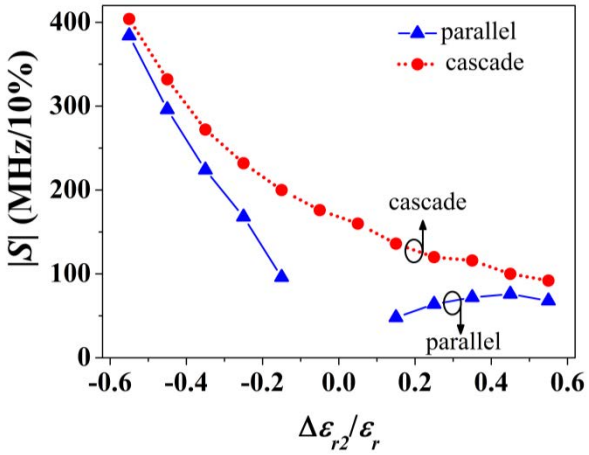

Fig. 11. Magnitude of the sensitivity derived from Fig. 10 by steps of $\Delta\varepsilon_{r2}/\varepsilon_r$ = ±0.1 (±10%). The sensitivity in the jump discontinuity of the parallel configuration is not calculated. As stated by (13), the sensitivity and the perturbation have the same sign.

It can be observed that the results in Fig. 10 are similar to those in Fig. 7. More specifically, the sensitivity to a permittivity perturbation ($\Delta\varepsilon_{r2}/\Delta\varepsilon_r$) is a bit smaller than that to a capacitive perturbation ($\Delta C_{s2}/\Delta C_s$) with the same amount of relative perturbation. This verifies again that the capacitance is not exactly proportional to the permittivity.

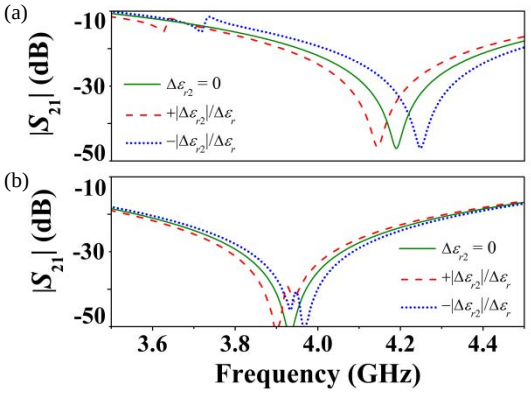

Fig. 12. Transmission coefficient obtained by electromagnetic simulations for small differential permittivity perturbations in (a) parallel and (b) cascaded SIRs. The perturbations are those necessary to obtain two −3-dB notches: $\Delta\varepsilon_{r2}/\varepsilon_r$ = ±0.06 and ±0.02 (6% and 2%), respectively.

The discrimination for small differential inputs, ε_{rd}, is of relevant importance in comparators. To gain insight into the performance of the considered topologies to operate as comparators, the discrimination from balanced to unbalanced perturbations should be defined as the minimum ε_{rd} necessary to produce a discriminable doubly notched response. It is assumed that two −3-dB notches suffice for reasonable accurate discrimination. For the considered topologies, these values are about ±6% and ±2% in the parallel and cascaded configurations. The transmission coefficients for these inputs are plotted in Fig. 12. Therefore, the cascade configuration exhibits higher discrimination than the parallel one, and it is an appropriate means to enhance the capability of detecting

inputs as small as possible (i.e., to enhance the discrimination). As was expected, wideband notches are required. Otherwise losses may mask the notches, as occurs in the lower notch for parallel SIRs when the input differential permittivity is close to zero. In summary, the discrimination is better with the cascaded configuration, where both notches are wide.

On the other hand, in the case of large perturbations and as proven in Fig. 13, the parallel and cascaded configuration have similar resonance frequencies and, in turn, sensitivities.

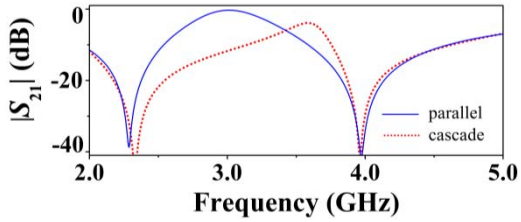

Fig. 13. Transmission coefficient obtained by electromagnetic simulations for a large differential permittivity perturbation: $\varepsilon_{r1} = 3.38$ and $\varepsilon_{r2} = 11.2$ resulting in $\Delta\varepsilon_{r2}/\varepsilon_r = +2.3$ (+230%).

IV. Experimental Validation of the Sensing Approaches and Discussion

In this section, permittivity perturbations are experimentally validated. To do so, the reference structures in Figs. 3 and 5 are considered again. In order to apply both positive and negative differential permittivity perturbations, the substrate in the vicinity of one of the SIRs is removed using a drilling machine, creating a cavity. Next, the cavity is either unfilled ($-|\Delta\varepsilon_{r2}|$) or filled with a *Rogers RO3010* substrate $\varepsilon_r = 11.2$ ($+|\Delta\varepsilon_{r2}|$), and covered with a metallic adhesive tape to act as the ground plane etched from the microstrip structure. Figure 14 shows different photographs to illustrate the cavities, and their filling and covering. Note that the effects of the air-gap present between the cavity and the SUT can be minimized by putting some pressure to the structure, as we have done in the measurements with the *Rogers* slab (in [5] a systematic method to eliminate the effects of the air gap is reported).

(a)

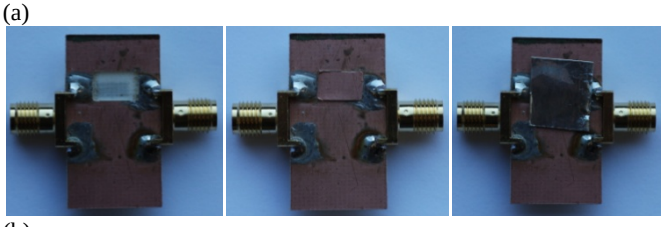

(b)

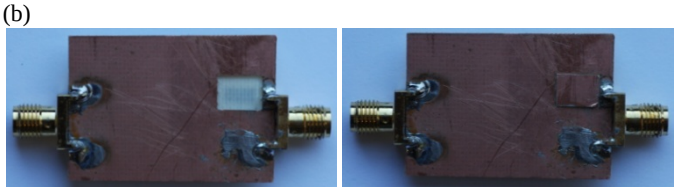

(c)

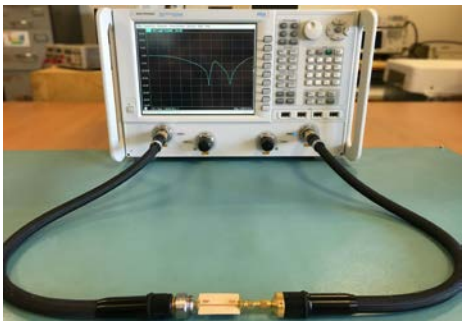

Fig. 14. Photograph of the reference structures composed of microstrip lines loaded with pairs of (a) parallel and (b) cascaded SIRs. From left to right: (*i*) cavity in one of the SIRs; (*ii*) filled cavity with *Rogers RO3010* with $\varepsilon_{r2} = 11.2$; (*iii*) cavity covered with a metallic tape. The photograph of the experimental set-up for measurement is shown in (c), including the *Agilent N5221A* network analyzer, cables, connectors and sensing system.

(a)

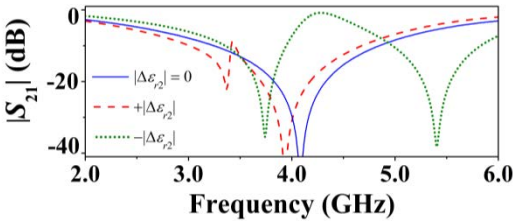

(b)

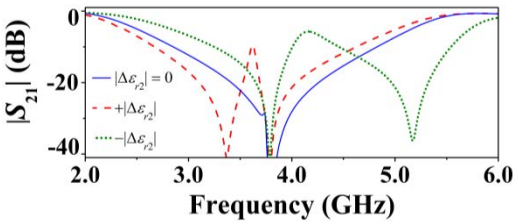

Fig. 15. Measured transmission coefficient magnitude for the (a) parallel and (b) cascaded topologies under dielectric loading. Three scenarios are considered: (*i*) without cavity ($\Delta\varepsilon_{r2} = 0$); (*ii*) unfilled cavity so that $\varepsilon_{r2} = 1$ ($-|\Delta\varepsilon_{r2}|$); (*iii*) filled cavity with *Rogers RO3010* with $\varepsilon_{r2} = 11.2$ ($+|\Delta\varepsilon_{r2}|$). No perturbation is applied to the other SIR ($\Delta\varepsilon_{r1} = 0$).

A. *Determining the dielectric constant of the SUT*

The measured results of the positive/negative perturbations, plotted in Fig. 15 together with those with no perturbation, are in accordance with theory. Even though the cavity dimensions cannot be controlled very accurately with the in-house drilling, these experiments validate the sensing principle under permittivity perturbation. Nevertheless, inspection of Fig. 15 reveals that the difference in notch frequencies is somehow smaller than the results of Fig. 10 for the considered dielectric constant values (1 for the unfilled cavity, and 11.2 for the filled cavity with the considered *Rogers* material). The reason

is that the cavity has been implemented by milling, and we have not completely removed all the substrate material, since the SIR needs some material for mechanical stability. Therefore, the unfilled cavity, including the remaining substrate layer, has an effective dielectric constant larger than 1, and the cavity filled with the *Rogers* substrate (dielectric constant 11.2) has actually an effective dielectric constant smaller than 11.2. In other words, the measurement provides the effective dielectric constant of the structure below the SIR, including not only the SUT but also the presence of a narrow dielectric layer of relative permittivity 3.38. Moreover, the thickness of the whole structure, layer on top the cavity plus SUT, is not necessarily the same as the thickness of the substrate. In the simulations that have been carried out to obtain the results of Fig. 10, we have not considered this substrate layer between the SIR metal level and the SUT. In practice, it is very difficult for us to precisely control the thickness of the remaining substrate between the SIR patch and the cavity. For this main reason such layer has not been considered in the simulations. However, note that with a more sophisticated fabrication technology (e.g., micromachining), such control would not be a problem.

Nevertheless, we have proposed a method to determine this thickness that subsequently allows us to obtain the dielectric constant of the SUT once the reference permittivity (the one of the substrate, i.e., ε_{r1}) and the thickness of the SUT are known. Let us consider that h_1 and h_c are the thicknesses of the substrate layer on top of the cavity and cavity, respectively, so that $h_1 + h_c = h$, the substrate thickness. Moreover let us assume that the SUT corresponds to a material with well-known dielectric constant, ε_{r2}, and thickness, h_2 (see Fig. 16). The method is based on the fact that the effective dielectric constant of the composite formed by the substrate layer on top of the cavity plus the SUT, ε_{eff}, is related to the respective dielectric constants by

$$\frac{\varepsilon_{eff}}{h} = \frac{\frac{\varepsilon_{r1}}{h_1}\cdot\frac{\varepsilon_{r2}}{h_2}}{\frac{\varepsilon_{r1}}{h_1}+\frac{\varepsilon_{r2}}{h_2}}. \qquad (20)$$

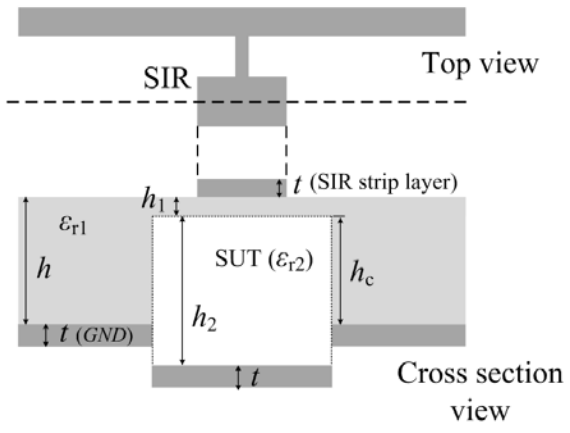

Fig. 16. Sketch (not drawn to scale) of the top and cross sectional view of the SIR and cavity loaded with the SUT.

From the previous expression, the dielectric constant of the SUT can be isolated:

$$\varepsilon_{r2} = \frac{\varepsilon_{eff}\varepsilon_{r1}h_2}{\varepsilon_{r1}h - \varepsilon_{eff}h_1}, \qquad (21)$$

ε_{eff} can be inferred from the split in frequency of the SUT and the curve of Fig. 10 corresponding to the cascade connection. Thus, if ε_{r2} and h_2 are known, h_1 can be obtained from (21). For the SUT corresponding to the *Rogers* substrate with ε_{r2} = 11.2 and h_2 = 635 μm, and taking into account that the notch frequencies of Fig. 15(b) provide ε_{eff} = 4.9, according to Fig. 10, the resulting thickness of the layer on top of the cavity is found to be h_1 = 369 μm. To verify the validity of this result, we have considered the curve of Fig. 15(b) corresponding to the unfilled cavity (ε_{r2} = 1). By introducing the corresponding effective dielectric constant ε_{eff} = 1.69 in (21), and h_1 = 369 μm, the air thickness is found to be h_2 = 371 μm, which is in reasonable agreement with the thickness of the cavity (note however that the metallic tape is somehow flexible and hence may reduce the effective value of the cavity thickness).

Once h_1 is known, we have calculated the dielectric constant of another SUT, an *Arlon* slab with ε_{r2} = 2.43 and h_2 = 490 μm. The measured transmission coefficient for the cascaded configuration is depicted in Fig. 17. The effective dielectric constant that results from Fig. 10 is ε_{eff} = 2.70, and using (21), the dielectric permittivity is found to be ε_{r2} = 2.50, very close to the nominal value (2.43).

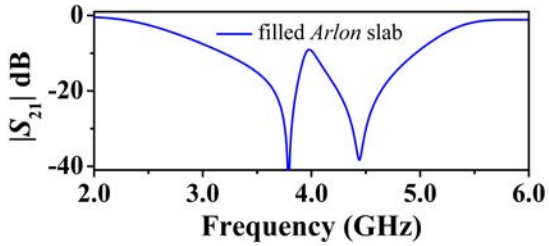

Fig. 17. Measured transmission coefficient magnitude for the cascaded topology with the cavity filled by an *Arlon* substrate with characteristics indicated in the text.

It is interesting to analyze expression (21), and the dependence of the dielectric constant of the SUT with the different parameters. Particularly, it depends linearly on the thickness of the SUT, h_2. Therefore, uncertainties in this parameter are directly translated to the dielectric constant. The dependence with the other geometrical parameters, h and h_1, can be appreciated in expression (21) as well. The thickness of the substrate, h, is typically known with good accuracy. On the other hand, the dependence on h_1 is modulated by ε_{eff}, and the effects of the uncertainty with this parameter are minimized in samples with small dielectric constant (and hence small ε_{eff}). In view of (21), and taking into account that ε_{eff} is roughly proportional to ε_{r1}, namely,

$$\varepsilon_{eff} = \varepsilon_{r1} + \Delta\varepsilon_{r2} = \varepsilon_{r1} + \frac{\Delta f}{S} \approx \varepsilon_{r1} + 2\varepsilon_{r1}\frac{\Delta f}{f_0}, \qquad (22)$$

it follows that ε_{r2} is proportional to ε_{r1} (see 21) and hence the uncertainties in the dielectric constant of the reference material are (roughly) directly translated to the one of the measured material.

Comparison of the proposed differential sensor with other permittivity sensors based on microstrip technology, such as those sensors based on CSRRs [3]-[5] is not easy. Nevertheless, the fact that the proposed sensors are differential represents advantages in several aspects. As comparators, common-mode stimuli are minimized by means of a differential-mode approach, as discussed before, and small changes between two (apparently identical) samples can be detected. Comparators based on this approach can be of interest to determine defects or abnormalities in a sample, as compared to a well known reference, as well as soft permittivity changes in circuits manufactured on microwave laminates. In a real scenario, two identical cavities must be present, each one below the corresponding SIR patch.

Concerning sensitivity, the capacitance of the SIR is broadside and hence very sensitive to the permittivity, as compared to the case of edge capacitances (such as the one of CSRRs). The sensitivity that can be inferred from the sensors reported in [3]-[5] is very reasonable but not as good as the one reported here [of the order of 0.6 GHz for small perturbations, according to Fig. 10 and expression (13) –note that we have considered the relative permittivity, i.e., dimensionless, in the denominator of (13)]. Note that according to expression (13), such sensitivity can be modulated by means of the SIR dimensions, which provide the resonance frequency for the unperturbed state.

B. Loss tangent estimation

Even though this paper is focused on low-loss substrates and SUTs (as mentioned before), let us discuss a procedure to estimate the loss tangent. It is based on the depth of the notch (similar to [4],[5]), and for this reason a structure with a single SIR is preferred (i.e., non differential). Otherwise, the presence of closed notches (as results in cases with small differential permittivities) may obscure the results. The initial assumption is that the substrate material below the SIRs is completely removed and replaced with the SUT. Let us consider two causes of losses, i.e., metallic losses, mainly associated to the narrow inductive strip of the SIR, and dielectric losses, related to the SUT. The model of the SIR-loaded line with losses included is the one of Fig. 1(b), but including a resistance, R_M, in series with the inductance L_s, plus a resistance, R_D, parallel connected to the capacitance C_s. The impedance of this shunt branch is

$$Z_{in} = R_M + \frac{R_D}{1+R_D^2 C_s^2 \omega^2} + j\left(\omega L_s - \frac{R_D^2 C_s \omega}{1+R_D^2 C_s^2 \omega^2}\right), \quad (23)$$

and this expression can be approximated by

$$Z_{in} = R_M + \frac{1}{R_D C_s^2 \omega^2} + j\left(\omega L_s - \frac{1}{C_s \omega}\right), \quad (24)$$

where it has been assumed that $R_D^2 C_s^2 \omega^2 >> 1$, corresponding to SUTs with moderate or low-loss levels (note that in an ideal lossless SUT, $R_D = \infty$). At the notch frequency, the reactive part of Z_{in} nulls, and the resulting resistance can be expressed as

$$R_{LOSS} = R_M + \frac{1}{C_s \omega Q_D}, \quad (25)$$

where Q_D is the SUT quality factor. Such resistance is related to the magnitude of the transmission coefficient at the notch frequency by

$$R_{LOSS} = \frac{Z_0 |S_{21}|}{2(1-|S_{21}|)}, \quad (26)$$

and therefore it can be inferred from the measured frequency response. On the other hand,

$$\tan\delta = \frac{1}{R_D C_s \omega} = Q_D^{-1}. \quad (27)$$

If R_M is known, (25) gives Q_D and hence $\tan\delta$ can be inferred from (27). To determine the contribution of the metallic losses, R_M, a possible procedure is to consider a reference SUT (or substrate) with a well-known $\tan\delta$ (and hence Q_D). From (25), R_M can be isolated, and used subsequently for the determination of the loss tangent of the SUT (it is assumed that R_M does not vary with the SUT).

The previous procedure cannot be directly applied in general to our proof-of-concept cascaded SIR based sensor since it is based on two SIRs, and, moreover, there is a remaining substrate layer on top of the cavity. However, for the considered SUT, the *Arlon* slab with nominal permittivity and thickness ε_{r2} = 2.43 and h_2 = 490 μm, the frequency response shows quite uncoupled notches and, therefore, we can modify the procedure and at least make an estimation of the $\tan\delta$. By introducing the SUT into the cavity, expression (25) can be re-written as

$$R_{LOSS} = R_M + \frac{1}{C_1 \omega Q_1} + \frac{1}{C_2 \omega Q_2}, \quad (28)$$

where the sub-index 1 and 2 refer to the layer on top of the cavity and SUT, respectively. By identifying the last two terms with the loss contribution of the composite, $(C_{eq}\omega Q_{eq})^{-1}$, it follows that

$$Q_{eq} = \frac{(C_1 + C_2) Q_1 Q_2}{Q_1 C_1 + Q_2 C_2}. \quad (29)$$

This expression depends on the ratio C_2/C_1, which can be determined from the thickness of the layer and SUT and from the dielectric constants. Using (25) with $C_s = C_{eq}$ and $Q_D = Q_{eq}$ and with R_{LOSS} inferred from (26), where S_{21} is obtained from the depth of the second notch in Fig. 17, we can determine Q_{eq}, which is found to be Q_{eq} = 366. Since Q_1 is known ($Q_1 = \tan\delta)^{-1}$ = 476, we can isolate Q_2 from (29), and the resulting

value is found to be Q_2 = 353, which gives $\tan\delta$ = 0.0028 (in reasonable agreement with the nominal value of 0.0020). Note that we cannot expect an accurate value of the loss factor with the considered in-house measurement system, necessarily affected by additional losses such as those derived from the connectors, soldering, metallic adhesive tape, etc. Nevertheless, a procedure to estimate the $\tan\delta$ of the SUT has been reported.

V. Conclusions

This paper analyzes two simple strategies to conduct differential measurements of permittivity. These strategies are based on loading pairs of stepped impedance resonators (SIRs), in either parallel or cascade connection, to a microstrip line. It has been shown that, although the most canonical symmetric configuration to perform a differential measurement is the one where the SIRs are parallel-connected, such a structure exhibits lower performance for small differential permittivities due to inter-resonator coupling, and hence the cascade connection is preferred in these situations. The differential technique is simple, as a transmission line is driven with a single-ended RF/microwave signal, and the SIRs are simply simultaneously and individually loaded with dielectric materials. The sensing principle is based on resonance frequency splitting, so that when the permittivities of the two dielectric materials are identical the sensor exhibits a single resonance frequency, whereas two resonances are present if such permittivities are different. The sensing principle has been experimentally validated by both shape and material perturbations. This main focus in this work has been on the differential measurement. A method to determine the dielectric constant of a certain sample under test (SUT), provided the one of the reference is known, has been proposed. Finally, in spite that the analysis of the present work has been carried out by excluding losses, a method to estimate the loss tangent of the SUT has been also reported. As is well known, changing environmental factors may change the permittivity and, therefore, miscalibration. By virtue of a differential measurement, sensing and comparison with some degree of immunity to these external factors is expected.

References

[1] E. Nyfor, "Industrial microwave sensors—A review," *Subsurface Sensing Technologies and Applications*, vol. 1, no. 1, pp. 23−43, Jan. 2000.

[2] M. Tiuri, "Microwave Sensor Applications in Industry," in *Europ. Microw. Conf.*, pp. 25−32, Sep. 1987.

[3] M. S. Boybay and O. M. Ramahi, "Material characterization using complementary split-ring resonators," *IEEE Trans. Instrum. Meas.*, vol. 61, no. 11, pp. 3039−3046, Nov. 2012.

[4] C.-S. Lee and C.-L. Yang, "Complementary split-ring resonators for measuring dielectric constants and loss tangents," *IEEE Microw. Wireless Compon. Lett.*, vol. 24, no. 8, pp. 563−565, Aug. 2014.

[5] C.-L. Yang, C.-S. Lee, K.-W. Chen, and K.-Z. Chen, "Noncontact measurement of complex permittivity and thickness by using planar resonators," *IEEE Trans. Microw. Theory Techn.*, vol. 64, no.1, pp. 247−257, Jan. 2016.

[6] M. Puentes, C. Weiß, M. Schüßler, and R. Jakoby, "Sensor array based on split ring resonators for analysis of organic tissues," in *IEEE MTT-S Int. Microw. Symp.*, Baltimore, MD, USA, pp. 1-4, Jun. 2011

[7] M. Puentes, *Planar Metamaterial Based Microwave Sensor Arrays for Biomedical Analysis and Treatment*. Springer, 2014.

[8] T. Chretiennot, D. Dubuc and K. Grenier, "A microwave and microfluidic planar resonator for efficient and accurate complex permittivity characterization of aqueous solutions," *IEEE Trans. Microw. Theory Techn.*, vol. 61, no. 2, pp. 972−978, Feb. 2013.

[9] A. Abduljabar, D. Rowe, A. Porch and D. Barrow, "Novel microwave microfluidic sensor using a microstrip split-ring resonator," *IEEE Trans. Microw. Theory Techn.*, vol. 62, no. 3, pp. 679−688, Mar. 2014.

[10] A. Ebrahimi, W. Withayachumnankul, S. Al-Sarawi and D. Abbott, "High-sensitivity metamaterial-inspired sensor for microfluidic dielectric characterization," *IEEE Sensors J.*, vol. 14, no. 5, pp. 1345−1351, May 2014.

[11] W. Withayachumnankul, K. Jaruwongrungsee, A. Tuantranont, C. Fumeaux and D. Abbott, "Metamaterial-based microfluidic sensor for dielectric characterization," *Sensor Actuat. A Phys.*, vol. 189, pp. 233−237, Jan. 2013

[12] H.-J. Lee and J.-G. Yook, "Biosensing using split-ring resonators at microwave regime," *App. Phys. Lett.*, vol. 92, no. 25, paper 254103, 2008.

[13] K. Grenier, D. Dubuc, P-E. Poleni, M. Kumemura, H. Toshiyoshi, T. Fujii, and H. Fujita, "Integrated broadband microwave and microfluidic sensor dedicated to bioengineering," *IEEE Trans. Microw. Theory Techn.*, vol. 57, no. 12, pp. 3246−3253, Dec. 2009.

[14] T. Chen, D. Dubuc, and K. Grenier, "Resonant-based microwave biosensor for physiological liquid identification", *Europ. Microw. Conf*, pp. 448-450, Amsterdam, Netherland, Oct-Nov, 2012.

[15] T. Chretiennot, D. Dubuc, K. Grenier, "Optimized Electromagnetic Interaction Microwave Resonator/Microfluidic Channel for Enhanced Liquid Bio-Sensor," *Europ. Microw. Conf.*, pp. 464-467, Nuremberg Germany, Oct.2013.

[16] T. Chretiennot, D. Dubuc, K. Grenier, "Double stub resonant biosensor for glucose concentrations quantification of multiple aqueous solutions," *IEEE MTT-S Int. Microw. Symp.*, pp. 1-4, Tampa (FL), June 2014.

[17] E. Ekmekci and G. Turhan-Sayan, "Multi-functional metamaterial sensor based on a broad-side coupled SRR topology with a multi-layer substrate," *App. Phys. A* , vol. 110, no. 1, pp 189−197, Jan. 2013.

[18] C. Damm, M. Schussler, M. Puentes, H. Maune, M. Maasch and R. Jakoby, "Artificial transmission lines for high sensitive microwave sensors," *IEEE Sensors Conf.*, Christchurch, New Zealand, pp.755−758, Oct. 2009.

[19] C. Damm, *Artificial Transmission Line Structures for Tunable Microwave Components and Microwave Sensors*, Shaker, 2011.

[20] M. Schueler, C. Mandel, M. Puentes and R. Jakoby, "Metamaterial inspired microwave sensors," *IEEE Microw. Mag.*, vol. 13, no. 2, pp. 57–68, Mar. 2012.

[21] J. G. Webster, *The Measurement Instrumentation and Sensors Handbook*. Boca Raton, FL, USA: CRC, 1999.

[22] J. Fraden, *Handbook of Modern Sensors: Physics, Design, and Applications*, 3rd ed. New York, NY, USA, Springer, 2004.

[23] J. Naqui, C. Damm, A. Wiens, R. Jakoby, L. Su and F. Martín, "Transmission lines loaded with pairs of magnetically coupled stepped impedance resonators: modeling and application to microwave sensors," in *IEEE MTT-S Int. Microw. Symp*., Tampa, FL, USA, pp. 1-4, Jun. 2014.

[24] J. Naqui, *Symmetry properties in transmission lines loaded with electrically small resonators: circuit modeling and applications*, Springer, 2016.

[25] A.K. Horestani, J. Naqui, Z. Shaterian, D. Abbott, C. Fumeaux and F. Martín, "Two-dimensional alignment and displacement sensor based on movable broadside-coupled split ring resonators," *Sens. Actuat. A Phys.*, vol. 210, pp. 18–24, Apr. 2014.

[26] J.-S. Hong and M. J. Lancaster, *Microstrip Filters for RF/Microwave Applications*. New York, NY, USA: Wiley, 2001.

[27] J. Bonache, M. Gil, I. Gil, J. García-García and F. Martín, "On the electrical characteristics of complementary metamaterial resonators," *IEEE Microw. Wireless Compon. Lett.*, vol. 16, no. 10, pp. 543−545, Oct. 2006.

[28] R. Mongia, I. Bahl and P. Barthia, *RF and Microwave Coupled Line Circuits*. Norwood, MA, USA: Artech House, 1999.

[29] C. Cui and Y. Liu, "Quad-band bandpass filter design by embedding dual-band bandpass filter with dual-mode notch elements," *Electron. Lett.*, vol. 50, no. 23, pp.1719–1720, Nov. 2014.

[30] M. Makimoto and S. Yamashita, “Compact bandpass filters using stepped impedance resonators,” *Proc. IEEE*, vol. 67, no. pp. 16−19, Jan. 1979.
[31] D. Girbau, A. Lazaro and R. Villarino, “Passive wireless permittivity sensor based on frequency-coded chipless RFID tags,” in *IEEE MTT-S Int. Microw. Symp.*, Montreal, Canada, pp. 1-4, Jun. 2012.
[32] J.-S. Hong, H. Shaman and C. Young-Hoon, “Dual-mode microstrip open-loop resonators and filters,” *IEEE Trans. Microw. Theory Techn.*, vol. 55, no. 8, pp. 1764−1770, Aug. 2007.
[33] V. A. Fedotov, M. Rose, S. L. Prosvirnin, N. Papasimakis and N. I. Zheludev, “Sharp trapped-mode resonances in planar metamaterials with a broken structural symmetry,” *Phys. Rev. Lett*, vol. 99, no. 14, paper 47401, Oct. 2007.

Jordi Naqui (S’11–M’14) was born in Granollers, Spain. He received the Telecommunication Technical Engineering diploma (specialty in Electronic Systems), the Telecommunication Engineering degree, the Master’s degree in Microelectronics and Nanoelectronics Engineering, and the Ph.D. degree in Electronics Engineering in 2006, 2010, 2011, and 2014, respectively, from the Universitat Autònoma de Barcelona (UAB), Bellaterra, Barcelona, Spain.
He was a recipient of a predoctoral fellowship by the Spanish Government. He was awarded with the Yarman-Carlin Best Student Paper Contest at 14th MMS, the Young Scientist Award at XXX URSI Spanish National Symposium, the IX Comerma Engineer Research Award by the Local Government of Ferrol and the University of A Coruña, and the Best Doctorate Student Award.
His research activities at UAB, from 2009 to 2016, were focused on circuit modeling, filters and sensors. He taught in the Department of Electronics Engineering from 2010 to 2016. Currently, he is a Senior Filter Design Engineer at Qorvo.

Christian Damm was born in August 1977 in Marburg, Germany. He studied theoretical electrical engineering and received his Dr.-Ing. degree in 2010 from Technische Universität Darmstadt, Germany. Since September 2014 he holds a full professor position at Technische Universität Darmstadt as head of the THz Sensors Group. Since more than 10 years his research has been focused on transmission line Metamaterials and tunable Metamaterials for microwave applications, e.g. phase shifters, matching networks and leaky wave antennas. With this comes a strong involvement in material characterization of artificial materials and liquid crystals as enabling material for tunable Metamaterials. Furthermore, his research activities include sensor applications based on Metamaterials and periodic structures. Recently, the frequency range for his research activities have been extended up to the THz regime.
He is currently involved in the coordination and research activities of the German Priority Programme "ESSENCE" SPP1857 focused on life science applications of electromagnetic sensors. He is a member of the IEEE since 13 years and is contributing to the scientific community as a reviewer for many journals including the T-MTT, T-TST, MWCL, AWPL and several conferences including the IMS, EUMW, RWW and Metamaterials Conference.

Alex Wiens, born 1984, received the Dipl.-Phys. degree in experimental physics from the University of Mainz, Germany, in 2011. Since 2012, he is working towards his PhD with the Microwave Engineering Group at Technische Universitaet Darmstadt in Germany. His research is currently focused on advanced RF devices employing tunable dielectrics on material, component and system level for high power applications.

Rolf Jakoby was born in Kinheim, Germany, in 1958. He received the Dipl.-Ing. and Dr.-Ing. Degrees in electrical engineering from the University of Siegen, Germany, in 1985 and 1990, respectively. In Jan. 1991, he joined the Research Center of Deutsche Telekom in Darmstadt, Germany. Since April 1997 he has a full professorship in “Microwave Engineering” at TU Darmstadt, Germany. His interdisciplinary research focuses mainly on 1.) ferroelectric (BST) thin- and thick film as well as microwave liquid crystal (LC) technologies for low-cost electronically reconfigurable/tunable passive devices with low power consumption such as frequency-agile filters and beam-steering antenna arrays and 2.) chipless RFID tags and wireless passive microwave sensors for wireless industrial process and environmental monitoring as well as for non- or minimal-invasive biomedical sensing. Rolf Jakoby is editor-in-chief of the Journal ”FREQUENZ”, De Gruyter, ISSN 0016-1136, a member of the VDE ITG, IEEE MTT and AP as well as co-founder of the start-up company ALCAN Systems, which focuses on smart antennas. He was chairman of the EuMC2007 and GeMiC2011, and treasurer of the EuMW2013 and 2017. He is involved in 20 patents and more than 320 publications. In 1992, he received an award from the CCI Siegen for his excellent PhD and in 1997, the ITG-Prize for an excellent publication in the IEEE AP Transactions. His group received 19 awards and prizes for best papers and doctoral dissertations.

Lijuan Su (S’14) was born in Qianjiang City, Hubei Province, China in 1983. She received the Bachelor degree of Engineering in Communication Engineering and the degree for Master of Engineering in Circuits and Systems from Wuhan University of Technology (China) in 2005 and 2013, respectively. Between 2005 and 2009, she worked as an engineer in China Telecom Corporation Ltd. She is currently working towards her PhD in the field of metamaterials applied to RF/microwave sensors in the Universitat Autonoma de Barcelona.

Javier Mata Contreras was born in 1976 in Málaga (Spain). He received the Ingeniería de Telecomunicación Degree from the Universidad de Málaga (UMA) in 2000 and the PhD degree from the same university in 2010, with the Thesis “Distributed Amplifiers and Mixers with Transmission Lines based on Metamaterials”. In 2000, he joined the UMA Department of Ingeniería de Comunicaciones UMA as Assistant Professor.
He is currently working at CIMITEC and the Universitat Autònoma de Barcelona as Visitant Professor. His research interests include active and passive microwave devices and active distributed circuits based on metamaterials, among others.

Ferran Martín (M’04-SM’08-F’12) was born in Barakaldo (Vizcaya), Spain in 1965. He received the B.S. Degree in Physics from the Universitat Autònoma de Barcelona (UAB) in 1988 and the PhD degree in 1992. From 1994 up to 2006 he was Associate Professor in Electronics at the Departament d’Enginyeria Electrònica (Universitat Autònoma de Barcelona), and since 2007 he is Full Professor of Electronics. In recent years, he has been involved in different research activities including modelling and simulation of electron devices for high frequency applications, millimeter wave and THz generation systems, and the application of electromagnetic bandgaps to microwave and millimeter wave circuits. He is now very active in the field of metamaterials and their application to the miniaturization and optimization of microwave circuits and antennas. He is the head of the Microwave Engineering, Metamaterials and Antennas Group (GEMMA Group) at UAB, and director of CIMITEC, a research Center on Metamaterials supported by TECNIO (Generalitat de Catalunya). He has organized several international events related to metamaterials, including Workshops at the IEEE International Microwave Symposium (years 2005 and 2007) and European Microwave Conference (2009), and the Fifth

International Congress on Advanced Electromagnetic Materials in Microwaves and Optics (Metamaterials 2011), where he has acted as chair of the Local Organizing Committee. He has acted as Guest Editor for three Special Issues on Metamaterials in three International Journals. He has authored and co-authored over 500 technical conference, letter, journal papers and book chapters, he is co-author of the book on Metamaterials entitled Metamaterials with Negative Parameters: Theory, Design and Microwave Applications (John Wiley & Sons Inc. 2008), author of the book Artificial Transmission Lines for RF and Microwave Applications (John Wiley & Sons Inc. 2015), and he has generated 15 PhDs. Ferran Martín has filed several patents on metamaterials and has headed several Development Contracts.

Prof. Martín is a member of the IEEE Microwave Theory and Techniques Society (IEEE MTT-S). He is reviewer of the IEEE Transactions on Microwave Theory and Techniques and IEEE Microwave and Wireless Components Letters, among many other journals, and he serves as member of the Editorial Board of IET Microwaves, Antennas and Propagation and International Journal of RF and Microwave Computer-Aided Engineering. He is also a member of the Technical Committees of the European Microwave Conference (EuMC) and International Congress on Advanced Electromagnetic Materials in Microwaves and Optics (Metamaterials). Among his distinctions, Ferran Martín has received the 2006 Duran Farell Prize for Technological Research, he holds the Parc de Recerca UAB – Santander Technology Transfer Chair, he has been the recipient of two ICREA ACADEMIA Awards (calls 2008 and 2013) and recipient of the Ingeniero Comerma Prize in 2015. He is Fellow of the IEEE since 2012 and Fellow of the IET since 2016.

IMS17(C)*

"Estimation of Conductive Losses in Complementary Split Ring Resonator (CSRR) Loading an Embedded Microstrip Line and Applications"

L. Su, J. Mata-Contreras, P. Vélez, and F. Martín

IEEE MTT-S International Microwave Symposium (IMS'17), Honolulu, Hawaii, USA, June 2017.

* Conference articles(C) included in this thesis for completeness but cannot be officially part of the compendium of the articles of the Ph.D. thesis.

Estimation of Conductive Losses in Complementary Split Ring Resonator (CSRR) Loading an Embedded Microstrip Line and Applications

Lijuan Su, Javier Mata-Contreras, Paris Vélez, and Ferran Martín
CIMITEC, Departament d'Enginyeria Electrònica, Universitat Autònoma de Barcelona
08193 Bellaterra, Barcelona, Spain
E-mail: Ferran.Martin@uab.es

***Abstract*—In this paper, a simple method to estimate the conductive losses in complementary split ring resonators (CSRRs) is proposed. It is based on the measurement of the transmission coefficient (insertion loss) in an embedded microstrip line with the CSRR under consideration etched in the ground plane, beneath the conductor strip. It is assumed that losses are due to the substrate (dielectric losses) and CSRR (ohmic and dielectric losses) since conductive losses in the strip of the line are negligible. By considering the circuit model of the CSRR-loaded line, including the substrate conductance plus the conductive (ohmic resistance) and dielectric losses of the CSRR, it is possible to infer from the insertion loss the real part of the shunt impedance at resonance. From this value, and assuming that the loss tangent of the considered substrate is known, the ohmic resistance of the CSRR can be estimated. Once this resistance is known, it is possible to use these CSRR-loaded structures to estimate the complex permittivity of dielectric samples and liquids.**

***Index Terms*—Embedded microstrip lines, complementary split ring resonators (CSRR), conductor and dielectric losses, permittivity sensors.**

I. Introduction

Complementary split ring resonators (CSRRs) [1] have been used in many different scenarios in recent years, particularly in the design of planar microwave filters [2], multiband components [3], and sensors [4]-[8]. In filters and sensors, a typical configuration consists of a microstrip line with the CSRRs etched in the ground plane. For design purposes, the lumped element equivalent circuit model of the CSRR-loaded line section (first reported in [9]) is necessary. Losses in the circuit model have been typically ignored. In filter and circuit design, this is justified since losses are usually neglected at the design level in order to discard an improper design if insertion losses are present, or unacceptable, in the final prototype. Obviously the insertion loss level can be predicted through electromagnetic simulators by including conductor and dielectric losses in the designed structure. In these applications, losses may degrade significantly device performance, but the inclusion of losses at the circuit level does not represent (in general) an advantage in terms of filter or circuit design.

However, in other applications, e.g., CSRR-based microwave sensors, the presence of losses in the circuit model cannot be ignored, especially if the output variable is related to the level of insertion loss, or if the variable under measurement is related to losses (e.g., complex permittivity of samples). In [5],[7] CSRR-loaded microstrip structures are used for the measurement of complex permittivity on the basis of the frequency response of the structure with the sample under test (SUT) placed below the CSRR. The considered circuit model of the CSRR with losses is a parallel RLC circuit including the inductance and capacitance of the CSRR (the later one influenced by the SUT) and a total equivalent loss resistance composed of the parallel combination of substrate losses, sample losses and metal losses [5],[7]. In [10], the total losses of a CSRR-loaded line were estimated from parameter extraction by considering such parallel RLC circuit for the CSRR. However, this method does not provide separately the CSRR losses related to the surrounding dielectric (substrate and SUT if it is present) and the metal (ohmic) losses.

In this paper, we propose a new circuit model of CSRR-loaded lines that takes into account substrate (dielectric) losses, and distinguishes between the metal and dielectric losses of the CSRR. This model is used for the estimation of the conductive losses of the CSRR in embedded microstrip lines, provided the loss tangent of the considered substrate is known. Moreover, we point out the potential of these structures for the estimation of the complex permittivity of lossy dielectric slabs or liquids, using the same method.

II. Model and Analysis

The cross section, layout, and proposed circuit model (including losses) of the considered CSRR-loaded line is depicted in Fig. 1. The line is described by the series inductance L and the capacitance C, which provides electric coupling between the line and the CSRR (note that with this CSRR orientation, magnetic coupling between the line and the CSRR is prevented, as discussed in [11]). In microstrip lines working at moderate microwave frequencies, ohmic losses related to the finite conductivity of the metallic strip are very small. Therefore, losses are assumed to be entirely due to the considered substrate (with known loss tangent) and CSRR. Substrate losses are accounted for by the resistance R_S, whereas CSRR losses are described by R_M, physically representing the ohmic losses of the narrow inductive strips

connecting the inner and outer metallic regions of the CSRR, and by R_D, corresponding to the losses associated to the dielectric material surrounding the CSRR. In the model, C_c and L_c are the capacitance and inductance, respectively, of the CSRR.

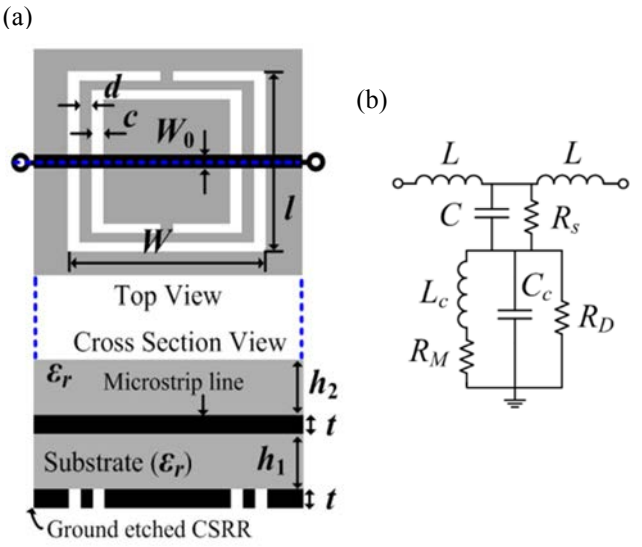

Fig. 1. Top and cross section views (a), and lumped element equivalent circuit (b) of the CSRR-loaded embedded microstrip line. Dimensions are: W = 4.8 mm, l = 7.86 mm, c = 0.2 mm, d = 0.2 mm, W_0 = 1.15 mm, h_1 = 1.27 mm, h_2 = 2.54 mm and t = 35 μm.

The real, R_{eq}, and imaginary, χ_{eq}, parts of the impedance of the shunt branch of the model of Fig. 1(b) can be expressed as

$$R_{eq} = \frac{1}{R_S C^2 \omega^2} + \frac{R_M R_D^2 + R_D L_c^2 \omega^2}{R_D^2 (1 - L_c C_c \omega^2)^2 + (L_c \omega + R_M R_D C_c \omega)^2} \quad (1)$$

$$\chi_{eq} = \frac{-1}{C\omega} + \frac{R_D^2 L_c \omega (1 - L_c C_c \omega^2) - R_M R_D (L_c \omega + R_M R_D C_c \omega)}{R_D^2 (1 - L_c C_c \omega^2)^2 + (L_c \omega + R_M R_D C_c \omega)^2} \quad (2)$$

where it has been assumed that $R_S^2 C^2 \omega^2 >> 1$, corresponding to a low-loss substrate, and $R_D >> R_M$, reasonable on account of the small resistivity of typical conductor layers (e.g., Cu).

In (1) and (2), C, L_c and C_c can be inferred from the response of the structure through parameter extraction [10], and R_S and R_D can be estimated from the loss tangent ($\tan\delta$) of the considered substrate (a known parameter) through [12]

$$\tan\delta = \frac{1}{R_S C \omega} \quad (3)$$

$$\tan\delta = \frac{1 + \varepsilon_r}{R_D C_c \varepsilon_r \omega} \quad (4)$$

where ε_r is the dielectric constant of the substrate (also a known parameter). To obtain (4), it has been assumed that the ground plane (or CSRR) is surrounded by air, and that the total capacitance of the CSRR, C_c, is given by the parallel connection of the CSRR substrate capacitance, C_D, and air capacitance, C_{air} (a valid assumption under the quasi-static limit, reasonable at the considered frequency, where the electric field lines do not cross the substrate/air interface in the slot regions of the CSRR, see Fig. 2). This means that the total capacitance can be expressed as $C_c = C_{air}\cdot(1 + \varepsilon_r)$, and hence the CSRR substrate capacitance is $C_D = C_c\varepsilon_r/(1+\varepsilon_r)$. Since, alternatively to (3), the loss tangent can also be expressed by $\tan\delta = 1/(R_D C_D \omega)$, with losses and capacitance restricted to the substrate region, expression (4) is straightforwardly inferred. Note also that expression (3) is valid as long as the metallic strip of the line is surrounded by a homogeneous material. For this reason, a homogeneous embedded microstrip line is considered in this paper.

According to the previous words, it follows that the single unknown in (1) and (2) is R_M. This parameter can be estimated from the response of the structure, since it provides the value of (1), according to the method to be explained in Section III.

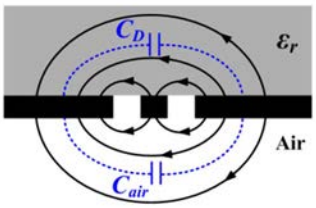

Fig. 2. Cross sectional view of the slot region of the CSRR, with electric field lines and contributions to the total CSRR capacitance.

III. Estimation of CSRR conductor losses

In a two-port structure described by the T-circuit model with series impedance Z_s and shunt impedance Z_p, the insertion loss can be expressed as

$$S_{21} = \frac{2Z_0 Z_p}{2Z_0 Z_p + 2Z_0 Z_s + 2Z_s Z_p + Z_s^2 + Z_0^2}. \quad (5)$$

Z_0 being the reference impedance of the ports. At the frequency, ω_0, where the reactance of Z_p equals zero, i.e., χ_{eq} = 0, we can express the magnitude of (5) as

$$|S_{21}|_{\omega_0} = \frac{2Z_0 R_{eq}}{\sqrt{(2Z_0 R_{eq} + Z_0^2 - L^2\omega^2)^2 + [2L\omega(Z_0 + R_{eq})]^2}}. \quad (6)$$

Note that the notch frequency (where $|S_{21}| = |S_{21}|_{min}$) does not coincide with the frequency where χ_{eq} = 0, ω_0, unless losses are absent. However, it is expected to be close to that frequency. Hence, the procedure is to make a guess of ω_0, obtain $|S_{21}|$ at that frequency, isolate R_{eq} from (6), and determine R_M from (1). With this value, (2) can be evaluated. If χ_{eq} = 0, then R_M is obtained; otherwise, the process is iterated until χ_{eq} = 0.

IV. Illustrative Example and Application to Complex Permittivity Estimation

We have applied the method in the CSRR-loaded embedded microstrip line of Fig. 1(a), with dimensions indicated in the caption. The considered substrate material has dielectric constant ε_r = 10.2 and loss tangent $\tan\delta$ = 0.0023. The measured response of the structure is depicted in Fig. 3, where the photograph of the fabricated embedded microstrip line is included [Fig. 3(b)]. The reactive elements of the circuit model have been inferred by parameter extraction from the measured response, and R_S and R_D by means of (3) and (4). Then we have applied the iterative process explained in Section III in order to estimate the conductive losses of the CSRR. The inferred result is R_M = 0.11 Ω. The circuit simulation of the equivalent circuit model, with parameters indicated in the caption of Fig. 3, is also depicted in that figure. The good agreement between the circuit simulation and the measured response in the region of interest is indicative of the validity of the proposed lossy model of the CSRR.

(a)

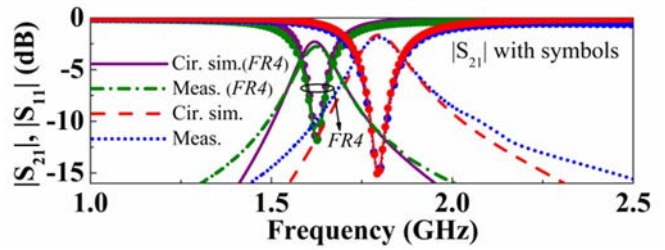

(b)

Fig. 3. Insertion and return losses (a) and photograph (b) of the considered CSRR-loaded line. The element values of the circuit model are L = 2.08 nH, C = 1.41 pF, C_c = 8.32 pF, L_c = 0.81 nH, R_S = 27356 Ω, R_D = 5085 Ω, and R_M = 0.11 Ω. For the case with *FR4* loading, the CSRR capacitor changes to C_c' = 10.44 pF.

With this CSRR-loaded line, once R_M is known, we can easily estimate the complex permittivity of a dielectric sample (sample under test –SUT) by placing it in contact with the CSRR in the back substrate side. To this end, the frequency response is obtained. From the resulting frequency shift, as compared to the one of the unloaded (i.e., without SUT) structure, we can infer the dielectric constant value according to

$$\varepsilon_{SUT} = 1 + \frac{(\omega_0'^{-2} - \omega_0^{-2})}{L_c C_c}(1 + \varepsilon_r) \cdot \qquad (7)$$

where ω'_0 is the resonance frequency with the presence of the SUT. R_D can be inferred from (6) and (1) by using a similar procedure to the one reported in Section III for the estimation of R_M. From the new value of R_D we can obtain the contribution of the SUT (since the contribution of the substrate to R_D is known), and the loss tangent can be inferred.

To validate this method for the estimation of the complex permittivity of a dielectric slab, we have loaded the CSRR-based line by means of a *FR4* slab (Fig. 3) with thickness 2.54 mm (much larger than c and d). The measured frequency response is also depicted in Fig. 3. From the new value of the notch frequency, the dielectric constant is found to be ε_r = 3.9 (using 7), and R_D = 2919 Ω. Consequently, the loss tangent is found to be $\tan\delta_{SUT}$ = 0.0056. These values are in reasonable agreement with the measured values for *FR4*, i.e., ε_r = 4.2 and $\tan\delta$ = 0.0074, obtained by means of the commercial *Agilent 85072A* split cylinder resonator.

V. Conclusion

In conclusion, a technique to estimate the conductive losses in CSRRs has been proposed. It uses an embedded microstrip line loaded with the CSRR, and the conductive loss resistance of the CSRR is inferred from the measured response through a method based on the lossy circuit model. Once such resistance is known, the CSRR-loaded embedded microstrip line is useful to estimate the dielectric constant and loss tangent of lossy dielectric samples and liquids.

Acknowledgment

This work was supported by MINECO-Spain under project TEC2013-40600-R and FEDER Funds. Thanks are also given to *Generalitat de Catalunya* for partially funding this research activity through the project 2014SGR-157. Ferran Martín is in debt to *Institució Catalana de Recerca i Estudis Avançats* for supporting his work. Lijuan Su acknowledges the China Scholarship Council (CSC) for the grant 201306950011.

References

[1] F. Falcone, T. Lopetegi, J.D. Baena, R. Marqués, F. Martín and M. Sorolla, "Effective negative-ε stop-band microstrip lines based on complementary split ring resonators," *IEEE Microw. Wireless Compon. Lett.*, vol. 14, pp. 280-282, Jun. 2004.

[2] J. Bonache, I. Gil, J. García-García and F. Martín, "Novel microstrip band pass filters based on complementary split rings resonators," *IEEE Trans. Microw. Theory Techn.*, vol. 54, pp. 265-271, Jan. 2006.

[3] J. Bonache, G. Sisó, M. Gil, A. Iniesta, J. García-Rincón and F. Martín, "Application of composite right/left handed (CRLH) transmission lines based on complementary split ring resonators (CSRRs) to the design of dual band microwave components," *IEEE Microw. Wireless Compon. Lett.*, vol. 18, pp. 524-526, Aug. 2008.

[4] M. S. Boybay and O. M. Ramahi, "Material characterization using complementary split-ring resonators," *IEEE Trans. Instrum. Meas.*, vol. 61, no. 11, pp. 3039−3046, Nov. 2012.

[5] C.-S. Lee and C.-L. Yang, "Complementary split-ring resonators for measuring dielectric constants and loss tangents," *IEEE* Microw. *Wireless Compon. Lett.*, vol. 24, no. 8, pp. 563−565, Aug. 2014.

[6] A. Ebrahimi, W. Withayachumnankul, S. Al-Sarawi and D. Abbott, "High-sensitivity metamaterial-inspired sensor for microfluidic dielectric characterization," *IEEE Sensors J.* vol. 14, pp. 1345−1351, May 2014.

[7] C.-L. Yang, C.-S. Lee, K.-W. Chen and K.-Z. Chen, "Noncontact measurement of complex permittivity and thickness by using planar resonators," *IEEE Trans. Microw. Theory Techn*., vol. 64, no.1, pp. 247−257, Jan. 2016.

[8] L. Su, J. Naqui, J. Mata-Contreras and F. Martín, "Cascaded splitter/combiner microstrip sections loaded with complementary split ring resonators (CSRRs): modeling, analysis and applications," *IEEE MTT-S Int. Microwave Symp*. (IMS'16), San Francisco (CA), USA, May 2016.

[9] J.D. Baena, J. Bonache, F. Martín, R. Marqués, F. Falcone, T. Lopetegi, M.A.G. Laso, J. García, I Gil, M. Flores-Portillo and M. Sorolla, "Equivalent circuit models for split ring resonators and complementary split rings resonators coupled to planar transmission lines," *IEEE Trans. Microw. Theory Techn.*, vol. 53, pp. 1451-1461, Apr. 2005.

[10] J. Bonache, M. Gil, I. Gil, J. Garcia-García and F. Martín, "On the electrical characteristics of complementary metamaterial resonators," *IEEE Microwav. Wireless Compon. Lett.*, vol. 16, pp. 543.545, Oct. 2006.

[11] J. Naqui, M. Durán-Sindreu and F. Martín, "Modeling split ring resonator (SRR) and complementary split ring resonator (CSRR) loaded transmission lines exhibiting cross polarization effects," *IEEE Ant. Wireless Propag. Lett*., vol. 12, pp. 178-181, 2013.

[12] D.M. Pozar, *Microwave Engineering*, 3rd Ed., Hoboken, NJ, Wiley, 2005.

Pavia17[(C)*]

"Estimation of Complex Permittivity of Liquids by means of Complementary Split Ring Resonator (CSRR) Loaded Transmission Lines"

L. Su, J. Mata-Contreras, P. Vélez, and F. Martín

IEEE MTT-S International Microwave Workshop Series on Advanced Materials and Processes (IMWS-AMP 2017)
Pavia, Italy, September 2017.
(Accepted)

* Conference articles[(C)] included in this thesis for completeness but cannot be officially part of the compendium of the articles of the Ph.D. thesis.

Estimation of the Complex Permittivity of Liquids by means of Complementary Split Ring Resonator (CSRR) Loaded Transmission Lines

Lijuan Su, Javier Mata-Contreras, Paris Vélez, and Ferran Martín
CIMITEC, Departament d'Enginyeria Electrònica
Universitat Autònoma de Barcelona
08193 Bellaterra, Barcelona, Spain
E-mail: Ferran.Martin@uab.es

***Abstract*— This paper presents a method to estimate the complex permittivity of liquids. The sensor consists of an embedded microstrip line with a complementary split ring resonator (CSRR) etched in the ground plane, beneath the conductor strip. A liquid container, surrounding the CSRR, is added to the structure in order to load the sensing element (CSRR) with the liquid under test (LUT). The complex permittivity of the LUT is inferred from the frequency response of the structure, particularly from the notch frequency and depth, without the need of reference samples for calibration. The proposed method is validated by measuring the dielectric constant and loss tangent of deionized (DI) water.**

Keywords—Metamaterials; complementary split ring resonator (CSRR); microwave sensors; complex permittivity measurements.

I. INTRODUCTION

Split ring resonators (SRRs) and complementary split ring resonators (CSRRs) have been used as sensing elements for dielectric characterization of solids and liquids [1]-[29]. For that purpose, three main sensing strategies based on SRR- or CSRR-loaded transmission lines have been considered: (i) the variation in the resonance frequency and notch depth caused by dielectric loading [1]-[11]; (ii) frequency splitting in transmission lines loaded with pairs of identical resonant elements, caused by asymmetric dielectric loading, [12]-[18]; (iii) coupling modulation in transmission lines symmetrically loaded with a single resonant element, caused by symmetry disruption [19]-[29]. The second approach (frequency splitting) is similar to differential sensing, and the permittivity of the sample under test is obtained by comparison to a reference sample. Coupling modulation sensors have been mainly used for the measurement of spatial variables (e.g. angular displacement and velocity) rather than permittivity, since symmetry disruption can be easily achieved by using movable resonant elements with regard to the host line.

In sensors based on resonance frequency variation, calibration curves, based on the use of samples with known permittivity, are typically required. In this paper, we deal with this type of sensors, in this case implemented by means of a CSRR-loaded embedded microstrip line. We report a method, based on the previous work [11], able to provide an estimation of the dielectric constant and loss tangent of a sample under test (a dielectric slab or liquid) in contact with the CSRR. The main advantage of this approach is the fact that it is not necessary to use reference samples for calibration. In particular, the objective in this paper is to apply the method for dielectric characterization of liquids. For that purpose, we have added to the CSRR-loaded embedded microstrip line a liquid container, similar to a small pool, surrounding the CSRR.

II. SENSING STRUCTURE AND SENSING METHOD

The top and cross section views and the photograph of the proposed sensor can be seen in Fig. 1. The validity of the sensing method (to be described later) is based on the uniformity of the medium surrounding the conductor strip and also on the uniformity of the dielectric load or liquid under test (LUT). For this reason, an (unusual) embedded microstrip line is considered. This uniformity refers to those regions where the electric field generated by the line and CSRR are significant. The thickness (h_2) of the dielectric layer on top of the conductor strip has been chosen to guarantee that the electric field lines do not reach the air on top of it. On the other hand, the liquid container must provide a sufficient depth (h_3) for the LUT so as to ensure that the electric field lines present in the slots of the CSRR do not cross the LUT/air interface.

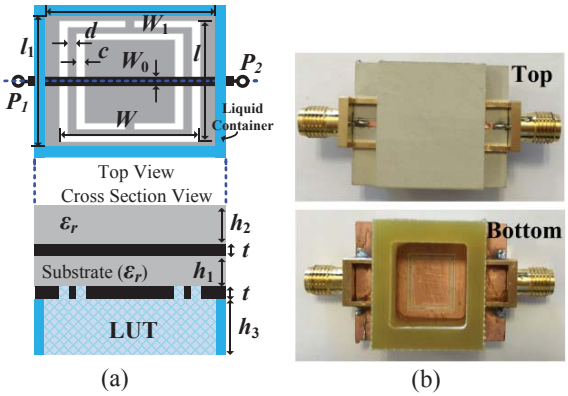

Fig. 1. Top and cross section views (a) and photograph (b) of the CSRR-loaded embedded microstrip line. Dimensions are: W = 9.6 mm, l = 11.72 mm, c = 0.4 mm, d = 0.4 mm, W_0 = 1.15 mm, W_1 = 14 mm, l_1 = 16 mm, h_1 = 1.27 mm, h_2 = 2.54 mm, h_3 = 4.8 mm and t = 35 μm.

The equivalent circuit model of the structure is depicted in Fig. 2. C_c and L_c are the capacitance and inductance, respectively, of the CSRR, whereas losses in this CSRR element include ohmic losses, R_M, plus dielectric losses, R_D, accounting for the losses in both the substrate and LUT. L models the inductance of the conductive strip and C the capacitance to the inner region of the CSRR. Note that the resistance in parallel with the line capacitance, R_s, models dielectric substrate losses. The sensing method is based on the following equations [11]

$$R_{eq} \cong \frac{1}{R_S C^2 \xi^2} \cdot \frac{R_M R_D^2 \cdot R_D L_c^2 \xi^2}{R_D^2 (1 - L_c C_c \xi^2)^2 \cdot (L_c \xi \cdot R_M R_D C_c \xi)^2} \quad (1)$$

$$\phi_{eq} \cong \frac{-1}{C\xi} \cdot \frac{R_D^2 L_c \xi (1 - L_c C_c \xi^2) - R_M R_D (L_c \xi \cdot R_M R_D C_c \xi)}{R_D^2 (1 - L_c C_c \xi^2)^2 \cdot (L_c \xi \cdot R_M R_D C_c \xi)^2} \quad (2)$$

providing the real and imaginary parts of the impedance of the shunt branch of the model, respectively, and also on the magnitude of the transmission coefficient at the frequency, ξ_0, where $\phi_{eq} = 0$, i.e. [11]

$$|S_{21}|_{\xi_0} \cong \frac{2 Z_0 R_{eq}}{\sqrt{(2 Z_0 R_{eq} \cdot Z_0^2 - L^2 \xi^2)^2 \cdot [2 L \xi (Z_0 \cdot R_{eq})]^2}} \quad (3)$$

In (1)-(3), ξ is the angular frequency and Z_0 is the reference impedance of the ports.

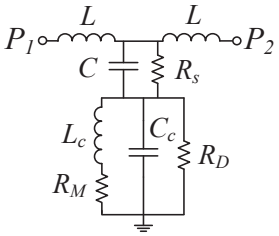

Fig. 2. Lumped element equivalent circuit of the CSRR-loaded embedded microstrip line.

All the reactive parameters of the circuit model can be extracted from parameter extraction [20],[30]. R_s and R_D (assuming that the CSRR is unloaded) can be inferred from the loss tangent of the substrate, a known parameter, according to [11]

$$\tan\gamma \cong \frac{1}{R_S C \xi} \quad (4)$$

$$\tan\gamma \cong \frac{1 \cdot \eta_r}{R_D C_c \eta_r \xi} \quad (5)$$

where η_r is the dielectric constant of the substrate. From the measurement of the transmission coefficient at ξ_0, the real part of the shunt impedance, R_{eq}, was obtained, and from it, R_M was inferred using (1). Once R_M is known, by loading the CSRR by a LUT, all the parameters remain invariable except C_c and R_D. The variation in C_c modifies the notch frequency, and the dielectric constant of the LUT can be obtained from [11].

$$\eta_{LUT} \cong 1 \cdot \frac{(\xi_0'^2 - \xi_0^2)}{L_c C_c} (1 \cdot \eta_r) \quad (6)$$

where ξ'_0 is the resonance frequency with the presence of the LUT. The resistance R_D with the presence of the LUT can be obtained from (3) and (1). Since R_D without the LUT is known, the loss associated to the LUT can be inferred, and from it, we can obtain the loss tangent of the LUT.

III. Results

The element values of the circuit model without LUT are L = 4.62 nH, C = 2.59 pF, C_c = 10.42 pF, L_c = 1.71 nH, R_s = 25088 Ω, R_D = 6839 Ω, and R_M = 0.10 Ω. By considering DI water as LUT, the dielectric losses and capacitance of the CSRR change to R'_D = 500 Ω and C'_c = 73.77 pF. These values have been inferred from the measured response of the sensor with and without LUT (DI-water), both shown in Fig. 3. From the variation of the resonance frequency, and from the new values of R'_D and C'_c, the dielectric constant and loss tangent of the LUT are found to be η_{LUT} = 69.08 and tanγ = 0.01. These values are in reasonable agreement with tabulated values of DI-water at the considered frequency (the dielectric constant is in the vicinity of 76.7-78.2, whereas the loss tangent varies between 0.005 at 100MHz and 0.157 at 3GHz).

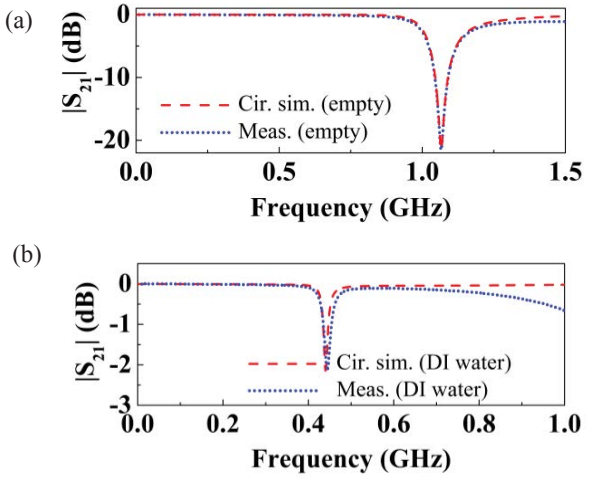

Fig. 3. Magnitude of the transmission coefficient for the considered CSRR-loaded line without (a) and with (b) LUT.

The validity of (4) and (5) is subjected to the uniformity of the dielectric below the CSRR (LUT) and substrate surrounding the conductor strip. For these reasons we have considered an embedded microstrip line. However, another approximation has been considered, i.e., it has been assumed that the thickness of the ground plane is null. This is not true in practice, and may give rise to certain tolerance in the measurement of the dielectric parameters of the LUT. Finally, it is worth mentioning that we have carried out the measurements with LUT just after loading, in order to avoid the effects of liquid absorption by the substrate. With DI-water, absorption is a slow process, but this is not the case

with other liquids such as ethanol. For this reason, the present method is valid for low-absorption liquids.

IV. Conclusions

In conclusion, we have reported a method useful to estimate the dielectric constant and loss tangent of liquids with low-absorption level. The method is based on an embedded microstrip line and the most interesting characteristic of this approach is the fact that calibration curves are not necessary. The method has been applied to the measurement of the dielectric parameters of DI-water.

Acknowledgment

This work was supported by MINECO-Spain (projects TEC2013-40600-R and TEC2016-75650-R), Generalitat de Catalunya (project 2014SGR-157), Institució Catalana de Recerca i Estudis Avançats (who awarded Ferran Martín), and by FEDER funds. Lijuan Su acknowledges the China Scholarship Council (CSC) for the grant 201306950011.

References

[1] M. Puentes, C. Weiß, M. Schüßler, and R. Jakoby, "Sensor array based on split ring resonators for analysis of organic tissues," in *IEEE MTT-S Int. Microw. Symp.*, Baltimore, MD, USA, Jun. 2011, pp. 1−4.

[2] M. Puentes, *Planar Metamaterial Based Microwave Sensor Arrays for Biomedical Analysis and Treatment*, Springer, Heidelberg, Germany, 2014.

[3] M. Schueler, C. Mandel, M. Puentes, and R. Jakoby, "Metamaterial inspired microwave sensors," *IEEE Microw. Mag.*, vol. 13, no. 2, pp. 57–68, Mar. 2012.

[4] M. S. Boybay and O. M. Ramahi, "Material characterization using complementary split-ring resonators," *IEEE Trans. Instrum. Meas*., vol. 61, no. 11, pp. 3039−3046, Nov. 2012.

[5] C.-S. Lee and C.-L. Yang, "Complementary split-ring resonators for measuring dielectric constants and loss tangents," *IEEE Microw. Wireless Compon. Lett.*, vol. 24, no. 8, pp. 563−565, Aug. 2014.

[6] C.-L. Yang, C.-S. Lee, K.-W. Chen, and K.-Z. Chen, "Noncontact measurement of complex permittivity and thickness by using planar resonators," *IEEE Trans. Microw. Theory Techn.*, vol. 64, no.1, pp. 247−257, Jan. 2016.

[7] A. Abduljabar, D. Rowe, A. Porch, and D. Barrow, "Novel microwave microfluidic sensor using a microstrip split-ring resonator," *IEEE Trans. Microw. Thory Techn*., vol. 62, no. 3, pp. 679−688, Mar. 2014.

[8] A. Ebrahimi, W. Withayachumnankul, S. Al-Sarawi, D. Abbott, "High-sensitivity metamaterial-inspired sensor for microfluidic dielectric characterization," *IEEE Sensors J.*, vol. 14, no. 5, pp. 1345−1351, May 2014.

[9] W. Withayachumnankul, K. Jaruwongrungsee, A. Tuantranont, C. Fumeaux, and D. Abbott, "Metamaterial-based microfluidic sensor for dielectric characterization," *Sensor Actuat. A Phys.*, vol. 189, pp. 233−237, Jan. 2013.

[10] A. Salim and S. Lim, "Complementary split-ring resonator-loaded microfluidic ethanol chemical sensor," *Sensors*, vol. 16, pp. 1-13, 2016.

[11] L. Su, J. Mata-Contreras, P. Vélez and F. Martín, "Estimation of conductive losses in complementary split ring resonator (CSRR) loading an embedded microstrip line and applications", *IEEE MTT-S Int. Microw. Symp.* (IMS'17), Honolulu, Hawaii, Jun. 2017.

[12] A. K. Horestani, J. Naqui, Z. Shaterian, D. Abbott, C. Fumeaux, and F. Martín, "Two-dimensional alignment and displacement sensor based on movable broadside-coupled split ring resonators," *Sensors and Actuators A*, vol. 210, pp. 18–24, Apr. 2014.

[13] J. Naqui, C. Damm, A. Wiens, R. Jakoby, L. Su, and F. Martín, "Transmission lines loaded with pairs of magnetically coupled stepped impedance resonators (SIRs): modeling and application to microwave sensors," *IEEE MTT-S Int. Microwave Symp*., Tampa, FL, USA, Jun. 2014, pp. 1–4.

[14] L. Su, J. Naqui, J. Mata-Contreras, and F. Martín "Modeling metamaterial transmission lines loaded with pairs of coupled split ring resonators," *IEEE Ant. Wireless Propag. Lett.*, vol. 14, pp. 68–71, 2015.

[15] L. Su, J. Naqui, J. Mata, F. Martín, "Dual-band epsilon-negative (ENG) transmission line metamaterials based on microstrip lines loaded with pairs of coupled complementary split ring resonators (CSRRs): modeling, analysis and applications", *9th International Congress on Advanced Electromagnetic Materials in Microwaves and Optics*, Metamaterials 2015, Oxford, UK, Sep., 7-12, 2015.

[16] L. Su, J. Naqui, J. Mata-Contreras, P. Vélez, F. Martín, "Transmission line metamaterials based on pairs of coupled split ring resonators (SRRs) and complementary split ring resonators (CSRR): a comparison to the light of the lumped element equivalent circuits", *International Conference on Electromagnetics for Advanced Applications*, ICEAA 2015, Torino, Italy, 7-11 Sep. 2015.

[17] L. Su, J. Naqui, J. Mata-Contreras, and F. Martín, "Modeling and applications of metamaterial transmission lines loaded with pairs of coupled complementary split ring resonators (CSRRs)," *IEEE Ant. Wireless Propag. Lett.*, vol. 15, pp. 154–157, 2016.

[18] L. Su, J. Mata-Contreras, J. Naqui, and F. Martín, "Splitter/combiner microstrip sections loaded with pairs of complementary split ring resonators (CSRRs): modeling and optimization for differential sensing applications," *IEEE Trans. Microw. Theory Techn*., vol. 64, pp. 4362-4370, Dec. 2016.

[19] J. Naqui, M. Durán-Sindreu and F. Martín, "Novel sensors based on the symmetry properties of split ring resonators (SRRs)," *Sensors*, vol 11, pp. 7545−7553, 2011.

[20] F. Martín, *Artificial Transmission Lines for RF and Microwave Applications*, John Wiley, Hoboken, NJ, 2015.

[21] J. Naqui, *Symmetry properties in transmission lines loaded with electrically small resonators: circuit modeling and applications*, Springer, Heidelberg, Germany, 2016.

[22] J. Naqui, M. Durán-Sindreu, and F. Martín, "alignment and position sensors based on split ring resonators," *Sensors*, vol. 12, pp. 11790−11797, 2012.

[23] A.K. Horestani, C. Fumeaux, S.F. Al-Sarawi, and D. Abbott, "Displacement sensor based on diamond-shaped tapered split ring resonator," *IEEE Sens. J*., vol. 13, pp. 1153–1160, 2013.

[24] A.K. Horestani, D. Abbott, and C. Fumeaux, "Rotation sensor based on horn-shaped split ring resonator," *IEEE Sens. J.*, vol. 13, pp. 3014–3015, 2013.

[25] J. Naqui and F. Martín, "Transmission Lines Loaded with Bisymmetric Resonators and Their Application to Angular Displacement and Velocity Sensors," *IEEE Trans. Microw. Theory Techn*., vol. 61, no. 12, pp. 4700–4713, Dec. 2013.

[26] J. Naqui and F. Martín, "Angular displacement and velocity sensors based on electric-LC (ELC) loaded microstrip lines," *IEEE Sensors J*., vol. 14, no. 4, pp. 939–940, Apr. 2014.

[27] A.K. Horestani, J. Naqui, D. Abbott, C. Fumeaux, and F. Martín, "Two-dimensional displacement and alignment sensor based on reflection coefficients of open microstrip lines loaded with split ring resonators," *Elec. Lett.*, vol. 50, pp. 620–622, Apr. 2014.

[28] J. Naqui and F. Martín, "Microwave sensors based on symmetry properties of resonator-loaded transmission lines: a review," *Journal of Sensors*, vol. 2015, Article ID 741853, 10 pages, 2015.

[29] J. Naqui, J. Coromina, A. Karami-Horestani, C. Fumeaux, and F. Martín, "Angular displacement and velocity sensors based on coplanar waveguides (CPWs) loaded with S-shaped split ring resonator (S-SRR)," *Sensors*, vol. 15, pp. 9628–9650, 2015.

[30] J. Bonache, M. Gil, I. Gil, J. Garcia-García and F. Martín, "On the electrical characteristics of complementary metamaterial resonators", *IEEE Microw. Wireless Compon. Lett*., vol. 16, pp. 543.545, Oct. 2006.